HIERARCHICALLY POROUS SILICATE MATERIALS FOR CATALYTIC APPLICATIONS

SHENG YUAN

(B. Eng. (Hons.), NUS)

A THESIS SUBMITTED

FOR THE DEGREE OF DOCTOR OF PHILOSOPHY

DEPARTMENT OF CHEMICAL & BIOMOLECULAR ENGINEERING

NATIONAL UNIVERSITY OF SINGAPORE

2016

DECLARATION

I hereby declare that this thesis is my original work and it has been written by me in its entirety. I have duly acknowledged all the sources of information which have been used in the thesis.

This thesis has also not been submitted for any degree in any university previously.

Sheng Yuan

22 Apr 2016

Acknowledgments

My doctoral study has been a fulfilling but by no means easy journey. On completion of the thesis, I would like to extend my gratitude to a number of important people, without whom I could not have made it.

I owe my deepest gratitude to Prof. Zeng Hua Chun, my thesis advisor, for his invaluable guidance on my research work and personal development in these years. Prof. Zeng is the best advisor and mentor I could ever imagine. His research philosophy has had profound influence on me, and his patience, encouragement and expertise have always kept me motivated. I thank Prof. Zeng for his unreserved help during my most difficult time.

I am heartily grateful to Dr. Xiong Shenglin, Dr. Xi Baojuan, Mr. Yec Christopher Cheung, Dr. Dou Jian, Dr. Liu Minghui, Dr. Li Ping, Dr. Li Zheng, Dr. Li Xuanqi, Dr. Li Chengchao, Ms. Zhou Yao, Mr. Zhan Guowu, Ms. Hua Dan, Mr. Tan Ying Chuan, Mr. Li Bowen, Mr. Kwok Mingyao, Mr. Qin Runze, and Ms. Wang Jingjing, for their helping hand, fruitful discussions and the warm, friendly atmosphere at work. I feel fortunate to have met and worked with them as a team.

My sincere thanks go to Ms. Khoh Leng Khim, Mr. Chia Phai Ann, Mr. Mao Ning, Mr. Liu Zhicheng, Dr. Yuan Ze Liang, Ms. Fam Hwee Koong, Mr. Rajamohan s/o K Suppiah, Ms. Lim Bee Kee, Ms. Ngai Kai Ting, Ms. Li Fengmei, Mr. Ng Kim Poi, Mr. Chan Chuin Mun, Mr. Ang Wee Siong, Mr. Tan Evan Stephen, and other laboratory staff for their technical support.

I would like to give special thanks to my wife, my parents, and other family members for their unconditional love and understanding.

Last but not least, the financial support from the National University of Singapore is gratefully acknowledged.

Table of Contents

Summary

Nanomaterials are a central topic of today's materials science research. As knowledge and experience in this field accumulate, materials with complex nanostructures have drawn increasing attention due to their highly integrated functionality. In particular, hierarchically porous nanomaterials have promising applications in catalysis, but their synthesis remains challenging to date. In this thesis, novel hierarchically porous silicate materials were developed for applications in catalytic hydrogenation of CO_2. The thesis consists of four self-contained works, each of which focuses on one type of material.

Firstly, single-walled copper silicate nanotubes (CuSiNTs) in the form of hierarchical assemblages were synthesized hydrothermally, followed by tuning of their composition *via* ion exchange of Cu^{2+} with Mn^{2+}, Fe^{2+}, Co^{2+}, Ni^{2+}, or Zn^{2+}. Two types of assemblages of CuSiNTs, *i.e.* hollow spheres and ordered bundles were obtained by tuning the growth kinetics of the copper silicate. Up to 80% of Cu in the CuSiNTs was successfully replaced by the dopant elements with the tubular structure kept intact. Methanol synthesis from catalytic CO_2 hydrogenation was then studied using the pristine and Zn- and/or Ni-doped materials, showing positive effects of the doping on activity and selectivity. A higher metal utilization was also achieved compared with commercial $Cu/ZnO/Al_2O_3$ catalysts.

Secondly, monodisperse silica/aluminosilicate spheres with tunable Al content and macro-meso-microporous structures were synthesized in one step for the first time. Simultaneous formation of pores in different length scales was made possible by sol-gel processing in a water-ethanol-toluene-CTAB microemulsion system. Hofmeister anion effects of the Al source, $[Al(OH)_4]^-$, were found to be an important factor determining the pore structure. Loading the hierarchically porous materials with Cu

and ZnO led to significant activity in methanol synthesis from CO_2 hydrogenation, and with the incorporation of Al, bi-functional catalysts were obtained which further produced dimethyl ether from the methanol formed *in situ*.

Thirdly, a sustainable, simple alcohol-assisted synthesis method of hierarchical EMT-type zeolite without using conventional organic structure-directing agents was developed. The alcohol used in the synthesis was recycled, and the mother liquor recovered after separation of zeolite product was used for further synthesis of the same zeolite, thus improving materials utilization and reducing waste production significantly. The role of alcohols in the control of zeolite polymorphism and the hierarchical structure was discussed. When impregnated with Pt and Na species, the hierarchical zeolite served as a highly selective, active and stable catalyst for low-temperature CO production from CO_2 hydrogenation.

Finally, integrated nanocatalysts with ZSM-5 zeolite cores and hierarchically assembled Cu/Zn silicate shells were prepared, highlighting the application of chemically resistant resorcinol-formaldehyde resin as removable structural spacer in the difficult construction of multicomponent silicate materials. The structural integrity and chemical properties of the zeolite cores were successfully preserved during the hydrothermal synthesis of the silicate shells. The bifunctional nanocatalysts were thus able to catalyze hydrogenation of CO_2 into methanol and further convert it *in situ* into dimethyl ether and hydrocarbons.

Publications Related to the Thesis

1. Sheng, Y.; Zeng, H. C., Structured assemblages of single-walled 3d transition metal silicate nanotubes as precursors for composition-tailorable catalysts. *Chem. Mater.* **2015,** *27*, 658-667

2. Sheng, Y.; Zeng, H. C., Monodisperse aluminosilicate spheres with tunable Al/Si ratio and hierarchical macro-meso-microporous structure. *ACS Appl. Mater. Interfaces* **2015,** *7*, 13578-13589

3. Sheng, Y.; Zeng, H. C., Hierarchical EMT-type zeolite for Pt-catalyzed selective CO production by CO_2 hydrogenation. (to be submitted)

4. Sheng, Y.; Zeng, H. C., Integration of ZSM-5 nanocrystals with Cu/Zn-based catalyst for direct dimethyl ether synthesis by CO_2 hydrogenation. (in preparation)

List of Tables

List of Figures

List of Schemes

List of Symbols and Abbreviations

Symbols

$1/T_1$	spin-lattice relaxation rate
A_i	peak area of element *i* in XPS spectra
a, b, c	lattice parameters
a_h	effective area of head group of a surfactant molecule
D_g	geometric mean diameter
D_{pore}	pore diameter
d	interplanar spacing
E_a	apparent activation energy
g	surfactant packing parameter
l	effective length of hydrophobic tail of a surfactant molecule
M_i	atomic weight of element *i*
R_w	weighted-profile *R*-factor in Rietveld analysis
R_{exp}	expected *R*-factor in Rietveld analysis
RSF_i	relative molar sensitivity factor of element *i* in XPS analysis
S_{BET}	specific surface area calculated by the BET method
V_{meso}	specific mesopore volume
V_{micro}	specific micropore volume
w_i	weight fraction of element *i*
λ	wavelength
θ	diffraction angle
σ_g	geometric standard deviation

Abbreviations

2-D / 3-D	2-dimensional / 3-dimensional
AAM	anodic alumina membrane
AcO	acetate
ATIP	aluminum triisopropoxide
acac	acetylacetonate
a. u.	arbitrary unit
BET	Brunauer-Emmett-Teller
BJH	Barrett-Joyner-Halenda
B.E.	binding energy
CTAB	cetyltrimethylammonium bromide
CTA^+	cetyltrimethylammonium ion
CuSiNT	copper silicate nanotube
DME	dimethyl ether
EDTA	ethylenediaminetetraacetic acid
EDX	energy dispersive X-ray spectroscopy
en	ethylenediamine
FFT	fast Fourier transform
FTIR	Fourier transform infrared spectroscopy
GC	gas chromatography
HAADF	high-angle annular dark-field (electron imaging technique)
ICP-OES	inductively coupled plasma optical emission spectroscopy
IR	infrared
IUPAC	International Union of Pure and Applied Chemistry
JCPDS	Joint Committee on Powder Dffraction Standards
MASS / MSS	macro-meso-microporous aluminosilicate / silica
MCM-41	Mobil Composition of Matter No. 41 (mesoporous material)

MTO	methanol-to-olefins
$mSiO_2$	mesoporous silica
MAS NMR	magic-angle spinning nuclear magnetic resonance
NLDFT	non-local density functional theory
NMR	nuclear magnetic resonance
N. A.	not applicable
OSDA	organic structure-directing agent
PDDA	polydiallyldimethylammonium chloride
PDF	Powder Diffraction File
PEO	polyethylene oxide
PS	polystyrene
PU	polyurethane
PVP	polyvinylpyrrolidone
RF	resorcinol-formaldehyde (resin)
RWGS / WGS	reverse water gas shift / water gas shift
SDA	structure-directing agent
SEM	scanning electron microscopy
STEM	scanning transmission electron microscopy
std	standard conditions
TEM	transmission electron microscopy
TEOS	tetraethyl orthosilicate
TOF	turnover frequency
TON	turnover number
TPAOH	tetra-n-propylammonium hydroxide
TTAB	tetradecyltrimethylammonium bromide
USY	ultra-stable zeolite Y
XPS	X-ray photoelectron spectroscopy
XRD	X-ray diffraction

Chapter 1. Introduction

1.1. Overview

In recent years, fast advance in nanoscience and nanotechnology has realized microscopic control of structure of materials on an unprecedented level. For example, catalytically active precious metal nanoparticles can be synthesized with very narrow size distribution and/or accurately controlled shapes.[1-2] Many materials traditionally used as catalyst supports such as carbon, SiO_2, Al_2O_3, and TiO_2 have also been produced with highly ordered mesoporous structures.[3-6] In terms of catalyst preparation, this has led to widespread interest in nanocatalysts which usually refer to free-standing, catalytically active nanoparticles,[7] though the active phase of many conventional catalysts also exists as nanoparticles. As the ability to manipulate materials in the nanometer range paved the way for the design and synthesis of more complex nanomaterials, studies on nanomaterials with more than one component and 3-dimensional structures have become common.[8-11] In fact, the structural complexity may be extended beyond the nanoscale, for example by organizing composite nanoparticles further into micrometer-scale assemblages, affording the possibility of preparing integrated nanocatalysts.[12] Such catalysts possess well-defined hierarchical structures consisting of one or more nanometer-scale active phases (*e.g.* precious metal nanoparticles) and nano-structured catalyst supports (*e.g.* mesoporous SiO_2), but their overall size may be large so that the catalysts can be easily separated from reactants/products. Obviously the active phase should be in the form of fine particles for maximal material utilization, and structure of the catalyst support essentially determines structure of the composite nanocatalyst. Synthesis of support materials with tightly controlled hierarchical structure and porosity is, therefore, critical to successful construction of complex nanostructured catalysts. While extensive

research has been carried out on porous materials, it is worth noting that synthesis of hierarchically porous materials suitable for integrated nanocatalysts still remains a challenging topic and complicated synthesis methods are often required.[13]

Among various materials commonly used in heterogeneous catalysis, silicates stand out as an ideal choice for the study of hierarchically structured catalyst supports. Silicates are the most abundant naturally occurring minerals. The basic unit of silicate materials, *i.e.*, the SiO_4 tetrahedrons, can connect in different ways either among themselves or with oxo/hydroxyl complexes of other metals, giving this group of materials enormous possibilities in terms of chemical property and microscopic structure.[14] In the presence of hard or soft templates, silicates form porous structures relatively easily (which will be elaborated in the following chapters), and silica sources used to prepare silicate materials are widely available at very low cost.[15] In addition, silicates generally do not pose significant impact on the environment.

In the field of environmental technologies, CO_2 utilization forms a fast growing area of research.[16] As global warming gains awareness of the public, there has been increasing attention to the development of technologies for reduction of carbon footprint. In contrast to CO_2 sequestration, conversion of CO_2 into useful chemicals is potentially a permanent solution to CO_2-induced greenhouse effect and probably more importantly, to the current dependence of industry on fossil fuels.[17] Considering the significant progress made in the production of H_2 with renewable energy, a future chemical industry based on CO_2 and H_2 may be possible, where fuels and basic chemical feedstocks such as ethylene are mainly produced by hydrogenation of captured CO_2 with renewable H_2, achieving zero net emission.[18] However, due to the chemical inertness of CO_2, its hydrogenation kinetics is sluggish.[17] Development of efficient catalysts for CO_2 hydrogenation is thus of paramount importance to the proposed sustainable chemical industry.

1.2. Objectives and scope

This thesis is focused on development of hierarchically porous silicate materials that are useful either as active catalysts or as catalyst supports in CO_2 hydrogenation reactions. It aims at exploration of novel synthesis strategies, understanding of the underlying science of the synthesis processes, and exploitation of unique properties of the abovementioned materials at the same time. More specifically, hierarchically porous structures are constructed from materials including clay-type transition metal silicate, amorphous silica/aluminosilicate, and aluminosilicate zeolites. According to the chemical properties of each type of material, hydrothermal or sol-gel synthesis method is chosen, and different methods of pore generation, *i.e.*, hard template-based, soft template-based or template-free syntheses is involved. TEM as the main tool of characterization is used extensively to understand the formation of the hierarchical structures, which in combination with other analytical techniques including XRD, SEM, EDX, FTIR, NMR, ICP-OES, and N_2 sorption gives a full picture of physicochemical properties of the materials. Applications of the materials are demonstrated in laboratory-scale catalytic CO_2 hydrogenation experiments. In some cases where the silicate material serves as catalyst support only, additional active components are introduced through impregnation. While mechanistic studies are necessary to a deep understanding of catalysis, extended research in this area is beyond the scope of the thesis, and the catalytic reactions are mainly discussed on the basis of the materials chemistry of the catalysts.

1.3. Organization of the thesis

This thesis consists of eight chapters that are summarized as follows:

Chapter 1 provides a very brief background and motivation for the present work. The significance of developing hierarchically porous silicate materials and CO_2 utilization technologies is highlighted, followed by the introduction of the general methodology adopted in this work.

Chapter 2 mainly reviews methods of synthesizing (hierarchically) porous silicate materials in sections that focus on clay-type silicates, amorphous silica, and zeolites, respectively. In addition, important catalysts for CO_2 hydrogenation are also discussed selectively in a separate section.

Chapter 3 concerns the characterization techniques involved in this thesis. The type of instrument, general sample preparation procedures, and other parameters affecting the results are described in detail. Information specific to individual projects, however, is included in the corresponding chapters.

Chapter 4 to Chapter 7 present four projects under the main topic of the thesis, featuring single-walled transition metal silicate nanotubes, macro-meso-microporous amorphous silica/aluminosilicate spheres, hierarchical EMT-type zeolite, and composite nanocatalysts with zeolite ZSM-5 cores and Cu/Zn silicate shells, respectively. Each of the chapters focuses on a different synthesis strategy and tackles a different challenge. In terms of synthesis strategy, Chapter 4 uses hard-templated, Chapter 5 dual soft-templated, Chapter 6 template-free method, and Chapter 7 uses a multi-step synthesis involving both hard and soft templates to integrate two materials closely related to Chapter 4 & 6. The difficulty of synthesis method in the four chapters follows an increasing trend. As for challenges addressed, Chapter 4 mainly deals with compositional tailoring, Chapter 5 with simultaneous control of meso/macropore size and overall particle size polydispersity, Chapter 6 with control

of zeolite polymorphism which determines its microporosity, and Chapter 7 with the instability of silicate materials during sequential hydrothermal synthesis. Together the four projects present a relatively full picture of property tuning of hierarchically porous silicate materials.

Finally, Chapter 8 includes general conclusions and recommendations for future research.

Chapter 2. Literature Review

This chapter mainly reviews the synthesis strategies for three types of porous silicate materials: clays, amorphous silica/aluminosilicate, and zeolites. Generation of hierarchical porosity, in particular, forms the focus of the review. In addition, catalysts used for CO_2 hydrogenation into methanol and CO in reported works are also briefly introduced.

2.1. Synthesis of porous clay materials

Clay materials are a group of phyllosilicates, which have layered structures as the name suggests. Figure 2.1 illustrates that in this type of materials, SiO_4 tetrahedrons share 3 of their 4 corner oxygen atoms to form six-membered rings in an extended sheet, leaving the fourth corner pointing to the same direction of the sheet. The "hanging" corners of the tetrahedrons are shared with a layer of metal ions (Al^{3+}, Mg^{2+} and/or Fe^{3+} typically) octahedrally coordinated by oxygen atoms. If the metal ions are divalent, all of the octahedral sites are occupied and the clay is trioctahedral. If the metal ions are trivalent, however, one third of the octahedral sites are vacant and the clay is dioctahedral. In addition, the octahedral layer may be connected to one tetrahedral layer on one side or to two tetrahedral layers on both sides, forming 1:1 or 2:1 clays, respectively. The silicate layers stack together, and the interlayer space is filled with water and metal ions that balance the negative charge of the silicate layers caused by isomorphous substitution of Si^{4+} with trivalent ions such as Al^{3+}.[19]

Due to weak interaction between silicate layers in clay materials, the interlayer contents are often exchangeable, leading to the possibility of generating pores by pillaring the silicate layers with bulky ion clusters.[20] On the other hand, the silicate

layers in a number of clay materials are flexible enough to curl to form pores outside the interlayer space. The two methods of pore generation will be discussed in separate sections to follow.

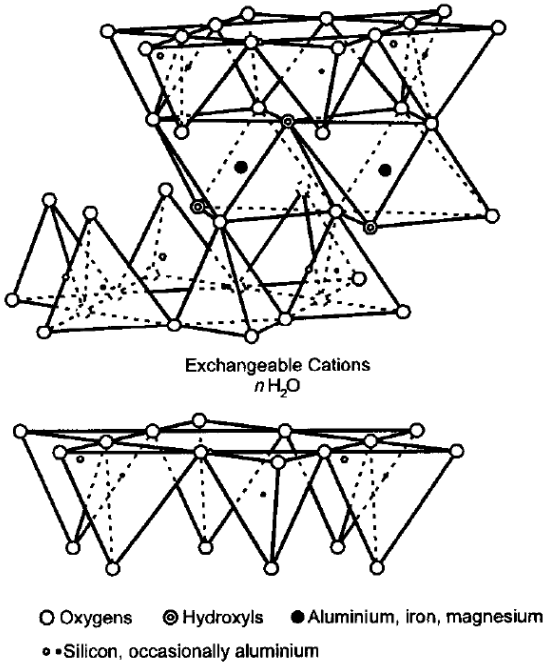

Figure 2.1. Structure of smectites, a class of 2:1 clay material.[21] Figure reproduced with permission from ref 21. Copyright 1999 Mineralogical Society of Great Britain and Ireland.

2.1.1. Pillared clay materials

The process of pillaring clay materials is essentially to force open the interlayer space and to fix the loosened structure for accessible pores. This is typically done by first saturating the interlayer space of a natural clay material with Na^+, then exchanging the Na^+ with bulky pillaring agents, and finally calcination to crosslink the pillaring agents with the silicate layers.[22] While there is a wide selection of pillaring agents as summarized in Table 2.1, the polyoxycation $[Al_{13}O_4(OH)_{24}(H_2O)_{12}]^{7+}$ (abbreviated as Al_{13}) is by far the most studied. In addition to the low cost of Al sources, advantages of using Al_{13} to prepare pillared clays are that the solution chemistry of Al^{3+} is well-established and that it can be synthesized with high yield from controlled hydrolysis of Al^{3+} salts.[23] Upon calcination, Al_{13}

converts to highly stable Al_2O_3 clusters and leaves uniform micropores in the interlayer space. Besides Al, other polycation-forming elements including Zr, Ti, Cr and Fe have also been frequently used in the synthesis of pillared clays. They generate slightly larger pores in the microporous range, but with a wider size distribution.[22]

Table 2.1. Selected examples of common pillaring agents[22]

Type of pillaring agent	Examples
Organic cations	Alkylammonium
	Dialkylammonium
Organometallic cations	$[Co(en)_3]^{3+}$
	$[Si(acac)_3]^{3+}$
	$[Fe_3O(AcO)_6AcOH]^{+}$
Metal clusters	$[Nb_6Cl_{12}]^{n+}$, $[Ta_6Cl_{12}]^{n+}$, $[Mo_8Cl_8]^{4+}$
Polyoxycations	$[Al_{13}O_4(OH)_{24}(H_2O)_{12}]^{7+}$
	$[Zr_4(OH)_8(H_2O)_{16}]^{8+}$
	$[(TiO)_8(OH)_{12}]^{4+}$
	$[Cr_n(OH)_m]^{(3n-m)+}$
	Hydrolyzed Fe salts
Oxide sols	TiO_2, TiO_2-SiO_2
	Imogolite

An interesting example of pillaring agents that lead to hierarchical pore structures is imogolite, being a microporous silicate material itself. Imogolite is an orthosilicate mineral that occurs naturally as nanotubes with an outer and inner diameter of *ca.* 2.3 nm and 0.8 nm, respectively. Its wall structure consists of a layer of orthosilicate SiO_4 tetrahedrons in the inner side and a layer of AlO_6 octahedrons in the outer side.[24] As depicted in Figure 2.2, imogolite nanotubes can intercalate other layered clay materials, probably facilitated by hydrogen bonding or positive charge of imogolite induced by a pH much lower than its isoelectric point.[25] The resultant pillared clay has both interlayer 2–3 mesopores and 0.8 nm micropores intrinsic to imogolite.

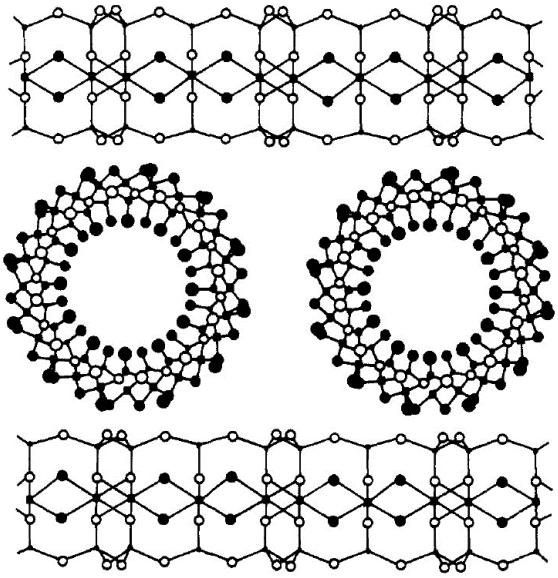

Figure 2.2. Structure of an imogolite-pillared montmorillonite clay.[25] Figure reproduced with permission from ref 25. Copyright 1988 American Chemical Society.

However, pillaring of clays has in general limited application in preparing hierarchical structures. Intercalation into the interlayer space becomes increasingly difficult for bulkier pillaring agents, and as a result, most pillared clays only possess micropores. Although colloidal pillaring agents such as SiO_2 and TiO_2 can afford mesopores, size control of the pores is poor.[26]

2.1.2. Curled layer clay materials

Compared with pillaring, directing the curling of silicate layers of clay materials is a better strategy of generating larger (*i.e.*, meso- or even macro-) pores. In fact, the structure of some clay materials causes an intrinsic tendency of curling, with halloysite being a good example. It is a 1:1 dioctahedral aluminosilicate clay closely related to kaolinite.[27] The mismatch between the tetrahedral layer (a = 5.02 Å, b = 9.164 Å) compared and the octahedral layer (a = 5.066 Å, b = 8.655 Å) of halloysite leads to a stress that favors curling towards the tetrahedral layer and hence formation of nanotubes. Depending on location of the deposit, naturally occurring halloysite nanotubes may have inner diameter ranging from 5 nm to 70 nm, wall thickness of up to 100 nm and length of up to several μm.[28] Besides the relatively large cylindrical

mesopore/macropore in the center of the nanotubes, halloysite also possesses smaller, slit-like micropore/mesopore formed in the interlayer space upon dehydration.[29] Various functional materials such as enzymes and precious metal nanoparticles can be loaded into the pores of different scales for applications in catalysis or drug delivery,[30-32] but wide variation in the properties of natural halloysite poses a significant problem in applications that require well-defined composition and pore structure.[28] In these cases, synthetic halloysite analogues show more potential.

Synthesis of halloysite-like materials takes advantage of the similarity between halloysite and kaolinite, a common mineral that can be obtained in high purity. The silicate layers in both minerals have essentially the same structure, the only difference being that halloysite is filled with a monolayer of water in the interlayer space while kaolinite is not.[27] Therefore the silicate layers in kaolinite stack more densely, giving a rigid, platy structure. However, under appropriate conditions the kaolinite structure can swell up and exfoliate, and subsequently the freestanding thin sheets curl into tubular shapes under the effect of the abovementioned intrinsic stress. An example of such exfoliation-rolling methods is illustrated in Scheme 2.1.[33] Briefly, silicate layers in kaolinite were first grafted with methoxy groups to enhance accessibility of the interlayer space. Cetyltrimethylammonium chloride was then used to induce further intercalation and exfoliation of the modified kaolinite, eventually leading to formation of halloysite-like nanoscrolls. Notably, the nanoscrolls contain significant quantity of the intercalated organics in their interlayer space and hence differ from typical halloysite nanotubes. Figure 2.3 shows that the halloysite-like materials prepared by this approach have a relatively uniform tubular structure with an interlayer space determined by the intercalation species. Other than long-chain quaternary ammonium salts,[33-34] a variety of organic compounds can be used for the intercalation/exfoliation that include but are not limited to urea, acetates, alkylamines, and hydrophilic polymers.[35-39]

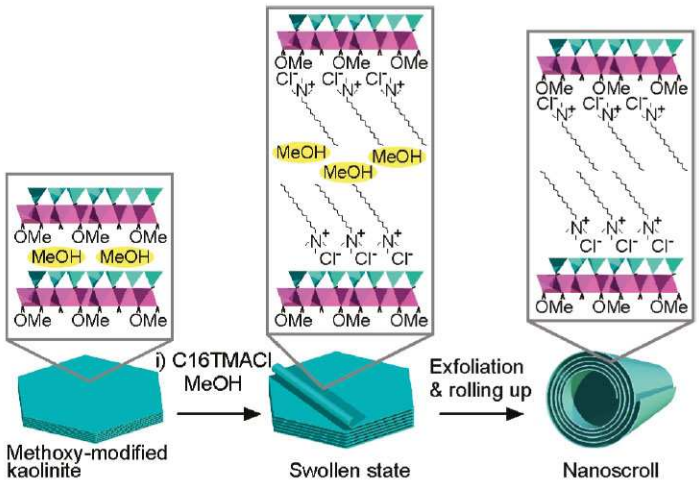

Scheme 2.1. Schematic illustration of synthesis of tubular halloysite-like materials from kaolinite.[33] C16TMACl stands for cetyltrimethylammonium chloride. Figure reproduced with permission from ref 33. Copyright 2011 American Chemical Society.

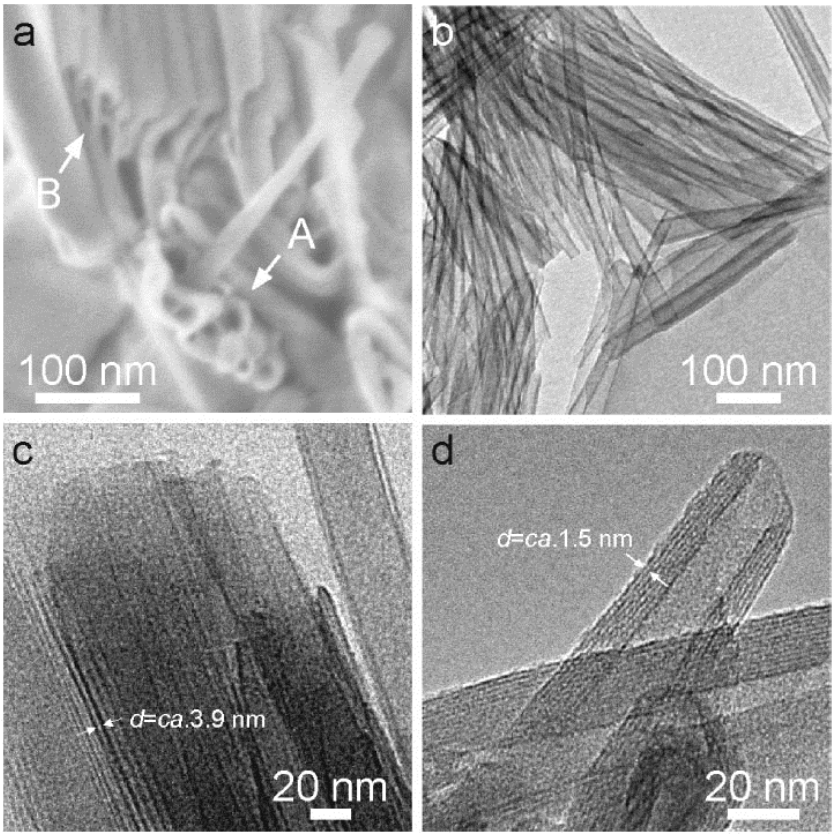

Figure 2.3. (a) SEM and (b–d) TEM images of halloysite-like material synthesized by intercalation of (a–c) C16TMACl or (d) 3-aminopropyltrimethoxysilane in kaolinite. Arrow A points to nanoscrolls while Arrow B points to exfoliated and folded silicate sheets.[33] Figure reproduced with permission from ref 33. Copyright 2011 American Chemical Society.

In contrast to the exfoliation-rolling methods which retain the layered structure of clay-type precursors, hydrothermal synthesis of curled layer clays relies less on the

structure of precursor, as extensive dissolution-reconstruction is involved and silicate layers in the products can be formed *in situ* from much simpler units such as silicate oligomers.[40] For example, starting from Na_2SiO_3 and soluble metal salts, Mg, Ni, Cu, Ca, Ba, and Cd silicate nanotubes with serpentine-type clay structure have been synthesized through hydrothermal treatment of amorphous silicate precipitates in alkaline conditions.[41-43] The nanotubes have uniform inner/outer diameters and are loosely aggregated. Due to the similar ionic radii of Mg^{2+} and many first-row transition metal ions (Table 2.2), isomorphous substitution between them occurs easily as it does in natural clay minerals. It provides large potential for functionalization of clay materials. Indeed, Mg-Ni silicate nanotubes with tunable Mg/Ni ratios have been obtained by hydrothermal methods and used for catalysis and chemical sensing.[44-45]

Table 2.2. Crystal ionic radius of Mg^{2+} and first-row transition metal ions[46]

Ion	Mg^{2+}	Mn^{2+}	Fe^{2+}	Co^{2+}	Ni^{2+}	Cu^{2+}	Zn^{2+}
Radius (pm)	86	97*	92*	88.5*	83*	87	88

*high spin assumed for these ions

A significant advantage of hydrothermally synthesizing porous clay is the possibility of directing the formation of organized secondary structures using templates. Ideally, primary clay structures (*e.g.* nanotubes) will assemble to form an outline of a solid precursor after its depletion, thus leading to a hierarchically organized structure. Amorphous SiO_2 often serves as the sacrificial template and metal ions are supplied from the solution. Through alkaline hydrothermal treatment, Mg, Mn, Fe, Co, Ni, Cu, and Zn silicates in the form of porous hollow spheres or tubes have been synthesized from SiO_2 spheres or tubes, respectively.[10, 47-52] In these materials, the metal silicates occur as thin, curled sheets. Due to fast formation and curvature of the sheets, they interact loosely with each other instead of stacking into dense layered structures. Large amount of mesopores and high surface areas

(exceeding 600 m^2/g for example)[51] are therefore obtained. It is worth noting that the hydrothermally synthesized Mn and Cu silicate clays exhibit particularly interesting primary structures of thin-walled nanobubbles[48] and nanotubes,[50] respectively, with diameters below 10 nm as seen in Figure 2.4. The morphology of the Mn silicate has been attributed to template effects of CO_2 gas bubbles formed *in situ*,[48] but formation mechanism of the Cu silicate nanotubes is poorly understood. Nevertheless, the examples above have demonstrated simultaneous structural control in different length scales, a prerequisite to syntheses of hierarchically porous materials.

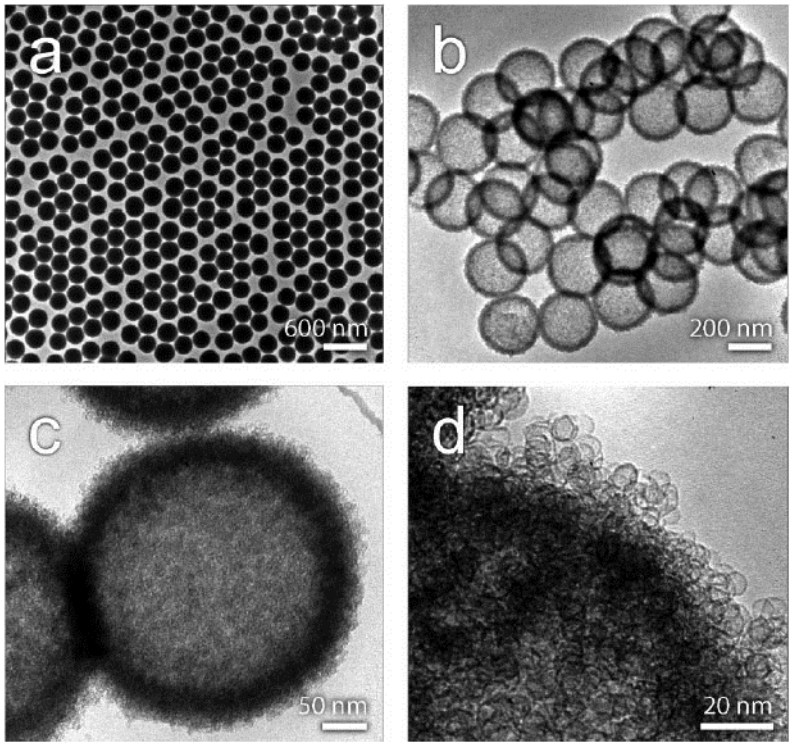

Figure 2.4. TEM images of (a) SiO_2 spheres and (b–d) hierarchical Mn silicate hollow spheres synthesized from the SiO_2 spheres.[48] Figure reproduced with permission from ref 48. Copyright 2014 American Chemical Society.

In addition to hollow structures, the hydrothermal method has also been used to prepare more complex yolk-shell composite materials. Basically, the "yolk" is encapsulated in amorphous SiO_2 prior to silicate synthesis, and remains in the void space left after dissolution of SiO_2. For example, Au nanoparticle yolks with hierarchical Mn silicate shells have been obtained from Au@SiO_2 core-shell spheres in an otherwise typical hydrothermal synthesis of hierarchical Mn silicate hollow

spheres (Figure 2.5).[53] Following the same strategy, other materials including Fe_3O_4, Ag, Au-Pd alloy, MoO_2, and carbon nanotubes have also been incorporated into hierarchically structured Mg, Cu, and Mn silicates.[49, 53-56] However, despite being convenient, this method exposes the encapsulated material to severe hydrothermal condition and is hence only suitable for integration of stable phases.

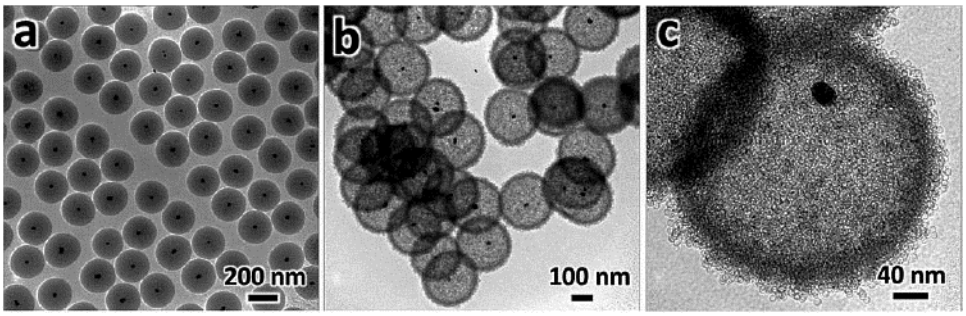

Figure 2.5. TEM images of (a) Au@SiO_2 core-shell spheres and (b,c) Au@hierarchical Mn silicate yolk-shell particles derived from the former.[53] Figure reproduced with permission from ref 53. Copyright 2015 Wiley.

2.2. Synthesis of hierarchically porous amorphous silica/aluminosilicate

Compared with clay materials, amorphous silica and aluminosilicate have much less defined crystal structure. Therefore no intrinsic tendency to form porous structures exists in this type of material, and templates are necessary to the generation of pores in amorphous silica/aluminosilicate. Since the first report on synthetic mesoporous molecular sieve MCM-41,[57] tremendous research has been carried out on the synthesis of ordered mesoporous silica. In most cases, it is synthesized by sol-gel processing where the product precipitates over time from a clear precursor sol containing silica source and templates. A large number of micelle-forming amphiphilic compounds including ionic surfactants,[58] non-ionic surfactants and block copolymers[59] are commonly used as template species. The nature and concentration of the template, polarity of solvent, temperature, ionic strength, acidity, and presence of micelle-swelling agents can all affect the geometry and size of mesopores in the

final product.[57, 60-62] Studies on this topic have formed a well-established field, and synthesis of ordered mesoporous silica with precisely controlled topology and pore size between 2–30 nm has become routine. However, pure silica is a rather inert material and its functionalization requires incorporation of other elements. Al is the most common heteroatom introduced to silica for catalytically active acid sites. Although the chemistry of silica and amorphous aluminosilicate is different, their syntheses generally follow the same template-based strategy; Al is either introduced together with Si sources or grafted onto pre-synthesized silica. The incorporation of Al will be covered in more details in Chapter 5. Considering the availability of excellent reviews on the synthesis of mesoporous silica,[4, 15, 63-64] this section will focus on hierarchically porous structures consisting of not only mesopores. To be specific, methods of simultaneously generating mesopores and macropores will be reviewed.

2.2.1. Combined hard and soft templates

While ordered mesopores are almost invariantly generated by micelle-forming soft templates, the most straightforward way of creating macropores seems to be replicating the shape of hard templates. Natural products with macroporous structures such as wood have been used as template, the mineralization of which in the presence of surfactant and silica source resulted in macro-mesoporous replica of the wood structure.[65] However, for more well-defined porosity, synthetic templates are required. One of the most widely used hard templates in the synthesis of ordered macro-mesoporous silica is polystyrene (PS) spheres. They are produced commercially through emulsion polymerization, and are readily available as monodisperse particles with diameter of several tens of nm to over 1 μm. As depicted in Scheme 2.2, the hard templates can be used either in an assembled, colloidal crystal form or in a free-standing particulate form (a close-packed superlattice of the PS particles is easily obtained by controlled evaporation of solvent in a PS colloid).[13, 66] In the first case, a precursor sol is allowed to fill the inter-particle voids in the hard template assemblage

and condense into a silica framework. In the second case, the colloidal hard template is suspended in a precursor sol and silica is coated onto the template to form a shell. With presence of an additional micelle-forming template in the sol, hierarchical macro-mesoporous silica is obtained.

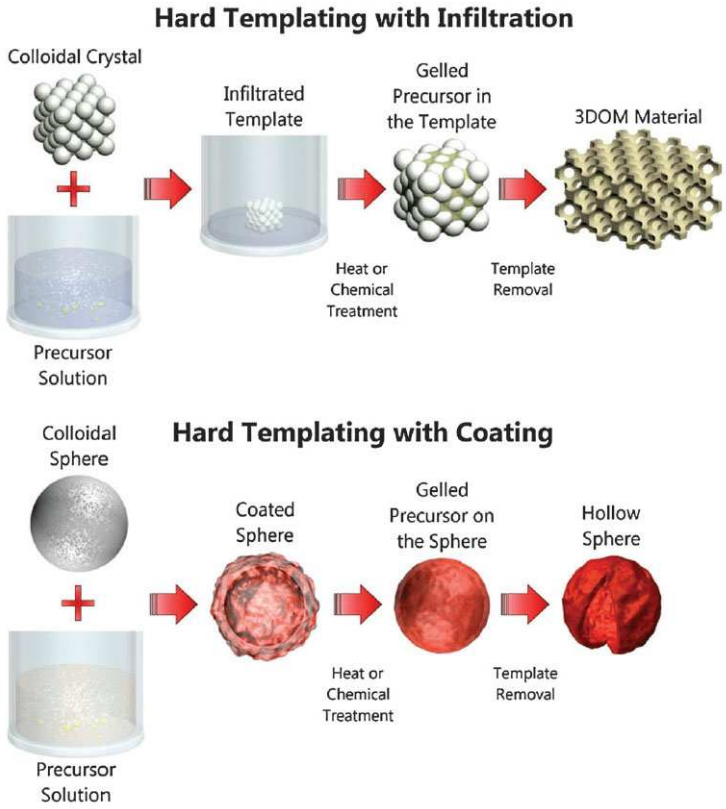

Scheme 2.2. Creation of macropores using colloidal hard templates.[13] Figure reproduced with permission from ref 13. Copyright 2013 Royal Society of Chemistry.

In one example shown in Figure 2.6, a sol containing TEOS, Pluronic F127 block copolymer and HCl was allowed to infiltrate the PS spheres assemblage, followed by gelation and calcination to form a hierarchically porous silica monolith with highly ordered structures in both the mesoporous and the microporous regime.[67] Importantly, the macropores are interconnected so that the whole internal surface is accessible. The interconnection is apparently a result of direct contact between template PS spheres. It was later shown that the size of such openings could be conveniently tuned by annealing the PS assemblage at different temperatures, as the contact area between PS spheres increased with more extensive heat treatment.[68]

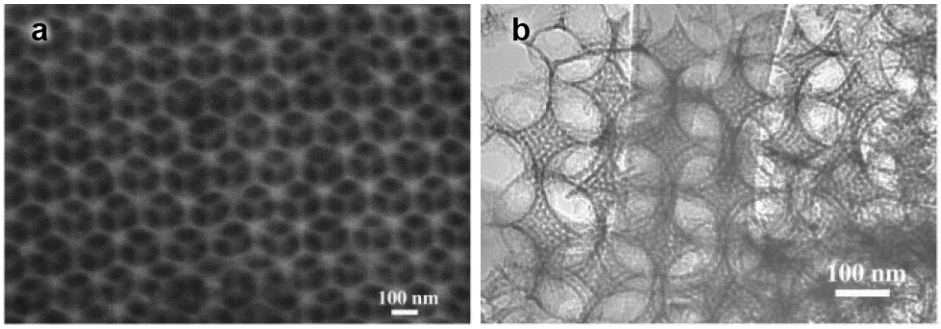

Figure 2.6. (a) SEM and (b) TEM images of a hierarchically macro-mesoporous silica monolith prepared with polystyrene beads-block copolymer dual templates.[67] Figure reproduced with permission from ref 67. Copyright 1998 American Association for the Advancement of Science.

On the other hand, when used in a free-standing state, PS spheres can direct the formation of relatively well-separated hollow mesoporous silica spheres. The material shown in Figure 2.7, for example, was obtained by sol-gel growth of CTA^+-templated silica on suspended PS spheres and subsequent removal of templates through calcination.[69] Unlike colloidal crystals that retain precursor sols by capillary forces, free-standing templates rely on affinity of silicate species to their surface. Use of bare PS spheres as template has the issue of weak interaction with silica sources due to the nonpolar nature of PS, and surface modification is necessary.[70] However, the modification step is not always mentioned because commercially available PS spheres are already modified by stabilizers used during production.[71]

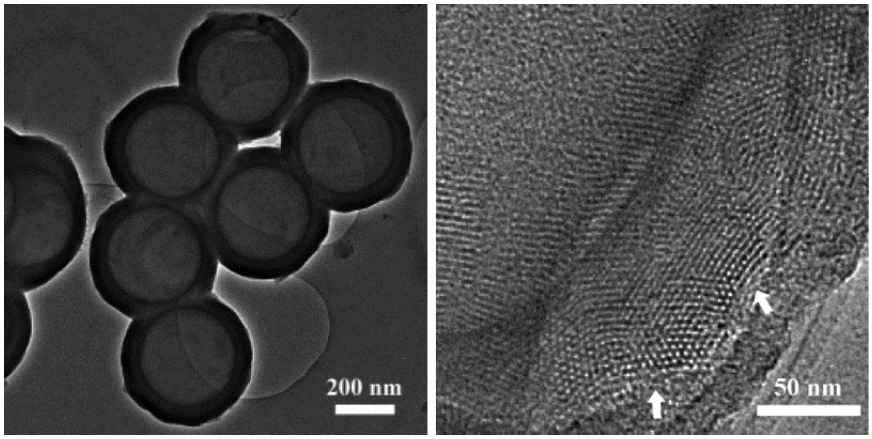

Figure 2.7. TEM images of hollow mesoporous silica spheres prepared with free-standing polystyrene spheres as hard template. Arrows indicate regions with hexagonally packed mesopores.[69] Figure reproduced with permission from ref 69. Copyright 2005 American Chemical Society.

Another useful polymeric hard template is polyurethane (PU) foam. It is produced in industrial scales at larger scale and lower cost than PS spheres. Unlike colloidal crystals assembled from individual particles, foams being continuous scaffolds are mechanically stable. However, the principle of foam-templated synthesis of hierarchical silica is similar to that of colloidal crystal-based methods; the foam is impregnated with precursor sol for deposition of mesoporous silica on its internal surfaces as illustrated in Scheme 2.3.[72] The surface of PU is hydrophilic due to the presence of highly polar urethane groups, which facilitates wetting by precursor sol and binding of silica. As a result, accurate replica of the foam structure can be achieved despite large pore size (sub-millimeter) of the foam (Figure 2.8). Similarly, polystyrene foam has also been used as template for the synthesis of macro-mesoporous scaffolds.[73]

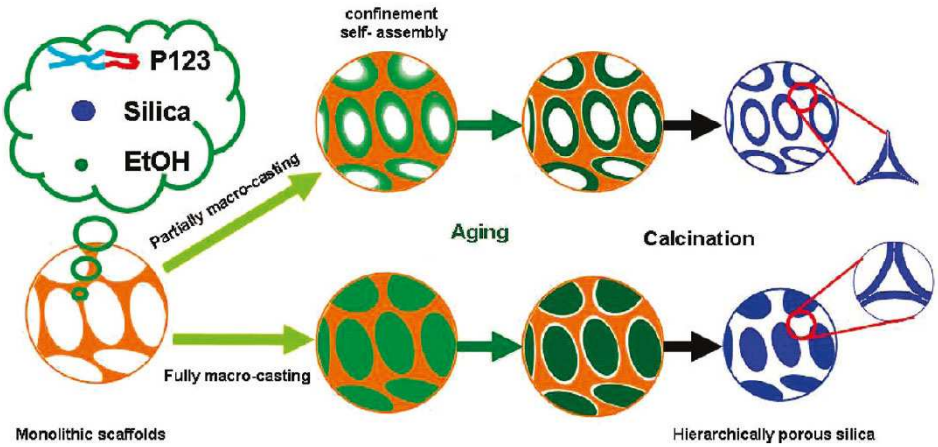

Scheme 2.3. Synthesis of hierarchical macro-mesoporous silica scaffolds with foam-type hard templates.[72] Figure reproduced with permission from ref 72. Copyright 2010 American Chemical Society.

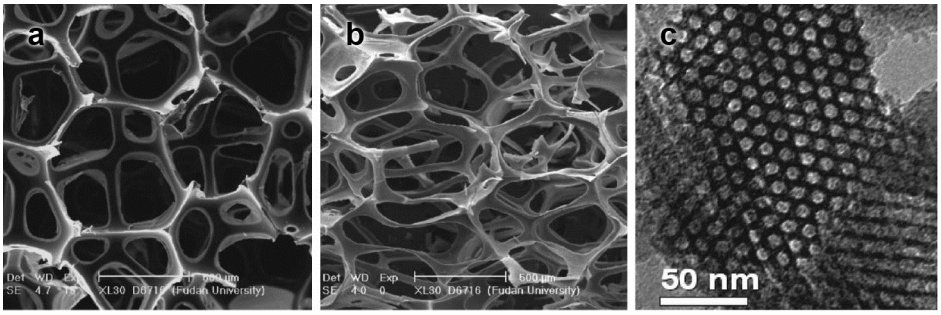

Figure 2.8. (a) SEM image of a commercial polyurethane foam, and (b) SEM and (c) TEM images of hierarchical macro-mesoporous silica synthesized with the foam template. The ordered mesopores were generated by the Pluronic P123 tri-block copolymer.[72] Figure reproduced with permission from ref 72. Copyright 2010 American Chemical Society.

Although not as widely applied as their polymeric counterparts, inorganic scaffolds are also used as hard templates in the synthesis of porous silica. Anodic alumina membranes (AAM) are a representative member in this class. They possess cylindrical pores running through the membrane's thickness as shown in Figure 2.9a. The pore structure is hence different from that of polymer foams and colloidal crystals, as pores are essentially 1-dimensional in AAM. When mesoporous silica is cast with AAM and the alumina is dissolved with acid, arrays of rods are obtained in a comb-like arrangement (*e.g.* Figure 2.9b).[74] An interesting phenomenon observed in AAM-templated synthesis is that the orientation of mesopores within the silica rods is controllable due to interaction between mesopore templates and surface of the high-aspect ratio channels of AAM.[75]

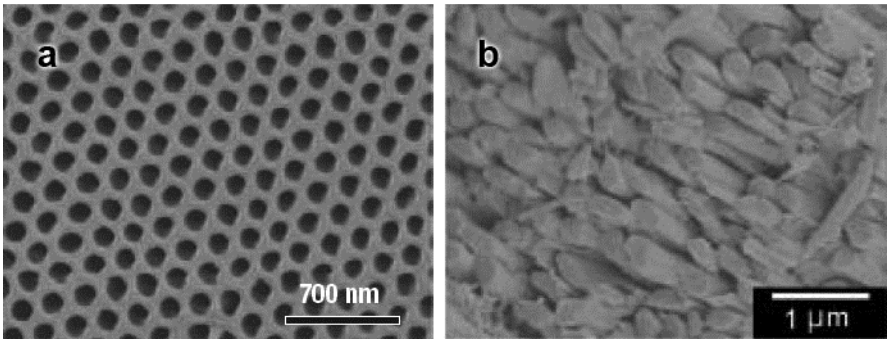

Figure 2.9. SEM images of (a) an anodic alumina membrane[76] and (b) an array of mesoporous silica rods synthesized with anodic alumina membrane as template.[74] Figure reproduced with permission from (a) ref 76, copyright 2006 Nature Publishing Group, and (b) ref 74, copyright 2003 Wiley.

In fact, silica itself can serve as templates, but since selective removal of template would be virtually impossible if mesoporous silica were to be simple grown on silica templates, synthesis procedures involving these templates are fundamentally different from those mentioned above. Instead of relying on externally supplied silica source while keeping the template intact, silica-templated synthesis consumes the template as hierarchical structures form. For example, by treating colloidal silica spheres with an alkaline aluminate solution in the presence of CTAB, hollow mesoporous aluminosilicate spheres have been obtained which have inner diameter close to the diameter of the template spheres.[77] Scheme 2.4 illustrates that the synthesis proceeds by a two-step mechanism. The silica template is first etched by OH^- and the dissolved silicate species then assembles with aluminate and CTA^+ on the surface of the template to form a shell.

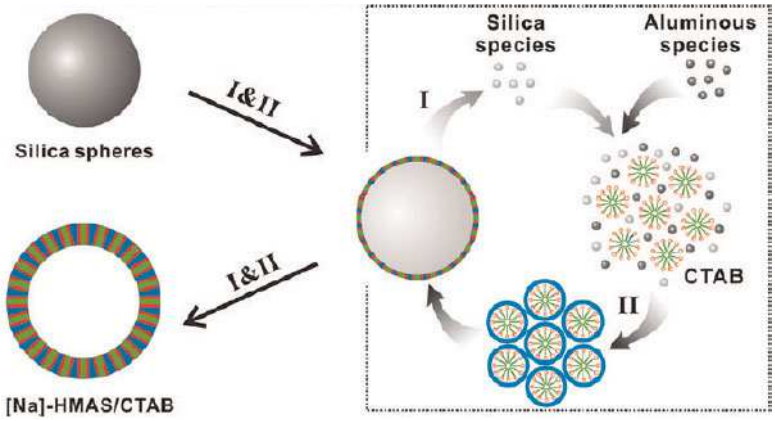

Scheme 2.4. Synthesis of hollow mesoporous aluminosilicate spheres (HMAS) using silica spheres as hard template. I: etching of silica spheres. II: assembly of aluminosilicate species with surfactant micelles.[77] Figure reproduced with permission from ref 77. Copyright 2012 American Chemical Society.

It is also possible to generate hollow structures with only an etching step that has to progress from inside out; the product will thus preserve the overall shape of the template. A surface-protected etching method has been developed where the interior of colloidal silica spheres coated with PVP is selectively dissolved with NaOH to form hollow spheres.[78] Figure 2.10a shows that the shells of the hollow spheres are porous as a result of partial dissolution. Later, it was discovered that a surface

protecting agent is optional in the etching process, as the silica spheres synthesized by sol-gel methods are chemically inhomogeneous and the interior, less condensed part is intrinsically more prone to dissolution.[79] The inhomogeneity was demonstrated nicely by etching template silica spheres synthesized with multiple sol-gel processes, which produced multi-shell particles (Figure 2.10b). Naturally one will expect ordered mesoporous silica spheres derived from a sol-gel process to have similar chemical inhomogeneity, and indeed preferential dissolution from inside out of such materials has been confirmed in hydrothermal conditions.[80] As is evident in Figure 2.10c,d, the resultant hollow spheres possess highly ordered mesopores in the shell.

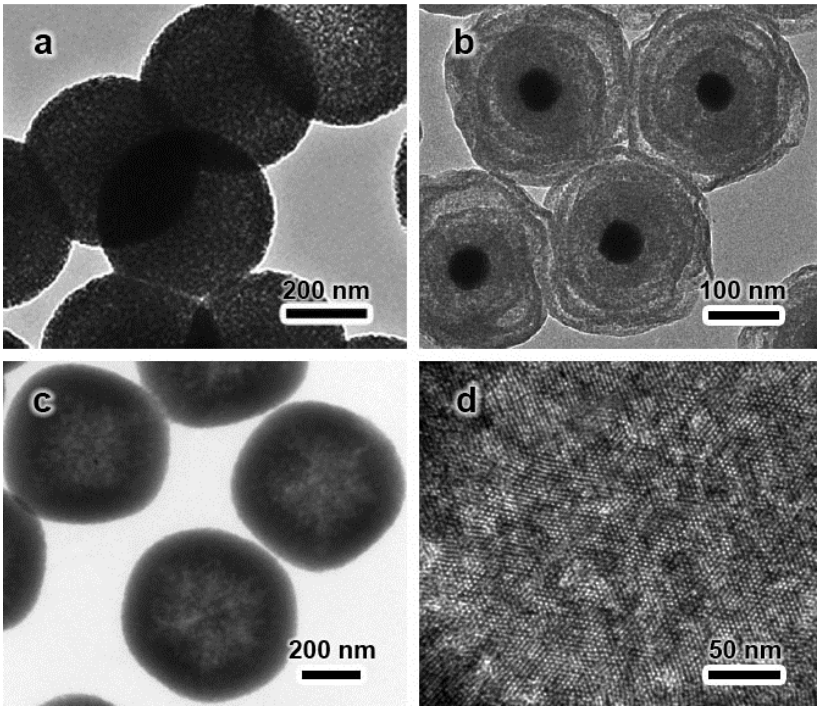

Figure 2.10. TEM images of (a) hollow silica spheres prepared by surface-protected etching,[78] (b) Au@silica multi-shell particles prepared by direct hot water etching,[79] and (c,d) hollow mesoporous silica spheres prepared by one-step hydrothermal synthesis.[80] Figure reproduced with permission from (a) ref 78, copyright 2008, and (b) ref 79, copyright 2011 American Chemical Society.

In the hard template-based methods discussed so far in this section, the templates are already formed with a definite morphology before being used for the syntheses of hierarchically porous silica. However, *in-situ* hard templates take shape simultaneously with the target product, *i.e.*, precursors for both the template and the

target product are introduced together to the synthesis procedure as one phase, and only as reactions proceed does the template form a separate solid phase to influence morphology of the product phase. Either chemical or physical processes can trigger the growth of the template phase. Polymerization of soluble precursors into insoluble macromolecules, for example, has been used for this purpose. In a recent work, a dual template method involving PEO-PS block co-polymer as template for mesopores and phenolic resin as *in-situ* template for macropores was adopted to synthesize hierarchically porous silica/titania.[81] As illustrated in Scheme 2.5, soluble precursor for the phenolic resin (resol) was introduced together with other reagents in a single sol. The resol condensed into a separate phase during the synthesis process, forcing the oxide phase along with the embedded block co-polymer micelles into a macroporous scaffold. Apparently, in such methods two template species influence each other in the self-assembly process, and their physicochemical properties should be sufficiently different for efficient phase separation. In this case, the stronger hydrogen bonding capability of the block co-polymer is cited as an important factor in the successful synthesis; it promotes selective inclusion of the block co-polymer in the inorganic phase.[81]

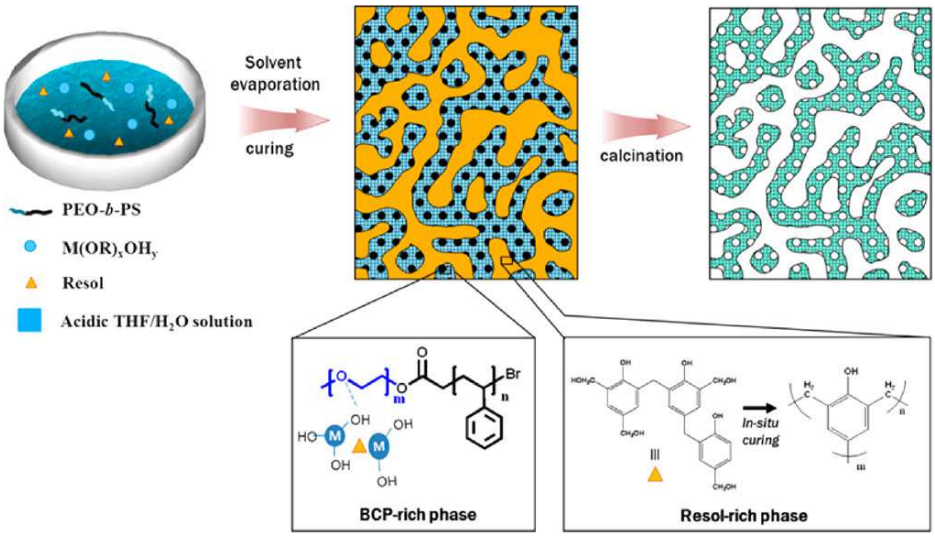

Scheme 2.5. Synthesis of hierarchically porous silica/titania scaffolds by *in-situ* hard template-based method. BCP: block co-polymer.[81] Figure reproduced with permission from ref 81. Copyright 2014 American Chemical Society.

Ice is also a unique *in-situ* hard template, the formation of which is triggered by physical freezing. The template effect of ice has been in extensive practical use, for example in food preservation by freeze drying. It is interesting from a material chemistry's perspective, though, that morphology of the ice template can be precisely controlled. Using a unidirectional freezing technique, growth of columnar ice crystals in arrays has been made possible in the condensation process of silica sol which resulted in highly porous silica microhoneycombs.[82] The advantage of ice template is obviously its low cost and facile removal. However, simultaneous generation of mesopores in ice-templated synthesis could be challenging, because common templates of mesopores require moderate temperatures for micelle formation.

2.2.2. Dual soft templates

The size of micelles formed by various amphiphiles differs greatly. As an example, block co-polymer micelles can be significantly larger than ionic surfactant micelles (4–20 nm *versus* 2–5 nm).[4] Construction of hierarchical pore structure is hence possible by combination of soft templates with different micelle sizes. However, pore size/shape control is not trivial in practice. Due to interaction between template species, the same soft template usually generates pores with different characteristics in a combined templates system compared with when used alone, and the template phases often merge and no hierarchical structure is obtained.[83-84] Careful selection of the template species is therefore of critical importance. The combination of block co-polymer (poly(ethylene-*co*-butylene)-*block*-poly(ethylene oxide)) and amphiphilic ionic liquid (1-hexadecyl-3-methylimidazolium chloride) is a successful example; the interlinked 12 nm and 2–3 nm mesopores seen in Figure 2.11 were generated by the block co-polymer and the ionic liquid, respectively.[85] Note that colloidal crystal of PS spheres was also used as hard template for the spherical macropores, adding a third hierarchy to the pore structure.

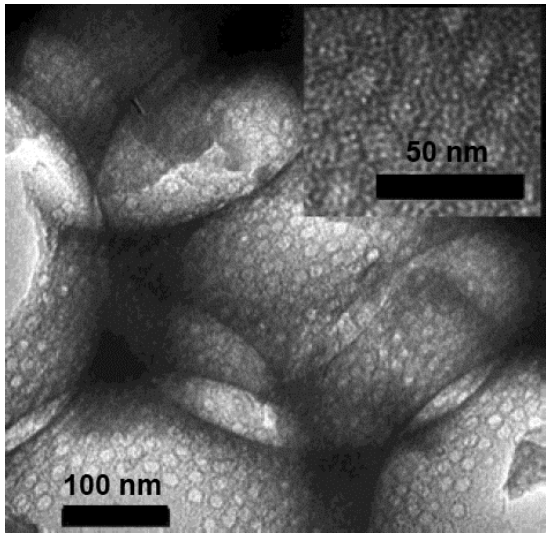

Figure 2.11. TEM images of hierarchically porous silica synthesized in a combined template system containing PS spheres, a block co-polymer and an amphiphilic ionic liquid. The inset shows the 2–3 nm mesopores.[85] Figure reproduced with permission from ref 85. Copyright 2004 American Chemical Society.

Micellar templates have the advantage of exhibiting well-defined morphology and to certain degree predictable sizes. However, pore sizes larger than *ca.* 30 nm are difficult to achieve with micellar templates even in the presence of swelling agents.[4] To direct formation of macropores using soft templates, micro-droplets of a separate phase serve the purpose better. The most apparent method of obtaining such templates is by generation of emulsions. For example, hollow mesoporous silica spheres with diameters of 1–100 μm have been synthesized in a kinetically stabilized oil-in-water emulsion, where oil micro-droplets are templates for the micrometer-sized central void and cationic surfactant micelles for mesopores in the wall.[86] The cationic surfactant served as stabilizer of the emulsion at the same time. Controlled condensation of silica at the oil-water interface is crucial to the success of the method. In this case, TEOS was preferentially dissolved in the oil phase while its hydrolysis catalyst and surfactant were supplied from the aqueous phase, which limits the reaction effectively at the surface of the oil droplets. Non-aqueous emulsions have also been used for the synthesis of hierarchically porous silica, but since silica is inevitably derived from hydrophilic intermediates in sol-gel processes, at least one of the phases in the emulsion system needs to be able to dissolve such intermediates.[80] It

is worth noting that in emulsions with very high content of dispersed phase and uniform droplet size, the micro-droplets can assemble into colloidal crystals similar to those formed by hard template spheres.[87] The assemblage is fixed by gelation of the continuous phase and ordered macropores scaffolds can be obtained. Although in this method it is not necessary to confine the condensation of silica at the interface, the preparation process of the emulsion is significantly more complicated than that in the synthesis of hollow silica spheres.

In contrast to ordinary emulsions which require continuous input of energy to prevent coalescence, microemulsions form spontaneously and are thermodynamically stable.[88] Processing of microemulsions is hence simpler, making them an attractive choice for synthesizing hierarchically porous materials. In addition, as droplet size in microemulsions is typically below 100 nm which is difficult to reach in ordinary emulsions, microemulsion-based syntheses fill in the gap between pore sizes achievable by micelle templates and by ordinary emulsion templates.[89-92] Droplet size and structure in a microemulsion are tuned by changing the composition. For example, Figure 2.12 shows that by adjusting the amount of the oil phase, hierarchically porous silica spheres with different macropore sizes were obtained through otherwise the same synthesis method.[90] The microemulsion was bicontinuous, leading to readily interconnected macropores and hence a wrinkled structure.

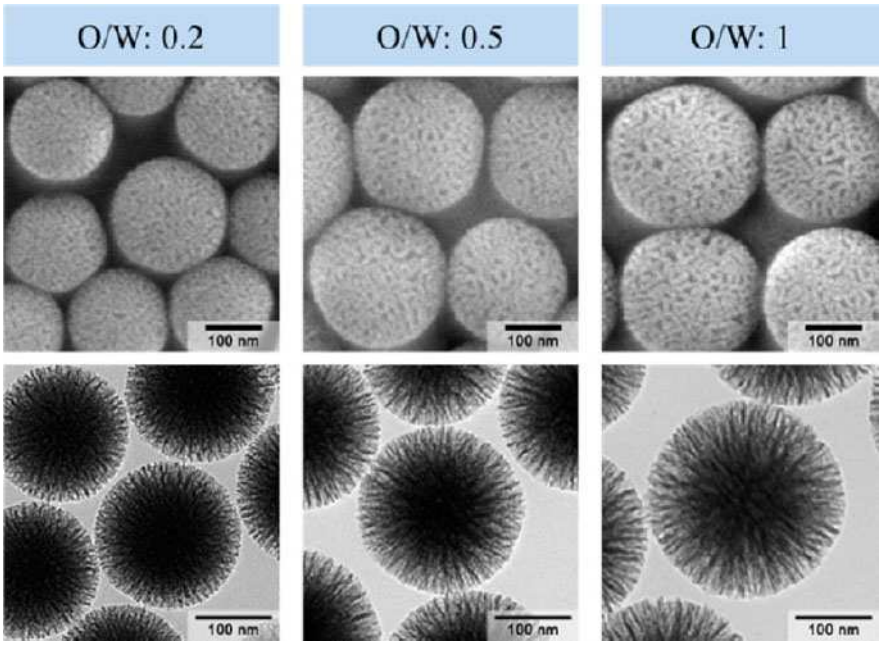

Figure 2.12. SEM and TEM images of macro-mesoporous silica spheres synthesized in a cyclohexane-isopropanol-water microemulsion with different oil/water ratios. Cetylpyridinium bromide was used as surfactant and template for mesopores.[90] Figure reproduced with permission from ref 90. Copyright 2012 American Chemical Society.

Organic solvents are not the only possible soft template for macropores. Concentrated electrolyte solution as an example has been reported to separate *in situ* into an individual phase from self-assembled composite of block co-polymer and silica gel, affording a hierarchically macro-mesoporous scaffold.[93]

2.3. Synthesis of hierarchically porous zeolites

Zeolites are microporous molecular sieves in general. Their basic structure units, *i.e.*, SiO_4 and AlO_4 tetrahedrons, are the same as those of amorphous aluminosilicate, but zeolites have highly ordered crystal structures that are intrinsically microporous. There is strict correspondence between crystal structure and micropore size of zeolites which is in the same range as the molecular size of refinery products.[94-95] Furthermore, unlike ordered mesoporous silica, many zeolites can be prepared without organic templates.[96] Development of synthetic zeolites hence started earlier, and wider application of zeolites as catalysts in petrochemical processes has been realized.[15, 95] While the well-defined micropore size of zeolites provides high

selectivity, limited mass transfer efficiency in the micropores causes problems such as poor accessibility to reactants and deactivation by coke deposition. Generation of larger, open pores interconnected to the micropores is necessary to the resolution of the issues, which has led to increasing interest in hierarchical zeolites.[97-99]

In contrast to the now well-established production methods of purely microporous zeolites, synthesis of hierarchical zeolites is a relatively young field of study. However, being an industrially relevant and academically interesting topic, it has attracted the attention of many research groups and significant progress has been made.[97, 100-101] The similar chemical composition of zeolites and amorphous silica/aluminosilicate suggests that template-based methods introduced in Section 2.2 can also be applied to the synthesis of hierarchical zeolites, which is indeed true. In addition, unique strategies of creating mesopores/macropores in zeolitic materials exist as a result of their crystalline structure and worth separate discussion. It should be mentioned here that structure-directing agents (SDAs), sometimes also referred to as templates, are usually needed to guide crystallization of a desired zeolitic phase. The templates to be discussed in this section are specifically those for the generation of pores not native to the crystal structure of a zeolite.

2.3.1. Template-based methods

Synthesis of zeolites requires arrangement and rearrangement of basic structure units to a significantly larger extent than that in the synthesis of amorphous silica.[102] Therefore, to achieve comparable throughput the synthesis conditions for zeolites are harsher (*e.g.*, higher temperature, pressure, and/or alkalinity), which demands higher stability of pore-generating templates. Furthermore, compared with amorphous silica the crystalline nature of zeolites makes it less favorable for the product to conform to the shape of the template. Synthesis of hierarchically porous zeolites is hence more difficult in general.

Carbon has been adopted as a stable template material for mesopores and macropores in zeolites.[103-105] Due to weak interaction between carbon and zeolites, carbon templates are usually used as fillers during synthesis of zeolites in confined space, *i.e.*, the space for growth of zeolite crystals is limited, so that the zeolite is forced to grow around the template.[103, 106-107] For such purpose, steam-assisted conversion has been developed as an effective strategy, where mixtures of carbon and zeolite precursors in solid forms are treated with steam and zeolites crystallize directly in the solid phase.[106] Alternatively, impregnation of carbon scaffolds with zeolite precursor gels can also be used to limit zeolite growth within the pores of the template.[108] In terms of synthesis procedure, this strategy is similar to the foam-templated synthesis of silica (Scheme 2.4). Depending on the morphology of the template (*e.g.* carbon black, nanotubes, ordered porous carbon, or irregular scaffold), ordered/disordered pore networks with sizes generally in the mesoporous range can be obtained after calcination in air.[98] In addition, it is worth mentioning that carbon template can be formed *in situ* during preparation of zeolite precursor gels, for example by decomposition of sugars mixed with zeolite precursors.[109] The resulting mesopore structure is irregular. The morphology of some reported carbon-templated zeolite products are shown in Figure 2.13. Other than carbon, stable inorganic materials such as $CaCO_3$ have also been used as hard templates which need to be removed by acid.[110]

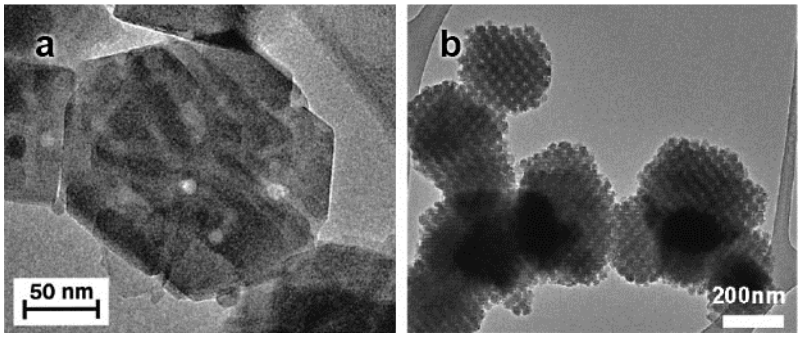

Figure 2.13. TEM images of (a) mesoporous silicalite-1 templated by carbon nanotubes[111] and (b) mesoporous zeolite beta templated by ordered carbon scaffold.[112] Figure reproduced with permission from (a) ref 111, copyright 2001, and (b) ref 112, copyright 2011 American Chemical Society.

Despite their lower stability compared with carbon, organic polymers can serve as hard templates in the synthesis of hierarchically porous zeolites. Colloidal crystal of PS spheres, for example, has been used to prepare macroporous silicalite-1 through a procedure similar to that for the synthesis of amorphous silica (Scheme 2.3).[113] However, there existed the difference that the PS spheres were mechanically unstable at the zeolite synthesis temperature of 130°C. To prevent collapse of the macropore structure, the zeolite precursor gel was allowed to fully harden after impregnation of the colloidal crystal template and crystallization of zeolite occurred in a pseudo-solid-state transformation. Besides PS, several other synthetic and natural polymer scaffolds including phenolic resin, starch and cellulose have been proven useful as hard templates in zeolite synthesis.[114-116] The hydrophilicity of these polymers facilitates interaction with zeolite precursors, which is an advantage over carbon templates. However, impurities in the natural materials could be an issue in sensitive applications.

Zeolite precursor materials themselves may function as hard templates in certain conditions and simplify the synthesis procedure of hierarchically porous zeolites by eliminating the template removal step. A good example is the synthesis of ordered macroporous silicalite-1 monolith using silica spheres as both the silica source and template.[117] Briefly, micrometer-sized mesoporous silica spheres were coated with silicalite-1 seed crystals with the assistance of polyelectrolytes, allowed to settle into a colloidal crystal by sedimentation and hydrothermally treated with a clear zeolite precursor solution (Scheme 2.6). Crystallization of zeolite occurred on the surface of the silica spheres due to the seed crystals, and as the template dissolved, interconnected zeolite shells formed a negative replica shown in Figure 2.14.

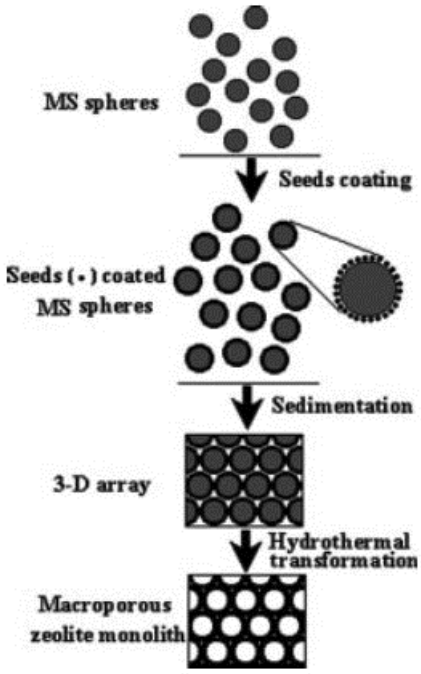

Scheme 2.6. Synthesis procedure of ordered macroporous silicalite-1 monolith.[117] Figure reproduced with permission from ref 117. Copyright 2002 Wiley.

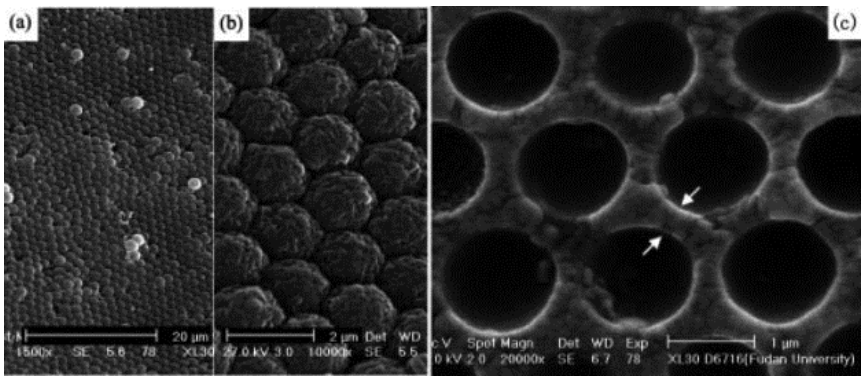

Figure 2.14. SEM images of (a,b) surfaces and (c) a cross-section of the ordered macroporous silicalite-1 monolith synthesized with silica spheres as template.[117] The arrows indicate the thickness of zeolite wall merged from two adjacent hollow spheres. Figure reproduced with permission from ref 117. Copyright 2002 Wiley.

As in the synthesis of amorphous silica/aluminosilicate, soft templates can generate mesopores and macropores during synthesis of zeolites. However, templates commonly used to synthesize mesoporous silica such as amphiphilic monocationic quaternary ammonium salts have failed to direct formation of mesoporous zeolites; separate microporous (zeolitic) and mesoporous (amorphous) phases were obtained instead, probably due to insufficient interaction between the mesopore template and the zeolite framework.[118] One way to enhance the template-zeolite interaction is

increasing charge of the template. For example, the commercial cationic polymer PDDA has been used to successfully synthesize mesoporous zeolite beta particles.[119] Figure 2.15 shows that the zeolite particles are single crystals with interconnected open mesopores. The size of the mesopores (up to 15 nm) is believed to correspond to the size of the solvated PDDA macromolecules, as the pore size could be tuned by changing the molecular weight of PDDA.

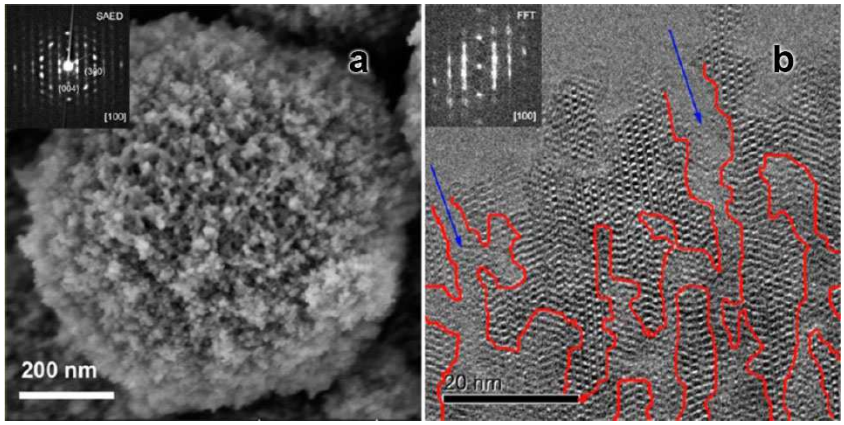

Figure 2.15. (a) SEM and (b) TEM images of mesoporous zeolite beta synthesized with PDDA as template. Inset in (a): SAED image of a zeolite particle. Inset in (b): FFT result of the shown TEM image. Mesopores are outlined by red drawings.[119] Figure reproduced with permission from ref 119. Copyright 2014 American Chemical Society.

An elegant strategy of synthesizing mesoporous zeolites takes the advantage of tight inclusion of structure-directing species in zeolitic micropores. Essentially, special templates have been designed that include extended hydrocarbon groups linked to known SDA molecules. While the structure-directing moiety acts as nucleation center of zeolite to ensure strong affinity of the zeolite to the template molecules, the nonpolar hydrocarbon groups are repelled by the zeolite framework and form spacers that eventually lead to mesopores upon calcination.[120-121] The same template molecules are thus responsible for both the framework micropores and extra-framework mesopores, and can be considered bifunctional. In a notable work using $C_{18}H_{37}$–$N^+(CH_3)_2$–C_6H_{12}–$N^+(CH_3)_2$–C_6H_{12}–$N^+(CH_3)_2$–$C_{18}H_{37}(Br^-)_3$ as template (abbreviated as 18-N_3-18),[121] MFI-type zeolite crystals were synthesized with hexagonally ordered mesopores as shown in Figure 2.16.

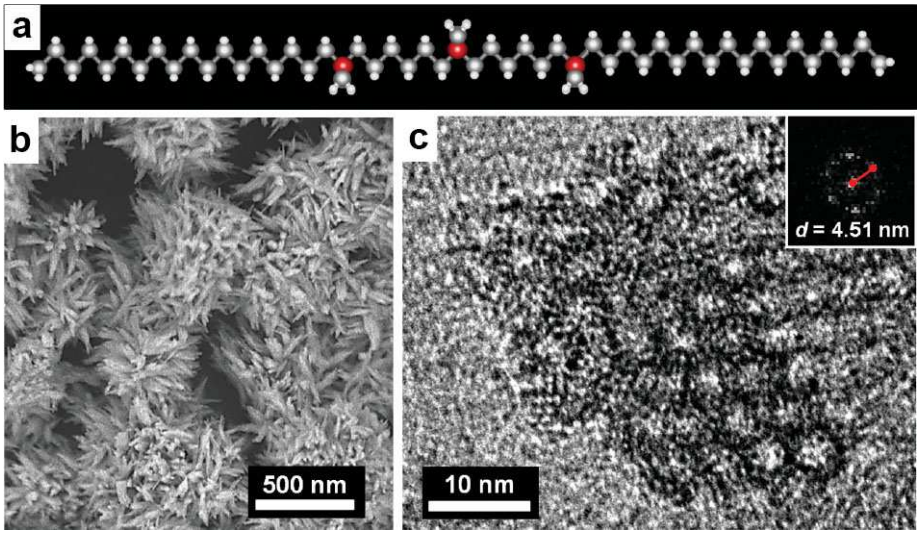

Figure 2.16. (a) Molecular structure of the 18-N_3-18 template, and (b) SEM and (c) TEM images of the ordered mesoporous MFI-type zeolite synthesized with the template. Inset: FFT result of the TEM image showing the meso-scale ordering.[121] Figure reproduced with permission from ref 121. Copyright 2011 American Association for the Advancement of Science.

To achieve even stronger interaction between mesopore templates and zeolite frameworks, covalent bonding needs to be involved. Typically, organosilanes with hydrolyzable silicate bonds are used as the reactive templates.[122-125] During zeolite synthesis, the silicate bonds are cleaved and condensation with silanol groups on the zeolite links the template molecules to the zeolite framework through Si–O–Si bridges. The remaining non-hydrolyzable group of the template then serves as spacer to create organic domains, and after calcination, textural pores within zeolite particles. The grafting of zeolite surface with organosilanes has remarkable inhibiting effects on the growth of zeolite crystals. As a result, hierarchically porous zeolites synthesized with this type of templates usually consist of nanometer-sized crystallites separated by disordered mesopore networks. Size of the mesopores can be tuned by changing the non-hydrolyzable group in the template.[122] However, success of the organosilane-based method is highly dependent on careful choice of the time and amount of template introduced to zeolite precursor gels; if the templates are added in excess or before zeolite seeds are formed, crystallization of zeolite is completely suppressed.[126-127]

2.3.2. Intergrowth and aggregation of zeolite nanocrystals

Compared with processes of conventional zeolite production, template-based syntheses of hierarchically porous zeolites involve more steps and/or more costly specialty chemicals that make applications in industrial scale prohibitive. However, approaches to generating textural pores during zeolite synthesis without corresponding templates do exist, one of which relies on the crystal structure of zeolites. Some pairs of zeolitic frameworks, for example MEL/MFI, EMT/FAU and CAN/SOD, have very similar basic building blocks but different overall topology, which facilitates twinning/intergrowth between individual crystallites at fixed angles.[128-130] If the crystal growth is anisotropic enough (*e.g.* leading to a sheet-like shape), such intergrowth generates space between crystallites, and a 3-dimensional network of crystals forms with a well-defined overall structure. For example, using tetrabutylphosphonium as the SDA which induces extensive MFI-MEL intergrowth, ultrathin MFI-type zeolite sheets have been synthesized in an orthogonally intergrown, house-of-cards form seen in Figure 2.17a,b.[131] No templates for mesopores were involved. It was believed that MEL domains were present at the joints of the MFI sheets to ensure their 90° intergrowth (Figure 2.17c). Similarly, synthesis of FAU-type zeolites in house-of-cards forms has also been reported without templates for mesopores (Figure 2.17d).[132] The FAU sheets interpenetrate at 109.5° angles due to intergrowth of FAU (cubic) and EMT (hexagonal) phases.[133]

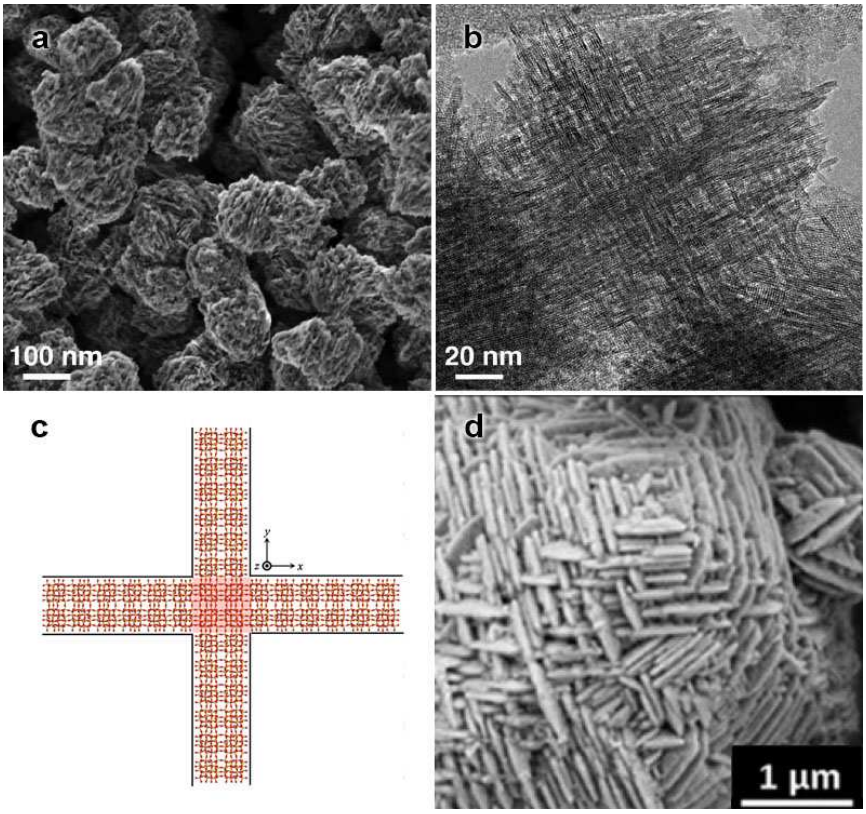

Figure 2.17. (a) SEM and (b) TEM images of a hierarchical MFI-type zeolite. (c) A possible formation mechanism of 90° intergrowth between MFI sheets. The central region highlighted in pink is an MEL-type tetragonal domain.[131] (d) SEM image of a hierarchical FAU-type zeolite synthesized in the presence of Zn^{2+}.[132] Figure reproduced with permission from (a–c) ref 131, copyright 2012 American Association for the Advancement of Science, and (d) ref 132, copyright 2015 Royal Society of Chemistry.

For zeolites without significant tendency towards intergrowth, generation of textural pores is also possible in the absence of templates, albeit with less morphological control over the final product. In such cases, stable mesopores form by random aggregation/assembly of zeolite nanocrystals. The formation of zeolite nanocrystals requires high concentrations of zeolite nuclei, and it seems that the strategy of increasing the concentration of precursor gels has gained the most success so far.[97-98] As mentioned in Section 2.3.1, steam-assisted conversion of solid precursors can create a confined space to enhance interaction between zeolite and inert templates. Apparently, interaction between individual zeolite crystallites is increased at the same time, and in addition, very high precursor concentrations are achieved. However, the drawbacks of the simple solid-phase conversion are relatively

poor mechanical stability of products and its sluggish kinetics due to limited mass transfer.

2.3.3. Etching of pre-formed zeolite

Processes for production of micrometer-sized zeolite crystals are well-established in large scales. From an economical perspective, it is desirable to develop methods of preparing hierarchically porous zeolites that require minimal modification of the conventional industrial processes. Therefore, post-synthesis etching of conventional zeolite products has so far been the most widely adopted strategy of obtaining mesoporosity in industry.[134] Generally, different treatments are required to remove Al or Si in zeolite frameworks while keeping the overall crystal structure stable. Voids are thus created in the originally continuous interior of zeolite crystals.

It has long been recognized that high-temperature calcination or steaming causes tetrahedrally coordinated Al to migrate out of the zeolite frameworks in octahedrally coordinated forms.[135-137] The extra-framework Al species can then be selectively dissolved by mild acid treatment, and an overall dealumination is achieved. Ultra-stable zeolite Y (USY) used in catalytic cracking of hydrocarbons, for example, is produced in this way.[138-139] As framework Al is removed, vacant sites are left which in sufficient amounts coalesce into mesopores.[140-141] Alternatively, leaching of framework Al can be achieved directly by etching with acid or chelating agents.[134] However, since zeolites useful in catalysis contain far less Al than Si as framework atoms, only limited mesoporosity can be generated through dealumination. It has also been found that pores derived from dealumination are often embedded in zeolite crystals and poorly accessible.[142] In addition, catalytic properties of zeolites are significantly affected by dealumination because their acidity is determined by the amount and chemical environment of framework Al atoms. These drawbacks lead to more interest in desilication as the main method of pore generation.

Selective desilication of zeolites is facilely performed by treatment with a dilute NaOH solution (*e.g.* 0.2 mol/L).[143-144] It is particularly effective in introducing mesopores to moderately silica-rich zeolites (Si/Al = 25–50), where leaching of Si is easily controlled and the mesopores obtained are open.[145] At lower Si/Al ratios, leaching is hindered by framework Al. Therefore to generate meaningful amount of mesopores in low-silica zeolites, dealumination is necessary which can be performed concurrently with desilication by more concentrated NaOH solutions (Al is amphoteric).[146] However, the process is accompanied by significant loss of yield and the efficiency of pore generation is still poor compared with desilication of more silica-rich zeolites. On the other hand, if the Si/Al ratio of the zeolite is too high (>50), desilication by NaOH proceeds uncontrollably leading to large pores with small surface area and crystal structure of the zeolite is destroyed. Improvement of the method has been observed with additional supply of Al in the alkali solution when extremely silica-rich zeolites were treated.[147] A more interesting finding is that organic SDA molecules (*e.g.* tetrapropylammonium in ZSM-5) hinder the desilication process, probably by blocking the access of OH^-. Compared with the moderating role of externally supplied Al, this effect is less dependent on the Si/Al ratio of zeolites.[147] New methods of desilication thus emerged which involve the use of tetraalkylammonium ions either in their free form in the alkali solution or as fixed species in as-synthesized zeolites. The tetraalkylammonium-assisted processes produce remarkably larger mesopore surface areas than processes based solely on NaOH at the same yield.[148] Notably, processes for continuous desilication of USY have been reported.[149] The quality of pores in the products is similar as that obtained from batch operations, which suggests large potential in industrial applications.

2.4. Catalysts for methanol and CO synthesis by CO_2 hydrogenation

Methanol is a basic petrochemical produced in large scales. Due to its simple structure and rich chemistry, there has been increasing interest in the potential role of methanol in green technologies. A bold idea of replacing oil and gas with methanol as the basis of industry has been proposed, where methanol is synthesized from captured CO_2 and renewable H_2 and converted to various hydrocarbons currently produced in the petrochemical industry.[18] In this way, emission is minimized and dependence on fossil fuels can be eventually eliminated.

Traditionally, methanol is produced from syngas which in turn is derived from steam reforming of natural gas or coal gasification.[150] ZnO/Cr_2O_3 catalysts were used in early years, but soon more efficient $Cu/ZnO/Al_2O_3$ catalysts that require milder reaction conditions dominated the industry, and have since remained as the standard.[151] Usually the catalysts are prepared by co-precipitation of Cu^{2+}, Zn^{2+} and Al^{3+} into mixed hydroxycarbonates and calcination of these intermediates. Active catalysts containing finely dispersed Cu nanoparticles are obtained after reduction of the resultant mixed oxides with H_2.[152] The industrial $Cu/ZnO/Al_2O_3$ catalysts generally have methanol selectivity of >99%, and one-pass conversion is moderately high in practice.[151] Extensive studies have been carried out on the industrial $Cu/ZnO/Al_2O_3$ catalysts. While detailed reaction mechanism is still under debate, the promoting effects of Zn and Al are definite: strong interaction between Cu and ZnO/Al_2O_3 support helps disperse the Cu phase, and evidence of Zn species modifying the surface of Cu has been obtained.[153-156]

In the development of catalysts for methanol synthesis from CO_2 hydrogenation, Cu-based formulations have naturally become the first choice given their prevalent status in industry. However, there are important differences between CO-based conventional processes and CO_2-based methanol synthesis, which make industrial

$Cu/ZnO/Al_2O_3$ catalysts not so efficient in the latter. Firstly, the higher stability of CO_2 than CO leads to sluggish reaction kinetics at high coverage of CO_2-derived reaction intermediates on the surface of Cu.[157] Secondly, Cu catalyzes reverse water gas shift (RWGS) along with methanol synthesis, lowering methanol selectivity. Lastly, significant amount of water is produced by CO_2 hydrogenation and accelerates deactivation of $Cu/ZnO/Al_2O_3$ catalysts.[158] More active, selective catalysts that are resistant to water vapor are therefore needed to make CO_2-based processes practical.

Remarkable amount of effort has been put on improving Cu-based catalysts for CO_2-based methanol synthesis, which involves the use of a variety of additives. Introducing ZrO_2 to the Cu/ZnO system has often been reported to enhance the performance of the catalyst mainly due to better Cu dispersion.[159-163] Interestingly, the crystal structure of ZrO_2 has significant influence on the activity with the monoclinic form being a more effective support than the tetragonal form.[164] Importance of the surface chemistry of the support materials is thus highlighted. Positive results have also been obtained with similar catalyst supports such as SiO_2, TiO_2 and CeO_2.[161-162, 165-167] Another frequently used additive is Ga_2O_3, which seems to partially cover Cu particles, modifying their surface chemistry in favor of methanol formation and preventing sintering.[168-170] Additionally, effects of oxides of B, Mg, V, Cr, Mn on $Cu/ZnO/Al_2O_3$ catalysts have been studied.[161, 171] Generally, benefits of incorporating oxide additives are attributed to metal-support interaction. On the other hand, introducing hydrogen-absorbing materials including carbon nanotubes and Pd to Cu-based catalysts has been shown to increase their hydrogenation efficiency, probably by spill-over of dissociated hydrogen onto Cu.[172-173]

Besides Cu, other transition metals, for example Ag, Au, and Pd in particular, also exhibit methanol synthesis activity through CO_2 hydrogenation.[16, 174] Catalysts combining Pd with known promoters of Cu-based catalysts including ZnO, Ga_2O_3, and carbon nanotubes have been developed with some success,[175-176] but significance

of these studies remains largely academic, as the cost of Pd-based catalysts is significantly higher than that of Cu-based counterparts, which offsets the advantage in catalytic performance brought by Pd. In this regard, recent theoretical and experimental works on non-precious metal catalysts (*e.g.* Ni-Ga) are more impactful, which in addition provide mechanistic insights of Cu-based catalysts from a different perspective.[167, 177]

Although attempts to commercialize the sustainable CO_2-to-methanol process have been made,[178] in the current stage it is still uncompetitive compared with conventional petrochemical technologies. Instead of direct methanol synthesis from CO_2 hydrogenation, conversion of CO_2 to CO (through RWGS) followed by conventional methanol production processes has been proposed as an alternative.[179] In fact, RWGS has been regarded as among the most promising routes of CO_2 utilization because the resultant syngas is a versatile feedstock for various chemical processes.[16-17, 180] As the reverse reaction of WGS, the crucial step of industrial hydrogen production, RWGS is also an important topic of research in catalysis.

Generally, active WGS catalysts can be used in RWGS. However, since RWGS is a moderately endothermic reaction, good CO yield requires high temperatures which put demands on different characteristics of RWGS catalysts from those of WGS catalysts. As mentioned earlier, Cu-based catalysts are active in RWGS; they are also the most studied catalysts for low-temperature WGS.[181] The RWGS performance of Cu catalysts supported on various oxides such as Al_2O_3, ZnO, SiO_2, and CeO_2 have been examined, and promoting effects of alkali metals were found.[16] A major problem of Cu catalysts is their susceptibility to sintering in RWGS conditions (>300 °C). To improve the stability of Cu nanoparticles in active catalysts, doping of Fe has been suggested which also created new active sites.[182-183] Indeed, Fe like several other transition metals including Ni and especially noble metals (*e.g.* Pd, Pt, Au) can catalyze RWGS with high activity and superior thermal stability compared

with Cu, but Ni catalysts suffer from deactivation caused by coking and the cost of noble metals prevents large-scale applications.[17]

Chapter 3. Characterization Methods

General information (manufacturer/model number of instruments, testing conditions, sample preparation procedures, etc.) about the characterization methods involved in the following chapters is presented in this section. Details specific to individual works will be included in corresponding chapters.

3.1. Transmission electron microscopy (TEM)

Two instruments manufactured by JEOL were used for TEM analysis: a JEM-2010 with LaB_6 thermionic-emission electron gun and a JEM-2100F with ZrO/W Schottky field-emission electron gun. Both operated at 200 kV. The JEM-2100F is equipped with an energy-dispersive X-ray (EDX) spectroscope from Oxford Instruments. High-angle annular dark field imaging (HAADF) and elemental mapping were performed only with the JEM-2100F in scanning transmission electron microscopy (STEM) mode.

Typically, sample was dispersed in anhydrous ethanol to form a visibly cloudy suspension. One drop of the suspension was added by a 200 μL pipette to the coated side of a carbon/formvar-coated 200 mesh copper grid (Electron Microscopy Sciences), which was placed on a piece of filter paper used to absorb excess sample suspension. The copper grid was usually dried naturally in laboratory air before analysis. For stable samples, drying was carried out in an electrically heated oven at 60 °C. Air-sensitive samples were dried in a vacuum desiccator at 50 mbar. In cases where elemental mapping of copper was needed, the samples were prepared in similar ways on carbon/formvar-coated nickel grids (if nickel was not of interest) or gold grids (if nickel was also to be analyzed).

3.2. Powder X-ray diffraction (XRD)

XRD analysis was performed using a Bruker D8 Advance diffractometer with Cu K_α radiation source. The X-ray tube operated at 40 kV, 30 mA. For samples in small amounts (<20 mg), sample powders were wetted with anhydrous ethanol and the pastes were loaded on single-crystal silicon holders. The ethanol was then allowed to evaporate at room temperature before analysis. For larger samples, dry powders were directly loaded on plastic holders and hand-pressed into pellets using glass slides. To minimize the effects of sample texture, the sample holders were set to spin during data acquisition. A step size of 0.02° was used.

3.3. Scanning electron microscopy (SEM)

SEM characterizations were performed using JSM-5600LV with thermionic-emission gun and JSM-6700F with field-emission gun from JEOL. The JSM-5600LV is equipped with an Oxford Instruments EDX spectroscope and operated at 15 kV. The JSM-6700F operated at 5 kV. In morphological studies, a thin layer of sample powder was loaded on a piece of double-sided carbon tape pasted on a 10 mm × 10 mm (diameter × height) copper holder. Sputter coating with Pt was then carried out in Ar at 2.5 Pa, 10 mA for 90–100 s using an automatic coater. The coated sample was immediately analyzed. For elemental analysis using EDX, a thick layer of sample powder was deposited on the carbon tape and no coating was applied. Elemental composition was measured at 5 different sites (each site is at least 100 μm × 100 μm in size) and the average is taken.

3.4. Nitrogen sorption

N_2 adsorption/desorption isotherms were measured at 77 K using a Quantachrome Instruments NOVA 4200e surface area and pore analyzer. 30–150 mg of dry sample was loaded into a 9 mm bulb-shaped glass sample cell and outgassed in flowing He or

vacuum for 3–14 h before analysis. Adsorbed gas volume was normalized by dry weight of outgassed samples to give the isotherms. Detailed outgassing conditions and data analysis methods will be specified in the following chapters.

3.5. Fourier transform infrared spectroscopy (FTIR)

FTIR spectra were obtained using FTS-3500ARX from Bio-Rad in transmission configuration. 100 mg of spectroscopic grade KBr and *ca*. 1 mg of dry sample were ground together with an agate mortar and pestle for 10 min. The powder was pressed between ½ in. stainless steel dies at 470 MPa for 15 min to form a translucent, self-standing pellet which was analyzed immediately. The sample chamber was purged with dry, de-carbonated air supplied by a Parker Balston FTIR purge gas generator. Data was acquired with a resolution of 1 cm^{-1}. Background spectrum was collected in each experiment using a pellet of 100 mg of pure KBr.

3.6. X-ray photoelectron spectroscopy (XPS)

XPS analysis was performed using an AXIS Ultra DLD spectrometer from Kratos Analytical. The instrument operated at ultrahigh vacuum (5×10^{-9} Torr) with a monochromated Al K_α X-ray source at 5 mA, 15 kV (X-ray energy = 1486.71 eV). The detector was positioned normal to sample surface. Sample powders were loaded onto *ca.* 3 mm × 3 mm glass slides with the help of double-sided tape. The glass slides were glued to a grounded metal holder. In cases where C and/or Si were to be analyzed, ethanol suspensions of the samples were deposited on copper tape pasted on the glass slides and allowed to dry at room temperature before analysis. The 1*s* binding energy of adventitious carbon was used for charge referencing. The value it is set to will be specified in the following chapters.

3.7. Nuclear magnetic resonance (NMR)

NMR experiments on liquid samples were carried out using a Bruker AVANCE I 500 spectrometer equipped with a 5 mm broadband observe probe. Dissolved oxygen in samples was removed by bubbling purified N_2 for 20 min, and the samples were handled in a N_2-filled glove box. For solid samples, magic-angle spinning (MAS) NMR experiments were performed using a Bruker DRX 400 spectrometer equipped with a 4 mm CP MAS probe. Dry powders were loaded in zirconia rotors for analysis. Detailed pulse programs and data analysis will be presented in the following chapters.

3.8. Inductively coupled plasma optical emission spectroscopy (ICP-OES)

Metal contents of catalysts were analyzed by ICP-OES using either PerkinElmer Optima 5300 DV or Thermo Scientific iCAP 6200 Duo. Samples were digested with 1 M HNO_3 and clear analyte solutions were obtained by centrifugation or filtration through 0.2 μm membrane filters. Calibration of the spectrometer was performed before each experiment using standard solutions of at least 4 different concentrations. The ICP system was flushed with 1 M HNO_3 for at least 30 s and with the analyte for 30 s before data acquisition. An average value of three exposures was taken as the result.

3.9. Catalytic hydrogenation of CO_2

Evaluation of catalytic performance in CO_2 hydrogenation was carried out using an in-house fixed-bed reactor. A 3/8" seamless 316 stainless steel tube with a length of 550 mm served as the reactor chamber, which was heated by a Carbolite MTF 12/25/400 tube furnace (length of heated zone = 400 mm). Catalyst was kept in the middle of the tube by glass wool plugs, and the rest of the space in the reactor was filled with 2 mm borosilicate glass beads. For calibration purposes, a K-type thermal couple was installed to have its tip positioned in the middle of the reactor chamber.

Differences of no more than 1 °C were found between the measured reactor temperature and the temperature reported by the integrated monitoring system of the furnace. During catalyst evaluation, no thermal couple other than that integrated in the furnace was installed in the reactor. Gases were fed through three lines and mixed before entering the reactor. In each line, a Brooks 5850E mass flow controller, a ball valve, and a check valve connected in series were used to control the gas flow. Gas flow rates were set through Brooks 0254 set point controller. The mass flow controllers were calibrated with the feed gases using a soap bubble flowmeter. Pressure inside the reactor was controlled by a back pressure regulator. The pressure at the inlet of the reactor was monitored by a Bourdon tube pressure gauge. All tubing connected downstream to the reactor was kept at 100–150 °C by a heating tape to prevent excessive condensation. The effluent was analyzed by gas chromatography.

3.10. Gas chromatography (GC)

Composition of the product stream from CO_2 hydrogenation experiments was analyzed by an Agilent 7890A gas chromatograph. Gas samples were taken by automated valves and processed in two channels. In one channel, the sample was separated by an Agilent HP-1 capillary dimethylpolysiloxane column and analyzed by a flame ionization detector. In the other channel, water and oxygenates were first removed by back flushing a HayeSep Q pre-column. CO_2 was then separated by a HayeSep Q packed column and other permanent gases by a MolSieve 5A packed column, which eventually led the gas to a thermal conductivity detector. Purified helium (>99.9995%) was used as the carrier gas in all experiments.

Chapter 4. Structured Assemblages of Single-Walled 3d Transition Metal Silicate Nanotubes for Methanol Synthesis by CO_2 Hydrogenation

4.1. Introduction

Tubular microscopic structures have attracted enormous attention since the discovery of carbon nanotube.[184] Their large surface area and molecular sieving properties lead to potential applications in catalysis,[185-186] chemical sensing,[187] and drug delivery.[188] For practical applications, nanotubes synthesized by facile template-free or soft-templated methods are particularly interesting. The majority of published works on this topic have been focused on crystalline elements or simple compounds, *e.g.*, carbon,[189] noble metals[190] and metal oxides.[191] Since their rigid structures prevent post-synthesis tuning of composition, unique synthetic methods are required for different materials with the same structure. It is thus difficult to study separately the effect of composition on material properties such as catalytic activity.

In recent years, several porous transition metal silicates have been synthesized from SiO_2 precursors,[41-42, 44, 47, 49-52, 55] and notably copper silicate was shown to form nanotubes.[41, 47, 50-51, 55] Nickel silicate[42, 44] and cadmium silicate nanotubes[41] with much thicker walls have also been synthesized. In terms of crystal structure, the reported silicate materials are layered clays, which are ubiquitous in Earth's crust. As shown in Scheme 4.1, structurally, each silicate lamella of 1:1 trioctahedral clays is composed of an octahedral metal hydroxide layer sharing oxygen atoms with another tetrahedral $[Si_2O_5]^{2-}$ layer. In many cases, metal ions and water also enter the interlamellar space where they can travel relatively freely, allowing for a certain degree of ion

exchange.[192] Such a property has been extensively explored for removal of aqueous heavy metal ions.[193-194] Since ion exchange is largely limited to the interlamellar space without affecting the octahedral layer, compositional tuning of clay materials to a significant extent remains difficult. In this work, controlled synthesis of single-walled copper silicate nanotubes (CuSiNT) is demonstrated and more importantly, a general method is developed to dope them with other 3*d* transition metals by extending ion exchange to the octahedral layer.

Scheme 4.1. Ion exchange of Cu^{2+} in CuSiNT with 3d transition metal ions†

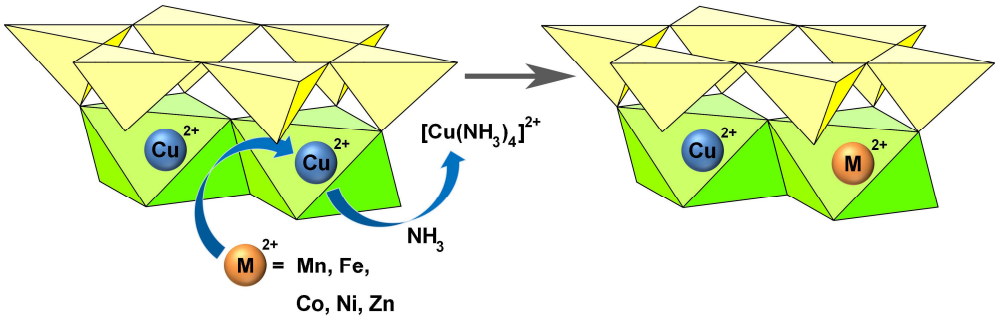

†Corner-sharing tetrahedrons are the $[Si_2O_5]^{2-}$ layer, and edge-sharing octahedrons are the transition metal hydroxide layer. The exchange process is facilitated by NH_3 complexation.

4.2. Experimental Section

4.2.1. Chemicals and reagents

Tetraethyl orthosilicate (TEOS), cetyltrimethylammonium bromide (CTAB), tetradecyltrimethylammonium bromide (TTAB), poly(diallyldimethylammonium) chloride solution (PDDA, 20%), vanadyl sulfate ($VOSO_4{\cdot}xH_2O$), chromium acetate hydroxide ($Cr_3(CH_3COO)_7(OH)_2$), manganese acetate ($Mn(CH_3COO)_2{\cdot}4H_2O$), zinc nitrate ($Zn(NO_3)_2{\cdot}6H_2O$), hydrazine hydrate solution ($N_2H_4{\cdot}H_2O$, 35%), trisodium citrate ($Na_3C_6H_5O_7{\cdot}2H_2O$), sodium hydrosulfite ($Na_2S_2O_4$) and Pluronic P-123 from

Aldrich, ammonia solution (NH_3, 32%), ferrous sulfate ($FeSO_4 \cdot 7H_2O$), nickel nitrate ($Ni(NO_3)_2 \cdot 6H_2O$), copper nitrate ($Cu(NO_3)_2 \cdot 3H_2O$) and sodium hydroxide (NaOH) from Merck, ammonium chloride (NH_4Cl) from BDH, ethanol from Fisher Scientific and cobalt nitrate ($Co(NO_3)_2 \cdot 6H_2O$) from Acros Organics were used as received without further purification. Deionized water was used throughout this work.

4.2.2. Synthesis of SiO_2 spheres

SiO_2 spheres used as precursors for CuSiNT were synthesized by a reported method with modification.[10] 3 mL of TEOS was dissolved in a mixture of 6 mL of water and 40 mL of ethanol, followed by the addition of 1 mL of 32% ammonia solution and 6 h of stirring at ambient temperature. The SiO_2 spheres were separated by centrifugation and washed with 1:1 ethanol/water solution. The product was then dispersed in deionized water at a concentration of *ca.* 1 mol/L.

4.2.3. Synthesis of CuSiNT-based hollow spheres

Unless specified otherwise, the following "standard" method was used to synthesize CuSiNT-based hollow spheres: 0.5 mL of 1 mol/L $Cu(NO_3)_2$, 1 mL of 32% NH_3 and 0.5 mL of the 1 mol/L SiO_2 suspension were added into 10mL of 1% Pluronic P-123 aqueous solution under stirring. The mixture (pH = 11.4) was sealed in a 30 mL Teflon-lined stainless steel autoclave and heated in an electrical oven at 150°C for 6 h, after which the autoclave was cooled in ambient air. The product was separated by centrifugation, washed with water, and dried at 60°C overnight.

In addition, CuSiNT-based hollow spheres were also synthesized by several other methods using different surfactants and Si sources as follows (the procedure for separation of product is the same as in the standard method):

CTAB as surfactant: 50 mg of CTAB was dissolved in 10 mL of water, to which 0.45 mL of 1 mol/L $Cu(NO_3)_2$, 1 mL of 32% NH_3 and 0.5 mL of the 1 mol/L SiO_2

suspension were then added under stirring. The mixture was heated in a 30 mL Teflon-lined autoclave at 150°C for 6 h.

TTAB as surfactant: The previous method was followed except that the CTAB was replaced with 150 mg of TTAB.

PDDA as surfactant: 0.5 mL of the 1 mol/L SiO_2 suspension was mixed with 0.25 g of 20% PDDA solution and stirred for 30 min. It was then added to a solution formed by 0.45 mL of 1 mol/L $Cu(NO_3)_2$, 1 mL of 32% NH_3, 0.16 g of NH_4Cl and 10 mL of water, and heated in a 30 mL Teflon-lined autoclave at 160°C for 20 h.

TEOS directly used as Si source: 100 μL of TEOS, 0.6 g of Pluronic P-123, 0.5 mmol of $Cu(NO_3)_2{\cdot}3H_2O$ and 1 mL of 32% NH_3 were dissolved in a mixture of 9 mL of water and 10 mL of ethanol in the order stated. The solution was then heated in a 30 mL Teflon-lined autoclave at 150°C for 3 h.

4.2.4. Synthesis of ordered CuSiNT bundles

Unless specified otherwise, the following "standard" method was used to synthesize ordered CuSiNT bundles: 0.16 g of NH_4Cl, 0.5 mL of 1 mol/L $Cu(NO_3)_2$, 1 mL of 32% NH_3 and 0.5 mL of the SiO_2 suspension were added into 10 mL of 1% Pluronic P-123 aqueous solution under stirring. The mixture (pH = 10.1) was heated in a 30 mL Teflon-lined autoclave by an electrical oven at 150°C for 20 h. The product was separated by centrifugation and washed repeatedly with water.

Synthesis using sodium silicate solution as Si source was also successful. The method is as follows: 0.21 g of NH_4Cl, 0.5 mL of 1 mol/L $Cu(NO_3)_2$, 1 mL of 32% NH_3 and 80 μL of sodium silicate solution were added to 10 mL of 1% Pluronic P-123 solution. The mixture was heated in a 30 mL Teflon-lined autoclave at 140°C for 24 h.

4.2.5. Increasing the Cu content of ordered CuSiNT bundles

After a standard synthesis of ordered CuSiNT bundles, 0.5 mL of 1 mol/L $Cu(NO_3)_2$ was added into the autoclave without the CuSiNT being separated, and the autoclave was sealed again and heated at 150°C for 6 h. The final product was separated by centrifugation and washed with water.

4.2.6. Doping of CuSiNT by post-synthesis ion exchange

10 mg of CuSiNT-based hollow spheres was treated in 4 mL of aqueous solution containing 1–4 mmol of NH_3, 2–4 mmol of NH_4Cl, 0–0.27 mmol of N_2H_4, 0–0.25 mmol of trisodium citrate and 0.14–0.25 mmol of dopant salts [$V_2(SO_4)_3$, $Cr_3(CH_3COO)_7(OH)_2$, $Mn(CH_3COO)_2$, $FeSO_4$, $Co(NO_3)_2$, $Ni(NO_3)_2$ or $Zn(NO_3)_2$] at 60–80°C for 2–6 h. The products were separated by centrifugation and washed with water. Details about the experimental conditions are tabulated in Table 4.1.

Table 4.1. Amounts of chemicals and reaction conditions for post-synthesis ion exchange of CuSiNT

Dopant	Metal source*	Amount of reagents (mmol)				Tem-perature (°C)	Time (h)
		NH_3	NH_4Cl	N_2H_4	$Na_3C_6H_5O_7$		
V	$V_2(SO_4)_3$[†]	1	4	0	0.25	60	2
Cr	$Cr_3(AcO)_7(OH)_2$	1	4	0	0.05	80	6
Mn	$Mn(AcO)_2$	4	2	0.27	0.25	80	6
Fe	$FeSO_4$	4	2	0.27	0.25	60	3
Co	$Co(NO_3)_2$	4	2	0.27	0.10	80	6
Ni	$Ni(NO_3)_2$	4	2	0	0	80	6
Zn	$Zn(NO_3)_2$	4	2	0	0	80	6

*0.25 mmol of metal source was used for all dopants except Fe, where 0.14 mmol was used

[†]synthesized *in situ* by reacting $VOSO_4$ with $Na_2S_2O_4$ at a mole ratio of 6:1

4.2.7. Scaled-up doping of CuSiNT

The doped CuSiNT for catalyst evaluation were prepared by a scaled-up method, where 240 mg of CuSiNT-based hollow spheres was dispersed in 40 mL of buffer solution containing 1 mol/L NH_3 and 0.5 mol/L NH_4Cl, added with a total of 2.5 mmol of $Ni(NO_3)_2$ and/or $Zn(NO_3)_2$ and heated in a 50 mL Teflon-lined autoclave at 80−120°C for 6 h. Details about the experimental conditions are tabulated in Table 4.2.

Table 4.2. Amounts of chemicals and reaction conditions for scaled-up doping of CuSiNT

Sample name*	$Zn(NO_3)_2$ (mmol)	$Ni(NO_3)_2$ (mmol)	Temperature (°C)	Time (h)
Zn34–CuSiNT	2.5	0	80	6
Zn43–CuSiNT	2.5	0	120	6
Ni4–Zn30–CuSiNT	2.0	0.5	80	6

*Numbers in sample names denote mole percentage of dopants with respect to total amount of metals in product.

4.2.8. One-pot synthesis of doped CuSiNT

Basically, the synthetic method of CuSiNT-based hollow spheres was followed, except that the 0.5 mL aliquot of 1 mol/L $Cu(NO_3)_2$ solution was replaced by 0.4 mL of 1 mol/L $Cu(NO_3)_2$ and 0.1 mL of 1 mol/L $Ni(NO_3)_2$ (for Ni-doped CuSiNT) or 0.1 mL of 1 mol/L $Zn(NO_3)_2$ (for Zn-doped CuSiNT).

4.2.9. Deposition of hydroxides on CuSiNT

10 mg of CuSiNT-based hollow spheres was dispersed in 3.6 mL of water. 30 μL of 1 mol/L $Co(NO_3)_2$, $Ni(NO_3)_2$ or $Zn(NO_3)_2$ solution was added for the deposition of $Co(OH)_2$, $Ni(OH)_2$ or $Zn(OH)_2$, respectively. 60 μL of 1 mol/L NaOH solution was then added under constant stirring in each case. After heating at 60°C for 1 h in an electrical oven, the product was separated by centrifugation and washed with water.

4.2.10. Calcination of nanotubes

The as-synthesized nanotubes were calcined in static air with a muffle furnace. The temperature was increased from room temperature to 100°C at the rate of 5 °C/min, and then to 500 °C at 1.5 °C/min. It was kept 500 °C for 4 h, and cooled naturally to room temperature.

4.2.11. Synthesis of Cu-based nanocatalysts

The calcined nanotubes were heated under a 50 mL/min flow of 10% H_2/N_2 in a tube furnace at 1 atm. The temperature was increased from room temperature to 200°C at the rate of 5°C/min, and kept 200°C for 2 h before naturally cooling down in the same atmosphere. The fresh products appeared black or brown, changing to dark green in air.

4.2.12. Evaluation of catalysts

200 mg of nanotubes calcined by the abovementioned method was loaded into a 3/8" stainless steel reactor to form a fixed bed. Details about the reactor set-up can be found in Section 3.9. *In-situ* activation was carried out in two stages (200 °C for 10 h and 240 °C for 1 h, with the same heating rate of 1 °C/min) under constant flow of 50 mL/min of 10% H_2/N_2 at 1 atm. The feed gas was then switched to 32 std mL/min of a 3:1 mixture of H_2 and CO_2 with 4% N_2 as internal standard. The reactor was slowly pressurized to 30 bar by a backpressure regulator. Online sampling and analysis of effluent were performed by an automated GC.

4.2.13. Materials characterization

In this work, charge reference for XPS analysis was made to the 1*s* binding energy of adventitious carbon at 284.6 eV. Outgassing of samples in preparation for N_2 sorption experiments was carried out in flowing He at 200 °C for 3 h.

4.3. Results and Discussion

4.3.1. Synthesis and characterization of undoped CuSiNT

As a precursor for CuSiNT, uniform SiO_2 spheres with diameters of *ca* 200 nm were prepared. When a suspension of the SiO_2 spheres was allowed to dry naturally on a carbon-coated copper grid, the spheres assembled spontaneously into 2-D arrays shown in Figure 4.1. The regular packing observed in such arrays reflects the uniformity of the spheres.

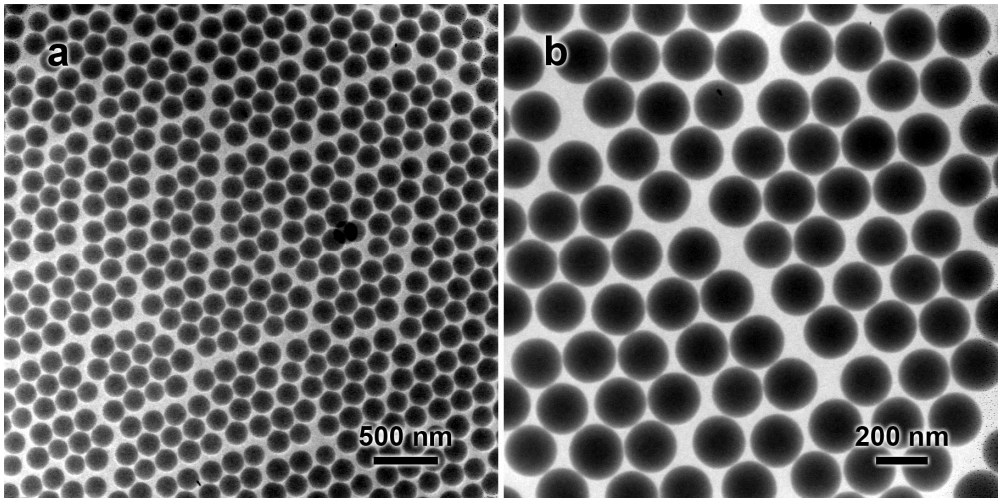

Figure 4.1. TEM images of SiO_2 spheres used to synthesize CuSiNT-based hollow spheres at (a) lower and (b) higher magnification.

CuSiNT-based hollow spheres were hydrothermally synthesized from the SiO_2 spheres. The dried product was a loose, light blue powder. Using EDX elemental analysis, typical yield was calculated to be 84% and 86% based on the amount of $Cu(NO_3)_2$ and that of SiO_2 in the precursor mixture, respectively. Figure 4.2a shows that the hollow spheres have internal diameters of *ca* 200 nm, matching the size of precursor SiO_2 spheres. The shells are hierarchically constructed of uniform open-ended nanotubes, with an average outer diameter and wall thickness of 6 nm and 1 nm respectively (Figure 4.2b,c). The wall thickness is homogeneous throughout the tubular structure. In Figure 4.2d lattice fringes with an interspace of 0.4 nm are also observed aligning perpendicularly to the tube axis, indicating the crystalline nature of

CuSiNT. Interestingly, the secondary structure of CuSiNT could be tuned by careful control over the pH of the precursor solution. The aforementioned hierarchical hollow spheres formed with 100% morphological yield at a higher initial pH of 11.4, while ordered CuSiNT bundles shown in Figure 4.2e,f were the only product when NH_4Cl was added to maintain the pH at 10.1. In addition, the average length of individual nanotubes increased under the effect of lower pH (compare Figure 4.2b and 4.2e). The differences are believed to be a manifestation of pH-dependent growth kinetics of the CuSiNTs, which will be discussed in more detail in Section 4.3.2.

To understand further their secondary structures, the powder samples of CuSiNT were analyzed by small-angle XRD. In Figure 4.3a,b, the results show the presence of mesoscale ordered assemblages of CuSiNT in both the hollow spheres and the bundles, with the latter exhibiting higher orderliness. The diffraction peaks can be assigned to a 2-D hexagonal packing with *p6mm* plane group. After profile fitting, the average axis-to-axis distance between two neighboring nanotubes in the hexagonal assemblage, which is equivalent to the edge length of the *p6mm* unit cell, was determined to be 5.0 nm for the hollow spheres of CuSiNT and 4.7 nm for the bundles of CuSiNT.

Formation of similar aggregated mesostructures has been reported for imogolite-type single-walled aluminum silicate nanotubes as a result of highly uniform tube diameter.[195-196] It was recently proposed that upon assembling the initially cylindrical imogolite nanotubes deform slightly to achieve close packing,[196] which in the present case explains the smaller axis-to-axis distance of nanotubes calculated from small-angle XRD patterns compared with the outer diameter observed by TEM. In addition, the denser packing of ordered CuSiNT bundles is also reflected by the smaller axis-to-axis distance. To the best of our knowledge, it is the first time ordered packing of transition metal silicate nanotubes has been studied.

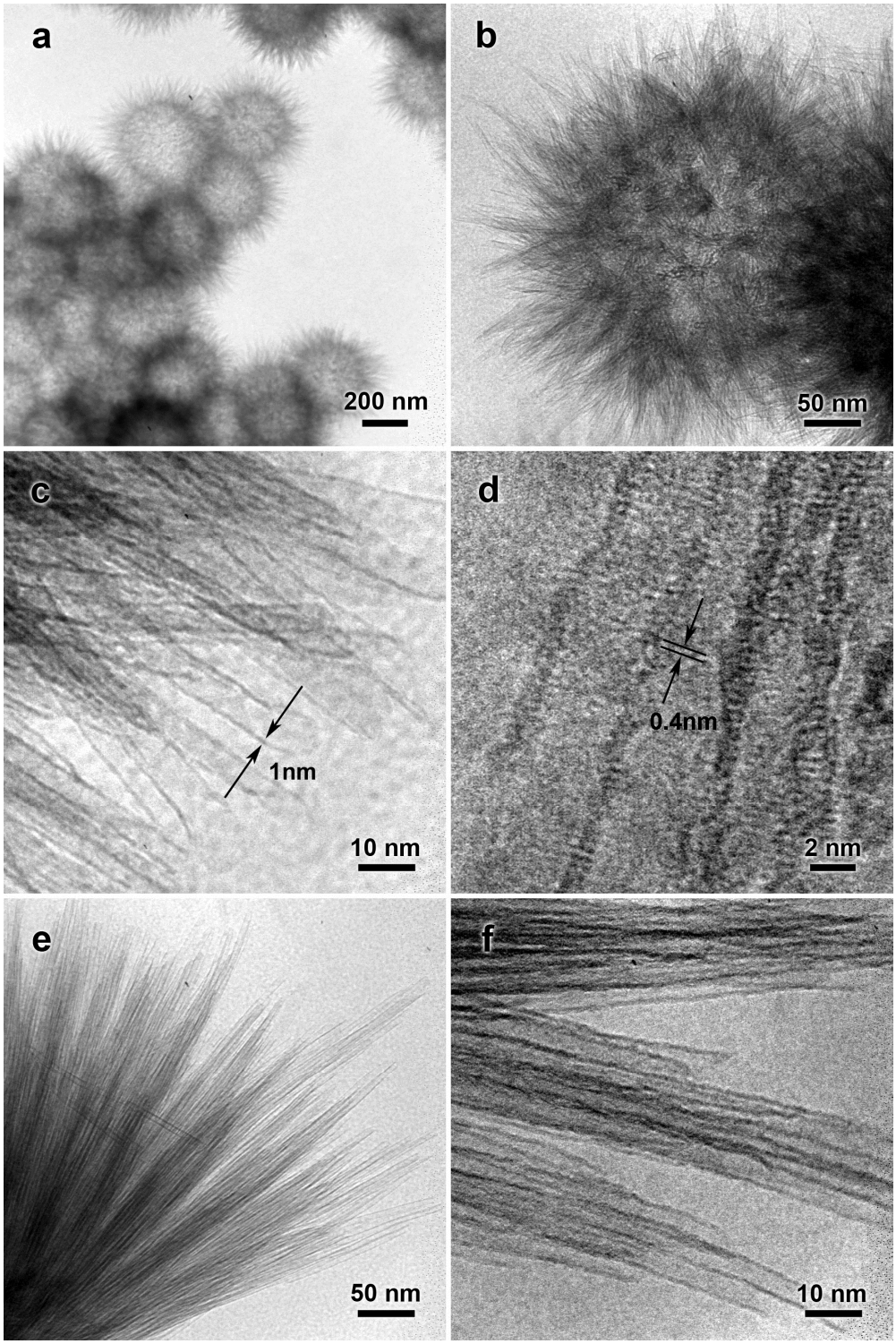

Figure 4.2. TEM images of as-synthesized (a–d) CuSiNT-based hollow spheres and (e,f) ordered CuSiNT bundles.

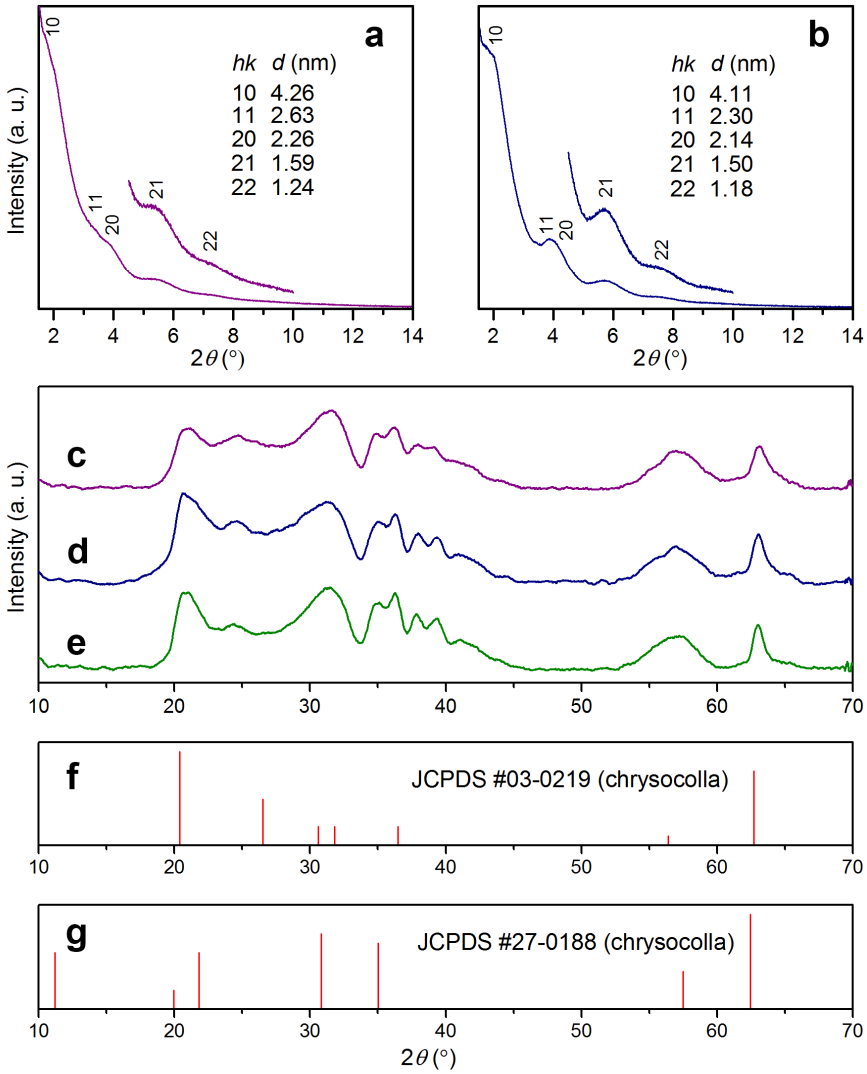

Figure 4.3. Powder XRD patterns of (a,c) as-synthesized CuSiNT-based hollow spheres, (b,d) as-synthesized ordered CuSiNT bundles, and (e) ordered CuSiNT bundles after treatment in Cu-rich environment. (f,g) JCPDS cards for reference.

Through EDX analysis, the atomic ratio of Cu/Si in the CuSiNT-based hollow spheres was found to be 1.05, an order of magnitude higher than that usually achieved in Cu-doped amorphous silica.[197] In comparison, the ordered CuSiNT bundles have a lower Cu/Si ratio of 0.85. As observed in Figure 4.2f, the lower Cu content has not affected the formation of nanotubes, which reflects the compositional flexibility of CuSiNT. Indeed, by treating the ordered CuSiNT bundles in a Cu-rich environment (see Section 4.2.5), the Cu/Si ratio could be increased to 0.99 without any morphological change.

In contrast to the differences in secondary structure and elemental composition, the crystal structure of CuSiNT remains the same according to wide-angle XRD analysis reported in Figure 4.3c–e. A series of weak peaks are resolved from the XRD patterns which could be best assigned to chrysocolla, among various other hydrated hydroxysilicates of Cu. Assignment of this phase to JCPDS card #03-0219 has been reported, as shown in Figure 4.3f.[50] Generally, chrysocolla is considered a clay material consisting of kaolinite-like lamellae, but its crystallographic structure has not been solved so far. Diffraction signals from chrysocolla have been indexed based on a proposed structure model where hydrated Cu hydroxide islands appear alternatively on both sides of silicate stripes.[198] The results were summarized in JCPDS card #27-0188 (Figure 4.3g), replacing card #03-0219 as the powder XRD standard. The diffraction signal at $2\theta = 11.2°$ or $d = 7.9$ Å corresponding to the inter-lamellar spacing is clearly missing in Figure 4.3a–e, which supports the single-walled structure of CuSiNT. The significant peak broadening is also consistent with such structure, and the relatively strong peak at $2\theta = 21.4°$ ($d = 4.15$ Å) matches well the lattice fringe spacing observed by TEM. However, it is worth mentioning that the standard powder XRD patterns of chrysocolla including JCPDS #27-0188 were acquired from poorly crystallized natural minerals using film-based techniques, whereby weak diffraction peaks could be overlooked. For example, the peaks at $37° < 2\theta < 45°$ in Figure 4.3c–e were not recorded in either of the JCPDS cards (Figure 4.3f,g). It is believed that the presence of the above-mentioned diffraction peaks is a combined result of relatively higher crystallinity of hydrothermally synthesized CuSiNT and modern XRD instrumentation.

To further confirm the nature of CuSiNT, FTIR and XPS analyses were performed. The FTIR spectra in Figure 4.4a–c display fingerprint signals typical for chrysocolla.[199-201] Briefly, two sharp peaks at 3618 cm^{-1} and 675 cm^{-1} can be assigned respectively to the stretching and bending modes of OH shared by three Cu atoms in

octahedral positions. The sharp peak at 502 cm^{-1} is due to Cu–O–Si bending. Stretching and bending modes of adsorbed H_2O appear as a broad band centered around 3453 cm^{-1} and a peak at 1636 cm^{-1}, respectively. The strongest peak at 1034 cm^{-1} is assigned to Si–O stretching of silicate tetrahedrons, and peaks at 825 cm^{-1} and 775 cm^{-1} are due to the stretching of silicate chains. The weak peaks in the ranges of 3000–2840 cm^{-1} and 1500–1220 cm^{-1} belong to Pluronic P-123. From the Cu $2p_{3/2}$ photoelectron spectra shown in Figure 4.4d–f, the only main peak resolved at the binding energy of 935.4±0.1 eV is also characteristic for Cu^{2+} in octahedral positions of clay materials (the three peaks at 939.4±0.2, 942.2±0.1 and 944.2±0.1 eV are satellite peaks of the same main peak, deconvoluted by assuming the same FWHM of the two satellite peaks at higher binding energies and the main peak).[202-204] In the mineralogical database of the RRUFF project, $(Cu_{2-x}Al_x)H_{2-x}Si_2O_5(OH)_4 \cdot nH_2O$ has become the generally agreed formula for chrysocolla,[205] where the $[Si_2O_5(OH)_4]^{6-}$ group reflects its 1:1 clay structure and protons balance the excessive negative charge of the hydroxysilicate framework.[201] Considering here the absence of Al and variable Cu content in CuSiNT, a general chemical formula of $Cu_{2-x}H_{2+2x}Si_2O_5(OH)_4 \cdot nH_2O$ can be written for them. With the CuSiNT identified as chrysocolla, it is reasonable to compare the wall thickness of CuSiNT with the lamellar thickness of clay materials (from 7 Å for kaolinite to 14 Å for chlorite) and draw the conclusion that CuSiNT synthesized with the present method have a single wall only.

Besides the "standard" methods discussed so far, other methods of synthesizing CuSiNTs have also been proven successful. Figure 4.5a–c and Figure 4.5d,e show the morphology of CuSiNT-based hollow spheres synthesized using CTAB and TTAB as surfactant, respectively. Compared with the product of the standard method, there is insignificant change of the tubular morphology in these cases. It suggests that the formation of nanotubes is largely a result of properties of CuSiNT itself, instead of template effects of the surfactants. Nevertheless, surfactants do help with

reproducible synthesis of regularly shaped nanotubes; without them less regular nanotubes were often obtained as reported in Figure 4.5f. When the Pluronic surfactant is replaced with PDDA, however, more pronounced effects are observed (Figure 4.5g,h). Since SiO_2 spheres synthesized by the Stöber method are usually negatively charged, they have high affinity to positively charged surface-protecting agents, especially polyelectrolytes like PDDA. The strongly adsorbed polymer provides inter-particle repulsive forces, which results in less aggregation and hence relatively well dispersed particles shown in Figure 4.5g.

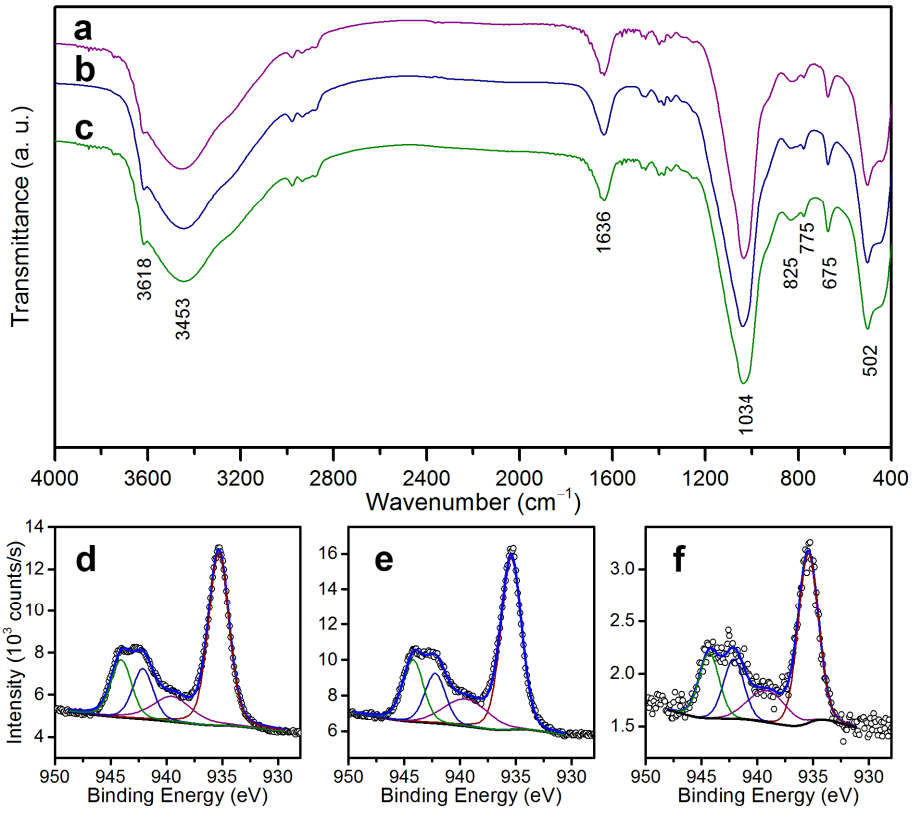

Figure 4.4. FTIR and XPS spectra of (a,d) as-synthesized CuSiNT-based hollow spheres, (b,e) as-synthesized ordered CuSiNT bundles, and (c,f) ordered CuSiNT bundles after treatment in Cu-rich environment. In d–f, open circles denote raw data and smooth curves are deconvolution results.

In addition, not only surfactant but Si source can also be replaced in synthesizing CuSiNT. For example, TEOS and sodium silicate were used as direct Si source to produce results comparable to the standard methods (Figure 4.5i–l). The presence of incompletely converted cores in Figure 4.5i,j and irregular particles in Figure 4.5k,

which are presumably SiO_2, indicates formation of CuSiNT through a SiO_2 intermediate.

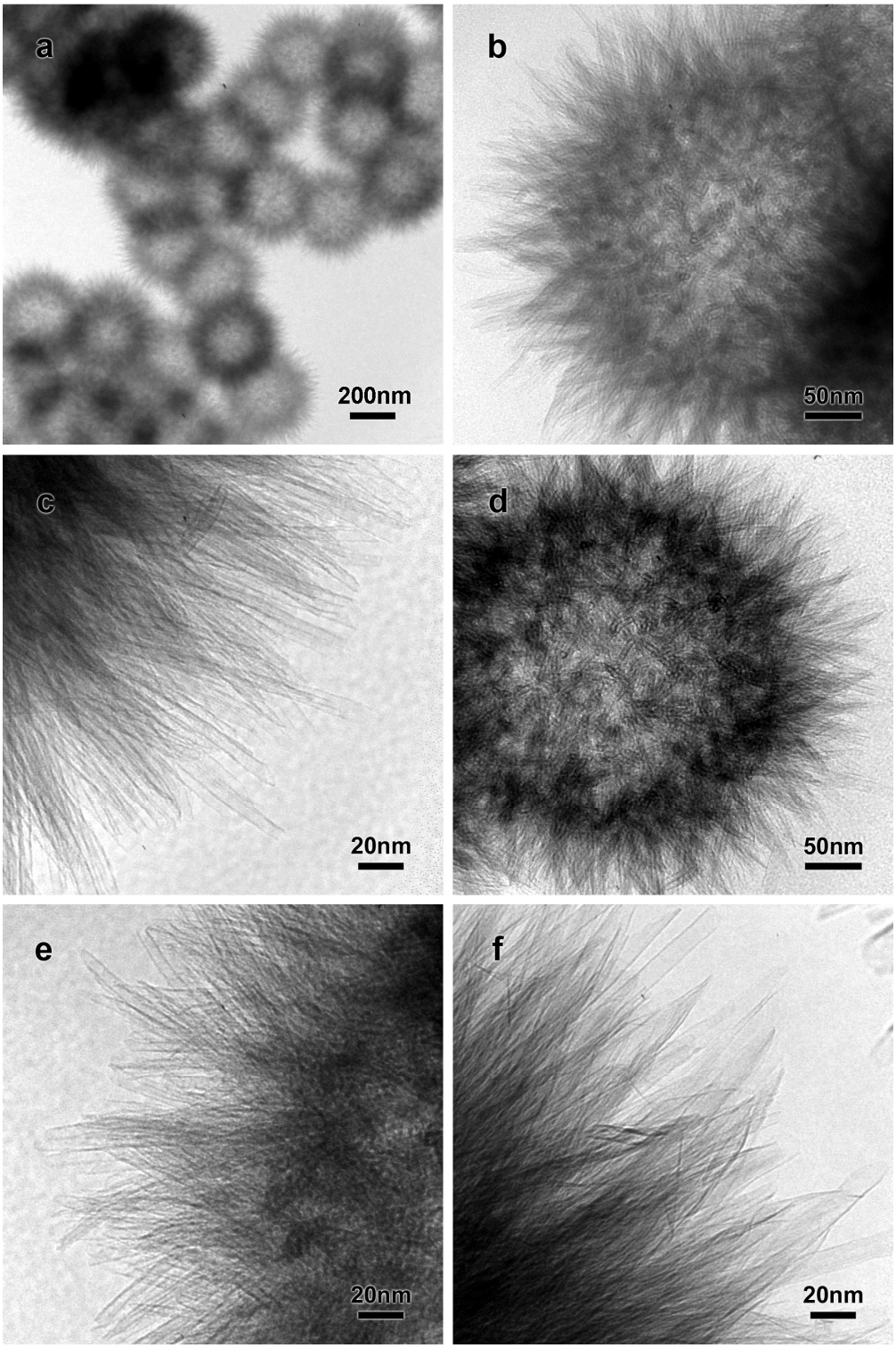

Figure 4.5. TEM images of CuSiNT-based hollow spheres synthesized with (a–c) CTAB as surfactant, (d,e) TTAB as surfactant, (f) no surfactant, (g,h) PDDA as surfactant, (i,j) TEOS as Si source, and (k,l) ordered CuSiNT bundles synthesized with sodium silicate as Si source.

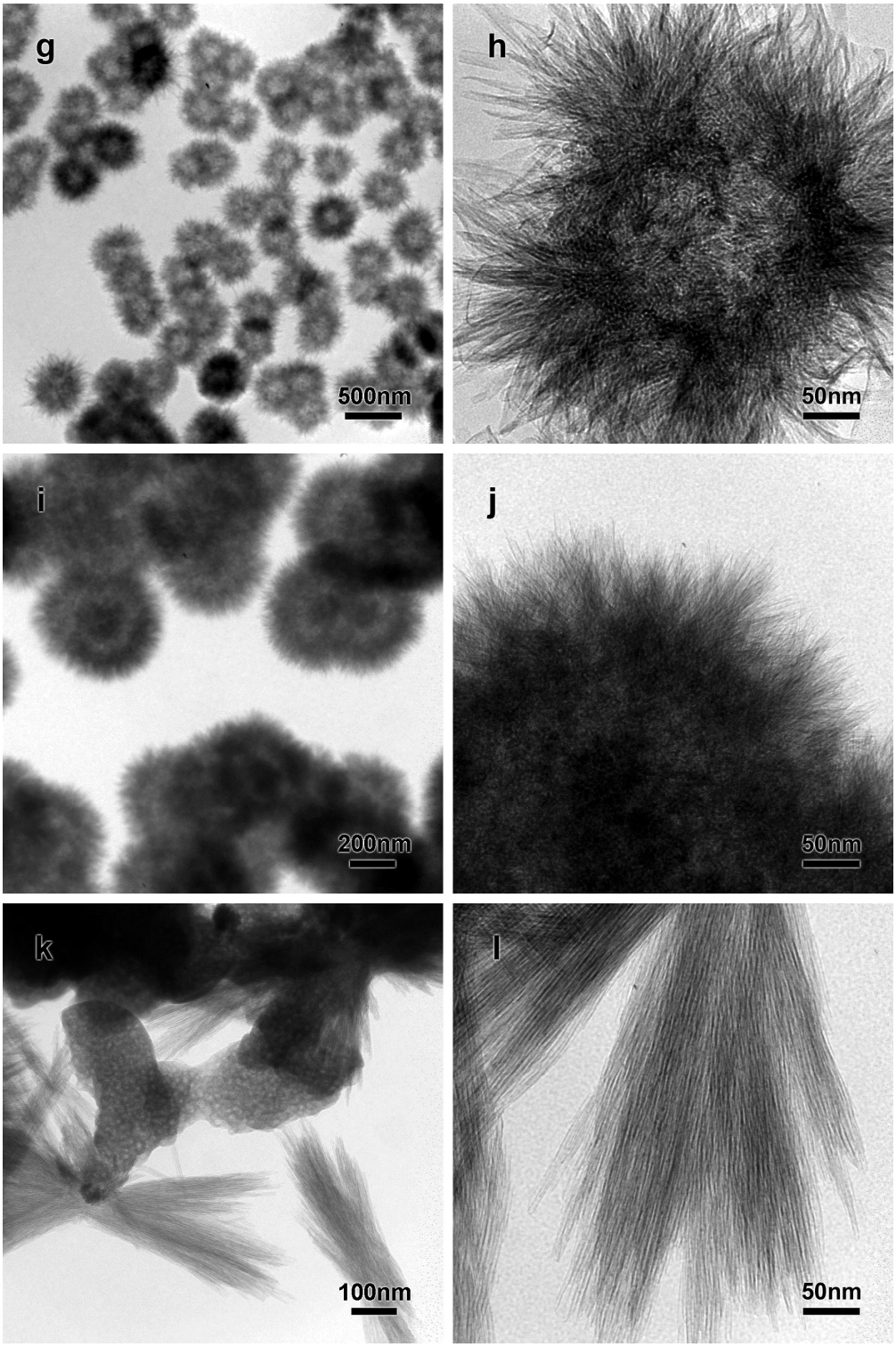

Figure 4.5 continued

4.3.2. Growth mechanism of undoped CuSiNT

The results obtained so far from X-ray and spectroscopic analyses do not explain the pH-dependent secondary structure of CuSiNT, and here their growth processes are monitored by time-resolved morphological studies for further insights. Figure 4.6a shows that at a high initial pH of *ca* 11.4, short CuSiNT have covered the surface of the SiO_2 precursor in the early stage of synthesis, forming a core-shell structure. The nanotubules continue to grow in length as the SiO_2 core dissolves until the hollowing is complete, as seen in Figure 4.6b,c. A dissolution-precipitation growth mechanism is thus proposed as follows: the SiO_2 precursor is first attacked by OH^- to release silicate ions (Equation 4.1), which then react with Cu^{2+} forming CuSiNT (Equation 4.2, where water of crystallization is omitted for clearer presentation).

$$SiO_2 + 4OH^- \leftrightarrow SiO_4^{4-} + 2H_2O \quad (4.1)$$

$$2SiO_4^{4-} + (2-x)Cu^{2+} + (5+2x)H_2O \rightarrow Cu_{2-x}H_{2+2x}Si_2O_5(OH)_4 + (4+2x)OH^- \quad (4.2)$$

Comparing Figure 4.6b,c with Figure 4.6d,e shows that the growth rate of CuSiNT on silica is significantly slower at the lower pH of 10.1. It seems that the lower alkalinity has slowed down the dissolution of SiO_2, allowing silicate ions to diffuse into the bulk solution and achieve a homogeneous concentration which in turn prevents excessive nucleation on the surface of SiO_2. As a result, CuSiNT grow from limited nucleation sites into bundles (Figure 4.6e,f). The greater length of individual nanotubules in ordered CuSiNT bundles can also be explained in this way. On the other hand, the effect of pH on CuSiNT growth is complicated by the availability of Cu^{2+} under the current experimental setting:

$$Cu^{2+} + 4NH_3 \leftrightarrow [Cu(NH_3)_4]^{2+} \quad (4.3)$$

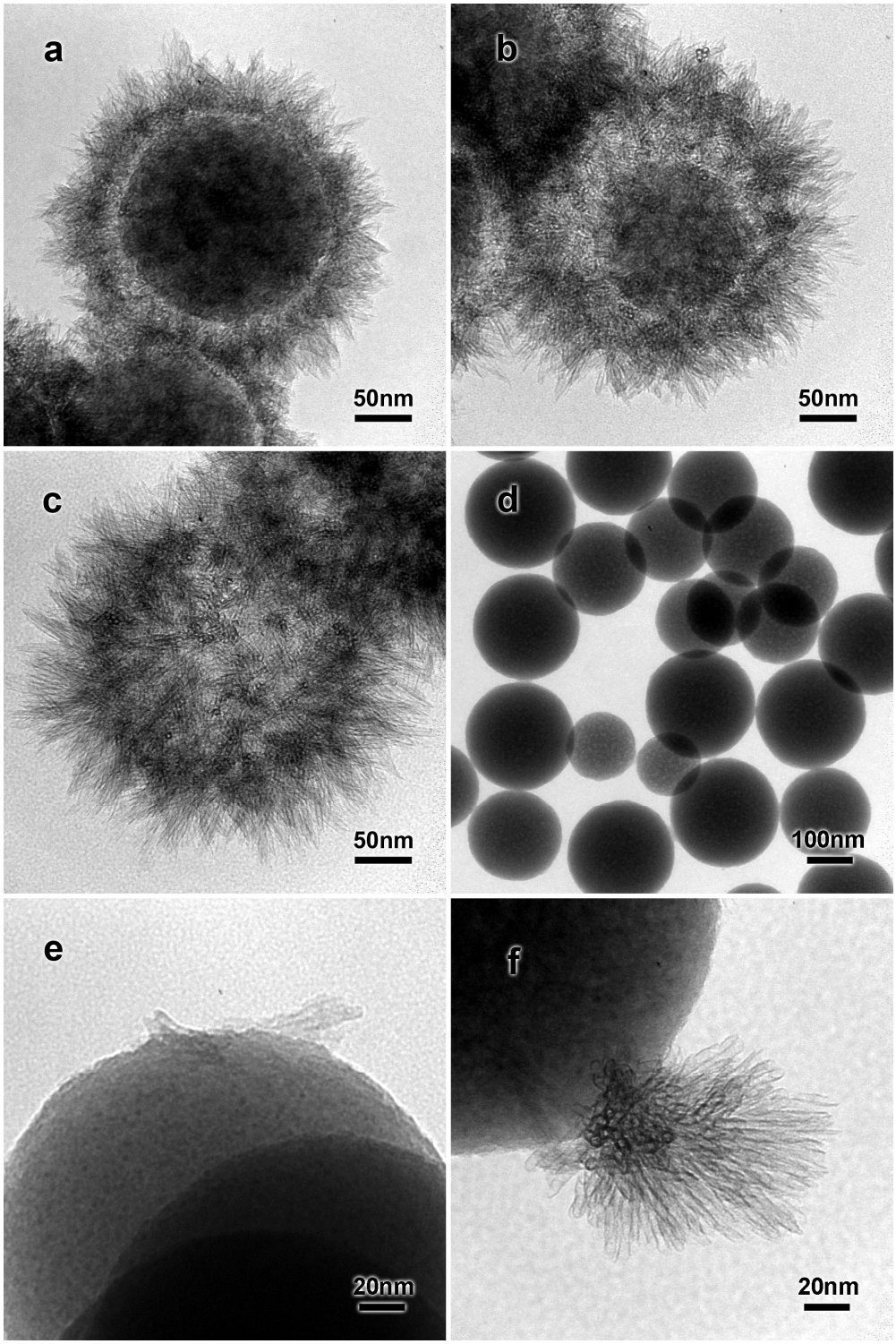

Figure 4.6. TEM images of intermediate products during the synthesis of CuSiNT-based hollow spheres (initial pH = 11.4) at (a) 0.5 h, (b) 1 h, and (c) 1.5 h, and during the synthesis of ordered CuSiNT bundles (pH = 10.1) at (d) 1 h, (e) 1.5 h, and (f) 2 h.

The equilibrium of Equation 4.3 is pH-dependent, with the formation of complex most favored at pH = 8.3–10.8.[206] Therefore at pH = 10.1 where ordered CuSiNT bundles are synthesized, the reaction rate may have also been controlled by free Cu^{2+}

concentration. To explore this effect, CuSiNT were synthesized at the same pH of 10.1 and double the amount of $Cu(NO_3)_2$. The morphology of the product confirms the role of Cu^{2+} concentration; CuSiNT assemblages similar to hollow spheres are formed when the Cu^{2+} is readily available (Figure 4.7a,b).

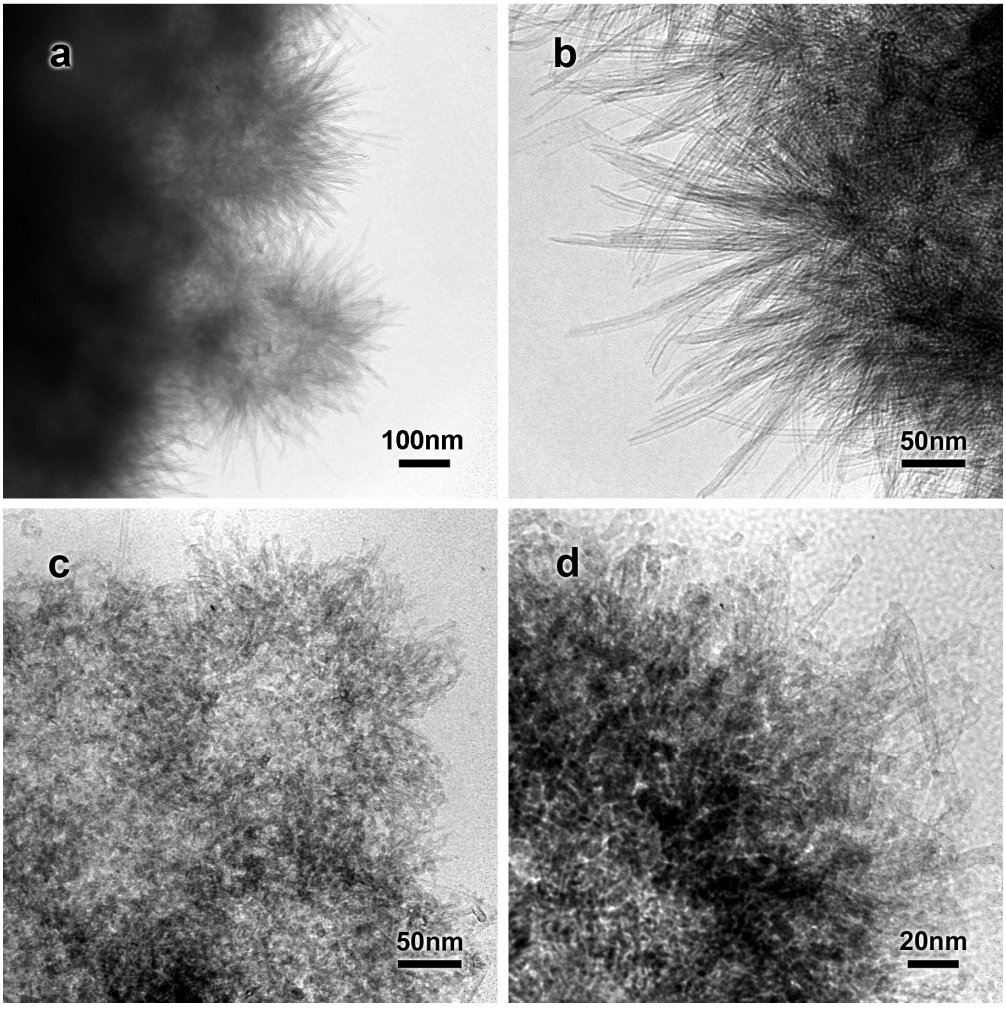

Figure 4.7. TEM images of (a,b) CuSiNT product obtained with the amount of $Cu(NO_3)_2$ in the standard synthetic method of ordered CuSiNT bundles doubled, and (c,d) CuSiNT-based hollow spheres after treatment by NH_3/NH_4Cl buffer.

Furthermore, the relation between pH and complexation equilibrium was studied by Cu leaching experiments on CuSiNT, where as-synthesized CuSiNT-based hollow spheres were treated with NH_4Cl solution, NH_3 solution or NH_3/NH_4Cl buffer solution and Cu content of the respective products was measured. The results are summarized in Table 4.3. It can be seen that copper leaching did not occur noticeably in either NH_4Cl or NH_3 alone, while the buffer solution formed by combining the two

extracted most of the copper, causing collapse of the tubular structure (Figure 4.7c,d). As explained before, the pH of the buffer solution falls in the middle of the range where formation of $[Cu(NH_3)_4]^{2+}$ is most favored, which limits the concentration of free Cu^{2+} significantly and creates a strong driving force for copper leaching. Meanwhile, the moderately alkaline condition provides still enough H^+ to replace Cu^{2+} balancing the negative charge of the silicate framework. In contrast, the significantly higher alkalinity of pure NH_3 solution may have rendered Cu^{2+} in CuSiNT more stable by promoting its hydroxylation. Therefore a combination of both moderate pH (*ca* 9.5) and presence of complexation agent (NH_3) is found necessary for the extraction of Cu from CuSiNT, which confirms the role of pH in the availability of Cu^{2+} in solution and meanwhile explains the different Cu contents in CuSiNT-based hollow spheres and ordered CuSiNT bundles.

Table 4.3. Leaching of Cu from CuSiNT-based hollow spheres in different conditions

Treatment	pH of solution	Cu/Si in product
None	N. A.	1.05
60°C, 3 h in 1 mol/L NH_4Cl	6.32	1.00
60°C, 3 h in 1 mol/L NH_3	11.60	1.15
60°C, 3 h in 1 mol/L NH_4Cl + 1 mol/L NH_3	9.52	0.30

However, attempts to synthesize other transition metal silicate nanotubes using the same synthetic method of CuSiNT did not succeed. The unique ability of copper silicate to form tubular structures is likely attributable to the special electronic properties of Cu^{2+}. Many clay materials have curved structures due to size mismatch between the octahedral and tetrahedral layers.[207-208] In the present case, strong Jahn-Teller effect renders 6-coordinated Cu^{2+} compounds an elongated octahedral configuration and the mismatch in chrysocolla lamellae may be anisotropic, which can lead to directional curving and hence formation of nanotubes.

4.3.3. Synthesis and characterization of doped CuSiNT

In order to incorporate other 3d metal elements, the as-prepared CuSiNT were treated with different metal salts dissolved in NH_3/NH_4Cl buffer solutions, in some cases together with hydrazine and/or trisodium citrate to stabilize the metal ions (the method is denoted as *post-synthesis ion exchange* from here onwards). It proved to be a versatile process to introduce almost all 3d transition metals (from V to Zn). Figure 4.8 shows the typical morphology of doped CuSiNT. Their elemental compositions are summarized in Table 4.4, where replacement of Cu with divalent dopants is apparent. The tubular structure of CuSiNT is well preserved after doping. The tube walls remain smooth except when doped with V^{3+} or Cr^{3+}. The doping behavior of trivalent V^{3+} or Cr^{3+} is somewhat different from that of divalent metal ions, which will be discussed later in this section.

Using Ni^{2+} and Zn^{2+} as examples, it is demonstrated that the degree of doping can be controlled by changing the temperature and duration of the doping process as shown in Figure 4.9. Furthermore, treating CuSiNT with an ion exchange bath containing both Ni and Zn results in simultaneous doping of the two elements (see Section 4.2.7). The product contains 4% of Ni and 30% of Zn by atomic percentage among its total metal content. In principle, the *post-synthesis ion exchange* method can be extended to incorporate any combination of 3d transition metals that have been successfully doped in this work.

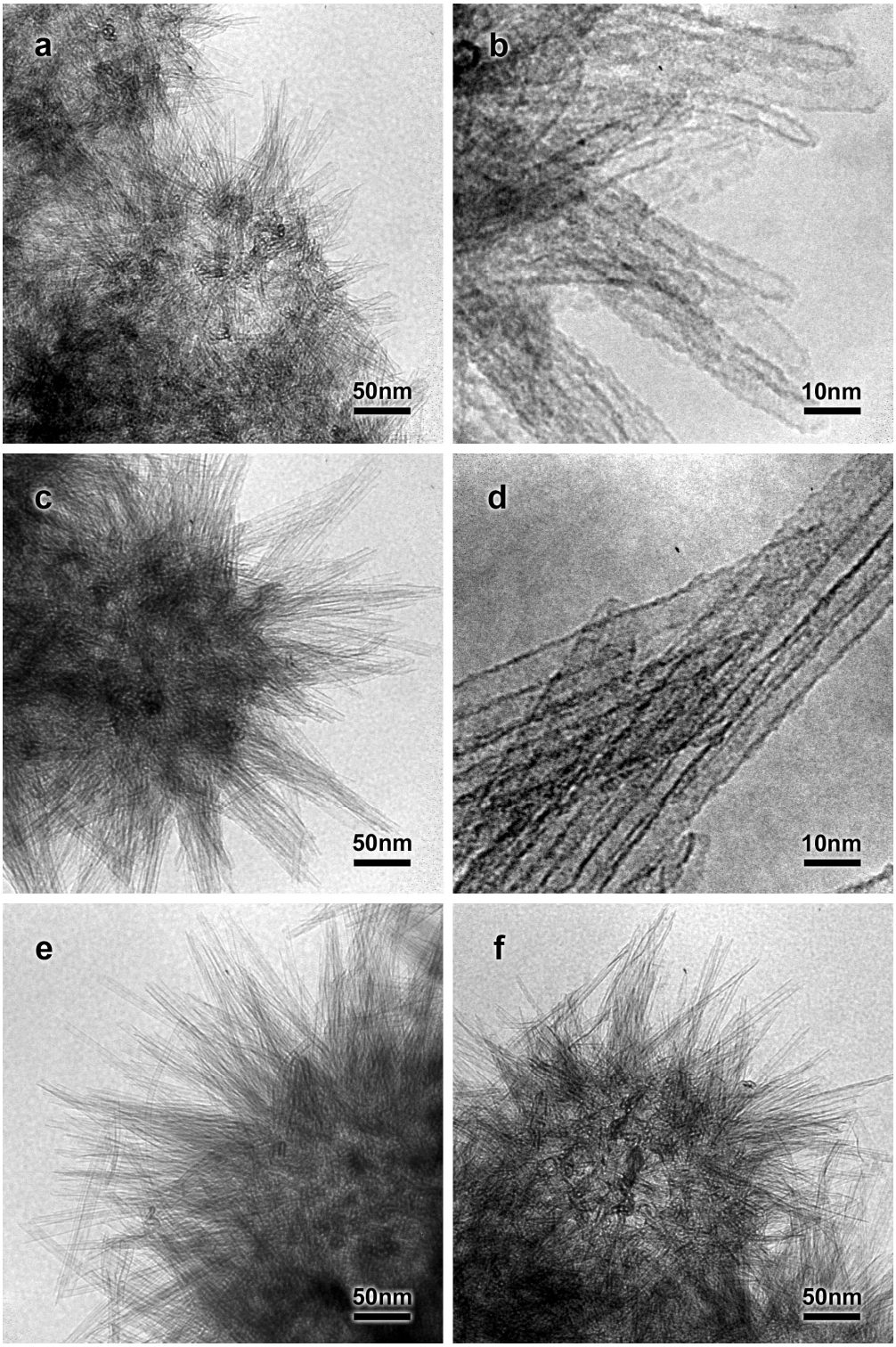

Figure 4.8. TEM images of (a,b) V-doped, (c,d) Cr-doped, (e) Mn-doped, (f,g) Fe-doped, (h) Co-doped, (i,j) Ni-doped, and (k,l) Zn-doped CuSiNT.

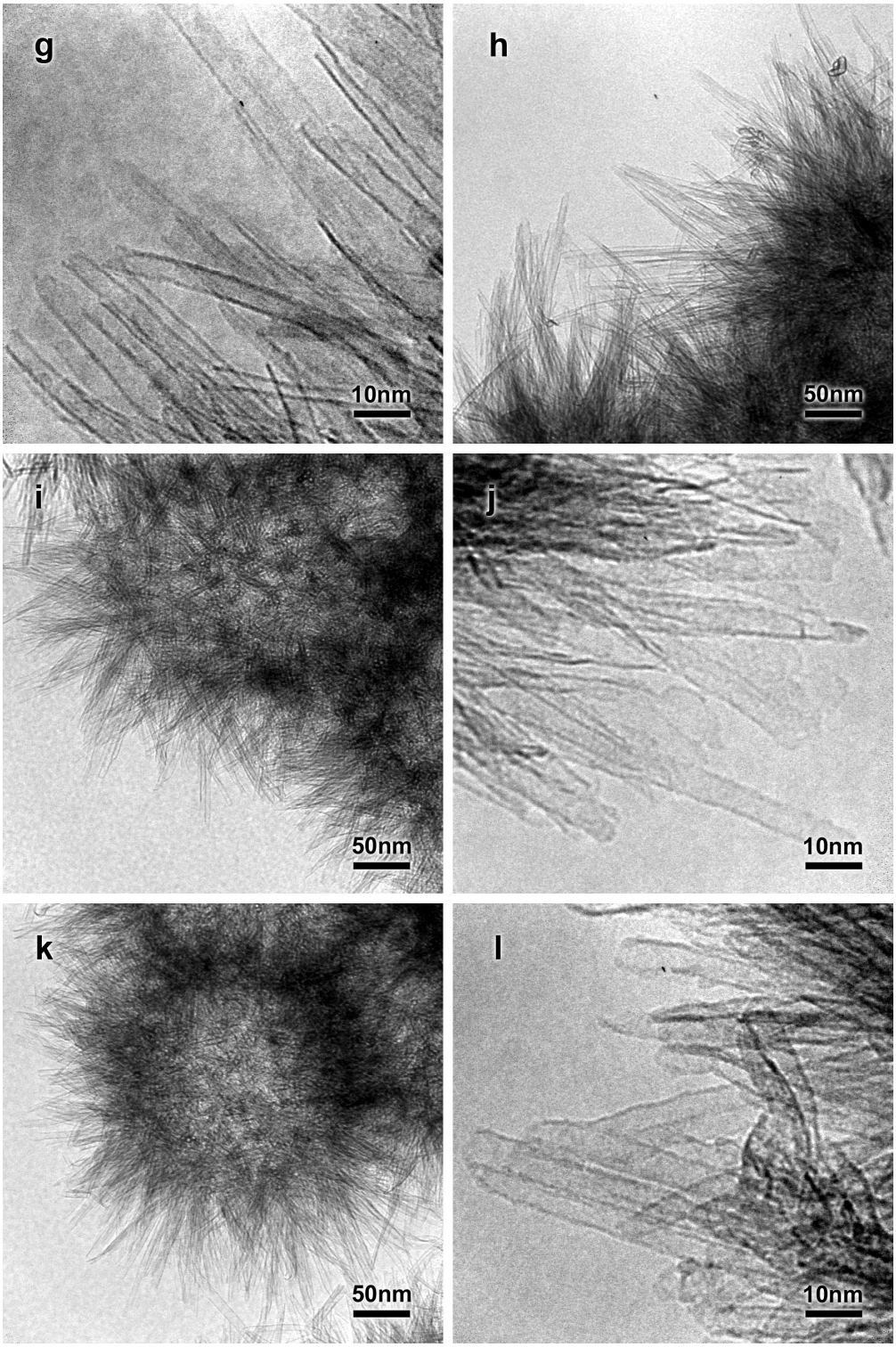

Figure 4.8 continued

Table 4.4. Selected characterization results of pristine and doped CuSiNT

Dopant	Cu/Si*	Degree of doping[◊] (%)	Shift in XRD peak[†] (°)	Shift in FTIR band[‡] (cm^{-1})
None	1.05	N. A.	0 (reference)	0 (reference)
V^{3+}	0.54	8	-0.09	0
Cr^{3+}	1.02	32	-0.01	0
Mn^{2+}	0.71	32	-0.93	-23
Fe^{2+}	0.19	87	N. A.	-50
Co^{2+}	0.84	35	-0.44	-15
Ni^{2+}	0.84	32	-0.19	-12
Zn^{2+}	0.77	32	-0.22	-8

*atomic ratios determined by EDX.

[◊]defined as atomic percentage of M/(M+Cu) where M denotes the dopant, determined by ICP-OES.

[†]compared with the peak of pristine CuSiNT at $2\theta = 63.11°$.

[‡]compared with the peak of pristine CuSiNT at 502 cm^{-1}.

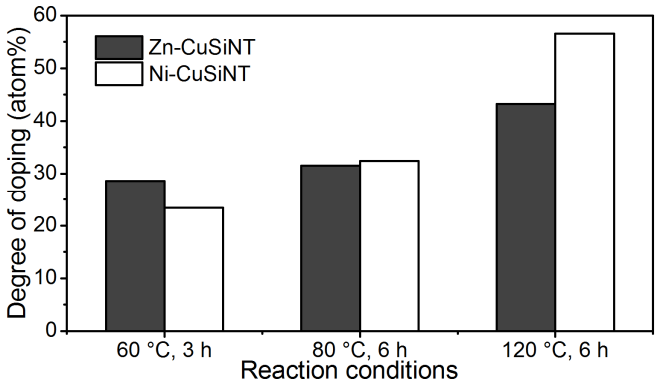

Figure 4.9. Tunable degree of Zn and Ni doping achieved under different experimental conditions. Doping at 120 °C was carried out in a Teflon-lined autoclave.

On the contrary, doping was not possible when CuSiNT was treated without ammonia. It is thus believed that the complexation of metal ions with ammonia has facilitated the doping process. Compared to that of Cu^{2+}, ammine complexes of Mn^{2+}, Fe^{2+}, Co^{2+}, Ni^{2+} and Zn^{2+} are less stable. The use of ammonia decreases the concentration of free Cu^{2+} to a larger extent than that of free dopant ions (M^{2+}),

creating a more significant concentration difference and hence a stronger driving force for the ion exchange to proceed towards the formation of M-doped CuSiNT, as shown in Equation 4.4.

$$Cu_{2-x}H_{2+2x}Si_2O_5(OH)_4 + yM^{2+} \leftrightarrow Cu_{2-x-y}M_yH_{2+2x}Si_2O_5(OH)_4 + yCu^{2+} \quad (4.4)$$

TEM observations reported in Figure 4.8j show that slight unfolding occurred in some doped CuSiNT samples, which is more noticeable at nanotube ends. The deformation can mainly be associated with the increased symmetry of the octahedral layer. As Cu^{2+} is replaced by dopant ions that exhibit weaker or no Jahn-Teller effect, the anisotropy of the mismatch between octahedral and tetrahedral layers in chrysocolla decreases, which creates considerable strain in the highly curved tube walls. Eventually the tube wall could be broken and cause unfolding. A related example is found in the case of halloysite, a layered clay material that can naturally occur as nanotubes. In halloysite, significant substitution of Al^{3+} by Fe^{3+} causes expansion of the octahedral hydroxide layer, which reduces the mismatch between octahedral and tetrahedral layers and inhibits the formation of tubular structures.[27] Such expansions are also expected to occur in the present doped CuSiNT samples, as the hydroxides of the dopants all have a longer unit cell *a*-edge than $Cu(OH)_2$ (Table 4.5).

Table 4.5. Lattice parameters of some transition metal hydroxides

Crystalline phase	*a*-edge length of hydroxide unit cell (Å)	Reference JCPDS card
$Mn(OH)_2$	3.315	#18-0787
$Fe(OH)_2$	3.258	#13-0089
$Co(OH)_2$	3.191	#45-0031
$Ni(OH)_2$	3.126	#14-0117
$Cu(OH)_2$	2.949	#13-0420
$Zn(OH)_2$	3.192	#24-1444

The isomorphous substitution of Cu in CuSiNT is supported by both powder XRD and FTIR analyses. In Figure 4.10, the peak of pristine CuSiNT at $2\theta = 63.11°$ shifts towards smaller angles after doping with Zn, Ni, Co and especially Mn. The peak shift is low in magnitude (Table 4.4) but highly reproducible. It indicates lattice expansion along the basal plane, which corresponds well to the expected expansion of the octahedral layer. In addition, no new phases are detected. In Figure 4.11a, shifts of FTIR band towards lower wavenumbers are observed for Cu–O–Si bending, which is also attributed to lattice expansion, *i.e.*, elongation of Cu–O bond or replacement of Cu–O bonds by longer dopant–O bonds. The magnitude of shifts in the XRD and FTIR peaks (Table 4.4) can be correlated to the unit cell dimension of the hydroxide of dopant; the longer the unit cell *a*-edge, the larger the shifts (Table 4.5). Fe-doped CuSiNT exhibit a particularly large FTIR band shift, presumably due to a high degree of doping. For the same reason, this sample has a relatively low crystallinity.

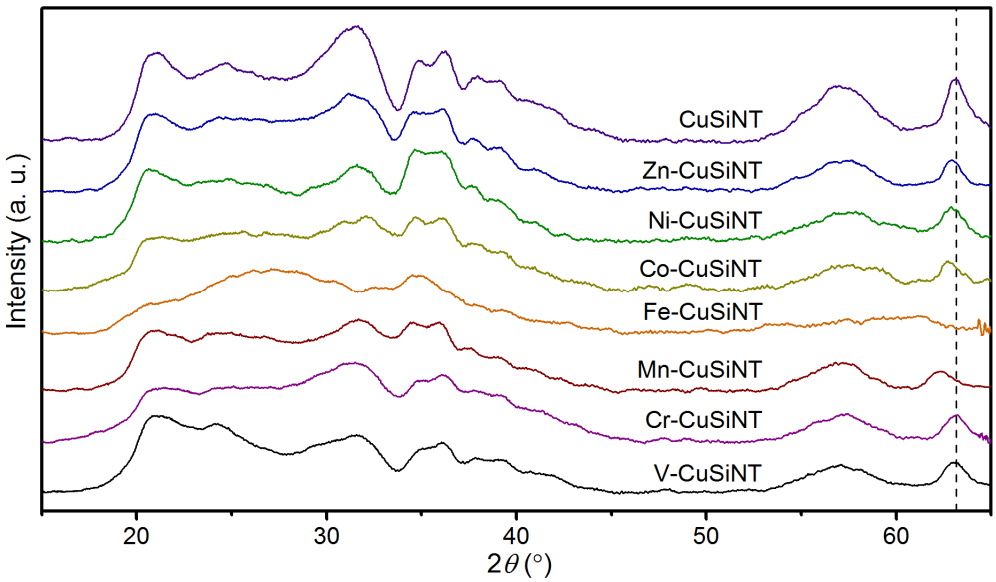

Figure 4.10. Powder XRD patterns of pristine and doped CuSiNT. The dashed line marks the peak position of pristine CuSiNT.

To further confirm the doping of CuSiNT by the divalent metal ions, other methods of introducing the dopants were tested and the products characterized for comparison. In one set of experiments, Ni-doped and Zn-doped CuSiNT were

synthesized by hydrothermal treatment of SiO_2 with a precursor solution that contained $Ni(NO_3)_2$ or $Zn(NO_3)_2$ in addition to $Cu(NO_3)_2$ as metal sources (the method is denoted as the *one-pot method* from hereafter). Compared with the *post-synthesis ion exchange*, the *one-pot method* involved higher temperature and pressure, and dopants were expected to readily enter the CuSiNT structure. Indeed, when analyzed by FTIR the products show similar band shifts in Figure 4.11b as in Figure 4.11a. Herein it is worth noting that other dopant ions are unstable under the hydrothermal conditions required to convert SiO_2, and the *post-synthesis ion exchange* remains to be the more general and versatile method to synthesize doped CuSiNT. In another set of experiments, $Co(OH)_2$, $Ni(OH)_2$ or $Zn(OH)_2$ was deliberately deposited onto surface of undoped CuSiNT. As expected, Figure 4.11b shows no shift in FTIR band for these samples. Thus, it rules out the possibility that deposition of hydroxides was mistaken as doping.

Different from that of divalent ions, the doping of V^{3+} and Cr^{3+} is more difficult due to their additional charge. Since V^{3+} and Cr^{3+} hydrolyze strongly, the amount of NH_3 was lowered to prevent precipitation. For Cr^{3+}, a stable solution could not be obtained with simple salts and $Cr_3(CH_3COO)_7(OH)_2$ was used, since the trinuclear complex is more resistant to hydrolysis. However, the composition of Cr-doped CuSiNT indicates negligible replacement of Cu^{2+} ions under such conditions. The increased roughness of tube walls (*e.g.*, Figure 4.8d versus Figure 4.2c) suggests that Cr is deposited on the external surface. This is further confirmed by the FTIR analysis of Figure 4.11a where no change in the Cu–O–Si bending frequency is found. In addition, carboxyl groups are detected, which originate from incompletely hydrolyzed Cr complexes. Compared to free Cr^{3+}, the larger size of Cr carboxylate complex ions may have inhibited the ion exchange process owing to steric hindrance. On the other hand, the attempt to introduce V^{3+} led to significant loss of metal in CuSiNT. A peak at 470 cm^{-1} is distinguishable in the FTIR spectrum of V-doped CuSiNT in Figure

4.11a, which can be assigned to Si–O–Si bending of SiO_2. The formation of SiO_2 indicates local depletion of metal, though the crystal structure and overall morphology are still maintained (Figure 4.8a,b). However, the large structural reconstruction, which requires 2 V^{3+} ions to replace 3 octahedral Cu^{2+} ions in the CuSiNT, seems unfavorable under the present conditions. No shift in Cu–O–Si bending frequency and negligible shift in XRD peak are observed in the V-doped CuSiNT. Nevertheless, it proves that the shifts in XRD and FTIR peaks observed after doping CuSiNT are indeed due to the ionic substitution of Cu^{2+} with the divalent metal ions.

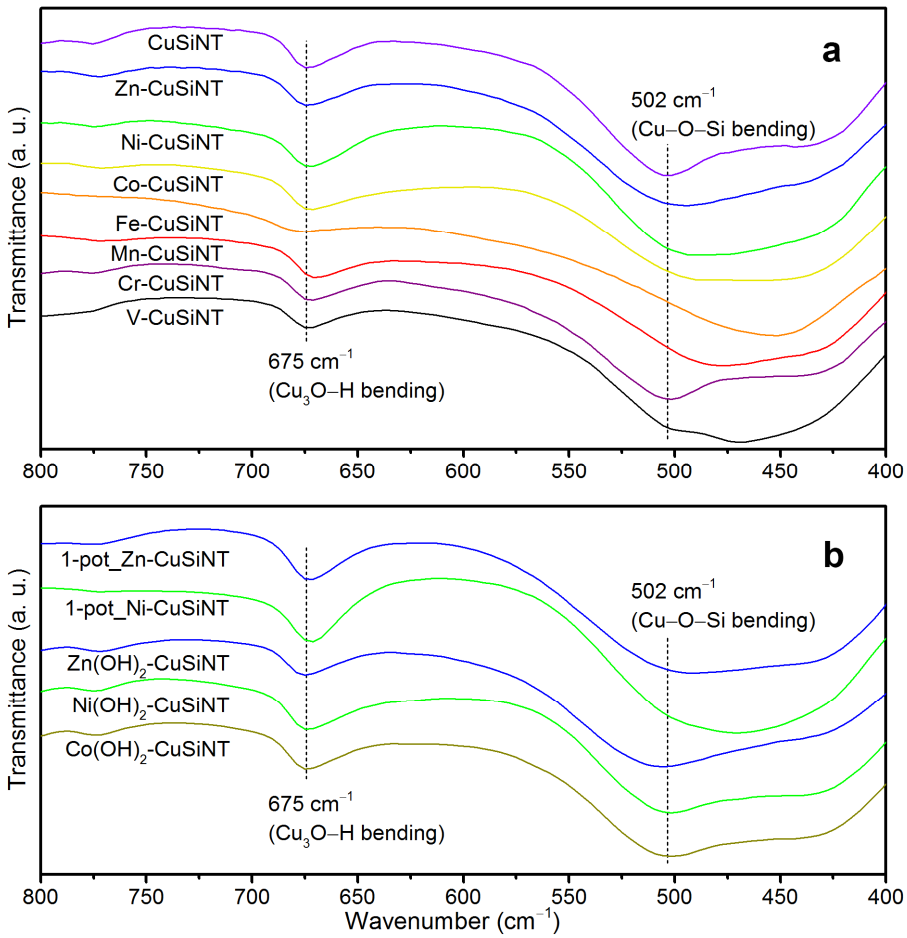

Figure 4.11. FTIR spectra of (a) CuSiNT samples before and after post-synthesis ion exchange, and (b) doped CuSiNT samples synthesized by the one-pot method (with prefix "1-pot") and undoped CuSiNT samples deposited with metal hydroxides. The dotted lines mark the major peaks of pristine CuSiNT.

4.3.4. Synthesis and application of Cu-based nanocatalysts

The above pristine and doped CuSiNT can be used as versatile solid precursors to prepare a wide variety of metal nanocatalysts with tailorable composition. For example, Cu-based catalysts have been demonstrated to be important to CO_2 hydrogenation.[16, 162] The single-walled tubular structure of CuSiNT maximizes the exposed surface, which in combination with the high metal content makes it a desirable heterogeneous catalyst. However, stability of highly porous structure is a prerequisite to the practical use of such catalysts. Surprisingly, despite the seemingly fragile structure, the morphology of pristine and doped CuSiNT survived calcination at as high as 500°C without noticeable changes as observed by TEM technique (Figure 4.12). Table 4.6 shows that the calcined samples have large BET surface areas, which are up to 150% higher than that of multi-walled copper silicate nanotubes.[41] Hereafter, the degree of doping will be specified when doped CuSiNT are addressed. The digits following the dopant denote its atomic percentage based on total amount of metals. For example, among its total metal content (Ni, Zn & Cu), the catalyst Ni4-Zn30-CuSiNT has 4 atom% Ni, 30 atom% Zn, and 66 atom% Cu.

The adsorption-desorption isotherms of the calcined nanotubes in Figure 4.13a are typical for mesoporous materials, including hysteresis loops that start at the same relative pressure. In Figure 4.13b, more detailed pore analysis using the BJH method shows narrow pore size distributions centered at 3.3 nm for all the samples; the *post-synthesis ion exchange* has apparently not affected the pore structure of CuSiNT. It needs to be pointed out that the pore size determined by the BJH method is smaller than that observed by TEM, but the difference is not unexpected, as underestimation of pore sizes has been proven associated with the BJH model.[209]

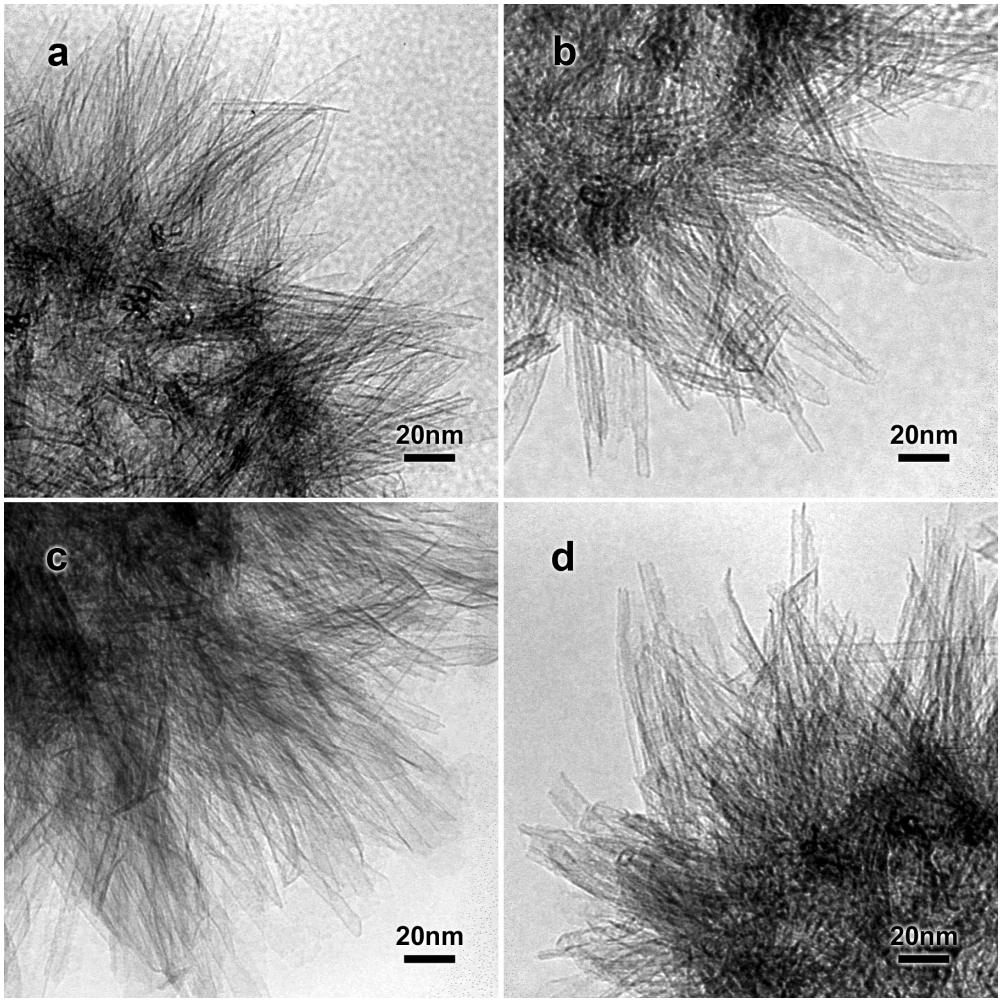

Figure 4.12. TEM images of nanotubes calcined at 500 °C: (a) undoped CuSiNT, (b) Zn34-CuSiNT, (c) Zn43-CuSiNT, and (d) Ni4-Zn30-CuSiNT.

Table 4.6. Selected properties of calcined nanotubes

Sample	Metal content (wt%)*	Surface area (m^2/g)†	Pore volume (cm^3/g)‡
CuSiNT	38.4	500	0.80
Zn34-CuSiNT	41.4	462	0.75
Zn43-CuSiNT	41.7	475	0.83
Ni4-Zn30-CuSiNT	41.6	470	0.70

*determined by EDX elemental anlysis

†calculated by the BET method

‡calculated from N_2 sorption data at relative pressures up to 0.98

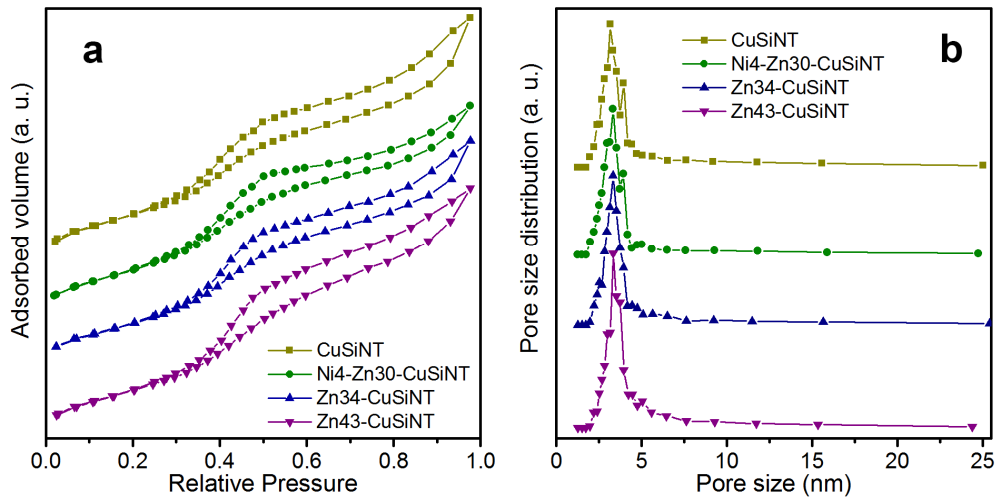

Figure 4.13. (a) N_2 sorption isotherms, and (b) volumetric pore size distributions of undoped and doped CuSiNT samples after calcination at 500 °C. The pore size distributions were calculated from the desorption isotherms using the BJH method.

Under reducing conditions, the nanotubes could be transformed into Cu-based nanocatalysts. Figure 4.14a,c show the nanoparticles-on-nanotube structures formed by reducing the undoped CuSiNT and Zn34-CuSiNT in dilute H_2. The nanoparticles formed are presumably metallic Cu, which are highly reactive as suggested by their small size. When exposed to air, the nanocatalyst derived from Zn34-CuSiNT turned from black to green within 1 h. Images acquired at higher magnifications in Figure 4.14b,d reveal lattice fringe spacing of 0.25 nm in the particles found in both samples. With powder XRD analysis (Figure 4.14e), the particles are determined to be mainly Cu_2O. The lattice fringes observed correspond well to its (111) planes. The Cu_2O phase most probably formed in laboratory air during the sample handling. A comparison between Figure 4.14a,c shows that smaller particles formed from Zn34-CuSiNT, and the weaker XRD signal from the Zn-doped nanocatalyst leads to the same conclusion. The difference in particle size explains the detection of metallic Cu in the undoped nanocatalyst as well, because larger Cu particles are not completely oxidized by air.

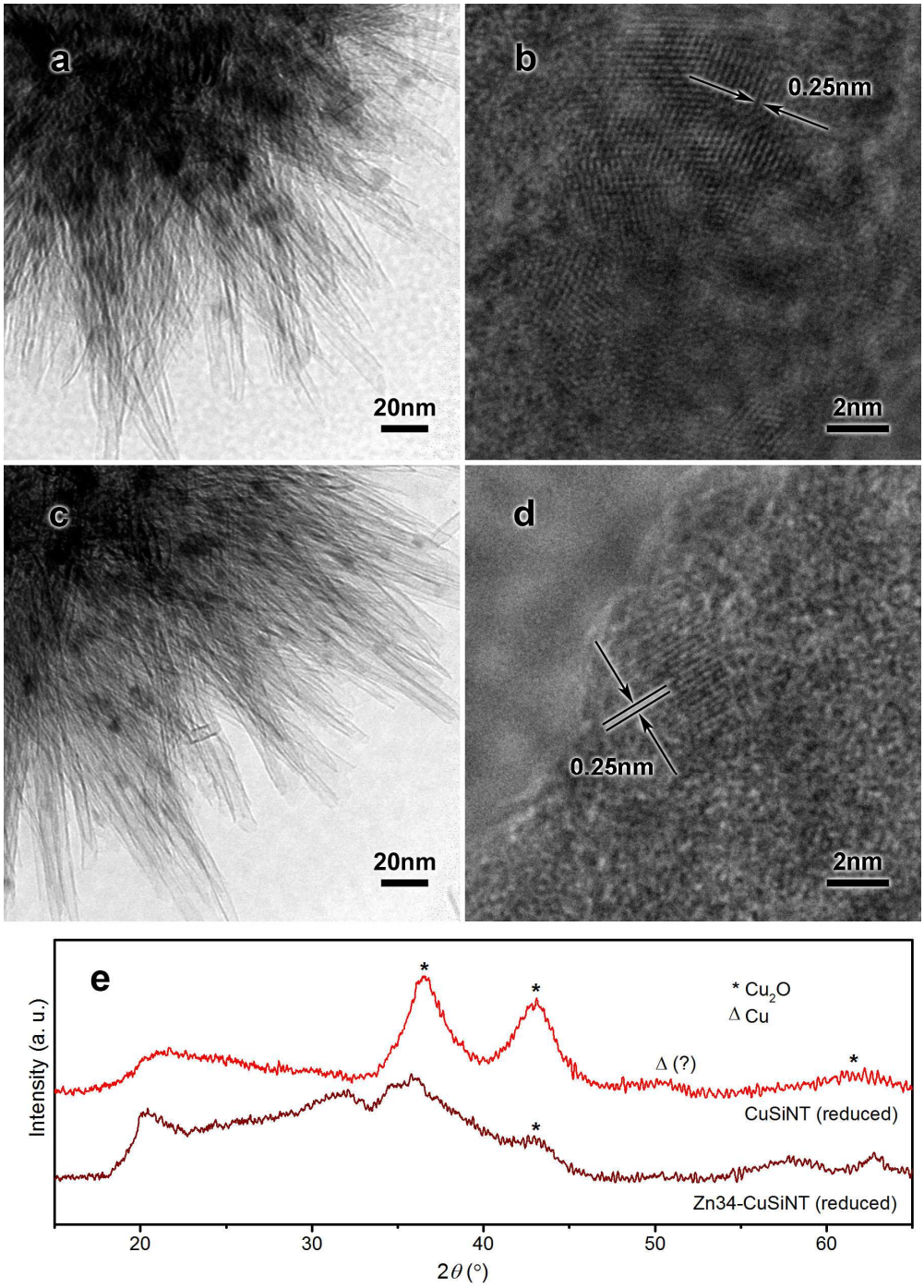

Figure 4.14. TEM images of nanocatalysts derived from (a,b) undoped CuSiNT and (c,d) Zn34-CuSiNT, with their powder XRD patterns shown in (e). The question mark in (e) denotes doubtful presence of metallic Cu. Unmarked peaks belong to the chrysocolla phase (see Figure 4.3c–e).

The effect of Zn doping on the particle size can be attributed to the well documented strong interaction between Cu and Zn, which is also the main factor in high methanol yield of commercial Cu-based methanol synthesis catalysts.[154-156, 210] In addition, a comparison of the XRD patterns in Figure 4.14e shows that the crystal

structure of CuSiNT is more resistant against reduction when doped with Zn. It is probably because Zn^{2+} is difficult to reduce with H_2 and it remains in the silicate framework. Such structural stability is desirable in catalysis, as it maintains the surface area needed for reaction.

Finally, nanocatalysts derived from undoped CuSiNT, Zn-doped CuSiNT, and Ni,Zn-co-doped CuSiNT were tested for their catalytic performance in CO_2 hydrogenation in a continuous flow tubular reactor at 240 °C and 30 bar. To prevent oxidation of catalysts during sample transfer, they were activated by dilute H_2 *in situ* after being loaded into the reactor. For all of the catalytic experiments, CH_3OH and CO were found to be the only carbon-containing products. Figure 4.15a shows that following an initial deactivation, relatively stable activity is established within 2 h, after which the Zn-doped CuSiNT catalysts exhibit least deactivation. Besides this, Zn doping also enhances the activity by up to 33% compared with the undoped catalyst, reaching 15% higher than the activity of a commercial $Cu/ZnO/Al_2O_3$ catalyst.[162] In contrast to Zn, Ni seems to act as a catalyst poison for Cu and reduces CO_2 hydrogenation activity, but in terms of methanol production, Ni has a more positive effect resulting in a methanol yield still significantly higher than that of the undoped catalyst as seen in Figure 4.15b,c. It suggests that Ni mainly suppresses the formation of CO, the side product.

The spent catalysts were also analyzed by TEM, powder XRD and N_2 physisorption techniques. Similar to the freshly prepared nanocatalysts, they were easily oxidized in air. The color change from black to green occurred in 5 min for the undoped and Zn-doped catalysts, while for the Ni4-Zn30-CuSiNT the process took several hours. The TEM images in Figure 4.16a–c show that the tubular structure is preserved even after the harsh reactions. Under higher magnification, lattice fringes spaced 0.25 nm apart are observed in the particles attached to the nanotubes (Figure 4.16d).

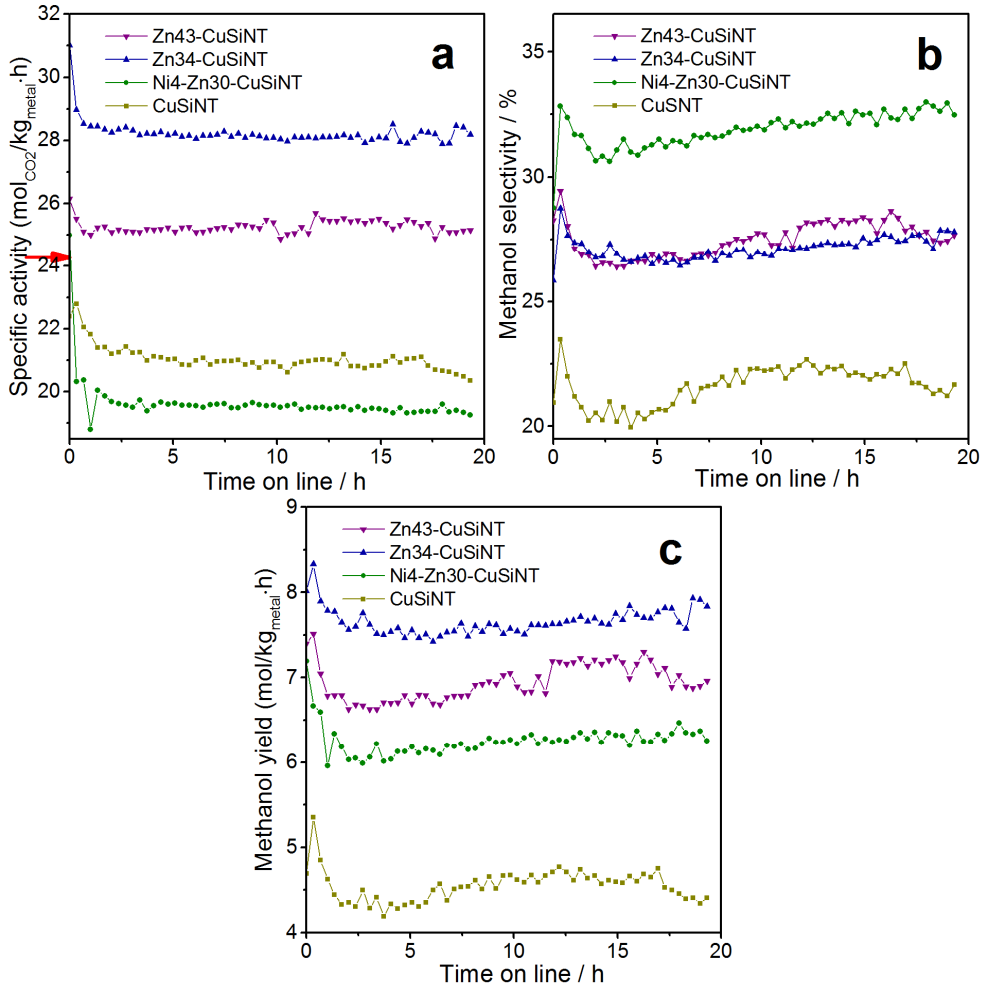

Figure 4.15. (a) Specific activity of CO_2 hydrogenation, (b) selectivity of methanol in mol%, and (c) methanol yield for various nanocatalysts. The activity and methanol yield are normalized by total amount of metal (Cu + dopants) in the catalysts. The arrow marks the activity of a commercial $Cu/ZnO/Al_2O_3$ catalyst evaluated at the same temperature, pressure and gas space velocity.

XRD results in Figure 4.17a–c confirm the particles observed by TEM to be Cu_2O again. In addition to Cu_2O, Cu is also present in the Ni4-Zn30-CuSiNT (Figure 4.17c) after use. By comparing the XRD patterns of the spent catalysts with those of unreduced fresh catalysts in Figure 4.17d–f, it is seen that the characteristic peak of the chrysocolla phase at $2\theta = 21.4°$ was retained to some degree after reaction, particularly in the doped catalysts. It supports the structure-stabilizing effect of the dopants as proposed earlier. Indeed, the decrease in surface area during reaction is also much less significant for Zn34-CuSiNT than for undoped CuSiNT (see Figure

4.17g,h, the BET surface area of spent undoped CuSiNT is 65 m^2/g and that of spent Zn34-CuSiNT is 252 m^2/g).

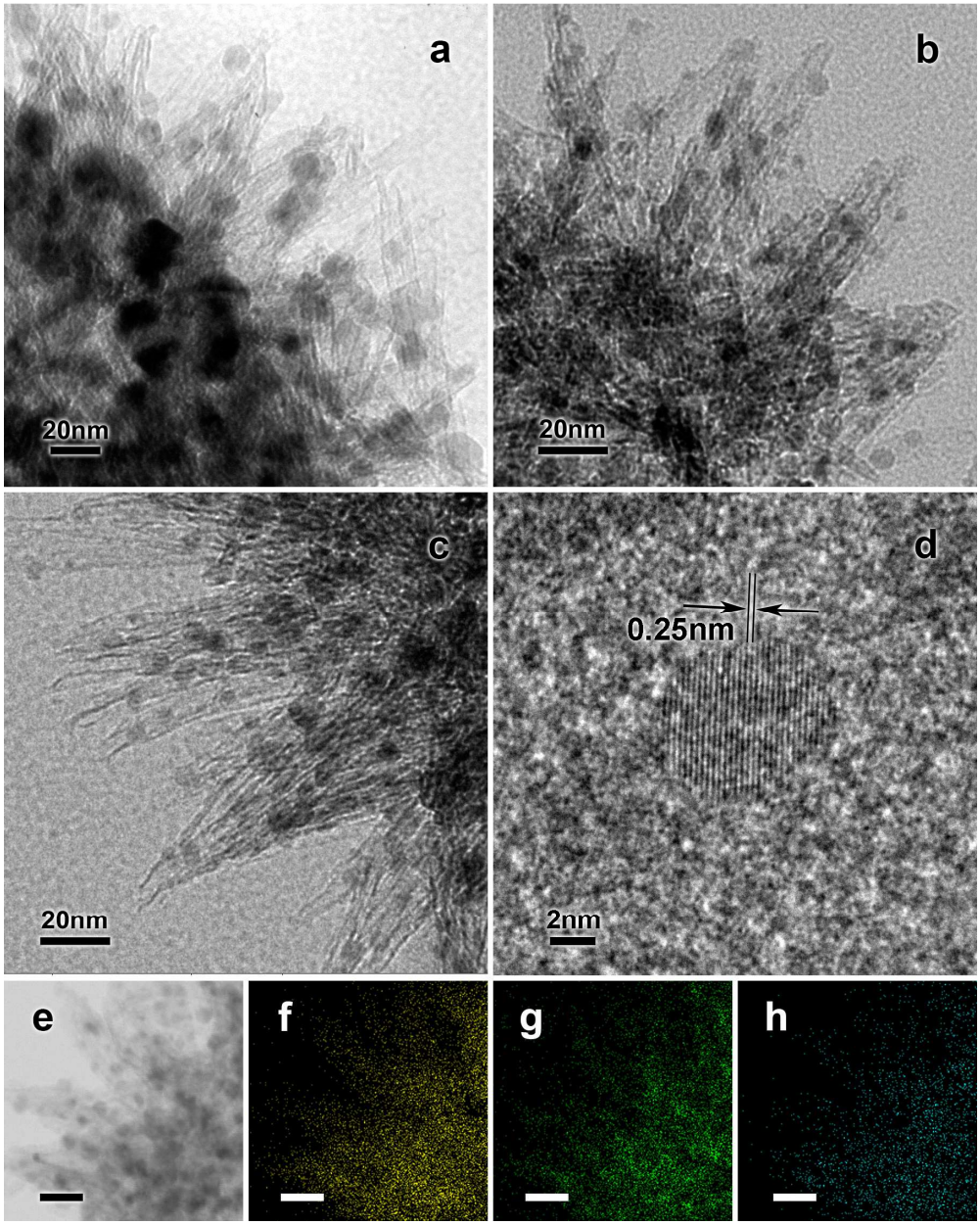

Figure 4.16. TEM images of spent catalysts: (a) undoped CuSiNT, (b,d,e) Zn34-CuSiNT, and (c) Ni4-Zn30-CuSiNT. EDX elemental mapping of the site in (e) is shown in (f) for Si, (g) for Cu, and (h) for Zn. Length of scale bars in (e–h): 20 nm.

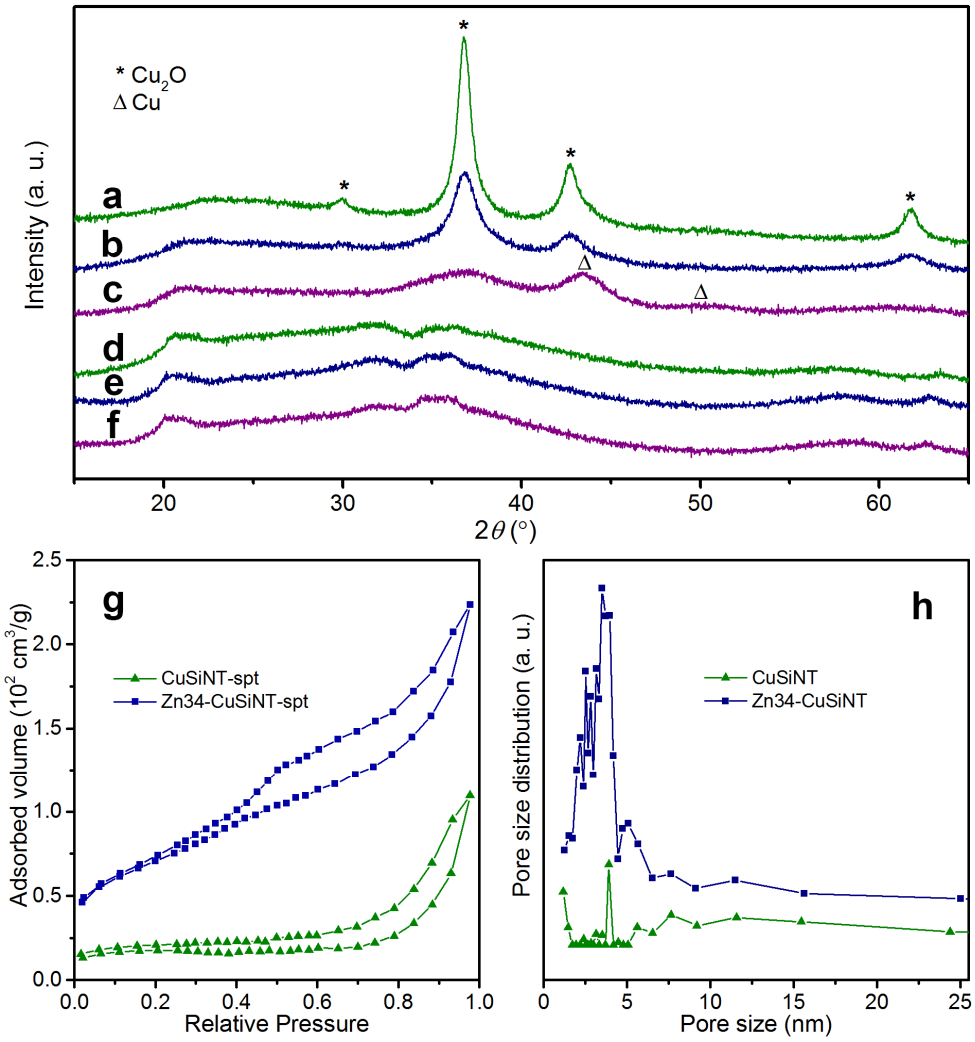

Figure 4.17. Powder XRD patterns of (a–c) spent catalysts compared with (d–f) freshly calcined catalysts, where (a,d) undoped CuSiNT, (b,e) Zn34-CuSiNT, (c,f) Ni4-Zn30-CuSiNT. (g) N_2 sorption isotherms and (h) BJH pore size distribution of spent catalysts.

From the broadening of XRD peaks, the crystallite size of Cu_2O is estimated to be 9, 5 and 2 nm for the spent CuSiNT, Zn34-CuSiNT and Ni4-Zn30-CuSiNT, respectively. The size of Cu particles in the Ni4-Zn30-CuSiNT is around 3 nm. The reduction of particle size in doped catalysts indicates a strong metal-support interaction which is probably the reason for the increase in activity and methanol selectivity. Similar effects are usually reported for the Cu/ZnO system in industrial catalysts,[155-156] but in the present work ZnO is not detected in the spent catalysts by either XRD or HRTEM. Because the elemental distribution of Zn is rather uniform in the used Zn34-CuSiNT (Figure 4.16e–h), it is believed that Zn remains as silicates

after catalyst activation, though transfer of trace amount of Zn species to Cu surface is still highly possible. In the doped CuSiNT catalysts, maximal promoting effect of Zn is apparently achieved at the lower Zn content of Zn34-CuSiNT, and further increase in Zn content does not improve Cu-support interaction because uniform distribution of Cu and Zn in the ultrathin tubular structure allows sufficient modification of Cu surface with Zn at relatively low Zn content. However, Zn species alone are almost inactive in CO_2 hydrogenation under the present experimental conditions. As the specific CO_2 hydrogenation activity is calculated on the basis of total metal content (Cu + Zn + Ni), the presence of excessive amount of Zn and hence decreased amount of active Cu species causes a lower specific activity of Zn43-CuSiNT.

In addition, the promoting effect of Ni in methanol synthesis from CO_2 hydrogenation has been proven,[211-212] which explains the high methanol selectivity for the Ni4-Zn30-CuSiNT. Apparently, the Ni dopant has also contributed to the stability of the Cu particles in the Ni4-Zn30-CuSiNT against oxidation. It is speculated that Ni was concentrated on the surface of Cu and formed a dense oxide layer to prevent the Cu underneath from oxidation. However, reliable determination of the spatial distribution of Ni is hindered by its low abundance in this system.

4.4. Conclusions

In summary, single-walled copper silicate nanotubes have been synthesized successfully with controllable secondary structures, and a general method of doping the CuSiNT with many 3*d* transition metals has been developed. All the divalent dopants (Mn^{2+}, Fe^{2+}, Co^{2+}, Ni^{2+} and Zn^{2+}) have replaced Cu through ion exchange in the octahedral sites of CuSiNT. Furthermore, the Zn- and Ni-doped CuSiNT have shown a significant improvement in catalytic activity and methanol selectivity for the

CO_2 hydrogenation, reaching values comparable or superior to commercial catalysts. This synthetic approach offers promising potential for design-made transition metal catalysts with tubular silicate supports.

Chapter 5. Monodisperse Aluminosilicate Spheres with Hierarchical Macro-Meso-Microporous Structure for Direct Dimethyl Ether Synthesis from CO_2/H_2

5.1. Introduction

Mesoporous silicate molecular sieves have gained increasing interest ever since the first synthesis of MCM-41.[57, 213] The large surface area and chemical inertness make this class of materials useful in separation,[214] drug delivery[89] and heterogeneous catalysis.[215] Compared with the crystalline structure of zeolites and metal-organic frameworks, the amorphous nature of mesoporous silica offers more flexibility in terms of structural tuning which is essential in the synthesis of complex, multi-functional materials.[12] In addition, the lower diffusion barrier of mesoporous structures allow for more efficient utilization of internal surface areas and higher resistance towards pore plugging.[216] With early works emerging in the 1990s,[86] the synthesis of hierarchically macro-mesoporous silica has been frequently reported recently,[13, 81, 89-91] illustrating well the versatility of amorphous siliceous materials. The interconnected mesopores and macropores of such materials lead to high accessibility of internal surfaces and provide enough space for integration with bulk phases that is impossible in solely mesoporous materials.[80] However, a majority of industrially important catalytic reactions involve molecular species sized below the mesoporous range, and to really explore the molecular sieving properties of porous silica, microporous structures are required.[15] Although it seems probable to tackle the conflict between pore accessibility and size selectivity by integrating microporous and mesoporous materials,[104, 217] a more facile single-step approach is still preferred

where hierarchical macro-meso-microporous structures can form simultaneously. Unfortunately no such works on aluminosilicate materials have been reported so far.

On the other hand, purely siliceous materials lack reactive sites and their functionalization relies entirely on incorporation of heteroatoms. In particular, Al is frequently introduced to create acidic sites in porous silica.[92, 218-229] It has been shown that the acidity of the resultant aluminosilicate is closely related to the coordination environment of incorporated Al which in turn depends on the chemistry of precursor solution.[220, 222-224, 226, 230] Tetrahedrally coordinated Al is capable of producing stronger acid sites than its octahedral counterpart, and to introduce Al as tetrahedral complexes an alkaline environment is beneficial due to the following equilibria,[231-232] where Roman numeral superscripts denote the coordination number of Al:

$$[Al^{VI}(H_2O)_6]^{3+} + 3OH^- \leftrightarrow Al^{VI}(OH)_3{\cdot}nH_2O + (6-n)H_2O \quad (5.1)$$

$$Al^{VI}(OH)_3{\cdot}nH_2O + OH^- \leftrightarrow [Al^{IV}(OH)_4]^- + nH_2O \quad (5.2)$$

However, direct introduction of Al compounds into the precursor solution poses negative effects on the morphological control of the aluminosilicate material. Unlike mesoporous silica particles which have been prepared with well-defined shape and sizes,[63] aluminosilicate was usually obtained in the form of non-uniform particles[216, 218, 224] or macroscopic aggregates.[225-226, 229] Attempts have been made to resolve the issue by a two-step approach whereby morphologically well-defined SiO_2 particles were first synthesized and then grafted with Al through hydrothermal processing,[92] but the relatively complicated synthetic procedure is a significant drawback. For practical purposes, the single-step approach is much more desired.

During the development of synthetic strategies of mesoporous silica, the nature of ionic species present in the precursor mixture have been found to strongly influence the pore structure of the product, especially for the combination of anions and

cationic surfactant templates.[4, 61, 229] Such effects are often referred to as Hofmeister anion effects, a terminology derived from Hofmeister's work on solubilization of proteins by different salts.[233] Briefly, anions are ordered in the "Hofmeister series" according to increasing potency of solubilizing proteins as follows:[234]

$$SO_4^{2-} < OH^- < F^- < Cl^- < Br^- < NO_3^- < I^-$$

According to general understanding,[234-235] the solubilizing power is related to the polarizability and hydration structure-forming (cosmotropic) or breaking (chaotropic) tendencies of the anions; those to the left of Cl^- or "cosmotropic ions" form strongly bound hydrated structures and exhibit weaker charge screening effects on surfactant micelles than ions to the right of Cl^- or "chaotropic ions". With the adsorption of cosmotropic ions, the effective charge of cationic surfactant micelles increases. The increased charge generates stronger repulsive Coulomb force and hence longer equilibrium distance between surfactant head groups in an individual micelle,[236] which in turn reduces the surfactant packing parameter:[4, 59] $g = V / (a_o l)$ where V is the effective volume of hydrophobic part of the surfactant, a_o is the effective area of surfactant head group at the micelle surface, and l is the kinetic length of the hydrophobic tail. Consequently the spontaneous assembling of surfactant molecules into surfaces with high curvature is favored. In addition, inter-micellar repulsion is also increased, preventing the coalescence of micelles. In fact, not only micelles but also liquid droplets in surfactant-stabilized emulsions experience similar effects.[237-238] So far remarkable success has been seen in applying Hofmeister anion effects to materials synthesis,[4, 61, 229, 239] but research on this topic has been largely limited to non-metal anions (*e.g.* Cl^-, NO_3^-, SO_4^{2-}, *etc.*) in mesoscopic systems. Recently, a study on the assembling of noble metal clusters and cetyltrimethylammonium bromide (CTAB) micelles showed profound morphological effects of the metal precursors, *i.e.*, $[AuCl_4]^-$, $[PtCl_4]^-$ and $[PdCl_4]^-$,[240] which is actually an example of Hofmeister anion effects (Class II ions with large polarizabilities).[234] In the present

work, the generality of Hofmeister anion effects is further demonstrated by controlled synthesis of macro-meso-microporous aluminosilicate spheres (MASS) in a microemulsion system. The microemulsion containing both nano-sized surfactant micelles and submicron giant vesicles serves as an ideal platform for the exploitation of the multi-scale Hofmeister anion effects of $[Al(OH)_4]^-$, and provides crucial morphological control during the incorporation of Al, leading to monodisperse MASS.

5.2. Experimental Section

5.2.1. Chemicals and reagents

Cetyltrimethylammonium bromide (CTAB), tetraethyl orthosilicate (TEOS), zinc nitrate ($Zn(NO_3)_2{\cdot}6H_2O$) and ethylenediamine (EDA) from Sigma-Aldrich, copper nitrate ($Cu(NO_3)_2{\cdot}3H_2O$), ammonia solution (NH_3, 32%) and sodium hydroxide (NaOH) from Merck, sodium aluminate ($NaAlO_2$) from Nacalai, ethanol (absolute, analytical grade) from Fisher Scientific, Aerosil 300 fumed silica from Degussa and toluene from J. T. Baker were used as received. The gases used for catalyst evaluation were of the purified grade (H_2: 99.9995%, N_2: 99.9995%, CO_2: 99.8%).

5.2.2. Syntheses of MSS and MASS

In a typical synthesis, 150 mg of CTAB, 180 μL of TEOS and 600 μL of toluene were dissolved in 24 mL of ethanol and stirred for 10 min. Meanwhile, 0–30 mg of $NaAlO_2$ and 0.75 mL of ammonia solution were dissolved in 26 mL of deionized water. The aqueous solution was then poured into the organic phase under stirring to form a clear mixture, which was aged at ambient temperature for 4 h. The precipitation was separated by centrifugation and washed with ethanol for 3 times before characterization. The products, macro-meso-microporous silica spheres and macro-meso-microporous aluminosilicate spheres, are named as MSS (without

adding $NaAlO_2$) and MASS-*X* respectively, where *X* stands for the amount (mg) of $NaAlO_2$ added. In some experiments the amount of water (w) or toluene (t) was varied, and the product is denoted as MASS-*X*w*Y* or MASS-*X*t*Y*, where *Y* stands for the amount of water (in mL) or the amount of toluene (in μL). The exact amounts of reagents used in each case are recorded in Table 5.1 below.

Table 5.1. Synthesis parameters* of important MSS and MASS samples

Sample	Toluene (μL)	Water (mL)	$NaAlO_2$ (mg)	1M NaOH (μL)	Calcination
MSS	600	26	0	0	No
MASS-7.5	600	26	7.5	0	No
MASS-15	600	26	15	0	No
MASS-30	600	26	30	0	No
MSS (pH = 11.57)	600	26	0	60	No
MSS (pH = 11.81)	600	26	0	120	No
MSS-cal	600	26	0	0	500 °C, 4 h
MASS-7.5cal	600	26	7.5	0	500 °C, 4 h
MASS-15cal	600	26	15	0	500 °C, 4 h
MASS-30cal	600	26	30	0	500 °C, 4 h
MASS-15w24	600	24	15	0	No
MASS-15w25	600	25	15	0	No
MASS-15w27	600	27	15	0	No
MASS-15w24cal	600	24	15	0	500 °C, 4 h
MASS-15w25cal	600	25	15	0	500 °C, 4 h
MASS-15w27cal	600	27	15	0	500 °C, 4 h
MASS-15t0	0	26	15	0	No
MASS-15t100	100	26	15	0	No
MASS-15t300	300	26	15	0	No
MASS-15t750	750	26	15	0	No
MASS-15t0cal	0	26	15	0	500 °C, 4 h
MASS-15t100cal	100	26	15	0	500 °C, 4 h
MASS-15t300cal	300	26	15	0	500 °C, 4 h
MASS-15t750cal	750	26	15	0	500 °C, 4 h

*Common synthesis parameters: 24 mL of ethanol, 150 mg of CTAB, 180 μL of TEOS, 0.75 mL of 32% NH_3

5.2.3. Drying and calcination of samples

The as-synthesized MSS and MASS were dried in an electrical oven at 60°C overnight. Calcination was carried out at 500°C for 4 h in static air (heating rate = 1.5 °C/min). The products are referred to as MSS-cal and MASS-*X*cal, respectively (see Table 5.1 for details).

5.2.4. Syntheses and evaluation of supported Cu/ZnO catalysts

The MSS-cal and MASS-15cal were wet-impregnated with drop-wise addition of an aqueous solution of calculated amounts of $Cu(NO_3)_2{\cdot}3H_2O$, $Zn(NO_3)_2{\cdot}6H_2O$ and ethylenediamine where metal/EDA = 1/2 (mol/mol). After being kept at ambient temperature for 1 h, the paste was dried at 100 °C for 30 min and calcined at 350°C for 2 h. The product is denoted as CZMSS or CZMASS-15 according to the support material used. 200 mg of such catalyst was diluted with 50 mg of Aerosil 300 SiO_2 and loaded into a tubular stainless steel reactor with a diameter of 3/8". Details about the reactor set-up can be found in Section 3.9. The catalyst was activated *in situ* with flowing 10% H_2/N_2 (50 std mL/min) at 275 °C for 4 h and cooled to ambient temperature in the same gas mixture. The temperature was then increased to 250 °C with a gas mixture containing 72% of H_2, 24% of CO_2 and 4% of N_2 fed to the reactor at 60 std mL/min, and the pressure was increased to 20 bar by a backpressure regulator. After the reactor was stabilized for 1 h, composition of the effluent was monitored by gas chromatography for 20 h.

Additionally, catalytic properties of some other catalysts based on MSS/MASS (*e.g.*, Cu/ZnO-loaded MASS with its Na content exchanged with Mg and $Cu/ZnO/Ga_2O_3$-loaded MASS) were also investigated. The results which are more remotely related to the focus of this chapter are presented in Section A1.4 of Appendix 1.

5.2.5. Materials characterization

In this work, ^{27}Al MAS NMR spectra were acquired at 104.3 MHz with a 5 μs pulse and 256 scans. The sample powders were contained in 4 mm zirconia rotors spinning at 8 kHz. Aqueous $Al(NO_3)_3$ was used as the reference for chemical shift. Before N_2 sorption experiments, the samples were outgassed in flowing He at 200 °C for 3 h.

5.3. Results and Discussion

5.3.1. Effects of $NaAlO_2$

Typical morphologies of macro-meso-microporous silica spheres (MSS) and macro-meso-microporous aluminosilicate spheres (MASS) with different Al contents synthesized in the CTAB-stabilized oil-in-water microemulsion system are shown in Figure 5.1a–h. Overall the products are uniform submicron spheres. As indicated in Figure 5.1i–l, the particle sizes exhibit unimodal distributions and the small geometric standard deviations of ≤1.1 indicate low polydispersity of the MSS and MASS. Open channels in the macroporous range are observed in all of the spheres, which formed presumably around toluene droplets. The FESEM images (Figure 5.1b,d,f) show clearly that increasing amount of $NaAlO_2$ in the precursor solution resulted in a shrink in channel width and a denser distribution of channels. For MASS-30, however, only shallow indentations can be observed by FESEM (Figure 5.1h). With better clarity of internal structures through TEM, the indentations are confirmed to be discontinuous ellipsoidal voids that have openings to the surface (Figure 5.1g). Such aluminate-induced morphological changes have not been reported before, and it is believed that they are a consequence of Hofmeister anion effects of $[Al(OH)_4]^-$ which will be discussed later in detail.

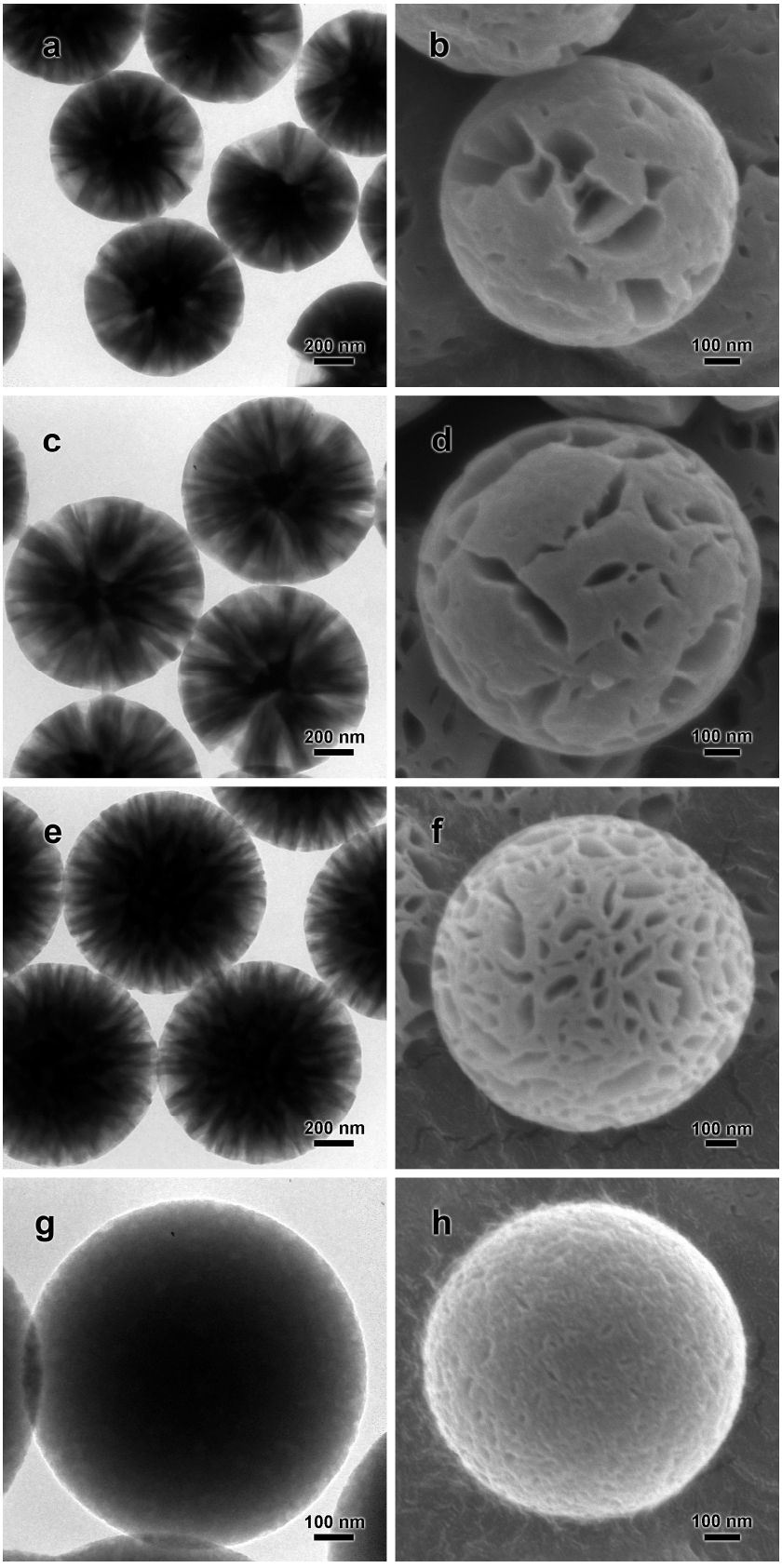

Figure 5.1. TEM and FESEM images and particle size histograms of (a,b,i) MSS, (c,d,j) MASS-7.5, (e,f,k) MASS-15, and (g,h,l) MASS-30. TEM images of MASS-5, 10, 20, 25, 35, 40 samples are reported in Section A1.1 of Appendix 1.

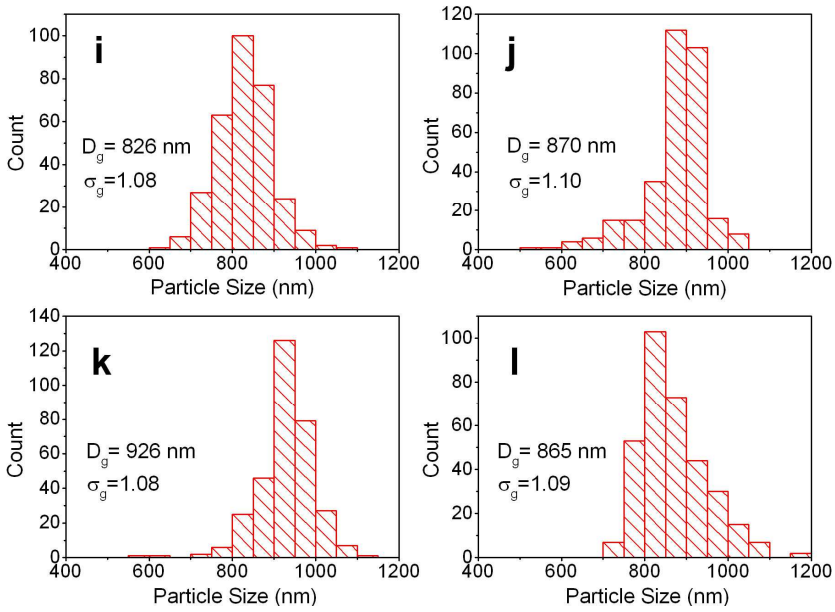

Figure 5.1 continued. The particle size distribution for each sample was determined by measuring at least 300 particles in TEM images. D_g: geometric mean diameter, σ_g: geometric standard deviation.

However, in the present system not only the concentration of $[Al(OH)_4]^-$, but also that of OH^- increases with the addition of $NaAlO_2$. In Table 5.2, noticeable increase of the precursor solution pH is observed as $NaAlO_2$ is added, due to the partial hydrolysis of $[Al(OH)_4]^-$ (Equation 5.2). Since OH^- is a cosmotropic ion, its effect has to be separated from that of $[Al(OH)_4]^-$ before attention is focused on the latter. A comparative study was therefore carried out where NaOH was used in place of $NaAlO_2$ to adjust the pH and all the other synthesis conditions were kept unchanged. As Figure 5.2a,b show, the increase of pH did not cause morphological changes of the channels, which suggests negligible effect of OH^- in the present experimental conditions. Moreover, this experiment proves the role of Na^+ in the morphological control to be insignificant (comparable amounts of Na^+ were introduced by $NaAlO_2$ and NaOH). On the other hand, the change in pH does explain the size differences in MSS and MASS (Figure 5.1i–l). The increase followed by decrease of mean particle size with increasing pH matches reported observations in sol-gel synthesis of mesoporous silica, where the solubilization of silicate species and hence limited

nucleation were cited as the reasons for larger particle size, and etching of silica as the cause of size reduction at a high pH range.[241-242]

Table 5.2. Solution pH and elemental composition of MSS and MASS with different amount of $NaAlO_2$ in precursor

Sample	Precursor solution pH	Product Al/Si	Product Na/Al
MSS	11.34	0	n. a.
MASS-7.5	11.44	0.09	0.14
MASS-15	11.56	0.18	0.28
MASS-30	11.75	0.35	0.57

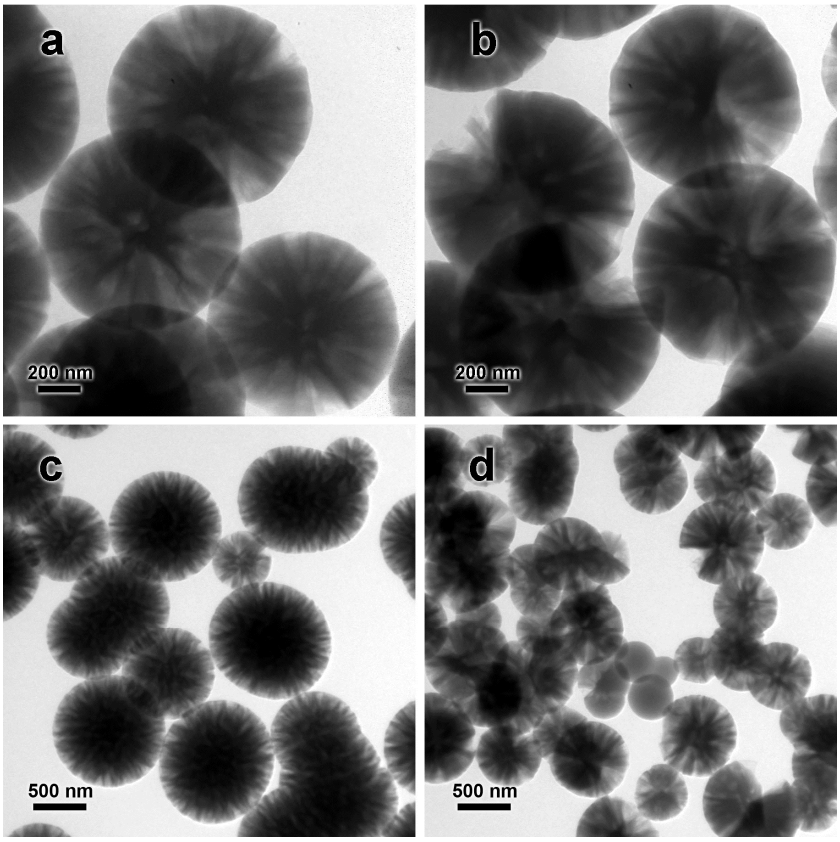

Figure 5.2. TEM images of (a,b) MSS synthesized with pH values adjusted to 11.57 and 11.81 respectively using a NaOH solution, and (c,d) MASS-15 synthesized with continuously stirring for 6 min and 10 min respectively after mixing of the organic phase and aqueous phase.

It is demonstrated in Figure 5.1i–l that the considerable variation in Al content of the precursor solution did not affect the uniformity of particle size pronouncedly,

while introducing Al during the sol-gel synthesis of silica particles has often been associated to ill-defined morphologies as mentioned in the Introduction. Comparing the present synthetic method to those in most published works, it is proposed that the formation of microemulsion is the key factor in the successful morphological control. A microemulsion exhibits variable viscosity that usually increases with the volume fraction of the dispersed phase and decrease with the droplets size of the dispersed phase.[88] Importantly, the apparent viscosity of the microemulsion can significantly exceed that of the pure phases forming it.[243] It is believed that the relatively higher viscosity impeded the Brownian motion of growing particles, preventing them from collision and aggregation. On the other hand, if mechanical energy is supplied to promote particle collision, the microemulsion establishment could also be disturbed, leading to less uniform products. To prove the role of collision in the particle growth, mechanical stirring was applied in the synthesis of MASS-15 to encourage turbulence and hence random motion of particles. Figure 5.2c,d show detrimental morphological effects of the stirring; the longer the stirring was applied, the lower the uniformity of formed products. As further evidence of the importance of forming microemulsion, MASS-30 has slightly higher numbers of large particles (Figure 5.1l) caused by particle aggregation. Considering the smaller volume of macrochannels in MASS-30 (Figure 5.1g,h) which indicates smaller volume of insoluble toluene droplets in the microemulsion, the aggregation of MASS-30 particles was very possibly due to relatively low viscosity of the precursor mixture.

Other than the morphological effects, direct consequences of the introduction of $NaAlO_2$ also include compositional changes of the product. In the synthesis of aluminosilicate functional materials the ability to tightly control the Al content is crucial for obtaining desired acidity, which has direct impact on their catalytic performance.[221, 228] Table 5.2 shows that in the present system the Al content can be tuned facilely in a wide range of Al/Si = 0–0.35 (The macrochannels disappear if

larger amount of Al is introduced. See Section A1.1 of Appendix 1); the Al/Si ratio in MASS is a simple linear function of the amount of $NaAlO_2$ in the precursor solution. Surprisingly, the Na/Al ratio also increases linearly as $NaAlO_2$ is added while in fact the amount of Na and Al introduced is always equal. To understand this phenomenon, other cationic species has to be considered, which in the present case is NH_4^+ originated from the hydrolysis of ammonia (Equation 5.3). Ion exchange property of amorphous aluminosilicates has been well documented.[244] It allows Na^+ and NH_4^+ to competitively adsorb onto the negatively charged MASS framework and as a result, the relative amount of both adsorbed ions depends on their concentrations in the precursor solution (Equation 5.4, where A stands for the MASS framework). On the one hand, increasing the amount of $NaAlO_2$ raises the concentration of Na^+, and on the other hand, increasing the pH shifts the equilibrium in Equation 5.3 towards the left. The combined effect is a larger Na^+/NH_4^+ ratio in solution which drives the equilibrium in Equation 5.4 towards the adsorption of Na^+. In addition, CTA^+ may also partially balance the negative charge of MASS framework but since the concentration of CTAB was maintained consistent, its role in the changing composition can be ignored.

$$NH_3 \cdot H_2O \leftrightarrow NH_4^+ + OH^- \quad (5.3)$$

$$Na^+ + NH_4A \leftrightarrow NH_4^+ + NaA \quad (5.4)$$

The mesostructures of the as-synthesized MSS and MASS samples were characterized by powder XRD and high-resolution TEM. Figure 5.3 shows that the purely siliceous MSS sample possesses 2D hexagonal symmetry which is assigned to the *p6mm* plane group with a = 2.77 nm. The peak assigned to the (20) plane is very broad and asymmetric, most probably due to presence of a partially overlapping (11) diffraction peak. With the addition of $NaAlO_2$, a coexisting mesophase appeared in MASS-7.5 and dominated in MASS-15. The new structure possesses cubic symmetry

and is best assigned to the *Pm*3*n* space group with a = 8.42 nm. The mesostructural transition is also reflected by increased pore size and altered pore arrangement directly observed by high-resolution TEM, as shown in Figure 5.4. However, further increase in the amount of $NaAlO_2$ did not change the symmetry, as indicated by the XRD pattern of MASS-30 (Figure 5.3). Mesostructural transition of siliceous materials due to Hofmeister anion effects has been reported in several works,[61, 229, 239] and a particularly relevant example[229] is the change from *p*6*mm* to *Pm*3*n* facilitated by the replacement of NO_3^-, a chaotropic anion, with cosmotropic SO_4^{2-}. In Scheme 5.1, comparison of the pore structures of the two mesophases shows higher curvature of pore walls and more discrete pore network in *Pm*3*n*, which reflect the dual effect of cosmotropic anions: smaller surfactant packing parameter and stronger intermicellar repulsion. The *p*6*mm*-to-*Pm*3*n* transition in the present system makes it reasonable to postulate a cosmotropic nature of $[Al(OH)_4]^-$.

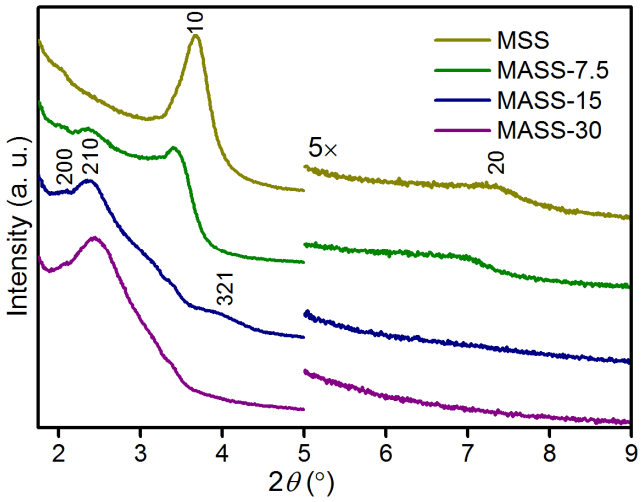

Figure 5.3. XRD patterns of as-synthesized MSS and MASS samples with different Al contents. Diffraction data above $2\theta = 5°$ is shown in 5× magnification. The curves have been shifted in the *y*-direction for better clarity.

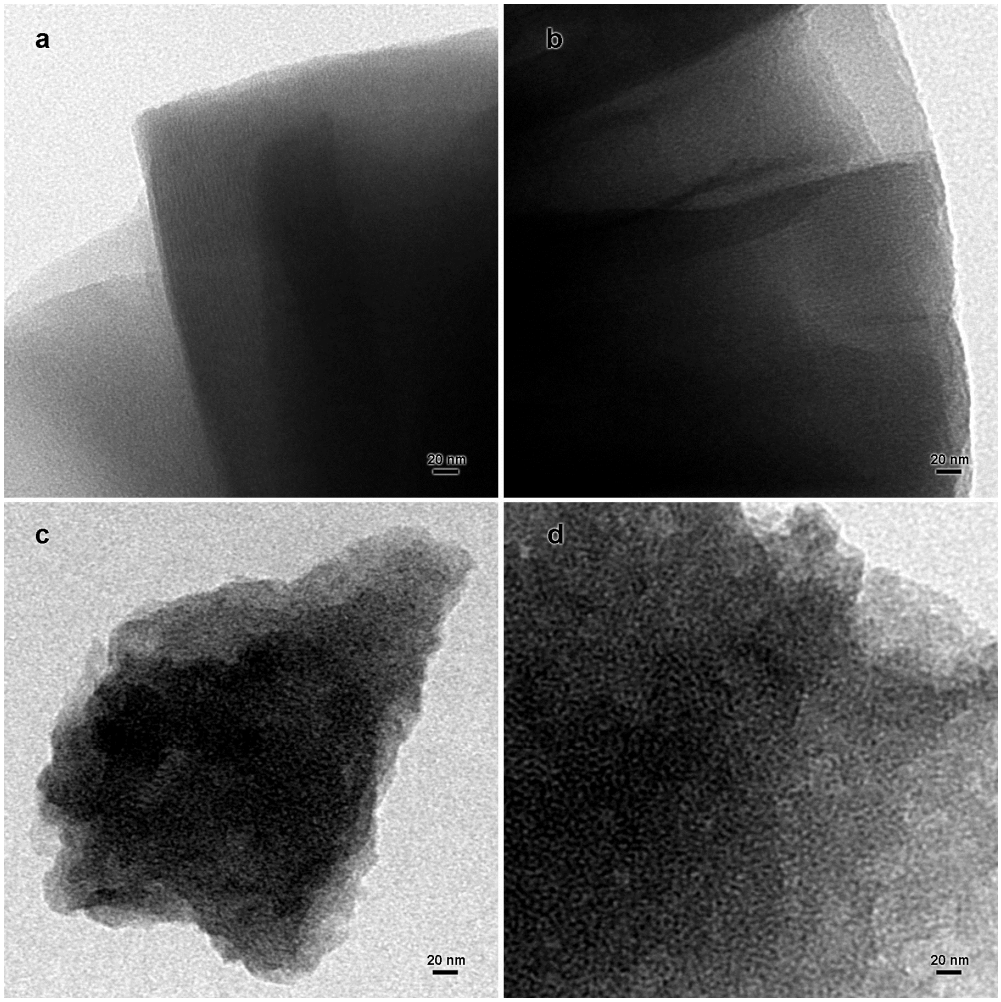

Figure 5.4. TEM images of (a) MSS, (b) MASS-7.5, (c) MASS-15 and (d) MASS-30 with high magnifications. The sample powders of MASS-15 and MASS-30 were crushed under a pressure of 390 MPa during sample preparation for better clarity.

The Hofmeister effects of $[Al(OH)_4]^-$ also explain the morphological change of the macrochannels. Scheme 5.2 illustrates that the toluene droplets in the present oil-in-water microemulsion are stabilized by CTA^+ ions and are thus positively charged. Similar to the smaller CTA^+ micelles more frequently encountered in the synthesis of mesoporous silica, they are expected to be subjected to Hofmeister effects. As the adsorption of more cosmotropic anions at the oil-water interface leads to higher stability and hence smaller sizes of the droplets,[237] the channels formed around the toluene droplets should also exhibit narrower widths, which has apparently occurred with the introduction of $NaAlO_2$ (Figure 5.1a–h). It is thus confirmed that $[Al(OH)_4]^-$, the dominant form of aluminate in solution, is cosmotropic in comparison to Br^-

originated from CTAB. Note that indeed $[Al(OH)_4]^-$ can bind easily to water molecules through hydrogen bonding.

Scheme 5.1. Mesostructural tuning of MASS* facilitated by the Hofmeister anion effect of $[Al(OH)_4]^-$

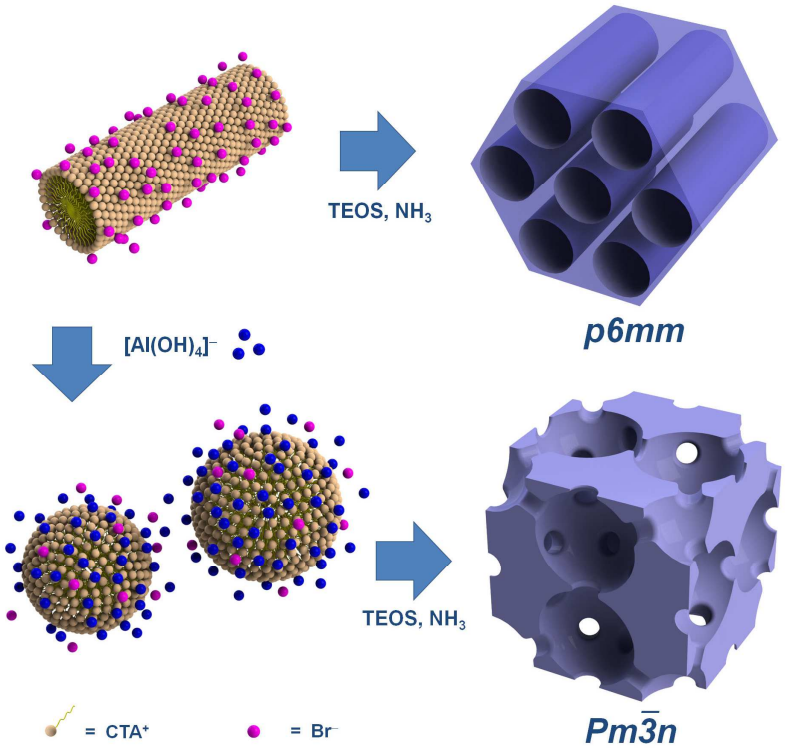

*The adsorption of $[Al(OH)_4]^-$ in replacement of Br^- on CTA^+ micelles increases the surface curvature, promoting the rod-to-sphere transformation. The difference in micelle shape is reflected in the mesostructures of the final MASS products.

Scheme 5.2. Shrinking of CTA^+-stabilized toluene nanodroplets under the Hofmeister anion effect*

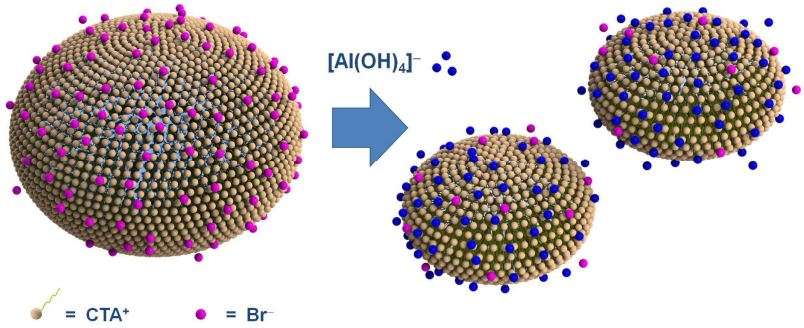

*The chaotropic bromide ion (Br^-) is replaced by cosmotropic $[Al(OH)_4]^-$. These nanodroplets (*i.e.*, giant vesicles) are flexible enough to serve as soft templates for the formation of cone-shaped radial macrochannels in the MSS or MASS (TEM/FESEM images, Figure 5.1).

To reveal the textural properties of MSS and MASS, N_2 physisorption experiments were performed on calcined samples. As Figure 5.5a displays, they exhibit type I isotherms with narrow H4 hysteresis in general, suggesting the coexistence of micropores and mesopores.[245] In particular, the extension of hysteresis loops below the relative pressure of 0.2 is strong evidence of the presence of micropores, but the possibility of MSS and MASS being crystalline zeolites is ruled out by the absence of corresponding peaks in the XRD patterns (Figure 5.3). Moreover, the near-saturation adsorption at the relative pressure of $P/P_0 > 0.9$ provides useful information about the size and amount of macropores that correspond to the macrochannels observed by electron microscopy (Figure 5.1a–h). From MSS to MASS-15, the increasing slope of adsorption isotherms in the near-saturation range indicates increasing amount of relatively small macropores (d_{pore} = 50–100 nm) which reflects the decrease in average channel width and/or increase in number of channels. However, as the channels continue to shrink and become discontinuous eventually in MASS-30, very few macropores are accessible to gas molecules and significant decrease in near-saturation adsorption is seen.

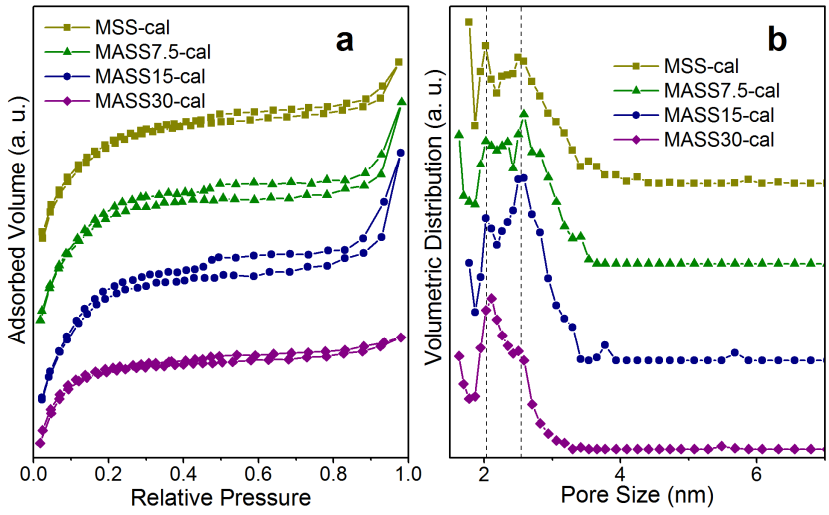

Figure 5.5. (a) N_2 physisorption isotherms and (b) differential volumetric pore size distribution of calcined MSS and MASS samples calculated by NLDFT. The curves have been shifted in the *y*-direction for better clarity. The dashed lines are visual guides.

More precise details about the pore structure of calcined MSS and MASS samples can be obtained from the pore size distribution reported in Figure 5.5b. It should be pointed out that in a *Pm*$\bar{3}$*n* mesostructure, spherical pores are expected, the size of which cannot be determined with decent accuracy by the commonly used BJH method; instead, non-local density functional theory (NLDFT) calculations covering a wider range of adsorption modes are preferred.[4] Here the NLDFT kernel of Quantachrome NovaWin was used assuming the adsorption of N_2 on silica with a cylindrical/spherical pore structure. The results in Figure 5.5b show clearly a bimodal size distribution of mesopores. As further evidence of the *Pm*$\bar{3}$*n* structure, the bimodal distribution is consistent with published studies on the pore structure of *Pm*$\bar{3}$*n* mesoporous silica.[246] Moreover, a comparison of micropore volume in Table 5.3 shows a decreasing trend as Al content increases, which matches the change in the XRD peak intensity of the *p*6*mm* mesophase (Figure 5.3). Considering in addition the relatively small size of pores that can be accommodated in the *p*6*mm* mesophase, the micropores are assigned to it while the mesopores in the size range of 2–3 nm are attributed to the *Pm*$\bar{3}$*n* mesophase. Note that although the micropore volumes of MASS-15cal and MASS-30cal are small compared with the samples containing less Al, they still contribute significantly to the total pore volume, which suggests possibility of *p*6*mm* mesophase in both samples. In fact, the shoulder peaks observed in Figure 5.3 for MASS-15 and MASS-30 at $2\theta = 3.4°$ may be caused by its presence. Similarly, the notable amount of mesopores in MSS-cal could also mean that MSS contains *Pm*$\bar{3}$*n* mesophase, but its diffraction signal might not be strong enough to generate well-resolved peaks.

Table 5.3. Textural properties of calcined MSS/MASS with different amount of $NaAlO_2$ in precursor

Sample	S_{BET} (m^2/g)	V_{micro}* (cm^3/g)	$V_{meso\ (2–30\ nm)}$* (cm^3/g)
MSS-cal	715	0.17	0.15
MASS-7.5cal	712	0.14	0.17
MASS-15cal	656	0.12	0.19
MASS-30cal	492	0.11	0.10

*Calculated with the NLDFT method

Overall the volume of mesopores increases with the Al content up to MASS-15 (Table 5.3), as also reflected by the height of hysteresis loops in Figure 5.5a. Such evolution is a result of the Hofmeister effect of $[Al(OH)_4]^-$; it causes the transformation of cylindrical micelles that form micropores in the *p6mm* mesophase into spherical micelles that are templates for mesopores in *Pm*$\bar{3}$*n*.[239] On the other hand, as depicted by Scheme 5.1 the narrow openings that connect the spherical pores in *Pm*$\bar{3}$*n* could limit access of gas molecules and lead to "concealed" surfaces in the physisorption experiments. As a result, decreased surface area is observed with the progressive dominance of the *Pm*$\bar{3}$*n* mesophase from MASS-7.5 to MASS-30 (Table 5.3). The dramatic drop in mesopore volume of MASS-30 can be attributed to the same effect. Interestingly, Figure 5.5b shows that the Al content does not affect the position of modes of the pore size distribution but only their relative height. The change in the relative population of larger and smaller mesopores is also reflected by the slight shift of XRD peaks of MASS-30 towards higher angles in Figure 5.3; it can be associated with the abundance of smaller mesopores which results in a smaller unit cell.

Indeed, the hierarchical pore structures are confirmed by direct observation of the calcined samples through TEM. The images with lower magnification, *i.e.*, Figure 5.6a,c,e,g show that the spherical shape and macrochannels in all of the samples are stable to calcination at 500 °C; no scaling or channel collapsing are found. Under

higher magnification (Figure 5.6b,d,f,h), micro- and mesopores are revealed. In MSS-cal and MASS-7.5cal particularly, pores aligned to the radial direction with openings 1.0–1.4 nm wide can be clearly seen. It becomes difficult to resolve the pore image as the Al content is further increased, most probably due to the spherical shape of pores in $Pm\bar{3}n$. For example, although extended pores can still be found by carefully observing the TEM image of MASS-15cal in Figure 5.6f, pores in MASS-30cal all appear as discrete low-contrast dots in Figure 5.6h.

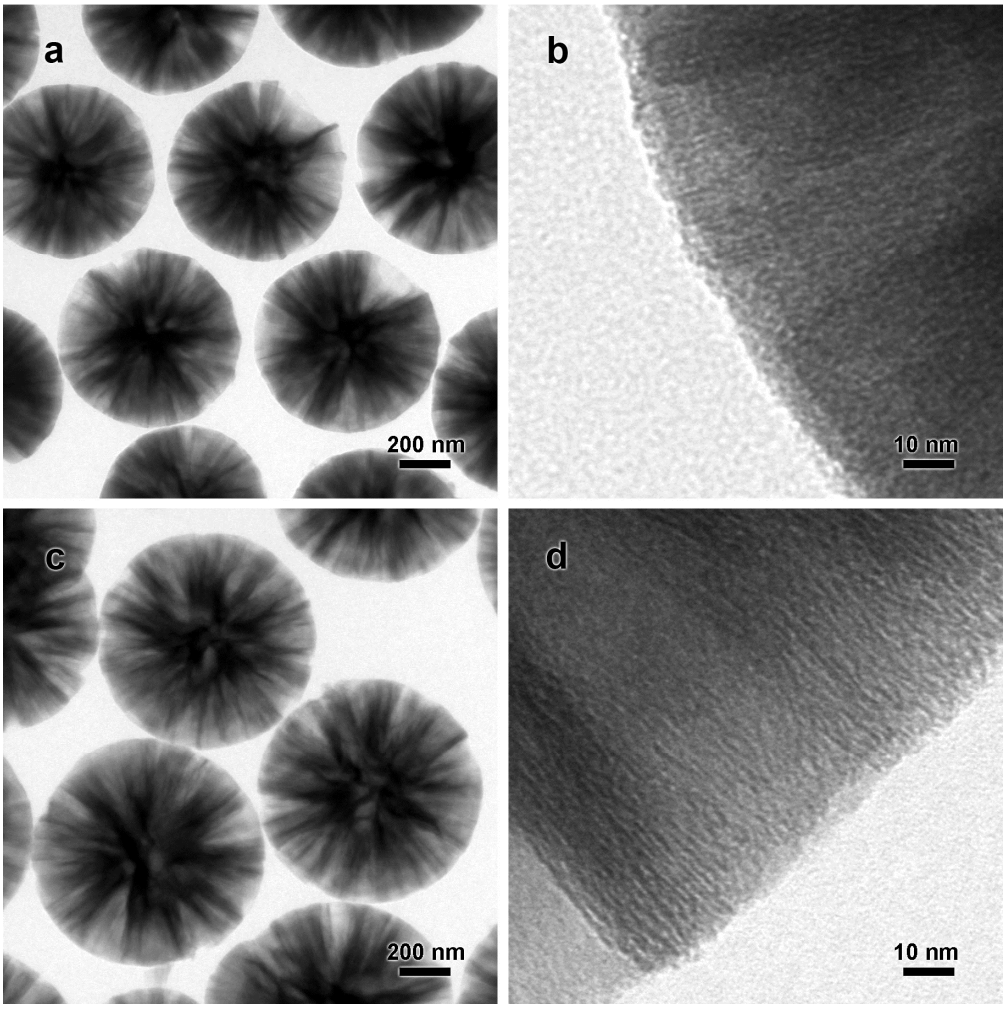

Figure 5.6. TEM images of calcined samples: (a,b) MSS-cal, (c,d) MASS-7.5cal, (e,f) MASS-15cal, and (g,h) MASS-30cal.

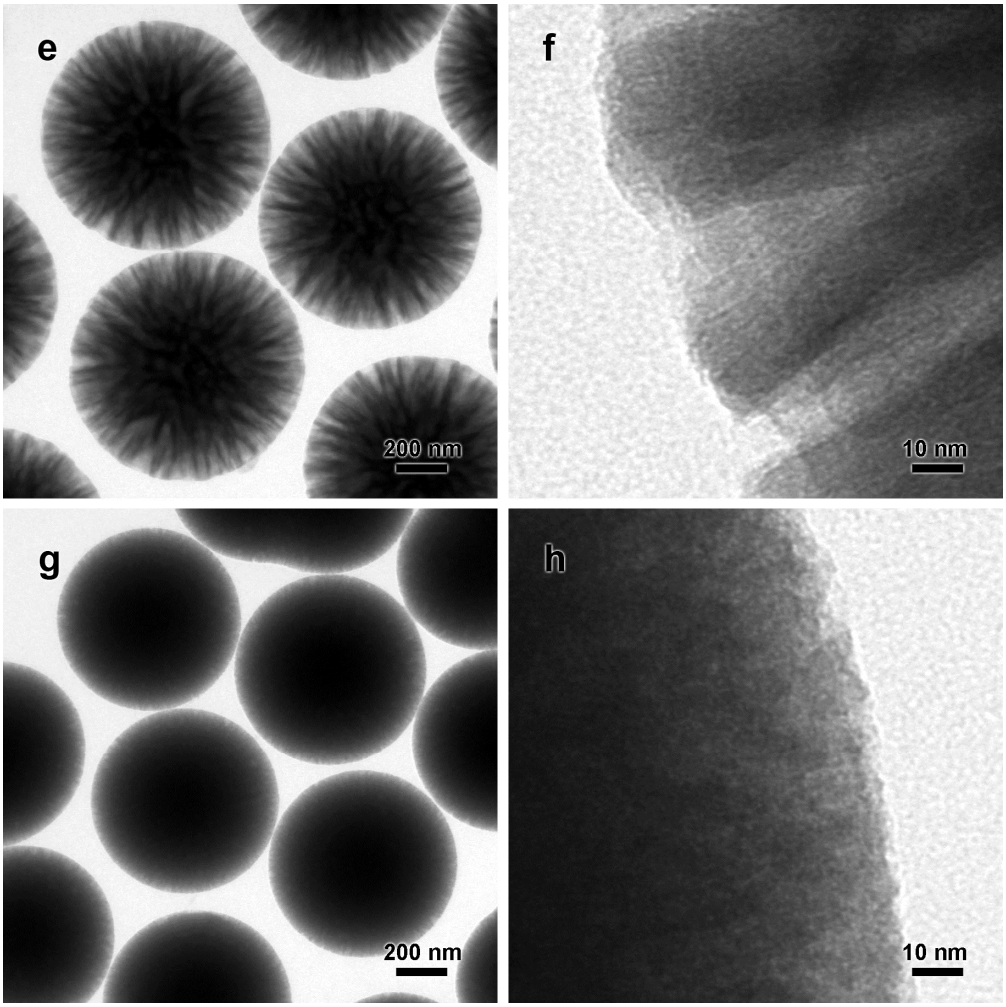

Figure 5.6 continued.

Taking a further step down the dimension, the atomic-scale structures of MSS and MASS were studied by NMR and FTIR techniques. The ^{27}Al magical-angle spinning NMR spectra in Figure 5.7 show only one type of Al in the as-synthesized MASS, whose signal strength increases with the Al content. The peak is located at around 54.5 ppm regardless of the Al content, indicating that 100% of the Al is tetrahedrally coordinated.[230] The incorporation of Al into tetrahedral centers of aluminosilicate framework is desirable in the synthesis of acidic catalyst supports, as the Al–OH–Si bridge thus formed provides stronger acid sites that are more active than those created by octahedral Al.[247] Compared with aluminosilicates synthesized in acidic and/or hydrothermal conditions,[92, 219-220, 225] the higher percentage of tetrahedrally coordinated Al is probably a result of the chemical state of Al in the precursor

solution. In neutral-to-acidic solutions, the principle forms of Al^{3+} are octahedral $[Al(H_2O)_6]^{3+}$ and its hydrolyzed hydroxy analogues. During the synthesis of aluminosilicates, the hydrolysis and condensation of octahedral Al^{3+} complexes compete with the incorporation of Al, usually resulting in noticeable formation of extra-framework Al species that appear as a peak at *ca.* 0 ppm in ^{27}Al magical-angle spinning NMR spectra.[230] In contrast, the present system was kept at a relatively high alkalinity and Al was introduced as a stable tetrahedral complex $[Al(OH)_4]^-$, which prevented the competing reactions during the mild sol-gel process. However, after calcination 5-coordinated Al (peaks at *ca.* 30 ppm in NMR spectra[230]) and octahedral Al species appear (Figure 5.7), though the majority of Al remains in tetrahedral centers, particularly in MASS-30cal.

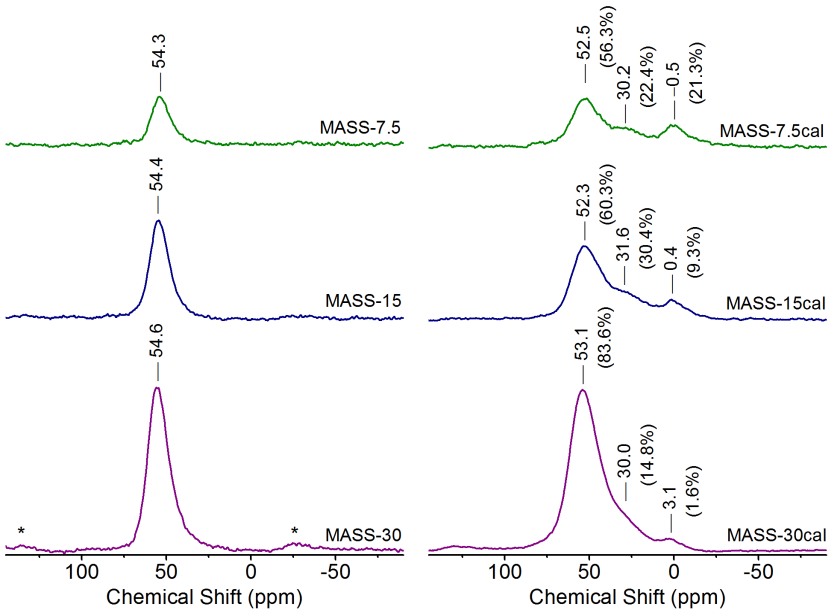

Figure 5.7. ^{27}Al magic-angle spinning NMR spectra of MASS samples before/after calcination. Numbers in parentheses are percentage of deconvoluted individual peak areas among total peak areas. Spinning sidebands are marked by asterisks.

The effect of Al incorporation is also reflected by FTIR spectroscopy. In Figure 5.8, typical mid-IR absorption bands of amorphous silica are observed for all of the as-synthesized and calcined samples. For as-synthesized MSS, the strong band at 1063 cm^{-1} with a shoulder at 1215 cm^{-1} and the band at 795 cm^{-1} can be assigned to

the asymmetric and symmetric stretching of Si–O in SiO_4 tetrahedra, respectively.[248] Another strong band at 455 cm^{-1} is due to vibration of interconnected SiO_4 tetrahedra.[249] A weak band near 580 cm^{-1} is attributed to the bending mode of surface silanol group Si–OH,[250] though its overlap with vibration modes of Si–O–Si ring structures is possible[224]. The surface silanol group should also exhibit a stretching mode at around 960 cm^{-1},[251] but in this case the latter cannot be resolved due to heavy overlap with absorption bands of CTAB. As the Al content increases in the as-synthesized samples, red-shift is observed in all of the Si–O vibration modes, which has been attributed to the incorporation of Al in silica frameworks.[249, 252] It is believed that the lower electronegativity of Al compared with Si causes the immediately neighboring O to gain extra electron density, thus weakening the Si–O bond. Notably, a new band at 870 cm^{-1} emerges in the spectrum of MASS-30 that is assigned to the interactive vibration of AlO_4 tetrahedra.[253] It is apparently a result of extensive incorporation of Al that increases the probability of neighboring Al coordination centers. In addition, two bands at 1408 cm^{-1} and 1397 cm^{-1} assigned to adsorbed NH_4^+ are also observed for MASS-30,[254-256] further confirming the competitive adsorption of NH_4^+ and Na^+ during the sol-gel synthesis (Equation 5.4). It is worth pointing out that NH_4^+ usually appears as a single peak at 1400 cm^{-1}, but in the present case the overlap with OH bending modes of hydrogen-bonded H_2O manifested the peak as a doublet.

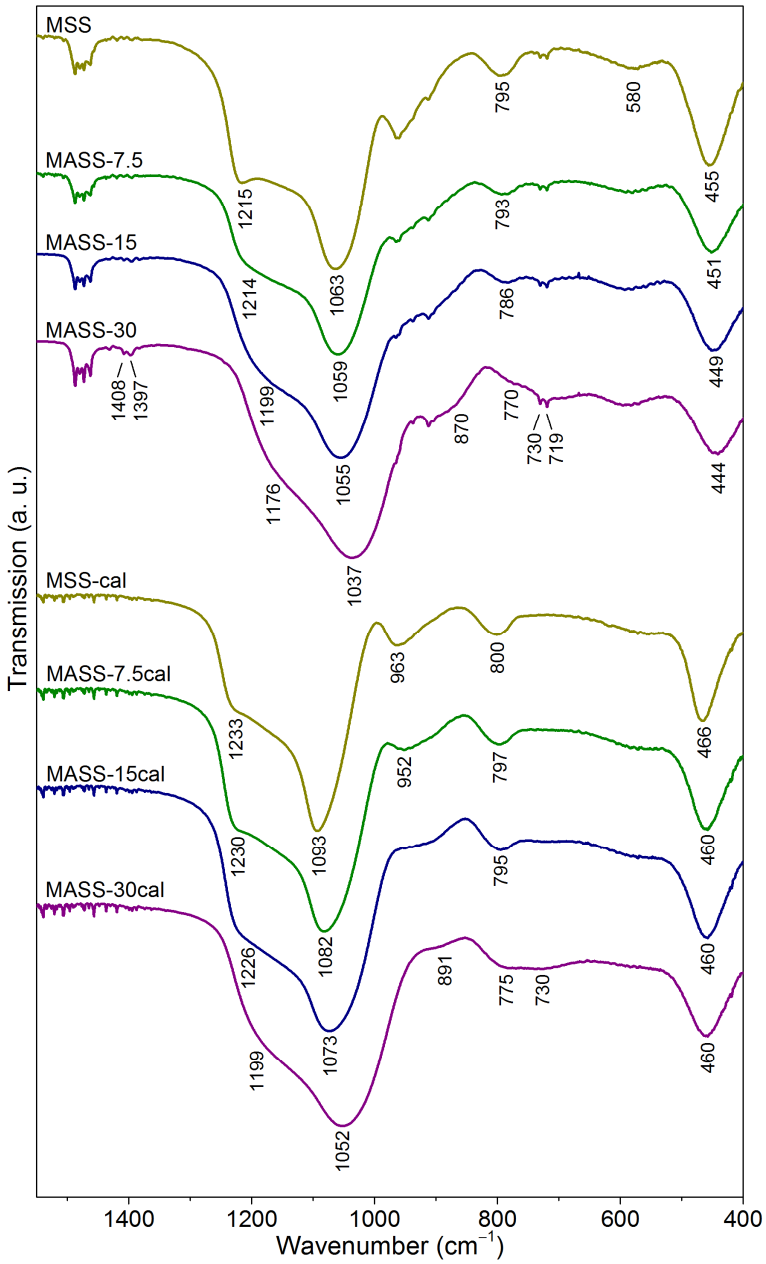

Figure 5.8. FTIR spectra of as-synthesized and calcined MSS and MASS samples.

After calcination, noticeable blue-shift occurred in all of the absorption bands related to the vibration modes of Si–O, which indicates a denser framework in general. Moreover, the red-shifts caused by Al incorporation persisted; the Al still remained in the framework. As a result of thermally induced condensation of surface silanol groups, the intensity of the broad bands near 580 cm^{-1} decreased. On the other hand, the complete removal of CTAB during calcination allowed for the stretching mode of Si–OH to be resolved. For MSS-cal it is located at 963 cm^{-1}. Similar to the

stretching modes of framework Si–O, it also experiences red-shift due to incorporation of Al and in the meanwhile, a decreasing trend in its intensity is observed. The red-shift can be explained by the presence of less electronegative Al neighboring the silanol, and the decreasing band intensity suggests that Al promotes the condensation of silanol groups, probably by forming Si–O–Al linkages.[257] Accompanying the attenuation of Si–OH vibration modes, two bands at 891 cm^{-1} and 730 cm^{-1} emerged gradually which are assigned to the vibration modes of interconnected and isolated AlO_4 tetrahedra, respectively.[253, 258] It should be pointed out that the absorption band of isolated AlO_4 is also present in the spectrum of as-synthesized MASS-30, but it is covered by the absorption bands of CTAB at 719 cm^{-1} and 730 cm^{-1}.

5.3.2. Effects of water

Figure 5.9 present the morphology of MASS-15 synthesized with varied amounts of water. The most obvious morphological effect of water is inhibition of particle aggregation, which can be partially understood as a result of a change in the relative rate of TEOS hydrolysis and silicate condensation. As shown in Equations 5.5 and 5.6, the sol-gel synthesis of siliceous materials can be considered a reactions series: TEOS is first hydrolyzed into less ethylated species which (represented by H_4SiO_4 here for clear presentation) then undergo condensation to form oligomers and eventually SiO_2 precipitate. The increase in water concentration speeds up the hydrolysis and hence the formation of poorly soluble condensed silicates. From the classic view of crystal growth,[259] the large degree of supersaturation favors burst nucleation. If followed by a controlled growth step, narrow particle size distribution can be obtained. In the present system it could be achieved by depletion of Si source before secondary nucleation occurred and/or particles coalescent due to Brownian motion-induced collision. The use of more than 25 mL of water has apparently

created such optimal conditions (Figures 5.9b,c & 5.1e). In addition, reaction between surface silanol groups and silica sources has been proposed to be important in the growth stage of mesoporous silica spheres,[260] which can be viewed as a heterogeneous condensation step (Equation 5.7). As shown in Equation 5.8, condensation between silanol groups is also possible, causing particles coalescence upon collision. The addition of water may stabilize the silanol group and prevent the formation of inter-particle linkages (Equation 5.8), hence contributing to a better size uniformity. On the other hand, the addition of water could also drive larger amount of toluene into the dispersed phase in the microemulsion and hence result in higher viscosity, which in turn slows down particle coalescence.

$$Si(OC_2H_5)_4 + xH_2O \rightarrow Si(OC_2H_5)_{4-x}(OH)_x + xC_2H_5OH \quad (5.5)$$

$$nH_4SiO_4 \rightarrow nSiO_2 + 2nH_2O \quad (5.6)$$

$$Si{-}OH + H_4SiO_4 \rightarrow Si{-}O{-}Si(OH)_3 + H_2O \quad (5.7)$$

$$Si{-}OH + HO{-}Si \rightarrow Si{-}O{-}Si + H_2O \quad (5.8)$$

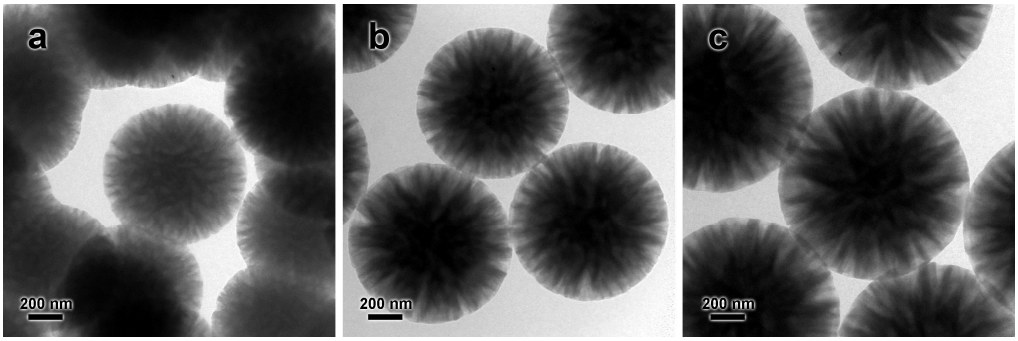

Figure 5.9. TEM images of as-synthesized (a) MASS-15w24, (b) MASS-15w25, and (c) MASS-15w27. Images of MASS synthesized with other amounts of water are reported in Section A1.2 of Appendix 1.

By comparing the N_2 sorption isotherms of MASS-15 synthesized with increasing amount of water (Figure 5.10a), slightly enhanced near-saturation adsorption can be observed which indicates an increase in macropore volume. Corresponding morphological evidence can also be obtained by careful comparison among Figure

5.9a–c. Such increase reflects the volume change of toluene nanodroplets due to lower solubility of toluene in a water-rich mixture. Moreover, a closer look at the textural properties of these samples in Table 5.4 shows that the surface area and mesopore volume are sensitive to the water content; they decrease to similar extends as the amount of water increases. The decrease can be attributed to the lower structural orderliness as a result of fast particle growth.[60] In contrast, the mesopore size distribution (Figure 5.10b) and micropore volume (Table 5.4) are not affected by the amount of water.

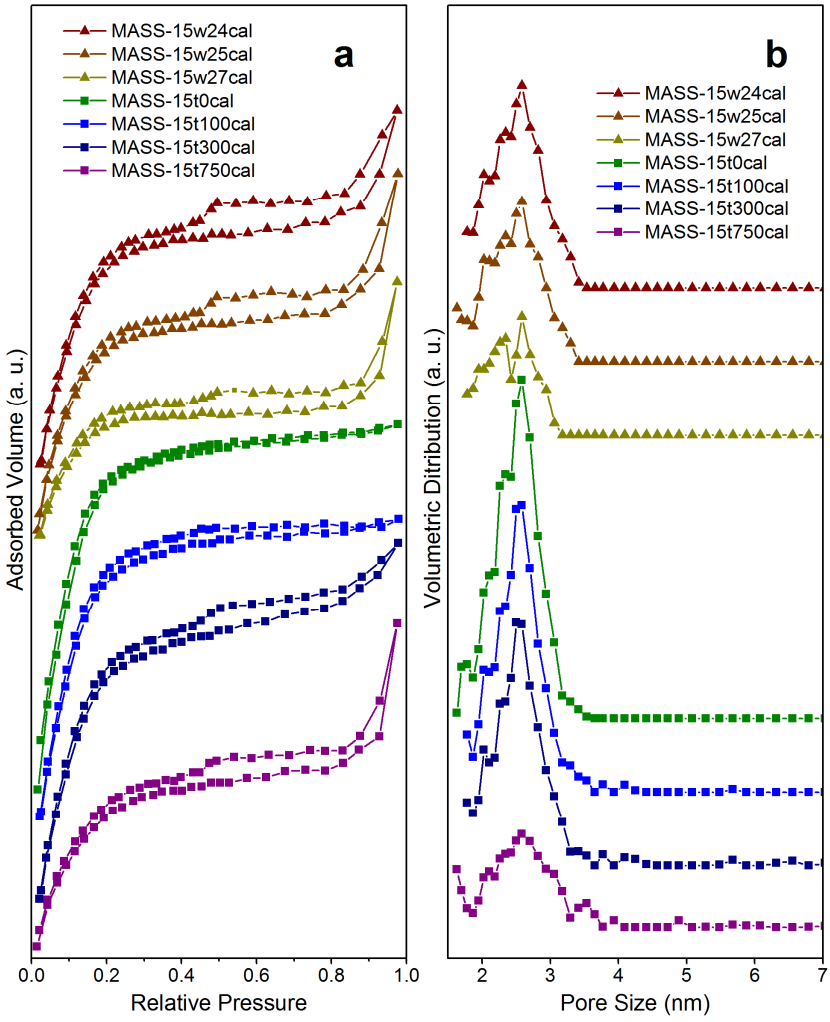

Figure 5.10. (a) N_2 physisorption isotherms and (b) differential volumetric pore size distribution of calcined MASS-15 synthesized with different amounts of toluene and water. The curves have been shifted in the *y*-direction for better clarity.

Table 5.4. Textural properties of calcined MASS-15 synthesized with different amount of water and toluene

Sample	S_{BET} (m^2/g)	V_{micro}* (cm^3/g)	$V_{meso\ (2–30\ nm)}$* (cm^3/g)
MASS-15w24cal	797	0.10	0.27
MASS-15w25cal	694	0.11	0.22
MASS-15w27cal	545	0.11	0.14
MASS-15t0cal	856	0.05	0.35
MASS-15t100cal	858	0.08	0.31
MASS-15t300cal	830	0.09	0.31
MASS-15t750cal	523	0.09	0.17

*Calculated with the NLDFT method

5.3.3. Effects of toluene

As the structure-directing agent of macropores, toluene significantly affects their formation in the present system. The electron microscope images in Figure 5.11a–d show that no macropores are formed without or with 100 μL of toluene added. In these cases the concentration of toluene is below the solubility limit, and instead of microemulsion a homogeneous precursor solution is formed. Particle aggregation can be observed, probably due to the lower viscosity of the homogeneous solution which could not damp the collision between forming particles effectively. When the amount of toluene is further increased to 300 μL and 750 μL, macropores emerge and grow in volume, and the uniformity of particle size is improved (Figure 5.11e–h). The changes in macropore volume are also reflected by N_2 sorption isotherms plotted in Figure 5.10a; the near-saturation adsorption is negligible for MASS-15t0cal and MASS-15t100cal, while it becomes significant for products synthesized with larger amounts of toluene. Additional effects of introducing toluene are reflected by a summary of textural properties in Table 5.4. It is clear that the surface area decreases significantly only when more than 300 μL of toluene is added, and the mesopore volume also follows a similar trend.

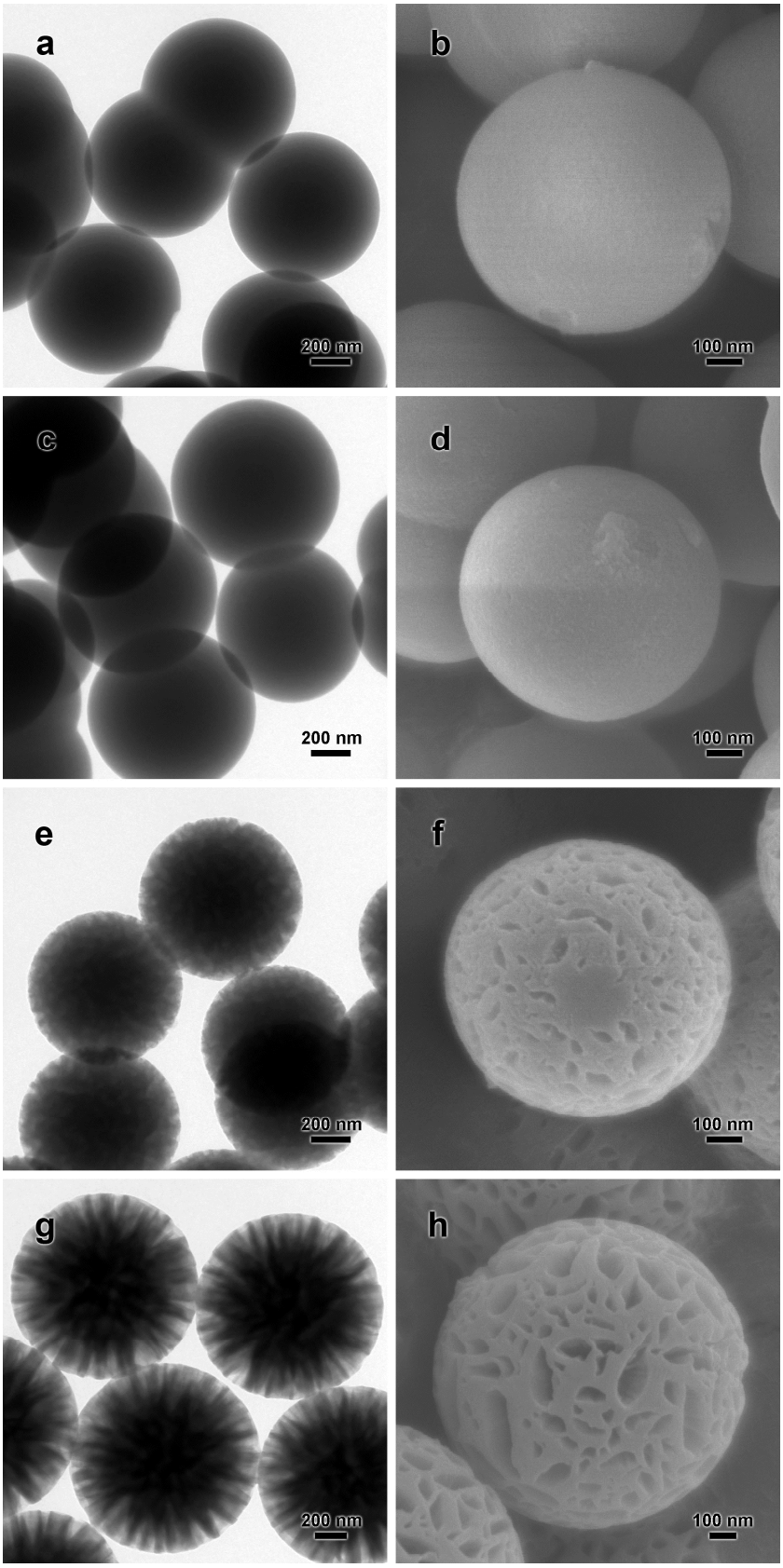

Figure 5.11. TEM and FESEM images of as-synthesized (a,b) MASS-15t0, (c,d) MASS-15t100, (e,f) MASS-15t300, and (g,h) MASS-15t750.

Considering the trend in the evolution of macropores, the change in surface area and mesopore volume should be associated with the presence of microemulsion. It is believed that the formation of microemulsion consumes CTA^+ as stabilizing agent at the oil-water interface and decreases the amount of CTA^+ available to form mesopore-directing micelles. Consequently the mesopore volume (Table 5.4) as well as the closely related surface area decreases. Since increase in amount of water can lead to larger volume of toluene nanodroplets, the same mechanism should also play a role in the dependence of surface area and pore volume on water content discussed earlier. In addition, the presence of toluene leads to formation of micropores, but a small amount (*e.g.* 100 μL) is enough to exhibit this effect; more toluene does not increase the amount of micropores noticeably. The pore size distribution in Figure 5.10b does not indicate any shift of modal sizes and the swelling of micelles can be excluded. It is thus speculated that the dissolved toluene enhances interaction between CTA molecules and leads to increased number of cylindrical micelles that form micropores.

5.3.4. Effects of other synthesis parameters

The effects of the amounts of NH_3, CTAB, and TEOS used for the synthesis of MASS were also studied. Basically, they exhibit less significant morphological effects. The results are presented in Section A1.3 of Appendix 1.

5.3.5. Catalytic experiments

Porous silica has a long history of being used as catalyst supports. In recent years as global warming gains public awareness, interest in the catalytic conversion of CO_2, the major greenhouse gas, has dramatically increased.[16] The majority of works under this topic have been focused on Cu-based catalysts which were traditionally used for methanol synthesis. In this context the application of the present MSS-cal and MASS-15cal (synthesized with 26 mL of water and 600 μL of toluene, see Table 5.1) is

illustrated by loading them with a Cu/ZnO composite to prepare CZMSS and CZMASS-15 catalysts, respectively, and testing the catalysts in the model reaction of CO_2 hydrogenation. The actual loading of the catalysts is shown in Table 5.5. During catalyst evaluation, CO, methanol, and dimethyl ether (DME) were detected to be the only carbon-containing products.

Table 5.5. Elemental composition of freshly calcined catalysts*

Catalyst	Cu (wt %)	Zn (wt %)	Al/Si (mol/mol)	Na/Al (mol/mol)
CZMSS	6.67	3.87	0	0
CZMASS-15	6.91	3.99	0.170	0.319

*Analyzed by EDX

Figure 5.12a shows that without incorporation of Al, the CZMSS exhibits high specific activity comparable to published results of fumed SiO_2-loaded Cu/ZnO catalysts (*ca.* 56 $mol_{CO2}/kg_{metal}\cdot h$ at steady state).[168] Slow increase in the activity and organics selectivity can be observed in Figure 5.12a and 5.12b, respectively, which indicates continuous surface reconstruction of the active component promoting the formation of methanol. It has been suggested that Zn-doped atom "steps" on Cu surface, having much higher methanol synthesis activity than their counterparts on pure Cu surface, are the active sites in industrial $Cu/ZnO/Al_2O_3$ catalysts,[155] and the aforementioned surface reconstruction can be regarded as diffusion of Zn towards Cu surfaces. However, Figure 5.12c shows that without functionalization of the silica support, no DME formed using the Al-free CZMSS catalyst.

As a result of Al incorporation, remarkable change in activity and product composition can be observed in Figure 5.12a,c. For example, CZMASS-15 catalyst shows a lower specific activity but a significant increase in DME product, which reflects the acidity of MASS-15. It has been generally accepted that in methanol synthesis, DME is formed at Brønsted acid sites by the dehydration of methanol.[16]

The CZMASS-15 can thus be viewed as a bifunctional catalyst where the Cu/ZnO composite catalyzes methanol synthesis and the aluminosilicate support acts as solid acid catalyzing methanol dehydration. Assuming that DME was only derived from methanol as the intermediate, the conversion of methanol to DME reached 61%. Although the calculated organics selectivity for CZMASS-15 fluctuates greatly in Figure 5.12b due to random error being magnified by the low conversion, the overall trend follows that of CZMSS. Surface reconstruction similar to that in CZMSS can be expected.

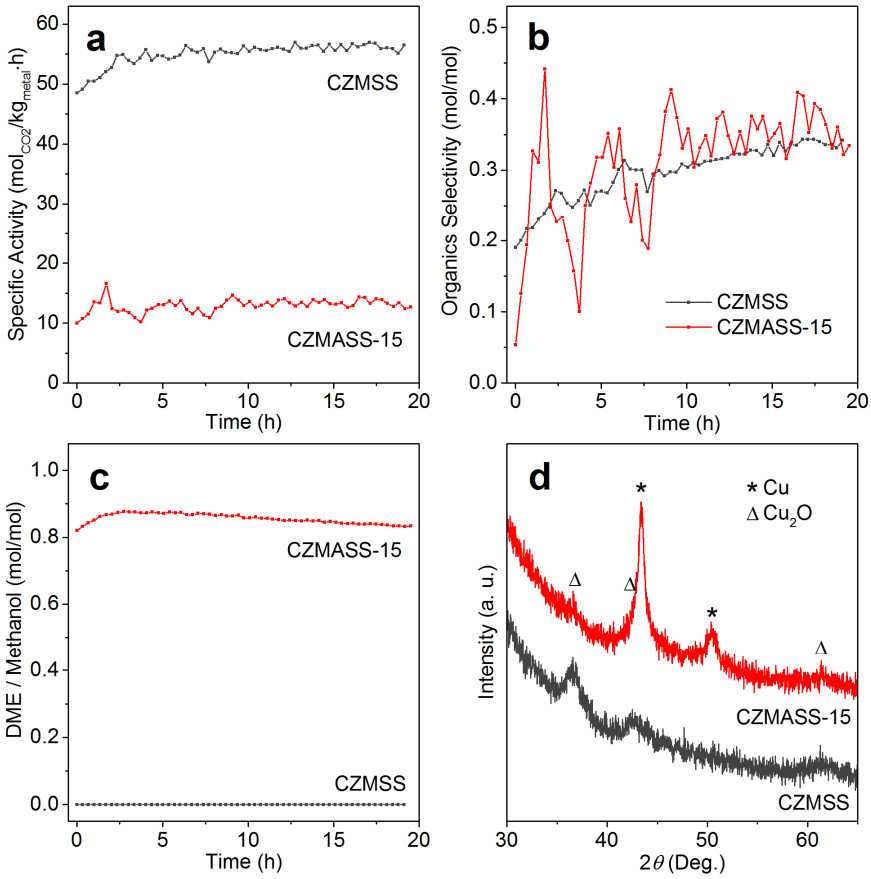

Figure 5.12. Results from catalysts evaluation of CZMSS and CZMASS-15: (a) specific activity (CO_2 consumption rate normalized by total amount of Cu and Zn in catalyst), (b) organics selectivity (rate of CO_2 converting to dimethyl ether and methanol divided by the total CO_2 consumption rate), (c) mole ratio between dimethyl ether and methanol in product stream, and (d) XRD patterns of spent catalysts.

After the catalytic reaction, the spent catalysts were analyzed by XRD. Figure 5.12d shows that Cu and/or Cu_2O were present in the samples. Considering the

strongly reducing environment of the reaction, Cu_2O should not exist in significant amounts during the reaction; it was formed presumably by the oxidation of Cu in air. Despite large efforts in controlling the exposure of the samples to air, their oxidation which continued in the sample chamber of the diffractometer was inevitable. Nevertheless, the degree of oxidation and status of the remaining unoxidized Cu particles provide valuable insights about the catalyst. CZMSS exhibits particularly weak diffraction peaks of Cu and the oxidation of Cu particles was practically complete. It suggests a highly dispersed status and very reactive surfaces of Cu, which explain the higher activity of CZMSS (Figure 5.12a). In contrast, CZMASS-15 shows strong diffraction signal from Cu, which is an indication of more severe sintering than CZMSS. Cu_2O formation is insignificant for CZMASS-15 probably due to limited Cu surface area. Indeed, the more severe sintering of Cu particles in CZMASS-15 is corroborated by high-angle annular dark-field (HAADF) images and corresponding EDX elemental mapping of the spent catalysts shown in Figure 5.13.

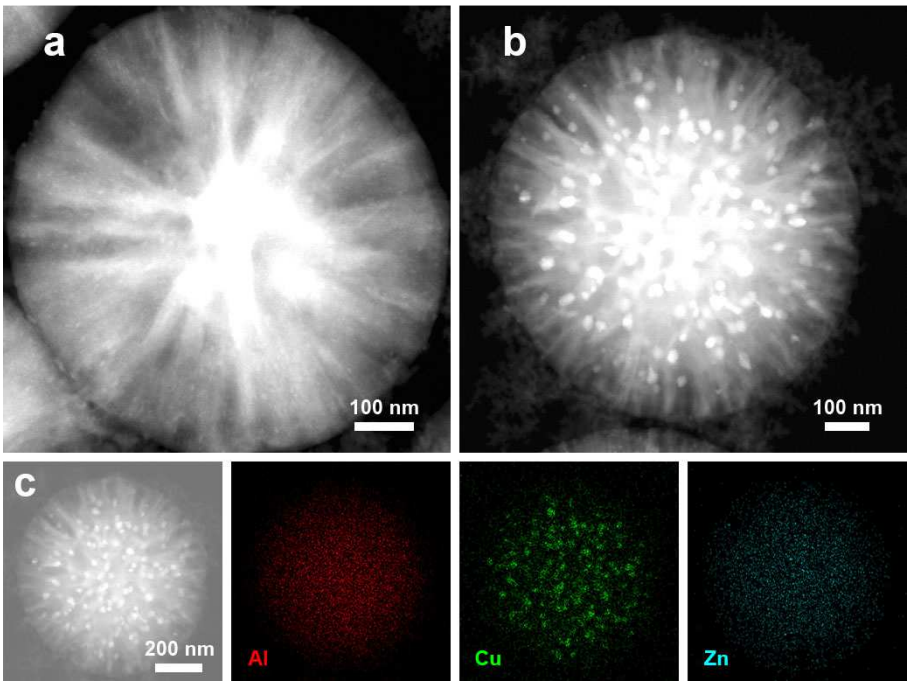

Figure 5.13. HAADF images of spent catalysts (a) CZMSS and (b) CZMASS-15. (c) EDX elemental mapping of spent CZMASS-15.

The main factor in the Cu sintering of CZMASS-15 is believed to be limited pore accessibility during impregnation. As discussed earlier, the $Pm\bar{3}n$ mesophase in MASS-15 consists of spherical pores connected by narrow holes where considerable surface tension may prevent solutions from wetting the entire pore network. Compared with the case of MSS where the cylindrical pores of the *p6mm* mesophase are more accessible, a larger portion of metal precursors might be kept near the surface of MASS-15. During calcination and catalyst activation, the metal precursors on the surface sinter more easily to reduce dispersity of the metal particles and hence activity. For CZMSS, it is possible that the metal particles formed deep inside MSS were confined by the pore walls, which prevented sintering.[261]

5.4. Conclusions

The single-step synthesis of monodisperse aluminosilicate spheres with hierarchical macro-meso-microporous structure at room temperature has been demonstrated for the first time. The CTAB-stabilized microemulsion system provided multi-scale soft templates for the hierarchical pore structure where micropores contributed up to over 50% of total pore volume. Meanwhile the formation of microemulsion was shown to be the key to obtaining monodisperse particles, most probably due to its rheological properties. In addition, the alkaline environment of precursor mixture allowed for stable existence of $[Al(OH)_4]^-$ and hence incorporation of Al in exclusively four-coordinated state with an Al/Si ratio conveniently tunable between 0 and 0.35. The present work has illustrated the generality and practicality of Hofmeister anion effects in materials synthesis, linking two important topics about siliceous materials, namely chemical functionalization and pore engineering. To the best of our knowledge, simultaneous tuning of macro-, meso- and micropores with the incorporation of heteroatom in silica and in particular, synthesis of monodisperse

aluminosilicate particles with such hierarchical structures have not been reported before. The possibility of achieving monodispersity of product particles will also facilitate future development and utilization of this class of novel porous materials.

Chapter 6. Hierarchical EMT-Type Zeolite for Pt-Catalyzed Selective CO Production from CO_2/H_2

6.1. Introduction

Zeolites are crystalline microporous molecular sieves with wide applications in catalysis, separation and even household cleaning.[213] As each type of zeolite exhibits unique catalytic and molecular sieving properties, control over crystal polymorphism is of great importance in their synthesis, which is often achieved with organic structure-directing agents (OSDAs). However, OSDA-free approaches are more desirable when cost-effectiveness is concerned.[262] In such approaches, M_2O–Al_2O_3–SiO_2–H_2O systems (M = alkali metals) are most frequently encountered, where hydrated M^+ ions are generally regarded as templates for zeolite crystallization.[102] Therefore, controlling the structure of hydrated M^+ ions provides a route toward selective synthesis of zeolites. Simple alcohols, for instance, are ideal additives due to their low cost and ability to alter the water structure.[263] However, study on this topic has been largely limited to fundamental chemistry. Although examples of alcohols influencing zeolite polymorphism exist,[264-265] deliberate experimental exploration on the role of cationic solvation therein has not been pursued.

EMT is a closely related polymorph of FAU which in oil refineries catalyzes the vital process of fluid catalytic cracking of hydrocarbons. EMT is also useful in such reactions with different catalytic properties,[266] but its practicality has been limited by high cost. As illustrated in Figure 6.1, both polymorphs are constructed by stacking of faujasite sheets. In EMT, adjacent sheets form mirror symmetry, resulting in hexagonal lattice with ABAB···· stacking. In FAU, adjacent sheets are related by inversion centers, forming cubic lattice with ABCABC····· stacking. The structural

similarity between EMT and FAU allows for extensive stacking faults. Synthesis of the less stable EMT (due to its lower symmetry) in pure form is hence more challenging than that of EMT-FAU intergrowths such as ZSM-2, ZSM-3, ZSM-20, ECR-30 and CSZ-1.[129] Since the first success,[267] synthesis of pure EMT had required the toxic OSDA of 18-crown-6, until EMT-type nanozeolite was obtained recently by an OSDA-free method where strictly controlled starting gel composition and heating procedure were crucial.[268] Attempt has also been made to synthesize EMT in aggregated forms with certain degree of secondary structure.[269] Compared with conventional zeolite products, nanozeolites have higher mass-transfer efficiency and are easier to integrate into complex nanostructures,[12, 270-271] but their energy-intensive separation process is an obstacle to large-scale applications. Therefore hierarchical zeolites that are relatively easy to separate and retain the mass-transfer advantages have gained widespread interest.[97-99, 131]

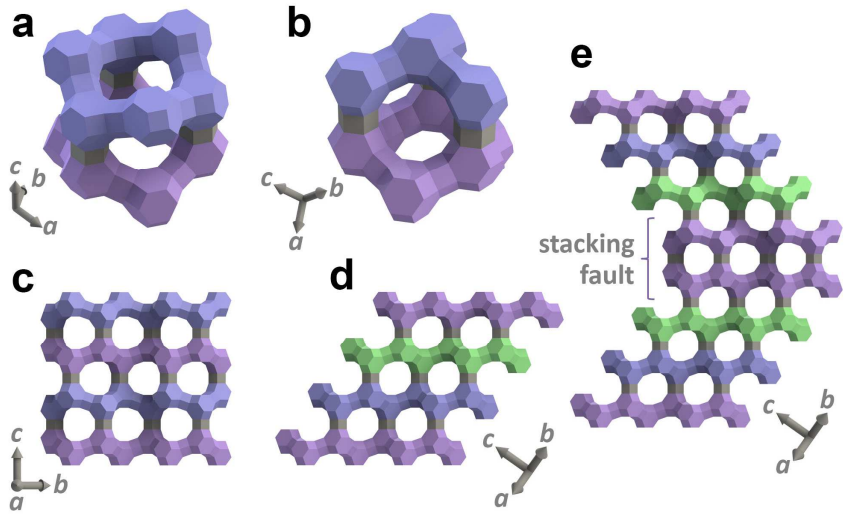

Figure 6.1. Structures of (a) EMT hypercage, (b) FAU supercage, (c) EMT lattice viewed from the [100], (d) FAU lattice viewed from the [110], and (e) a stacking fault normal to FAU [111].

It is worth mentioning that EMT-type zeolites synthesized so far without OSDAs have low Si/Al ratios (<1.5) due to high alkalinity of starting gels.[102] Although the relatively weak acidity and low stability associated with low-silica (Si/Al < 2.0) zeolites make them unsuitable for application in refinery processes,[95] their abundant

alkali metal content and surface hydroxyl groups become beneficial in other reactions. A notable example is water gas shift (WGS) reaction. Noble metal species such as Pt–OH_x and Au–$O(OH)_x$ stabilized by alkali ions and surface hydroxyl have been found highly active in low-temperature WGS.[272-273] Low-silica zeolites are potentially good catalyst supports, because their surface chemistry apparently favors formation of these active sites and in the mild conditions of low-temperature WGS, stability of the support materials is less problematic. On the other hand, significant progress in renewable hydrogen production has drawn increasing attention to reverse water gas shift (RWGS) as a starting point of converting CO_2 to useful chemicals.[16] Experiment on the abovementioned noble metal WGS catalysts in the reverse reaction is a logical step, and catalysts such as Pt/TiO_2 have indeed shown high RWGS activity.[274] However, reports on the use of low-silica zeolites in WGS/RWGS are scarce.[275-277] To the best of our knowledge, the WGA/RWGS activity of alkali- and hydroxyl-stabilized noble metal species has not been explored on low-silica zeolite catalyst supports.

In this work, the EMT/FAU polymorphism is controlled with alcohols, and hierarchical EMT-type zeolite is synthesized thereby in the absence of traditional OSDAs. The potential of this low-silica zeolite as catalyst support will then be explored and compared with commercial zeolite X in Pt-catalyzed RWGS reaction.

6.2. Experimental Section

6.2.1. Chemicals and reagents

Sodium silicate solution (Merck, 27.2% SiO_2, 8.3% Na_2O), sodium aluminate (Nacalai, 40.2% Al_2O_3, 28.3% Na_2O), sodium hydroxide (NaOH, Merck), sodium carbonate (Na_2CO_3, Merck), platinum chloride ($PtCl_2$, Aldrich), methanol (MeOH,

Fisher Scientific), ethanol (EtOH, Fisher Scientific), n-propanol (n-PrOH, Aldrich), isopropanol (i-PrOH, Merck), ammonia solution (NH_3, Merck, 32%), and zeolite X (Sigma, Na-type, Si/Al = 1.2, size <10 μm) were used as received. The SiO_2 content of the sodium silicate solution was determined by gravimetric analysis after condensation and precipitation of silicate species with NH_4Cl/HCl. The Na_2O content of the same reagent was determined by HCl titration. Elemental composition of the sodium aluminate was measured by ICP-OES method after HNO_3 digestion. The Si/Al ratio of the commercial zeolite X was determined by EDX.

6.2.2. Small-scale synthesis

In a typical synthesis with starting gel composition of $51.5Na_2O–Al_2O_3–nSiO_2–1590H_2O–x$ROH where n = 13.8, 0.29 g of sodium aluminate and 2.0 g of sodium hydroxide were dissolved in 15 g of deionized water to form solution A. Meanwhile 3.5 g of sodium silicate solution and 2.23 g of sodium hydroxide were dissolved in 14.5 g of deionized water to form solution B. In experiments where n value of starting gel is different from 13.8, the amounts of sodium silicate, sodium hydroxide and water in solution B were adjusted accordingly (Table 6.1). With constant magnetic stirring, solution A was added slowly into solution B (in about 3 min), and calculated amount of alcohol was also added slowly. Due to its wide availability from renewable sources, ethanol forms the focus of this work. The methanol-, ethanol-, and isopropanol-containing starting gel will be hereafter referred to as "M*x*", "E*x*", and "iP*x*", respectively, with "*x*" representing the amount of alcohol added. For example, a starting gel with the composition of $51.5Na_2O–Al_2O_3–13.8SiO_2–1590H_2O–150$EtOH is thus coded as "E150". Without addition of any alcohol, the starting gel is coded as "Ctrl". The n value of a starting gel will be specified only when it is not 13.8.

The starting gel was aged under stirring for 1 h at room temperature, sealed in a polypropylene test tube and allowed to crystallize in a water bath at 60 °C. After a

desired time of heating, the test tube was cooled in tap water. Precipitate thus formed was separated by repeated cycles of centrifugation and wash with deionized water until pH ≤ 8. The product was dried in an electrical oven at 60 °C overnight. To identify products obtained with *y* hours of crystallization, suffixes of "-*y*h" are added to the codes of the starting gels. For example, "E150-9h" denotes the product obtained from E150 after 9 h of crystallization.

Table 6.1. Amounts of reagents used in zeolite syntheses*

Starting gel composition			Code	Sodium silicate solution (g)	NaOH in solution B (g)	Water in solution B (g)	Alcohol (mL)
n	*x*	ROH					
13.8	37	MeOH	M37	3.5	2.23	14.5	1.7
13.8	150	MeOH		3.5	2.23	14.5	6.9
13.8	37	EtOH	E37	3.5	2.23	14.5	2.5
13.8	75	EtOH	E75	3.5	2.23	14.5	5
10.8	150	EtOH		2.75	2.25	14.8	10
11.8	150	EtOH		3.0	2.25	14.8	10
13.8	150	EtOH	E150	3.5	2.23	14.5	10
15.8	150	EtOH		4.0	2.18	14.1	10
13.8	19	n-PrOH		3.5	2.23	14.5	1.6
13.8	37[†]	n-PrOH		3.5	2.23	14.5	3.2
13.8	19	i-PrOH		3.5	2.23	14.5	1.6
13.8	37	i-PrOH	iP37	3.5	2.23	14.5	3.2
10.8	0	None		2.75	2.25	14.8	0
11.8	0	None		3.0	2.25	14.8	0
13.8	0	None	Ctrl	3.5	2.23	14.5	0

*0.29 g of sodium aluminate, 2.0 g of NaOH and 15 g of water were used in solution A for all experiments.

[†]About 50% of n-PrOH was not dissolved.

6.2.3. Scaled-up synthesis

For the scaled-up synthesis of hierarchical EMT-type zeolite, a starting gel composition of $51.5Na_2O–Al_2O_3–13.8SiO_2–1590H_2O–150EtOH$ was used. The process consists of two synthesis cycles with a materials recycle step in between.

Synthesis cycle 1: The procedures for the small-scale synthesis was followed, with a 10-fold increase in the amounts of all reagents (*i.e.*, 2.9 g of sodium aluminate, 20 g of sodium hydroxide and 150 g of water in solution A, 35 g of sodium silicate solution, 22.3 g of sodium hydroxide and 145 g of water in solution B, amount of ethanol was 100 mL). The starting gel was sealed in a 500 mL polypropylene bottle and subjected to crystallization for 9 h at 60 °C. Zeolite product settled at the bottom of the bottle at the end of the hydrothermal treatment. 250 mL of clear mother liquor on top was decanted and stored. The product in the remaining slurry was separated by centrifugation, and the supernatant was combined with the mother liquor collected earlier. Purification of the product required 3 cycles of centrifugation and wash with deionized water. Drying was carried out at 60 °C overnight.

Materials recycle: The mother liquor from synthesis cycle 1 was loaded into a 1 L Teflon flask equipped with a fractional distillation setup. The Teflon flask was heated gently in an oil bath. Distillate (ethanol solution) exiting at *ca.* 78 °C from the fractionating column was collected until the exit temperature started to rise. 100 mL of water was then distilled off from the remaining mother liquor.

Synthesis cycle 2: 5 g of sodium silicate solution was added to the concentrated, ethanol-free mother liquor produced by the recycle step. 2.5 g of sodium aluminate was dissolved in the recycled 100 mL of water and added to the mother liquor under magnetic stirring. Preparation of starting gel was completed by addition of the recycled ethanol and another 8 mL of fresh ethanol. Subsequent aging, crystallization and separation procedures were identical to those in synthesis cycle 1.

6.2.4. Catalyst preparation

300 mg of catalyst support (either EMT-type zeolite synthesized by the scaled-up method or commercial zeolite X) was dispersed in a clear solution prepared by dissolving calculated amount of $PtCl_2$ and in some cases 10 mg of Na_2CO_3 in a mixture of 0.3 mL of 32% NH_3 and 0.6 mL of water. The paste was outgassed at 40 mbar for 3 min, aged for 30 min in ambient conditions and dried in an electrical oven at 100 °C overnight. The catalysts are named according to nominal Pt loading ("01" for 1%, "02" for 2%), type of support material and whether Na_2CO_3 was co-impregnated. For example, Pt02Na-EMT has a nominal Pt loading of 2% and co-impregnation of Na_2CO_3 on the hierarchical EMT-type zeolite.

6.2.5. Catalyst evaluation

200 mg of catalyst was ground into a fine powder and loaded into a 3/8" stainless steel reactor to form a fixed bed. Details about the reactor set-up can be found in Section 3.9. The catalyst was activated at 280 °C for 4 h (heating rate 2 °C/min) in 10% H_2/N_2 (flow rate 50 std mL/min) and cooled to room temperature. A 3:1 mixture of H_2/CO_2 containing 4% of N_2 as internal standard was then fed to the reactor at 1 atm and a rate of 24 std mL/min. Temperature was increased at 2 °C/min to different values for measurement of activation energy, where effluent was analyzed for 3 times at each temperature and the average composition was taken. Stability test was performed afterwards where samples of the effluent was taken by an automated sampler at intervals of 30 min.

6.2.6. Materials characterization

In this work, spin-lattice relaxation rate ($1/T_1$) of ^{23}Na was measured at 300 K and 132.29 MHz by inversion recovery experiments. ^{27}Al MAS NMR spectra were acquired at 104.26 MHz with a 0.6 μs pulse and 925 scans. ^{29}Si MAS NMR spectra

were acquired at 79.49 MHz with a 4 μs pulse and 400 scans. Aqueous $Al(NO_3)_3$ and $Si(CH_3)_4$ were used as references of chemical shift for ^{27}Al and ^{29}Si, respectively. Before N_2 sorption experiments, zeolite samples were outgassed in vacuum at 225 °C overnight.

6.3. Results and Discussion

6.3.1. Zeolite synthesis

Crystallization of EMT is strongly promoted by the addition of alcohols. Figure 6.2 shows that the alcohol-free Ctrl only produced FAU-dominant intergrowths, but the alcohol-containing starting gels could crystallize into EMT in general. As the amount of ethanol increases, duration of heating required for the gel to start crystallizing also reduces from *ca.* 9 h for Ctrl to 5–7 h for E150. In addition, with the same amount of different alcohols added (x = 37), the onset of crystallization occurs in the order of iP37, E37, M37 from fastest to slowest. (A complete XRD survey of the crystallization process of starting gels with other compositions is reported in Appendix 2.1.)

As seen in Figure 6.3, whole pattern fitting of the XRD pattern of E150-9h is successful with a pure EMT structure model,[278] giving lattice parameters of a = 17.68 Å and c = 28.31 Å which compare very closely to those of EMC-2, the type material of EMT.[279] Existence of an FAU phase has also been considered for fitting, but when the results are compared in Figure 6.3 and Table 6.2, it is clear that quality of fitting increases monotonically with decreasing percentage of FAU assumed. The whole pattern fitting thus indicates E150-9h to be pure EMT.

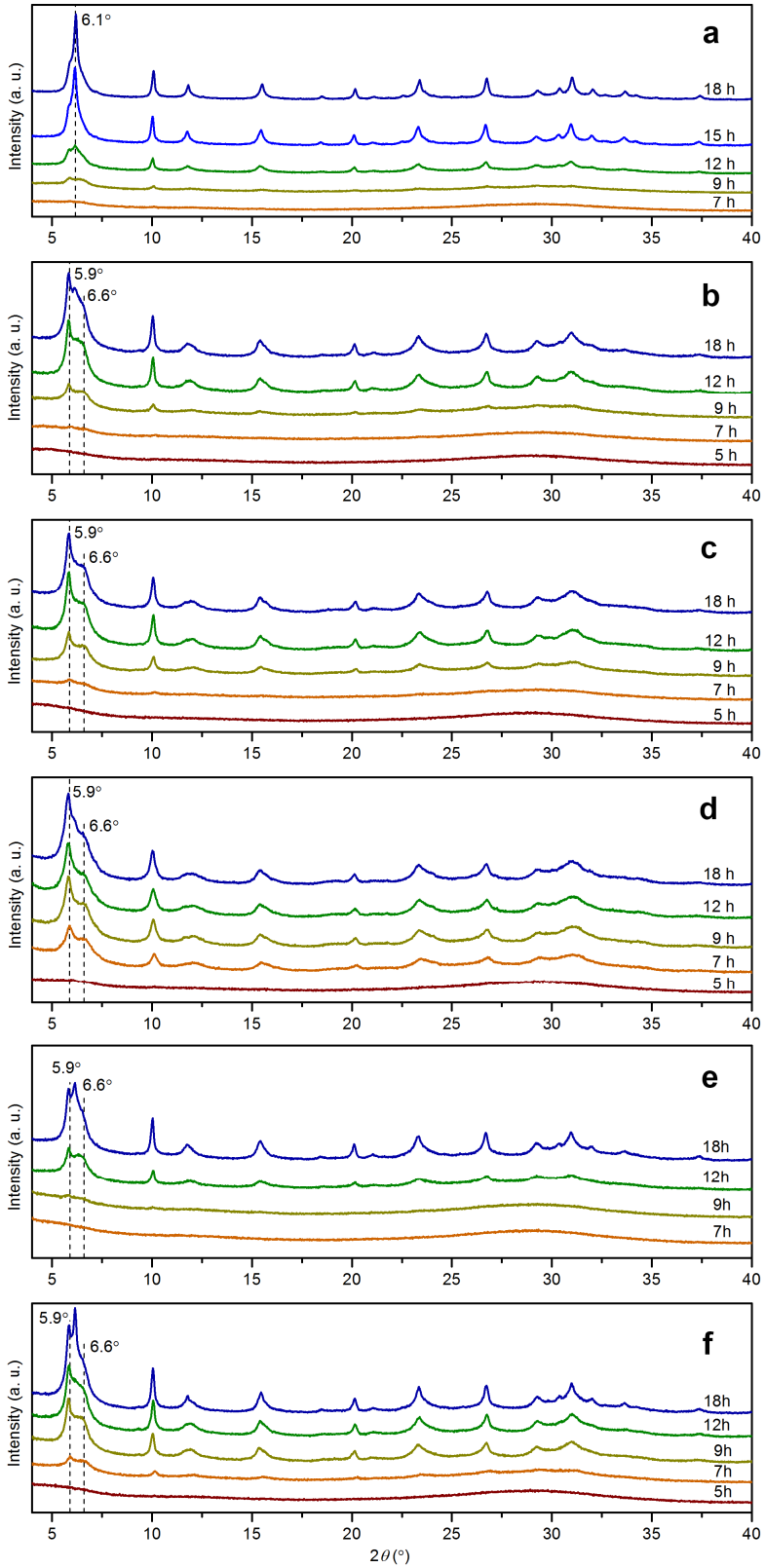

Figure 6.2. Powder XRD patterns of products from (a) the alcohol-free Ctrl and (b) the ethanol containing E37, (c) E75, (d) E150, (e) M37, and (f) iP37 starting gels. Characteristic peaks marked by dashed lines; $2\theta = 6.1°$: FAU (111), $2\theta = 5.9°$: EMT (100), $2\theta = 6.6°$: EMT (101).[278]

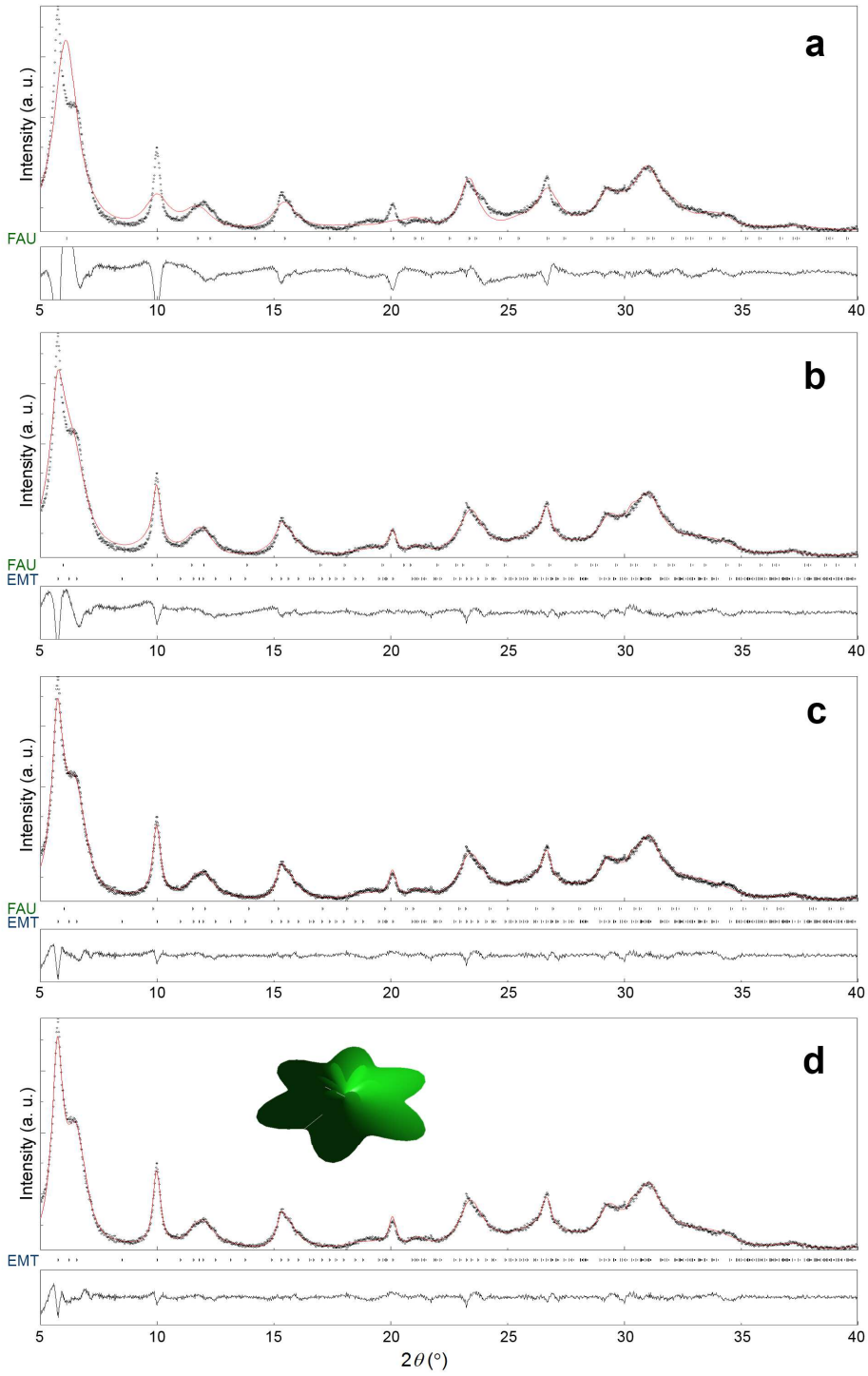

Figure 6.3. Results of whole pattern fitting for E150-9h, with the assumption that it contains (a) 100% of FAU, (b) 50% of FAU and 50% of EMT, (c) mixture of FAU and EMT with unconstrained relative contents which were optimized to be 88% of EMT and 12% of FAU, or (d) 100% of EMT. Inset: calculated crystallite shape. Vertical ticks: peak positions of the structure models. Residual between original data and fitted pattern plotted at the bottom of each subfigure. Fitting performed using the Rietveld refinement-based MAUD program,[280] with Popa rules[281] and arbitrary texture model[282] implemented to describe anisotropic size/strain and orientation of crystallites.

Table 6.2. Comparison of whole pattern fitting results of E150-9h

Fitting*	Phase composition (EMT:FAU)	R_w (%)	R_{exp} (%)	a (Å)	c (Å)
a	0:100	20.6	2.0	24.97 (FAU)	
b	50:50	12.7	2.0	17.68 (EMT)	28.31 (EMT)
				25.56 (FAU)	
c	88:12	7.2	2.0	17.68 (EMT)	28.31 (EMT)
				25.43 (FAU)	
d	100:0	7.1	2.0	17.68 (EMT)	28.31 (EMT)

*See Figure 6.3.

It is worth noting that coexisting EMT and FAU could only be modeled as a physical mixture by the above fitting procedure, while in reality they often form intergrowths where boundaries between EMT and FAU domains exhibit fixed symmetry (Figure 6.1e). To account for such symmetry, the DIFFaX program was used to simulate XRD patterns of EMT-FAU intergrowths with various phase compositions, crystallite sizes and modes of intergrowth.[283] Regarding the modes of intergrowth there are two possibilities being concerned: one where intergrowth takes the form of randomly occurring stacking faults, and the other where EMT and FAU form segregated domains in individual crystallites. In Figure 6.4 simulated XRD patterns of intergrowths with randomly occurring stacking faults are reported. The most pronounced changes resulting from difference in phase composition are observed in the peaks between $2\theta = 5°$ to 7°. Specifically, the intensities of EMT (100) and (101) reflections at $2\theta = 5.9°$ and 6.6° respectively increase with EMT content significantly, while in between the abovementioned two peaks the intensity of overlapping FAU (111) and EMT (002) reflections ($2\theta = 6.1°$) decreases at the same time. Another remarkable change occurs in the EMT (103) reflection at $2\theta = 11°$, which increases in intensity with EMT content. The same trends are observed in simulation results for both bulk and nanocrystals. Note that for nanocrystals (Figure

6.4b) the EMT (101) shoulder peak only starts to develop at EMT contents higher than 80%.

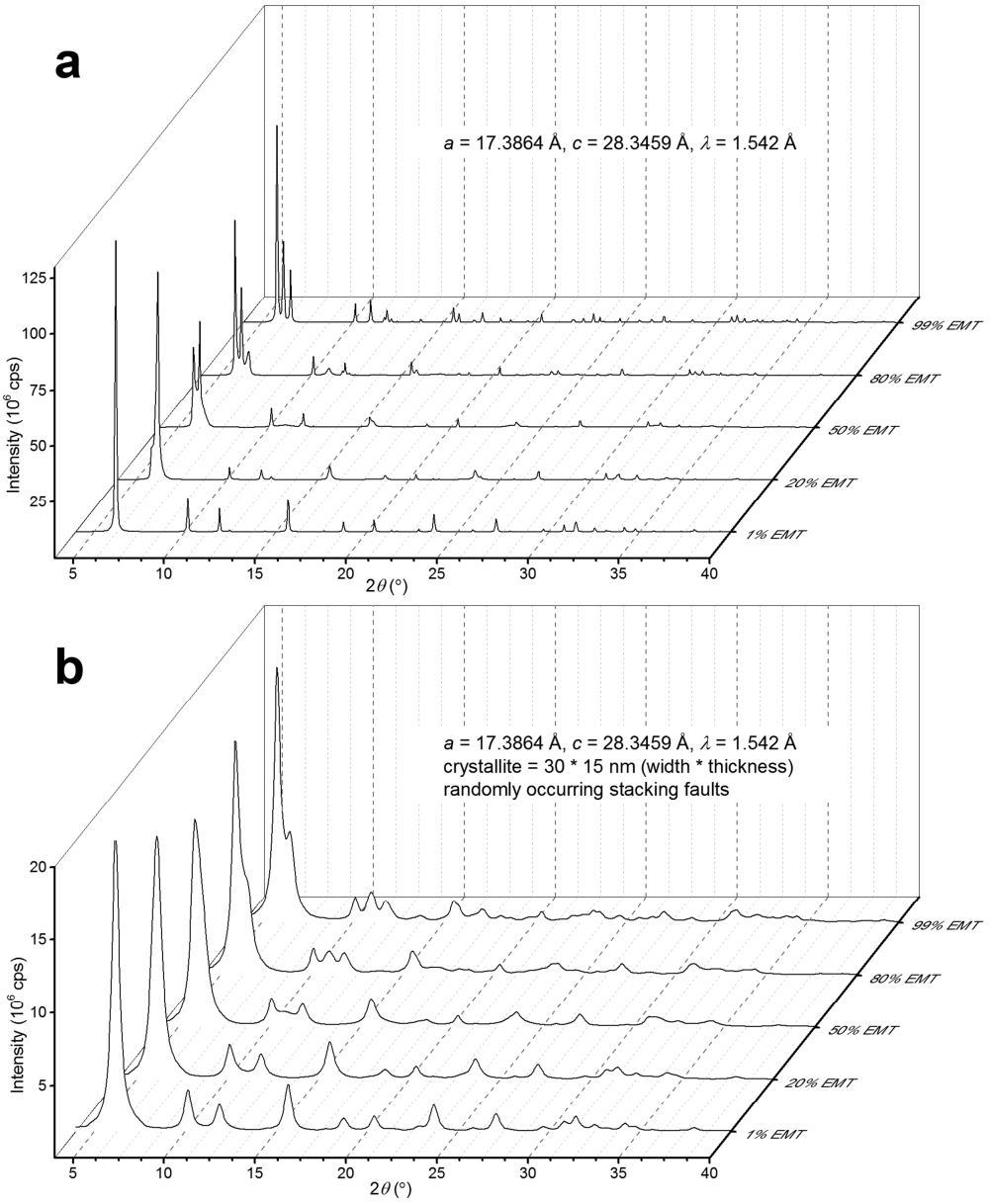

Figure 6.4. Powder XRD patterns of EMT-FAU intergrowths simulated by DIFFaX, using the same structural model and lattice parameters as those reported in literature.[279] Crystallites are assumed to be (a) infinitely large or (b) 30 nm wide and 15 nm thick according to TEM observations. EMT- and FAU-type stacking are assumed to occur randomly; probability of the occurrence of each type of stacking thus equals relative content of the corresponding phase.

However, considering the different stabilities of EMT and FAU phases, one anticipates the spatial distribution of the two phases in a zeolite crystal to be uneven. Because unsaturated coordination of surface atoms usually renders surface of a

crystal more energetic than the interior, the more stable FAU phase is probably concentrated at the surfaces of the intergrowths to minimize their overall energy. Such models were therefore built to test for possible effects of stacking sequence. As shown in Figure 6.5, simulation results from the new models present insignificant difference from the previous ones (Figure 6.4b).

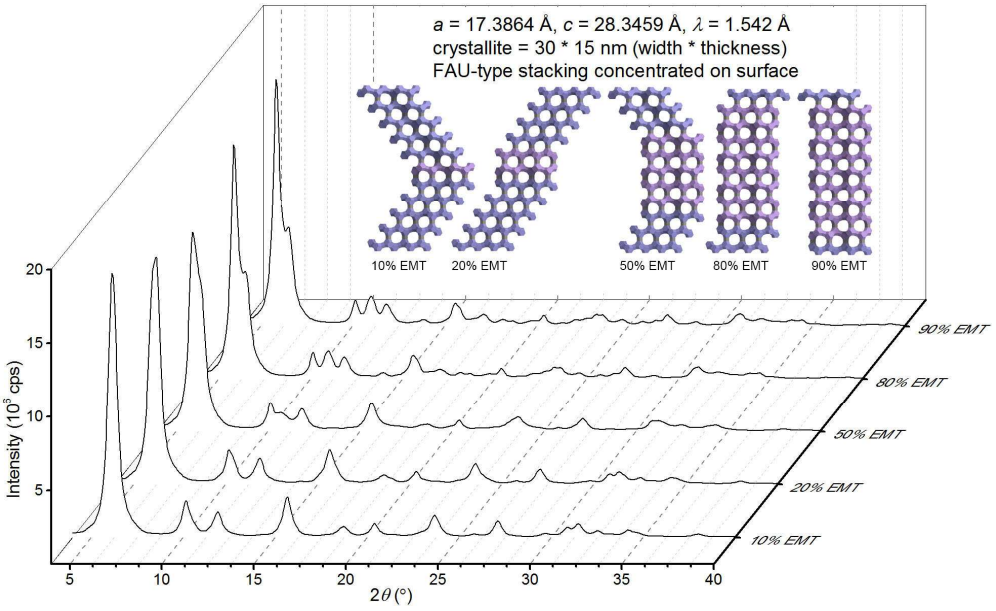

Figure 6.5. Powder XRD patterns of EMT-FAU intergrowths simulated by DIFFaX, using the same structural model and lattice parameters as those reported in literature.[279] Crystallites are assumed to be 30 nm wide and 15 nm thick. FAU-type stacking is assumed to occur only close to surface of the crystallites. Insets: stacking sequences used for the simulation.

For a better intuitive comparison, a finer series of simulated XRD patterns using lattice parameters derived from the whole pattern fitting are plotted in parallel with the experimental XRD pattern of E150-9h. Although without as good a fitting as that achieved by MAUD (Figure 6.3d), Figure 6.6 shows that E150-9h resembles more closely the simulated intergrowths with higher EMT contents (90% for example), when its well-developed shoulder peak at $2\theta = 6.6°$ is considered. On the other hand, the completely undetectable EMT (103) reflection ($2\theta = 11°$) from E150-9h cannot be explained by the current simulation where the evolutions of EMT (101) and (103) reflections follow the same trend. It may be due to crystal defects other than stacking

faults, which could not be modeled by DIFFaX. In addition, textural effects may also play a role in shaping the experimental XRD pattern, which are again not considered by DIFFaX. Nevertheless, the relative content of EMT in E150-9h can be conservatively estimated to be >80% on the basis of low-index reflections ($2\theta < 10°$), as these signals are the strongest and appear to be most sensitive to phase composition.

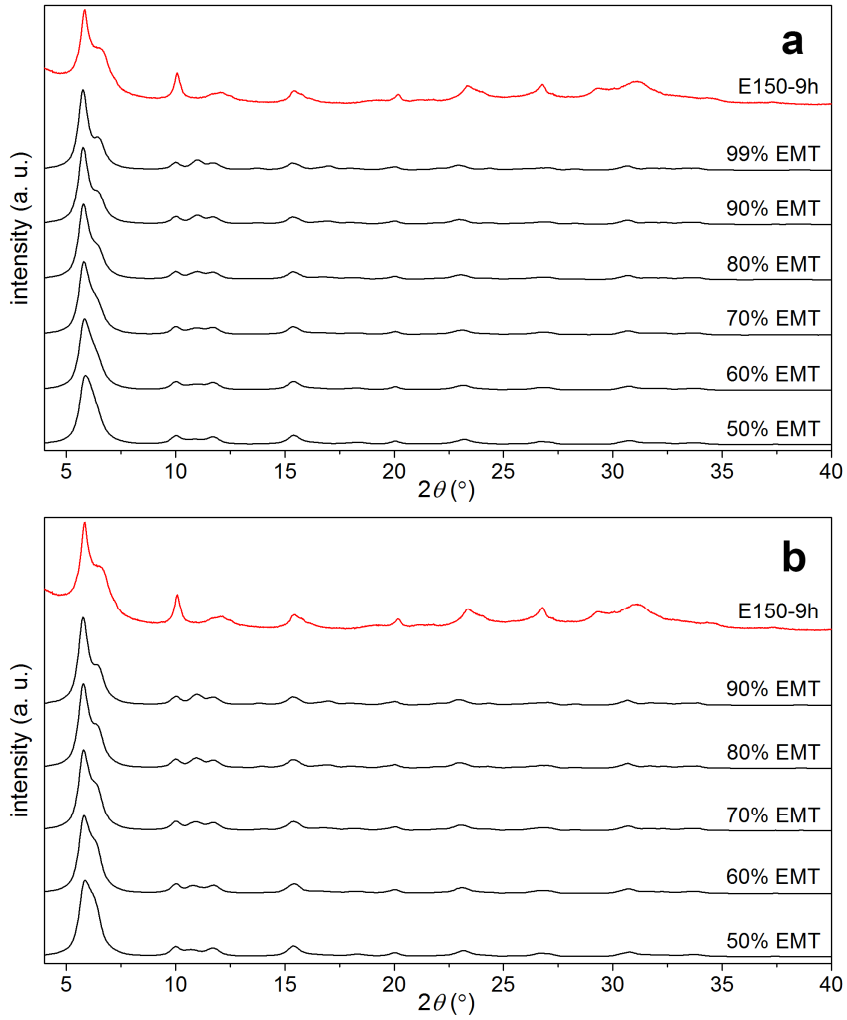

Figure 6.6. Experimentally acquired and simulated powder XRD patterns of EMT-FAU intergrowths. Occurrence of EMT- and FAU-type stacking is assumed to be (a) random and (b) segregated with FAU concentrated on surface. Instrumental broadening data and lattice parameters (a = 17.68, c = 28.31 Å) obtained from whole pattern fitting are used in the simulation. Crystallites are assumed to be 30 nm wide and 15 nm thick.

Interestingly, the XRD pattern of Ctrl-9h also exhibits some characteristics of an EMT phase (Figure 6.2a). However, crystallization of the alcohol-free gel (Ctrl) is far

from complete at this stage. FAU forms immediately as crystallization continues, which indicates its higher thermodynamic stability compared with EMT. The EMT phase thus appears to be a short-living intermediate in the growth process where no additional structural control is present.[268] In contrast, during the ethanol-assisted syntheses, the metastable EMT phase is stabilized substantially by ethanol; in the presence of enough ethanol (*e.g.* E75 and E150) no change in crystal structure is detected despite extended hydrothermal treatment (Figure 6.2c,d). Such stability is essential in practical applications, because it provides a wide-spanned time window for product of consistent quality to be recovered. On the other hand, the addition of ethanol accelerates the crystallization, affording a more efficient process. Importantly, yield of zeolite based on Al input is improved from 50% for Ctrl to 81% for E150. The increased yield is attributable to lower solubility of aluminosilicate species in the presence of ethanol.[264]

TEM images reveal that the EMT-type zeolite of E150-9h has a hierarchical structure; the rather uniform submicron particles seen in Figure 6.7a,b are assembled from single-crystals approximately an order of magnitude smaller in size, as reported in Figure 6.7c. Hexagonally packed channels are clearly visible along the ***c*** axis of the EMT-type crystallites (for example, Figure 6.7d). A majority of the crystallites are plate-like, as shown in Figure 6.7e where a crystallite is observed from perpendicular to its ***c*** axis. The hexagonal platelet shape of the E150-9h crystallites is matched by the results from whole pattern fitting (inset of Figure 6.3d). In comparison, the FAU-dominant zeolite of Ctrl-15h consists of significantly larger crystallites. Occurrence of stacking faults is extensive in this sample. Figure 6.7f gives an example of consecutive stacking faults in Ctrl-15h which form local ABAB···· stacking identical to that of EMT. It explains the detection of diffraction signals characteristic for EMT in the products from Ctrl (Figure 6.2a).

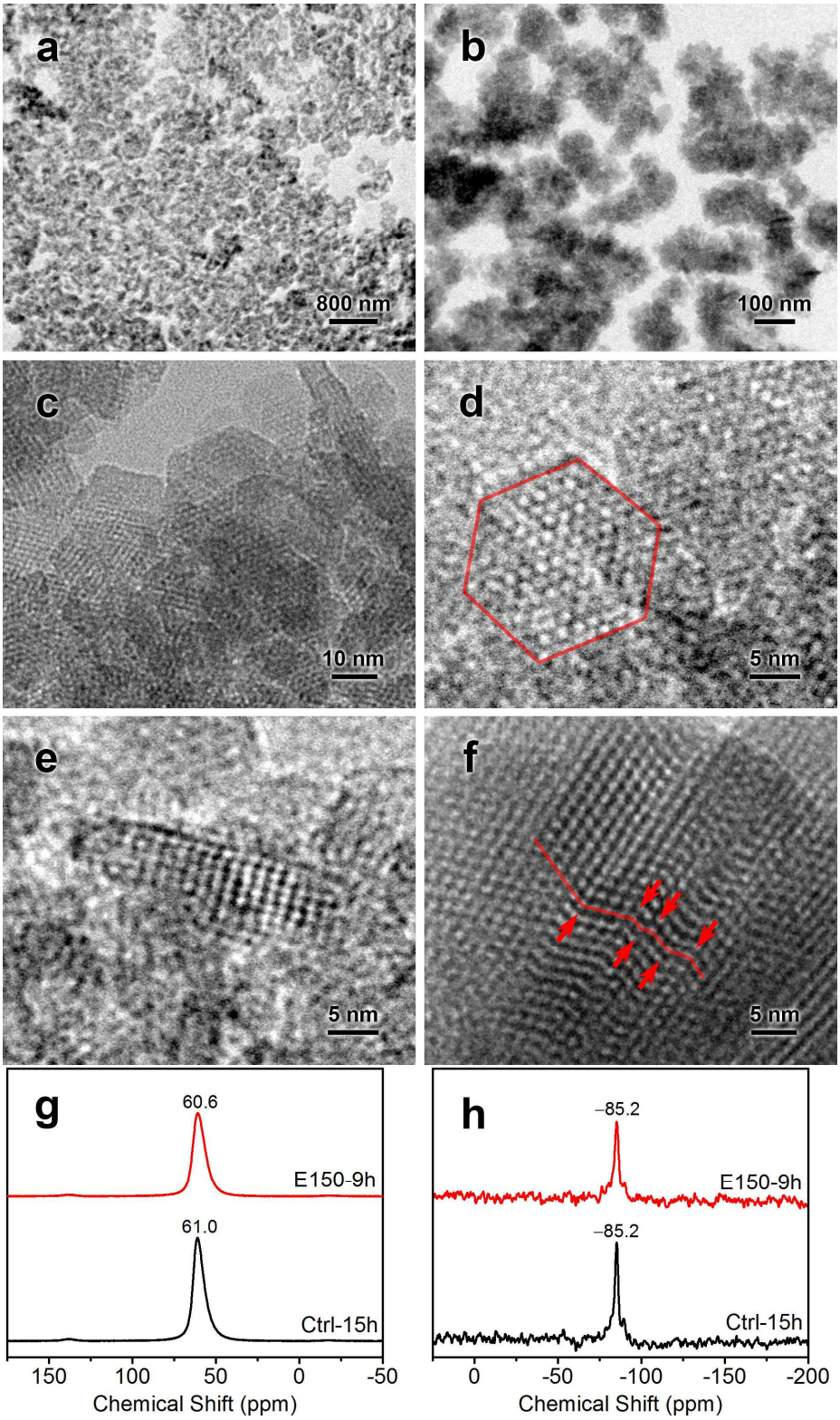

Figure 6.7. TEM images of (a–e) E150-9h and (f) Ctrl-15h. (g) ^{27}Al and (h) ^{29}Si MAS NMR spectra of the two samples. Red drawings on the TEM images are visual guides.

To understand the formation of the relatively uniform hierarchical structure of E150-9h, the morphological change of gel particles in E150 and Ctrl was investigated

by electron microscopy. Figure 6.8a,e show that in both of the gels, "seed" crystals start to appear on the surface of amorphous gel particles, indicating a heterogeneous nucleation process. Crystal growth then proceeds at the expense of the amorphous gel (Figure 6.8b,f,g). Further morphological change is insignificant after the amorphous materials are consumed completely (Figure 6.8c,d,h), which corroborate the XRD results in Figure 6.2a,e. The heterogeneous nucleation, probably occurring throughout the crystallization process, increases the possibility of stacking of individual zeolite particles and hence formation of hierarchical structures. At the same time, local fluctuation of chemical environment is likely in the highly heterogeneous systems and can induce intergrowth of EMT/FAU phases. It has been proven that even in the presence of very small amount of one phase, such intergrowth can lead to hierarchical structures.[133] The two factors discussed above are apparently independent of the presence of alcohol, and indeed the zeolite products of both E150 and Ctrl have hierarchical structures (Figure 6.8d,h). The difference, however, is that nucleation seems to be promoted significantly by ethanol and much smaller sizes of primary zeolite crystallites and hierarchical assemblages are achieved (compare Figure 6.8a,e and c,g). In addition, ethanol accelerates the crystallization, which is also important in size control of the zeolite particles. A complete TEM survey of the crystallization process of starting gels with different compositions is reported in Appendix 2.2.

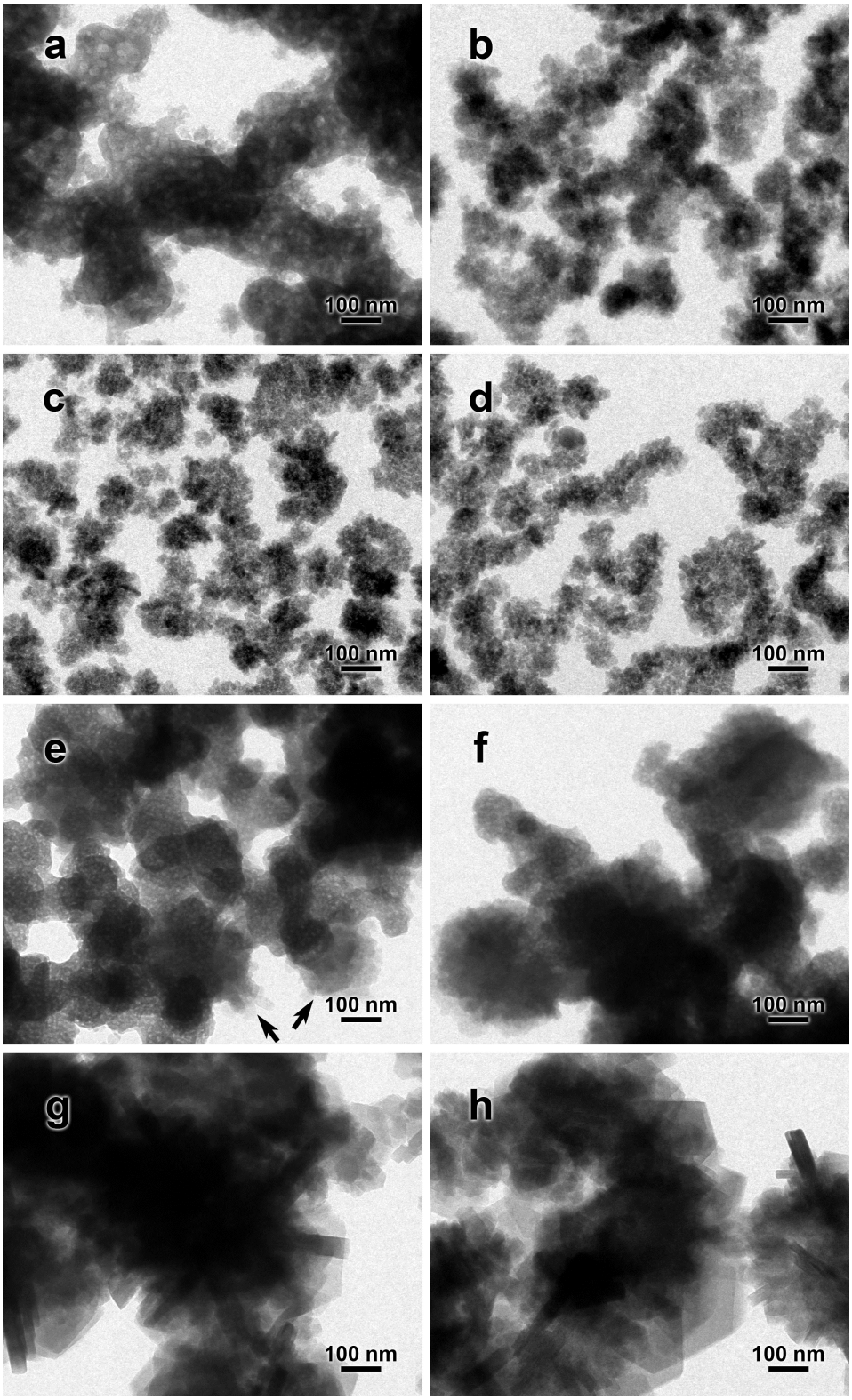

Figure 6.8. TEM images of (a) E150-5h, (b) E150-7h, (c) E150-9h, (d) E150-18h, (e) Ctrl-7h, (f) Ctrl-9h, (g) Ctrl-12h, and (h) Ctrl-18h. Arrows point to growing zeolite crystals.

In contrast to the crystallographic and morphologic differences between E150-9h and Ctrl-15h, their short-range structures (within 1–2 chemical bonds) are practically

identical according to solid-state NMR analyses (Figure 6.7g,h). In both materials, Al exists exclusively in zeolitic tetrahedral coordination centers and virtually all of the Si atoms are in $Si(OAl)_4$ sites.[284-285] The chemical environment of Si indicates Si/Al ratios of close to unity, consistent with X-ray spectroscopic results which give Si/Al = 1.17 for E150-9h and 1.15 for Ctrl-15h. The low Si/Al ratio is possibly the reason for the observation of only one type of signal from Si nuclei at different crystallographic T sites. The similarity in short-range structures (*i.e.*, basic building units) suggests that in the present system EMT/FAU polymorphism is not determined by structure of the basic building units present at the initial stage of zeolite synthesis; their assembling process where ethanol could participate is probably more important. In fact, Appendix 2 reveals that other simple alcohols including methanol, n-propanol and isopropanol also promote the crystallization of EMT. It is proposed that such an effect derives from structural changes in solvated Na^+, the template for assembling zeolite building units.

To study the solvation structure of Na^+, spin-lattice relaxation rate ($1/T_1$) of ^{23}Na in solution was measured by NMR. Table 6.3 shows significant increase in $1/T_1$ with addition of alcohols, indicating enhanced hydration of Na^+ [286-287] and/or its co-solvation by water and alcohol.[288-289] Increase in $1/T_1$ with amount of alcohols added is also evidence for more alcohol molecules participating in solvation of Na^+.[288] Since an EMT hypercage is slightly larger than an FAU supercage,[279] more strongly hydrated Na^+ with its larger effective size favors formation of EMT hypercages. On the other hand, as illustrated in Figure 6.9, partial replacement of water molecules in the solvation sphere of Na^+ with bulkier alcohol molecules results in lower symmetry, making it difficult for the solvated Na^+ to pack into the compact tetrahedral network required in FAU. Formation of EMT where additional space in adjacent hypocages can contain the asymmetry of template may then be favored. Because of their larger molecular sizes and resultant less symmetric co-solvation (Figure 6.9a), ethanol and

propanols promote the crystallization of EMT more strongly compared with methanol. As a result, with the same amount of the different alcohols added (x = 37), isopropanol leads to the fastest onset of EMT crystallization at 7 h of heating, followed by ethanol at 9 h and methanol at 12 h (Figure 6.2b,e,f). This explanation is in line with the extent of increase in $1/T_1$ caused by the alcohols (Table 6.3).

Table 6.3. Spin-lattice relaxation rate of ^{23}Na in mother liquors of zeolite syntheses

Alcohol added	x (mol alcohol / mol Al_2O_3)	$1/T_1$ (s^{-1})
None	0	45.5
Methanol	37	50.8
Ethanol	37	55.9
n-Propanol	37	55.6
Isopropanol	37	56.1
Methanol	150	69.7
Ethanol	150	85.7

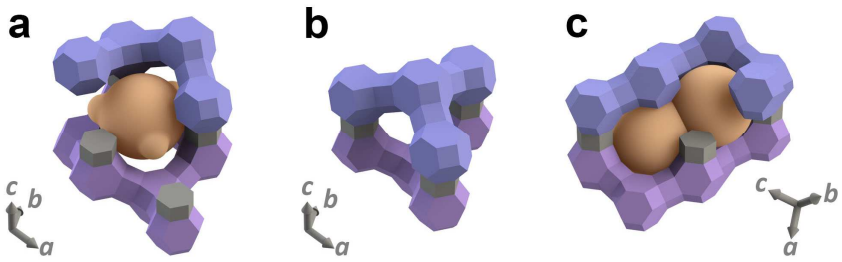

Figure 6.9. (a) Conceptual illustration of a Na^+ ion co-solvated by water and alcohol serving as template for EMT. Bulges on the solvation sphere of Na^+ depict larger size of alcohol molecules, which is accommodated by adjacent EMT hypocages shown in (b). (c) Conceptual illustration of Na^+ ions solely solvated by water as template for FAU.

Advantages of the alcohol-assisted synthesis of EMT-type zeolite are further demonstrated by its robustness against varying composition of starting gel. Figure 6.10a shows no detectable FAU-type impurity in zeolite products when the SiO_2/Al_2O_3 ratio of E150 starting gels is changed to n = 11.8–15.8, and Table 6.4 does not reflect any remarkable change in yield or Si/Al ratio of the products. The micropore volumes compare closely to published data for nano-sized EMT zeolites

(0.14–0.18 cm^3/g),[268] which confirms their crystallinity. Moreover, the products possess large surface area and mesoporosity as a result of their hierarchical structure. As reported in Figure 6.10c, size distribution of the mesopores is centered around 4–5 nm, differentiating these samples from free-standing zeolite nanoparticles that form larger mesopores upon drying.[268, 290]

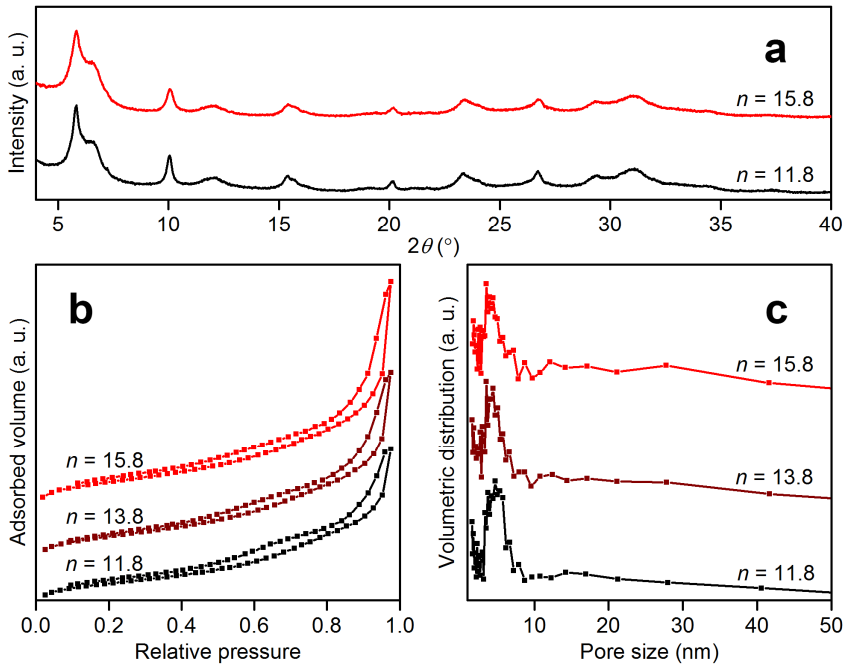

Figure 6.10. (a) Powder XRD patterns, (b) N_2 sorption isotherms and (c) Barrett-Joyner-Halenda pore size distributions of zeolites synthesized from E150 starting gels with different SiO_2/Al_2O_3 ratios (n = 11.8–15.8, 9 h of crystallization)

Table 6.4. Effects of SiO_2/Al_2O_3 ratio in E150 starting gel on properties of zeolite products

Precursor SiO_2/Al_2O_3	Product Si/Al*	Yield (%)†	S_{BET} (m^2/g)‡	V_{meso} (cm^3/g)◊	V_{micro} (cm^3/g)•
11.8	1.13	80.0	587	0.38	0.18
13.8	1.17	80.5	592	0.45	0.17
15.8	1.18	78.6	609	0.53	0.17

*determined by EDX

†based on Al input

‡specific surface area calculated by the Brunauer-Emmett-Teller (BET) method

◊mesopore volume calculated by the Barrett-Joyner-Halenda (BJH) method

•micropore volume calculated from V-t plots

The scalability and economy of the present synthetic approach have also been examined. A 10-time scaled-up synthesis process of E150-9h consistently produced >4 g of EMT-type zeolite per batch. Results in Table 6.5 and Figure 6.11a–e confirm that at yields generally exceeding 90%, these products have the same quality as that of the zeolite produced in the small scale. Their hierarchical structure promotes sedimentation and facilitates separation, which is evident in Figure 6.11f. After separation of product, >90% of ethanol fed to the scaled-up synthesis was recovered through fractional distillation. Importantly, the recycled ethanol and mother liquor can be used for further production of zeolites with consistent yield and quality. The recycling renders the process highly efficient in terms of materials utilization, and minimizes its environmental impact by dramatically reducing release of alkaline wastes.

Table 6.5. Results of scaled-up synthesis of hierarchical EMT-type zeolite

Synthesis cycle	Product Si/Al*	Yield (%)[†]	Ethanol recovery (%)	Concentration of recycled ethanol (wt %)
Cycle 1, run 1	1.19	88	92	92
Cycle 2, run 1	1.15	97	N. A.[‡]	N. A.
Cycle 1, run 2	1.18	94	91	92
Cycle 2, run 2	1.17	92	N. A.	N. A.

*determined by EDX

[†]based on Al input

[‡]not applicable

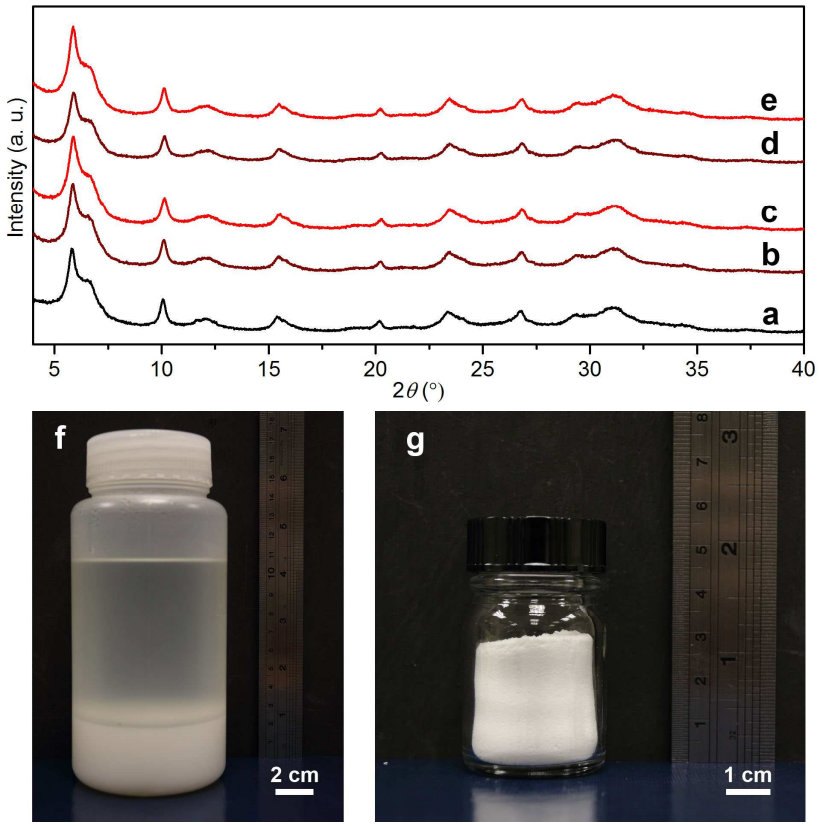

Figure 6.11. (a–e) Powder XRD pattern of (a) E150-9h synthesized in the small scale compared with those of products synthesized in the large scale: (b) synthesis cycle 1 of run 1, (c) synthesis cycle 2 of run 1, (d) synthesis cycle 1 of run 2, and (e) synthesis cycle 2 of run 2. (f) Photograph of a synthesis gel after complete crystallization in the scaled-up process. (g) Photograph of EMT-type zeolite produced in one batch (4 g in mass) in the scaled-up process.

6.3.2. Catalyst preparation and evaluation

Wet impregnation of the zeolites with ammoniac solutions of $PtCl_2$ (and Na_2CO_3 in some cases) results in highly dispersed Pt and Na species; the XRD patterns of the as-synthesized catalysts in Figure 6.12 show no signals of additional crystalline phases other than the support materials. At the same time, certain extent of amorphization of the EMT-type zeolite is observed when Na_2CO_3 is co-impregnated. Sensitivity of low-silica zeolites to degradation is well-recognized, and in this case the degradation is accelerated by the large surface area and higher pH in the presence of CO_3^{2-}.[291] Amorphization of the EMT-type zeolite is unnoticeable in the absence of Na_2CO_3.

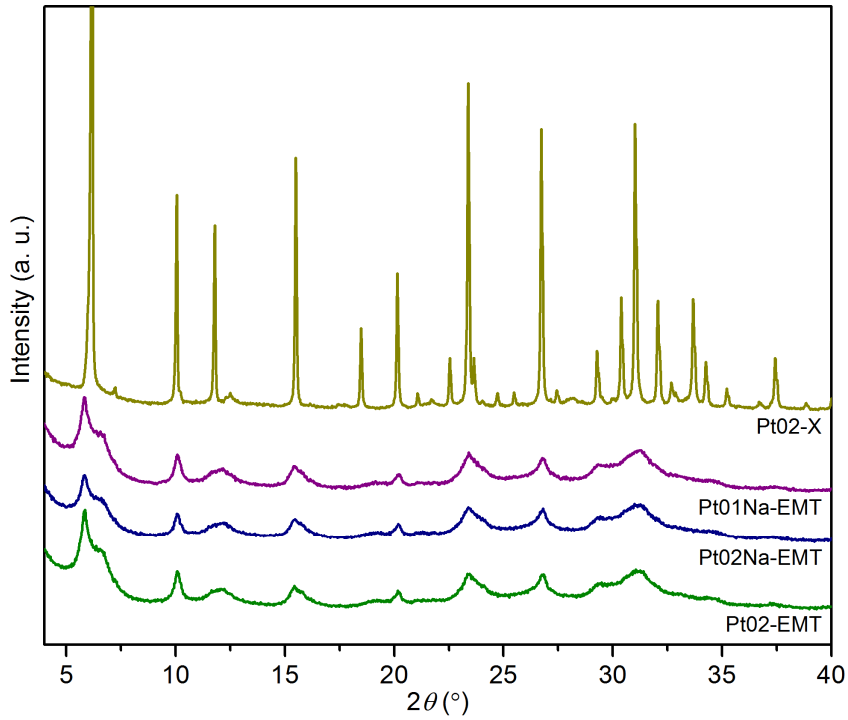

Figure 6.12. Powder XRD patterns of as-synthesized catalysts. The strongest peak of Pt02-X is truncated for clear presentation of other peaks.

The XRD results about stability of the EMT-type zeolite during impregnation are confirmed by N_2 sorption characterization, the results of which are summarized in Table 6.6. Compared with the pristine support material (Table 6.4), Pt02-EMT possesses similar specific surface area and micropore volume which indicates negligible amorphization. The decreased surface area and pore volume of Pt01Na-EMT and Pt02Na-EMT also correspond well to the trend observed in the XRD results.

Table 6.6. Composition and textural properties of as-synthesized catalysts

Catalyst	Pt content (wt %)*	S_{BET} (m^2/g)	S_{ext} (m^2/g)†	V_{meso} (cm^3/g)	V_{micro} (cm^3/g)
Pt01Na-EMT	0.93	524	175	0.32	0.15
Pt02Na-EMT	1.91	449	121	0.31	0.13
Pt02-EMT	2.05	611	191	0.38	0.17
Pt02-X	1.83	588	25	0.03	0.23

*determined by ICP-OES

†external surface area calculated by combination of BET method and V-t plots

At 1 atm and 240–280 °C, all of the catalysts convert CO_2 to CO with 100% selectivity. Their activity, however, differs greatly. As shown in Table 6.7 and Figure 6.13a, the catalysts supported on hierarchical EMT-type zeolite are in general 2.5–8 times more efficient than that supported on commercial zeolite X, in terms of activity normalized by Pt content. Beneficial effects of decreased Pt loading and co-impregnated Na are also clearly observed. From the Arrhenius-type plots in Figure 6.13b, similar activation energies of 59.7±1.6 kJ/mol are measured for CO_2 hydrogenation as reported in Table 6.7 (CO_2 conversion <10% except for Pt02Na-EMT at 280 °C where it is 11.1%, but inclusion of this data point has minimal effect on the result). The activation energy is remarkably lower than that of alkali-free Pt catalysts in RWGS (82 kJ/mol)[292] and closer to that of Na-promoted counterparts measured in WGS reaction (65 kJ/mol).[293] It is most likely that the same type of active site, *i.e.* Na-stabilized Pt–OH_x, is responsible for the activity of the four catalysts, and the difference in activity should be attributed to different densities of available active sites. The dispersion of Pt and interaction between Na and Pt which determine the amount of active sites will hence be investigated.

Table 6.7. Catalytic properties and post-reaction characterization of catalysts

Catalyst	TOF×10^3 (s^{-1})*	E_a (kJ/mol)†	Primary Pt crystalline size (nm)‡	Surface Pt concentration (wt %)◊	Surface Na/Pt (mol/mol)◊
Pt01Na-EMT	40.2	58.8±1.3	10	0.6	203
Pt02Na-EMT	25.2	58.1±1.2	14	0.8	167
Pt02-EMT	14.5	61.3±1.7	13	0.8	145
Pt02-X	5.2	58.6±1.6	36	7.3	10.2

*turnover frequency measured at 280 °C at the end of stability test, defined as moles of CO_2 converted per mole of total Pt content per second

†apparent activation energy measured at 240–280 °C, with 95% confidence level

‡calculated from broadening of Pt (111) peak in XRD patterns

◊measured by XPS

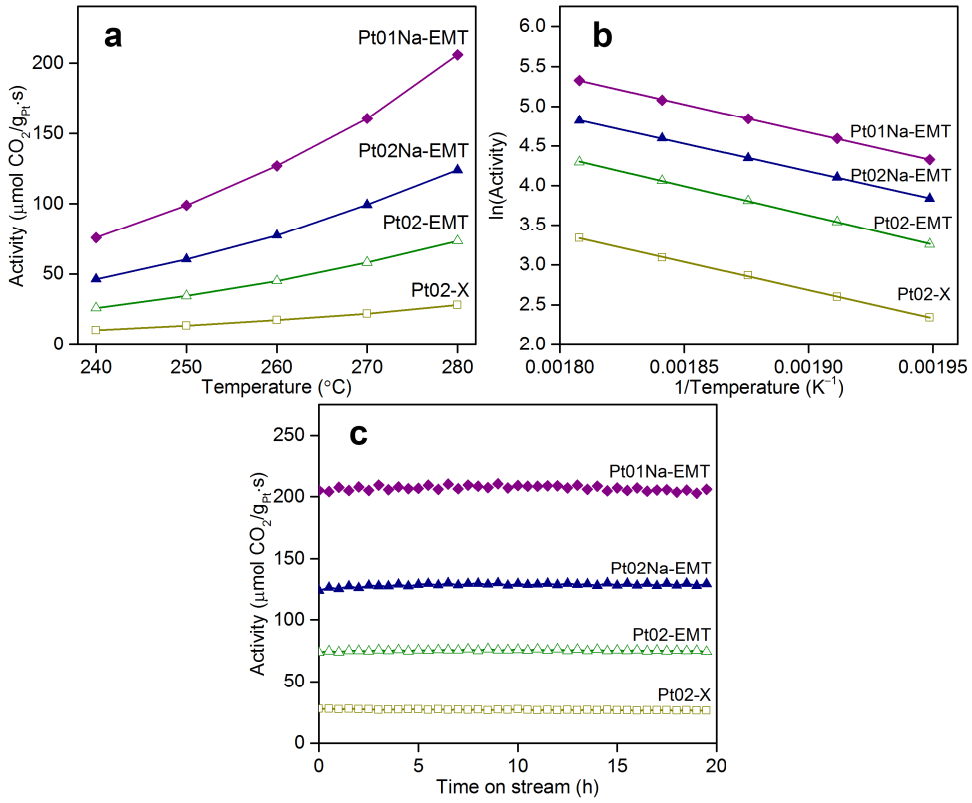

Figure 6.13. (a) Normalized CO_2 hydrogenation activity, (b) Arrhenius-type plots, and (c) stability of the catalysts. Selectivity of CO formation was 100% in all experiments.

As an indicator of metal dispersion, size of primary Pt crystallites in spent catalysts was calculated from XRD patterns presented in Figure 6.14. The results in Table 6.7 show smaller crystallite size of Pt on the EMT-type support compared with that on the commercial zeolite X, suggesting higher metal dispersion in the EMT-supported catalysts. The advantage can be related to the larger external surface area and mesopore volume of the EMT-supported catalysts (see Table 6.6); farther separation of individual Pt nanoparticles is possible in such conditions, which inhibits sintering and hence particle growth during activation of the catalysts.[261] For the same reason, Pt01Na-EMT has higher metal dispersion than Pt02Na-EMT because a lower Pt loading can also lead to longer inter-particle distance. The effects of textural properties of catalyst support are further revealed by comparison between bulk content (Table 6.6) and surface concentration of Pt (Table 6.7). The surface concentration is calculated using Equation 1 where w_{Pt} stands for surface mass

fraction of Pt, M_i for atomic weight of element i, A_i for area under the peak of element i measured by XPS, RSF_i for the corresponding molar relative sensitivity factor, and i = Pt, O, Na, Al, Si:

$$w_{Pt} = M_{Pt}A_{Pt}/RSF_{Pt}\Sigma(M_iA_i/RSF_i) \quad (1)$$

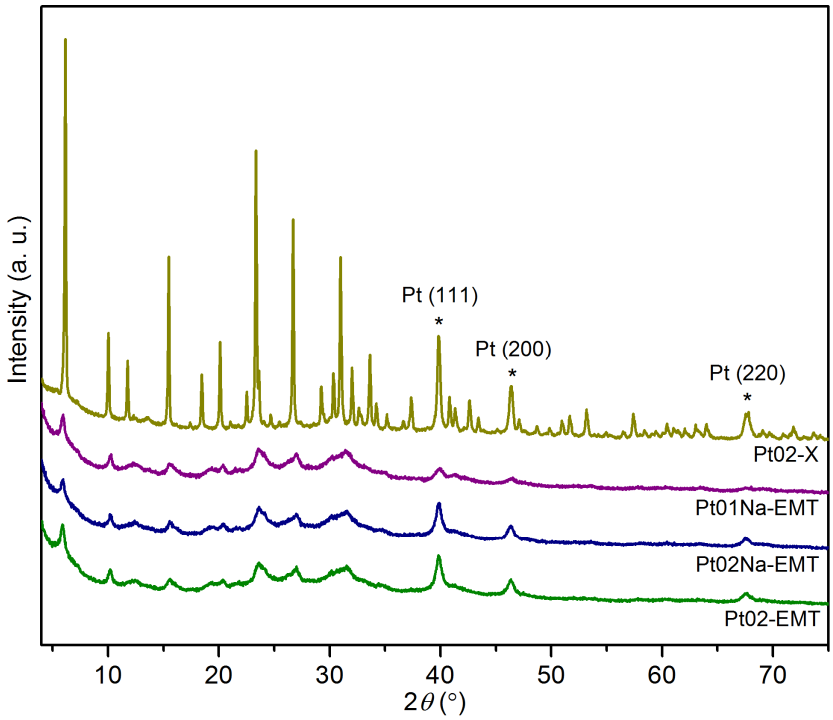

Figure 6.14. Powder XRD patterns of spent catalysts.

The surface Pt concentration of Pt02-X is 4 times that in the bulk. In view of the short analysis depth of XPS (generally <10 nm) and large size of Pt crystallites in Pt02-X, the actual amount of Pt on the surface may be even higher. In contrast, surface concentration of Pt seems to be lower than in the bulk for the EMT-supported catalysts. While the effect of limited analysis depth on the XPS characterization still cannot be ignored in these cases, less underestimation of surface Pt content is expected due to the relatively smaller sizes of Pt particles. It can thus be concluded that surface enrichment of Pt is less on the EMT-type support compared with commercial zeolite X; instead, significant amount of Pt is probably accommodated by the pores within the submicron assemblages of EMT crystals where XPS analysis

cannot reach. The negligible difference in the micropore volumes of Pt02Na-EMT and pristine support material suggests that the XPS-invisible Pt particles are located in mesopores.

Electron microscopic examination of the spent catalysts in Figure 6.15 confirms the different distribution of Pt particles: they are concentrated on the outer surface of the commercial zeolite X particles, but evenly spread across the entire volume of the hierarchical EMT-type zeolites. In all of the catalysts Pt particles with sizes of 2–3 nm are found much more numerous than the larger ones detected by XRD, and are probably responsible for the major part of catalytic activity. The larger number of such Pt nanoparticles in the EMT-supported catalysts should therefore be an important factor in their high activity (compare Figure 6.15b,d,f with h).

On the other hand, correlation between surface Na/Pt ratio and activity of the catalysts cannot be neglected (Table 6.7). The relation is most obvious when Pt02Na-EMT and Pt02-EMT are compared, since the former has no apparent advantage in terms of metal dispersion and textural properties. It has been reported that Na forms Na–O–Pt structures in active water gas shift catalysts and appears at a binding energy (B.E.) of *ca.* 1072 eV in Na 1*s* XPS spectra.[294] Indeed, a Na 1*s* peak at B.E. = 1072.1 eV is found for Pt02-X and Pt02-EMT as shown in Figure 6.16a. Co-impregnation of Na_2CO_3 leads to a convoluted peak centered at 1071.8 eV, presumably due to contribution of signals from Na_2CO_3 at B.E. = 1071.5 eV and/or $NaHCO_3$ at B.E. = 1071.3 eV.[295] However, in the present work quantification of Na–O–Pt species is complicated by the close B.E. of the abovementioned species, and more importantly by the presence of abundant zeolitic Na which has 1*s* B.E. values also around 1072 eV.[296] Nevertheless, the detection of excess Na_2CO_3 or $NaHCO_3$ in Pt01Na-EMT and Pt02Na-EMT suggests saturation of Pt surface with Na, which serves as an indirect evidence of higher surface coverage of Na–O–Pt in these catalysts. In addition, a

weak shoulder at B.E. = 1073.3 eV is detected in all of the Na 1*s* spectra, which is attributed to NaO_xC_y species.[297]

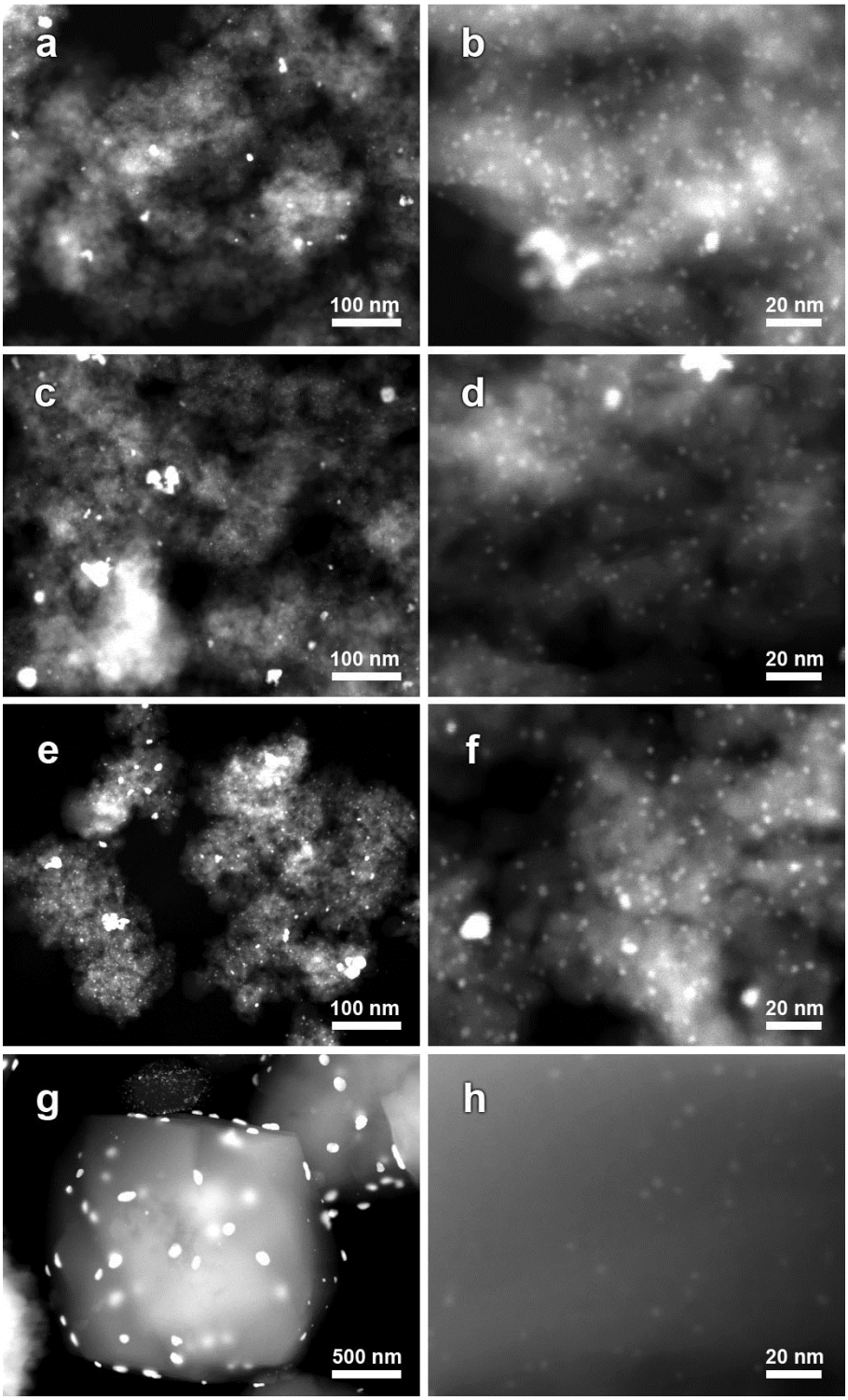

Figure 6.15. HAADF images of spent catalysts: (a,b) Pt01Na-EMT, (c,d) Pt02Na-EMT, (e,f) Pt02-EMT, and (g,h) Pt02-X.

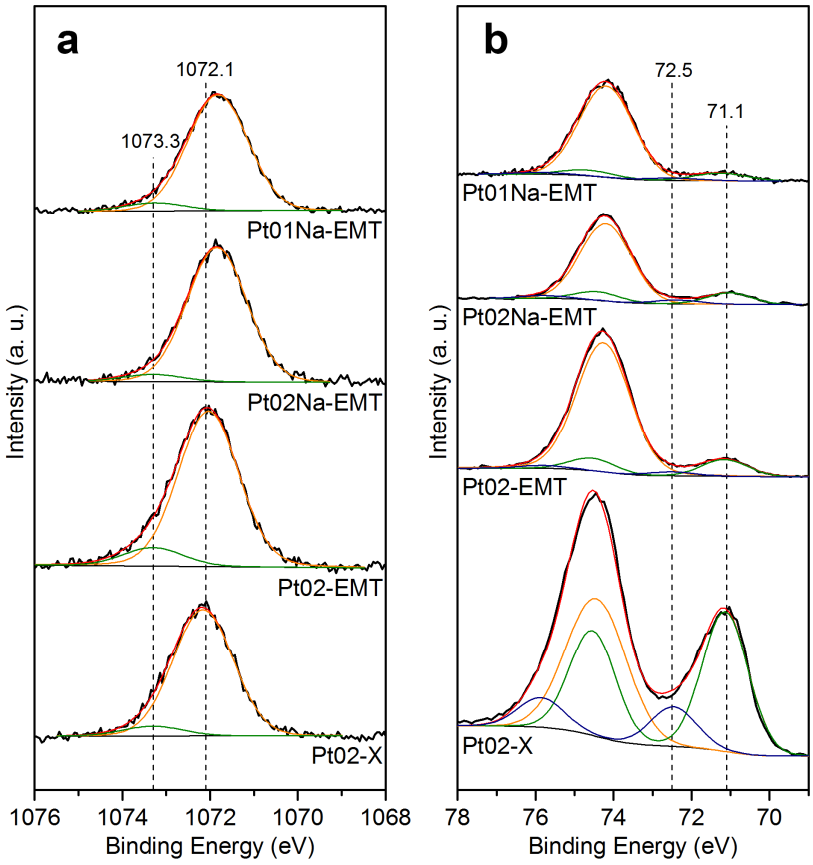

Figure 6.16. Deconvolution of XPS spectra for (a) Na 1*s* and (b) Pt 4*f* / Al 2*p* of spent catalysts.

From the Pt 4*f* XPS spectra in Figure 6.16b, coexistence of Pt(0) and Pt(II) which have B.E. of 71.1 and 72.5 eV respectively is identified in all of the catalysts (Al 2*p* signals at a B.E. of *ca.* 74.3 eV overlap with Pt $4f_{5/2}$, and deconvolution was achieved by setting Pt 4*f* spin-orbit splitting to be 3.4 eV).[295] The fraction of Pt(II) among total amount of Pt species detected by XPS increases from 19% in Pt02-EMT to 25% in Pt02Na-EMT as a result of stabilization effects of Na on Pt(II) complexes.[272]

Finally, high stability of the catalysts is demonstrated in Figure 6.13c. At 280 °C, no decrease in activity was detected for the EMT-supported catalysts and the activity of Pt02-X decreased marginally by 4.5% over a 20 h period. The activity is apparently not affected by change in crystallinity of the support material as is evident in a comparison between Figure 6.12 and Figure 6.14. It indicates that the active sites are located on the exterior of the zeolite particles, and in turn corroborates the

advantage of the EMT-type support to be large external surface area and high mesoporosity which result from its hierarchical structure.

6.4. Conclusions

A robust and sustainable method of synthesizing hierarchical EMT-type zeolite without conventional OSDAs has been successfully developed. The present approach to the control of zeolite polymorphism exploits the ubiquitous phenomenon of sodium ion solvation with water and alcohol molecules. This unconventional template-based method may be extendable to syntheses of other types of zeolites in future, and in the meanwhile provides a different perspective on the understanding of formation of zeolitic materials. While higher Si/Al ratios remain to be desired for application in a wider spectrum of catalytic reactions, it has been shown that highly selective and stable Pt catalysts for RWGS can be prepared using the low-silica EMT-type zeolite as support material. Its hierarchical structure leads to significant advantages over commercial zeolite X in terms of metal utilization, and the low cost makes it a more economical choice than reducible supports such as CeO_2 and TiO_2. The present work thus demonstrates considerable potential of the hierarchical EMT-type zeolite for practical applications.

Chapter 7. Integration of Porous Cu/Zn Silicate Assemblages with ZSM-5 Nanocrystals for Direct Dimethyl Ether Synthesis from CO_2/H_2

7.1. Introduction

In Chapter 4, it has been demonstrated that phyllosilicates can be synthesized in highly porous, ordered forms. Compared with amorphous silica/aluminosilicates, their well-defined crystallographic structure provides basis for the accommodation of large amount of metal elements and hence activity in a wider range of reactions such as catalytic hydrogenation of CO_2. However, the synthesis of these metal silicates and another important group of crystalline silicates, zeolites, requires harsh conditions (*e.g.* hydrothermal treatment) that are unnecessary in the sol-gel processing of amorphous silica/aluminosilicates.[63, 102] Although not an issue in the study of single-phase materials, the harsh synthesis environment creates significant challenges in the construction of multi-phase, multi-functional nanostructures which has been an increasingly popular field of research; once exposed to such synthesis conditions, unstable component materials cannot be preserved and choice of materials for direct integration into complex structures are very limited. For example, while it is relatively common to deposit mesoporous amorphous silica on various stable and unstable materials, integration of hydrothermally grown phyllosilicates has only been successful with robust Fe_3O_4 and noble metals.[49, 54-56, 298]

To tackle the issue of stability during synthesis of composite materials, a protective layer can be introduced onto the unstable phase. Apparently, the choice of material for the protective layer is important to the success of this strategy; it should

(i) be synthesized in mild conditions, (ii) closely conform to the outline of the protected phase, (iii) be chemically and structurally resistant, and (iv) be easily removable. Resorcinol-formaldehyde resin (RF), for example, is a good candidate. It is a thermosetting polymer with excellent stability, and can be synthesized at low temperature by condensation of resorcinol and formaldehyde in weakly alkaline conditions.[299] Preparation of RF coatings with homogeneous and tunable thickness on nanomaterials has been reported,[300-302] and being composed of only C, H, and O, RF can be completely removed by calcination. However, in the field of materials chemistry, RF has been mainly used as a precursor for pyrolytic carbon with its application in the construction of composite nanomaterials largely ignored.[3, 303-304]

In this work, a method of integrating zeolite nanocrystals in hydrothermally synthesized, porous transition metal silicates is developed for the first time using RF as a protective spacer. The zeolite of interest, ZSM-5, has been one of the most extensively studied zeolites in nanometer-sized forms.[105-106, 131, 305-306] It has been shown to catalyze the dehydration of methanol into dimethyl ether (DME) and the methanol-to-olefin (MTO) reaction.[173, 307-308] The combination of ZSM-5 with a methanol synthesis catalyst therefore provides a possible route for direct production of DME and olefins from syngas or CO_2/H_2 mixture. Indeed, hybrids of ZSM-5 and other zeolites with conventional metal oxide-based methanol synthesis catalysts have been studied for such purposes with positive results.[178, 309-312] It is thus interesting to explore the composite system consisting of ZSM-5 and Cu/Zn silicate nanostructures that are also active in the methanol synthesis reaction. Bringing methanol synthesis and conversion catalysts into intimate proximity by structural integration improves mass transfer between the two catalysts. As synthesis of methanol from CO_2 is thermodynamically more limited than its subsequent conversion to hydrocarbons, the integration may break chemical equilibrium on the methanol synthesis catalyst in high-conversion conditions and enhance overall performance.

7.2. Experimental Section

7.2.1. Chemicals and reagents

Tetraethyl orthosilicate (TEOS), cetyltrimethylammonium bromide (CTAB), poly(diallyldimethylammonium) chloride solution (PDDA, 20%), aluminum triisopropoxide (ATIP), resorcinol, formaldehyde solution (HCHO, 37%), and zinc nitrate [$Zn(NO_3)_2 \cdot 6H_2O$] from Sigma-Aldrich, tetra-n-propylammonium hydroxide solution (TPAOH, 40%) and ZSM-5 zeolite (NH_4-type, Si/Al = 80) form Alfa Aesar, copper nitrate [$Cu(NO_3)_2 \cdot 3H_2O$], sodium hydroxide (NaOH), and ammonia solution (25%) from Merck, and ethanol (EtOH) from Fisher Scientific were used as received without further purification. Deionized water was used throughout the work.

7.2.2. Synthesis of ZSM-5 nanocrystals

ZSM-5 nanocrystals with a Si/Al ratio of 56 were synthesized using a modified version of a reported method.[131] 60 mg of ATIP was first dispersed with 6.25 g of TEOS by stirring for 20 min. A mixture of 30 mg of 50% NaOH solution, 4.58 g of 40% TPAOH solution, and 2.65 g of water was then added to the organic phase. After being stirred overnight at room temperature, the zeolite precursor having the composition of $60SiO_2$–$0.3Al_2O_3$–18TPAOH–0.75NaOH–$600H_2O$–240EtOH was sealed in a 30 mL Teflon-lined stainless steel autoclave and kept in an electrically heated oven at 120 °C for 48 h. The autoclave was cooled naturally and the zeolite product was separated by 3 cycles of centrifugation and wash with water.

7.2.3. Coating of ZSM-5 nanocrystals with RF resin

The as-synthesized ZSM-5 nanocrystals were dispersed in 20 mL of 2% PDDA solution and stirred at room temperature for 2 h. The treated ZSM-5 particles were separated by 2 cycles of centrifugation and wash with water. The washed particles were then dispersed in water at a concentration of 80 mg/mL based on calcined

weight of the zeolite. 1 mL of such suspension was diluted with 4 mL of ethanol and 10 mL water, in which 55 mg of resorcinol and 150 μL of 5% NH_3 solution were dissolved. The mixture was stirred for 20 min before addition of 70 μL of 37% HCHO solution, aging at room temperature overnight, and curing in an oven electrically heated at 60 °C for 2 h. The resultant precipitate was separated by centrifugation and washed with ethanol. It was finally dispersed in 10 mL of ethanol so that the zeolite content was 8 mg/mL. The product is denoted by nZ@RF.

7.2.4. Coating of commercial ZSM-5 with RF resin

100 mg of commercial ZSM-5 was dispersed in 5 mL of 4% PDDA solution and stirred at room temperature for 2 h before being separated by 2 cycles of centrifugation and wash with water. The particles were dispersed in a solution containing 11 mL of water, 4 mL of ethanol, 55 mg of resorcinol and 150 μL of 5% NH_3 solution. After 20 min of stirring, 70 μL of 37% HCHO solution was added and stirring was continued at room temperature overnight. Curing was then performed in an oven electrically heated at 60 °C for 2 h. Finally, the precipitate was separated by centrifugation, washed with ethanol and dispersed in 12.5 mL of ethanol to achieve a zeolite content of 8 mg/mL. The product is denoted by cZ@RF.

7.2.5. Coating of ZSM-5@RF particles with mesoporous silica

2–4 mL of the ethanol suspension of either the nZ@RF or the cZ@RF particles was diluted with ethanol to a total volume of 8 mL. 100 mg of CTAB and 120 μL of TEOS was dissolved in the suspension by 10 min of stirring. 9 mL of water and 100 μL of 25% NH_3 solution were then added, followed by vigorous stirring at room temperature overnight. The product was separated by centrifugation and washed with ethanol for 3 times before being dried at 60 °C. Depending on the amount of particles added, the product is denoted by 2nZ@RF@mSiO_2 (synthesized from 2 mL of

nZ@RF), 4nZ@RF@$mSiO_2$ (4 mL of nZ@RF), or 4cZ@RF@$mSiO_2$ (4 mL of cZSM-5@RF).

7.2.6. Conversion of silica to Cu/Zn silicate

The double-coated sample was dispersed in 10 mL of water, to which 0.75 mL of 1 mol/L $Cu(NO_3)_2$ solution, 0.1 mL of 1 mol/L $Zn(NO_3)_2$ solution, and 1 mL of 25% NH_3 solution were added. The mixture was sealed in a 30 mL Teflon-lined stainless steel autoclave and kept in an electrically heated oven at 150 °C for 4 h. The autoclave was cooled naturally and the product was separated by 3 cycles of centrifugation and wash with water. Drying of the product was carried out at 60 °C. The product is named 2nZ@RF@CZS, 4nZ@RF@CZS, or 4cZ@RF@CZS according to the precursor particles used.

7.2.7. Calcination of samples

The as-synthesized ZSM-5 nanocrystals and ZSM-5@RF@CZS composites were calcined in static air using a muffle furnace. The temperature was increased from room temperature to 500 °C at 2 °C/min, and kept at 500 °C for 4 h before the samples were cooled down naturally. The calcined composites are denoted by 2nZ@CZS-2, 4nZ@CZS and 4cZ@CZS.

7.2.8. Evaluation of catalysts

200 mg of catalyst was loaded into a 3/8" stainless steel reactor to form a fixed bed. Details about the reactor set-up can be found in Section 3.9. The catalyst was activated *in situ* in a 50 mL/min flow of 10% H_2/N_2 at 1 atm, 260 °C for 4 h (heating rate = 2 °C/min). The feed gas was then switched to a 3:1 H_2/CO_2 mixture containing 4% of N_2 as internal standard. The flow rate was kept at 32 std mL/min and the pressure was increased to 30 bar. The effluent was sampled and analyzed by an automated GC.

7.2.9. Materials characterization

In this work, charge reference for XPS analysis was made to the 1*s* binding energy of C bonded only to C and H at 284.8 eV. Samples were outgassed in vacuum at 225 °C for 4 h before N_2 sorption experiments.

7.3. Results and Discussion

7.3.1. Synthesis of ZSM-5 nanocrystals

During the preparation of the precursor mixture for zeolite synthesis, TEOS hydrolyzed in the highly alkaline condition created by TPAOH to form a visibly cloudy colloid. After 48 h of hydrothermal treatment a stable colloid of ZSM-5 nanocrystals was obtained with a SiO_2-based yield of 87%. The product was easily dispersed in water or ethanol. TEM results in Figure 7.1a show that the particles have slab-like shapes with sizes of 50–200 nm. At higher magnification, lattice fringes extending through the entire particle are clearly observed, indicating the single-crystal nature of the particles. For example, the fringes shown in Figure 7.1b are 1.0 nm apart from each other, which corresponds to the (200) spacing of MFI-type framework.[278] Intergrowth is not found among the nanocrystals examined. Powder XRD pattern of the as-synthesized particles matches closely the Powder Diffraction File #42-0023 of the International Centre for Diffraction Data (orthorhombic ZSM-5, a=20.022, b=19.899, c=13.383 Å) as presented in Figure 7.1c. After calcination at 500 °C to remove the organic template, the crystallinity of the zeolite nanocrystals was not affected.

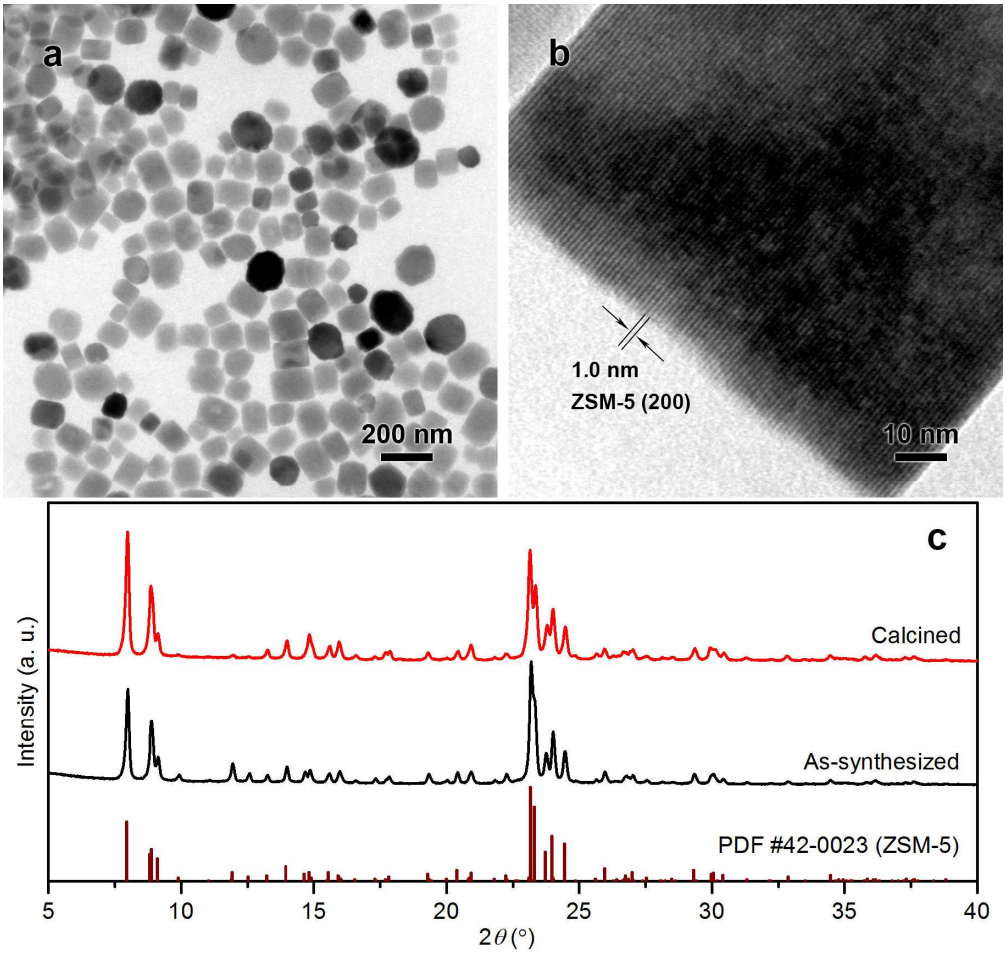

Figure 7.1. (a,b) TEM images of as-synthesized ZSM-5 nanocrystals and (c) powder XRD patterns of the as-synthesized and calcined ZSM-5 nanocrystals compared with the PDF card of ZSM-5.

7.3.2. RF resin and mesoporous silica coating

In alkaline environments where RF resin is synthesized, the surfaces of both the zeolite and the RF resin are negatively charged.[302, 313] The coulombic repulsion prevents strong bonding of RF coating with the zeolite and decreases its protective effect. However, by modifying the zeolite surface with the cationic polymer PDDA which renders it positively charged,[10] a dense and even RF coating is achieved as shown in Figure 7.2a,b. The thickness of the RF coating on the ZSM-5 nanocrystals and commercial ZSM-5 is 20 nm and 70–180 nm, respectively. Considering the fact that a lower RF/zeolite ratio was used in coating the commercial ZSM-5 (5 mmol of resorcinol per gram of zeolite for cZ@RF *versus* 6.25 mmol/g for nZ@RF), the

thicker RF layer is apparently a result of the much smaller external surface area of the micrometer-sized commercial ZSM-5.

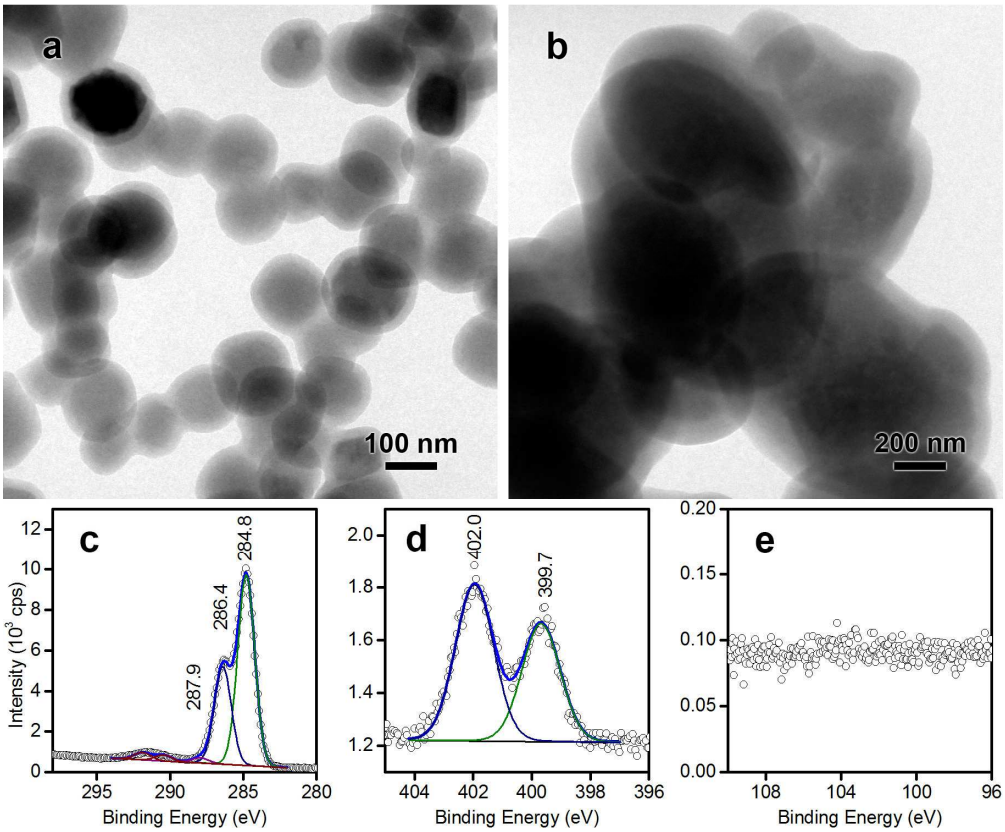

Figure 7.2. TEM images of (a) nZ@RF and (b) cZ@RF samples, and XPS spectra of nZ@RF: (c) C 1*s*, (d) N 1*s*, and (e) Si 2*p*.

The quality of RF coating on the ZSM-5 nanocrystals was further examined by XPS. The C 1*s* spectrum in Figure 7.2c indicates the presence of three types of C atoms in a typical RF resin.[314] The peak at the binding energy (B. E.) of 284.8 eV can be assigned to C atoms bonded with C and H only, including those in benzene rings and in methylene bridges. The signal of C–O (*i.e.*, C atoms at O-substituted positions in the benzene ring and in ether bridges) appears at the B. E. of 286.4 eV. A weak peak at B. E. = 287.9 eV can also be resolved which corresponds to carbonyl groups, indicating a low degree of oxidation of resorcinol. In addition, satellite peaks at higher B. E. due to the delocalized π bond in benzene rings are observed.[315] Figure 7.2d shows two types of N atoms: a positively charged quaternary ammonium type at the B. E. of 402.0 eV that is assigned to PDDA molecules and a charge-neutral type

at the B. E. of 399.7 eV that is probably due to amines produced by condensation of ammonia and formaldehyde.[316] As the depth of analysis for XPS is usually less than 10 nm, the detection of the supposedly underlying PDDA in the 20-nm thick RF coating indicates significant mixing and hence interaction between the two polymers, which in turn reflect the mediating role of PDDA in the coating process. The Si 2*p* spectrum in Figure 7.2e shows negligible signal from Si, thus confirming full coverage of the zeolite particles with the RF coating.

Similar to the situation of coating zeolite with RF resin, deposition of SiO_2 was carried out in alkaline conditions where bonding of pure SiO_2 with RF is also hindered by repulsion between their negatively charged surfaces. The cationic surfactant, CTAB, was therefore used to modify the surface of RF and at the same time served as the template for mesopores in SiO_2.[317] Figure 7.3 shows that mesoporous SiO_2 ($mSiO_2$) coatings with even thicknesses are obtained which conform closely to the outline of the underlying RF layer. In the bright-field TEM images (Figure 7.3a–c), the inner RF coating is discernable as low-contrast areas between the zeolite cores and outer $mSiO_2$ layer. The wormhole-like mesopores within SiO_2 are visible in Figure 7.3a,b. Higher contrast between the different layers is achieved by HAADF imaging (Figure 7.3d) where signal strength correlates directly with atomic number of elements forming the material.[318] The C- and H-rich RF layer thus appears darker in Figure 7.3d compared with the zeolite core and $mSiO_2$ layer, as Si is one period heavier than C. The thickness of the $mSiO_2$ coating is controlled by the ratio between the amounts of Si precursor and substrate particles. In 2nZ@RF@$mSiO_2$ the thickness is *ca.* 70 nm while it decreases to 30 nm in 4nZ@RF@$mSiO_2$ due to less Si source available per unit weight of nZ@RF substrate. However, with a Si/substrate ratio close to that in the synthesis of 4nZ@RF@$mSiO_2$, the 4cZ@RF@$mSiO_2$ has a thicker $mSiO_2$ layer (*ca.* 90 nm) because of the smaller external surface area of cZ@RF.

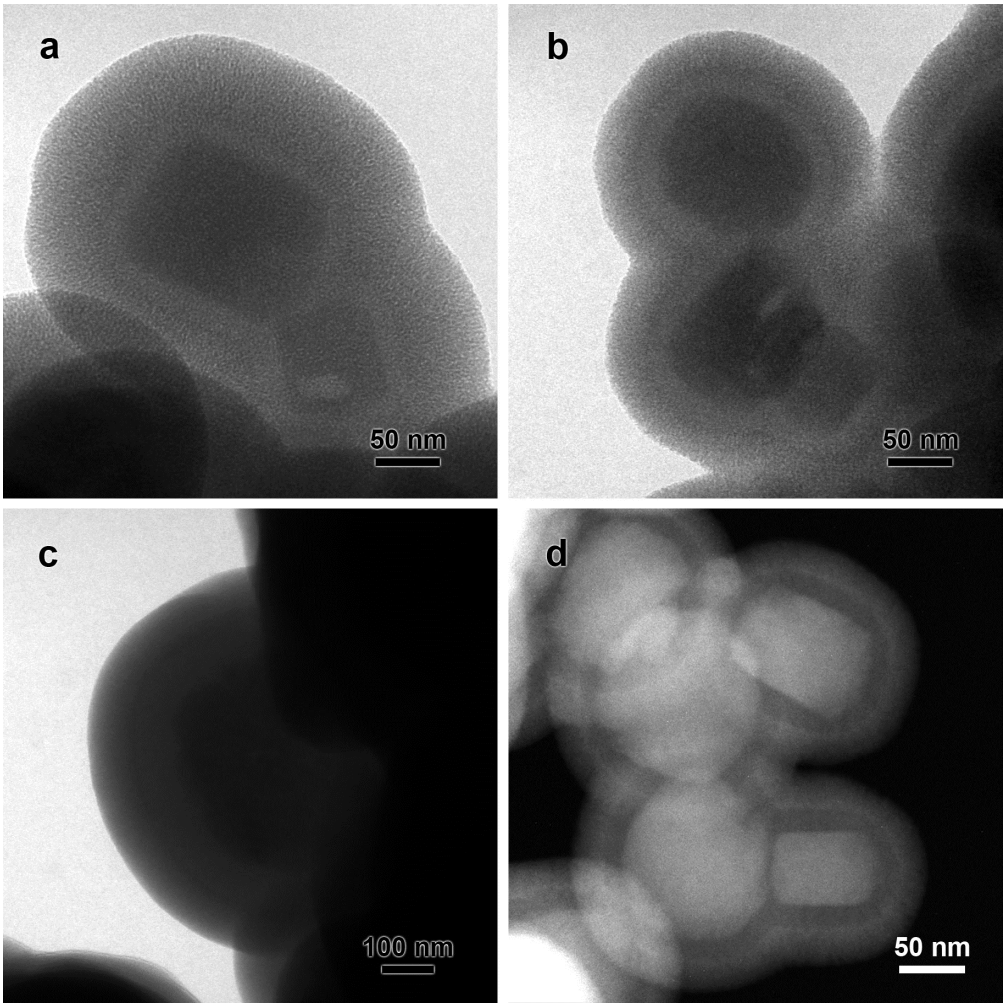

Figure 7.3. TEM images of (a) 2nZ@RF@$mSiO_2$, (b) 4nZ@RF@$mSiO_2$, (c) 4cZ@RF@$mSiO_2$, and (d) HAADF image of 4nZ@RF@$mSiO_2$.

7.3.3. Conversion of $mSiO_2$ to copper/zinc silicate

The $mSiO_2$ layer of the composite particles was converted to silicate materials in ammoniac solutions of Cu^{2+} and Zn^{2+} under hydrothermal conditions. The CTAB in $mSiO_2$ was not removed prior to the hydrothermal treatment, because in Section 4.3.1 it has been shown that CTAB can serve as soft template in the synthesis of single-walled copper silicate nanotubes. Figure 7.4 shows that the $mSiO_2$ coating in 2nZ@RF@$mSiO_2$ was dissolved and replaced with silicate materials of different morphologies after the hydrothermal treatment. In contrast, the zeolite core and the RF coating remained intact. In terms of morphological characteristics, two types of silicates can be observed covering the nZ@RF particles: a tubular type (Figure 7.4a)

and a flaky type (Figure 7.4c,d). The tubular type forms the major part of the silicate shell and nZ@RF particles covered with only the flaky type are found less frequently. Mixtures of both where the flaky silicate is on the outside (Figure 7.4b), however, seem to be the most common. In addition, bare nZ@RF particles without a silicate shell are also found in low numbers. Given the similar synthesis methods in Chapter 4 and in this work, the single-walled tubular silicate is most probably Cu-rich chrysocolla. In Figure 7.4d, stacking of individual lamellae in the flaky silicate is clearly visible. The interspace between the lamellae is *ca.* 1.4 nm wide, suggesting a high possibility of the silicate being of the chlorite group.[319]

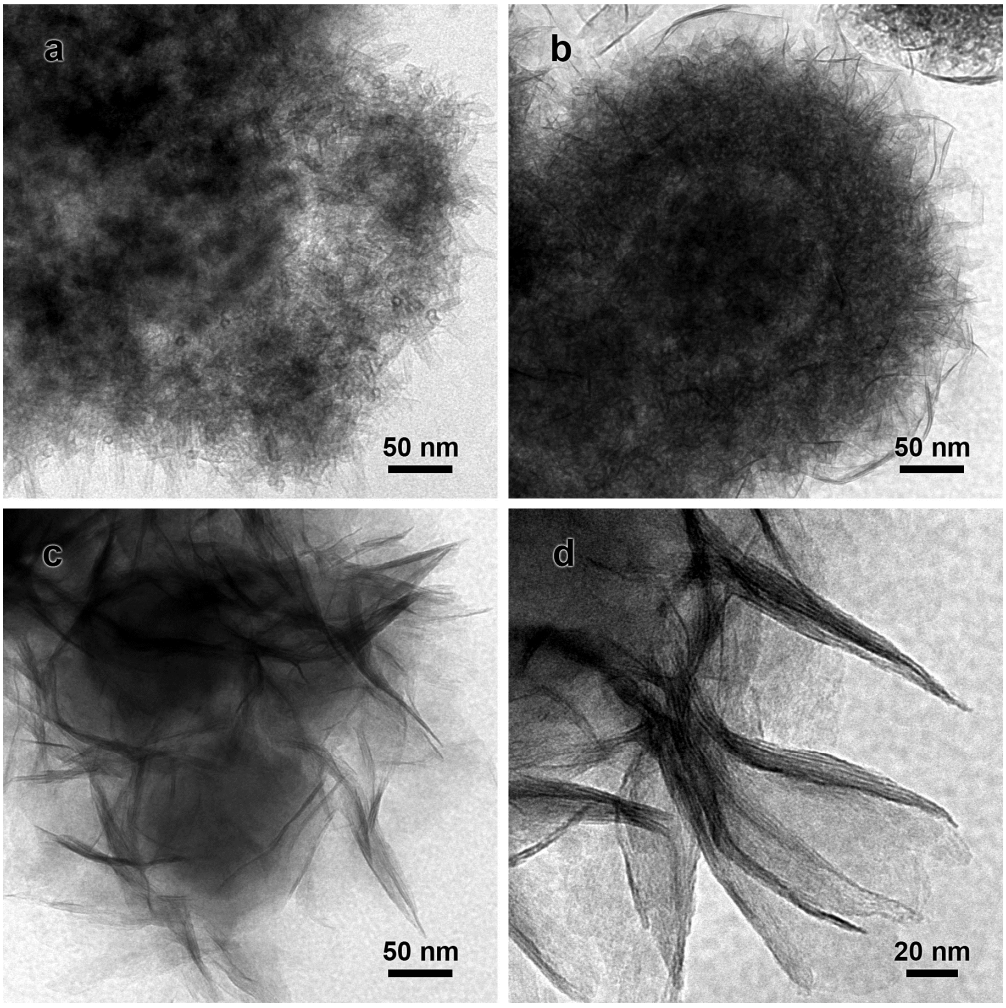

Figure 7.4. TEM images of 2nZ@RF@CZS.

Further characterization of 2nZ@RF@CZS with STEM-EDX reveals different relative abundance of Cu and Zn in the two types of silicate shells. Figure 7.5a,b

shows highly matched distributions of Si, Cu, and Zn in the shells due to formation of Cu/Zn silicate solid solutions, and the EDX spectra taken at the two sites indicate significantly higher Zn content in the flaky silicate (compare Figure 7.5d,e). It therefore seems that a high Zn content favors the growth of flaky silicates, which is in line with the observation in Chapter 4 that substitution of Cu in single-walled chrysocolla nanotubes by other transition metal elements resulted in unfolding of the tubular structure. However, the precise nature of the change in crystal structure is difficult to determine, because the thin, curled silicate sheets generate poorly resolved XRD patterns that overlap with strong diffraction signals of the ZSM-5.

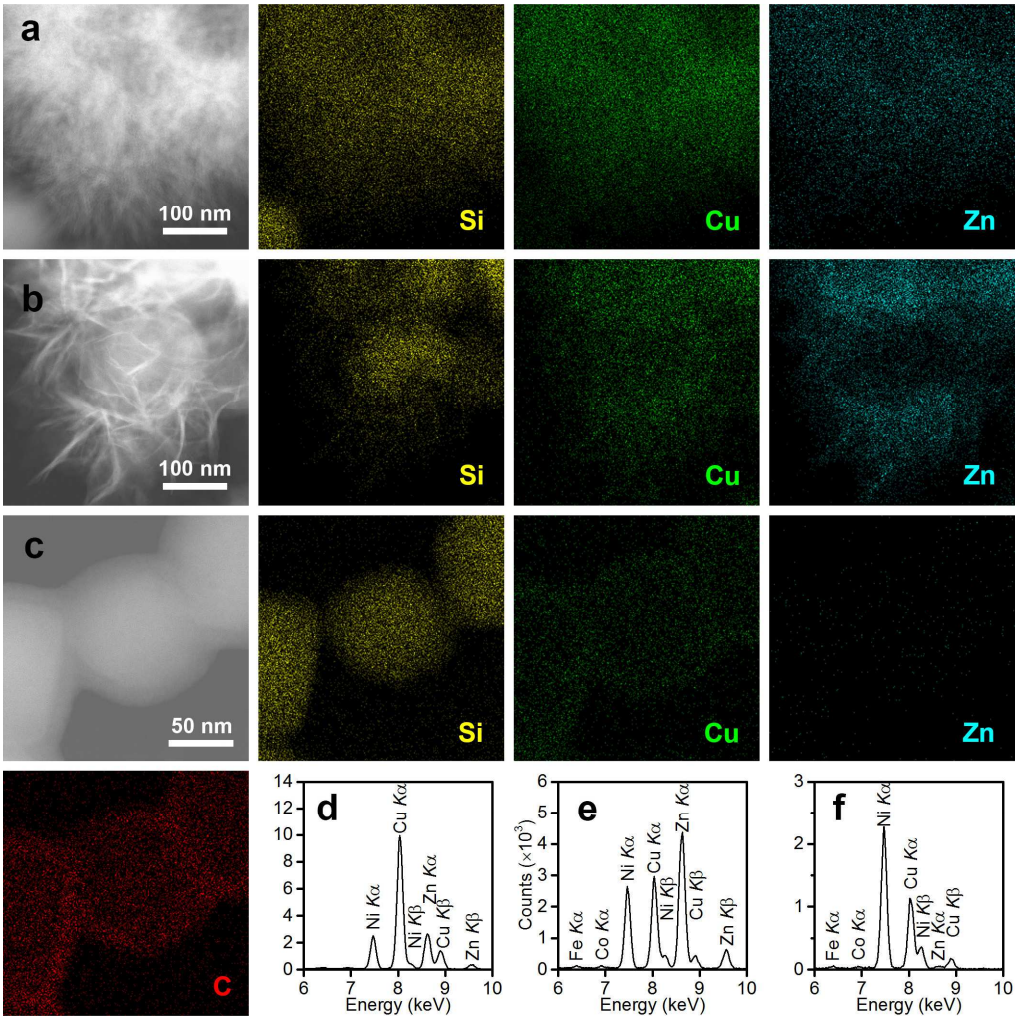

Figure 7.5. (a–c) STEM-EDX elemental mapping of 2nZ@RF@CZS particles: (a) with tubular silicate shell, (b) with flaky silicate shell, and (c) without silicate shell. (d–f) EDX spectra corresponding to (a–c). The signals of Fe and Co originated from the metal parts of the electron microscope, and the signal of Ni was due to the use of a Ni grid as sample holder.

In addition to forming the silicate shells, Cu is also incorporated readily into the RF layer as indicated by Figure 7.5c,f. It reflects the ion exchange property of RF resin due to ionization of the resorcinol units.[320] Compared with the silicate shells, the RF layer has a Cu/Zn ratio of *ca.* 20 which is significantly higher than that in the tubular and flaky silicate shell at Cu/Zn = 3.8 and 0.7, respectively (Figure 7.5d–f). While the amounts of Cu^{2+} and Zn^{2+} introduced to the precursor mixture have Cu/Zn = 7.5, the ratio between the concentrations of available Cu^{2+} and Zn^{2+} during synthesis is affected by complexation with NH_3. The formation constant of $[Cu(NH_3)_4]^{2+}$ from aqueous Cu^{2+} and NH_3 is generally reported to be at least 3 orders of magnitude larger than that of $[Zn(NH_3)_4]^{2+}$,[321-322] suggesting that during the initial stage of the hydrothermal treatment the amount of free Cu^{2+} is negligible compared with Zn^{2+}. The flaky Zn-rich silicates are therefore the most probable product in this stage, where Zn in the precursor solution is first consumed. However, since the amount of Zn is insufficient to fully convert the SiO_2 coating into silicates (the input Si/Zn ratio in the precursor mixture is 5 but the maximal possible Si/Zn ratio in pure zinc silicate clay is 1.33), the tubular Cu-rich silicates form after depletion of Zn in the solution. Apparently when the SiO_2 coating has completely reacted and the RF layer is exposed to the precursor solution, Cu^{2+} is significantly more available than Zn^{2+}, which explains the higher Cu/Zn ratio in the RF layer than in the silicate shells. The above mechanism is also consistent with the observation that the flaky silicate is only found on the outside of the silicate shells (Figure 7.4b).

The morphology of 4nZ@RF@CZS and 4cZ@RF@CZS presented in Figure 7.6 is similar to that of 2nZ@RF@CZS. The thicknesses of their silicate shells are noticeably different due to the different thickness of the SiO_2 coatings in the precursor particles. The zeolite cores and the RF layer are intact.

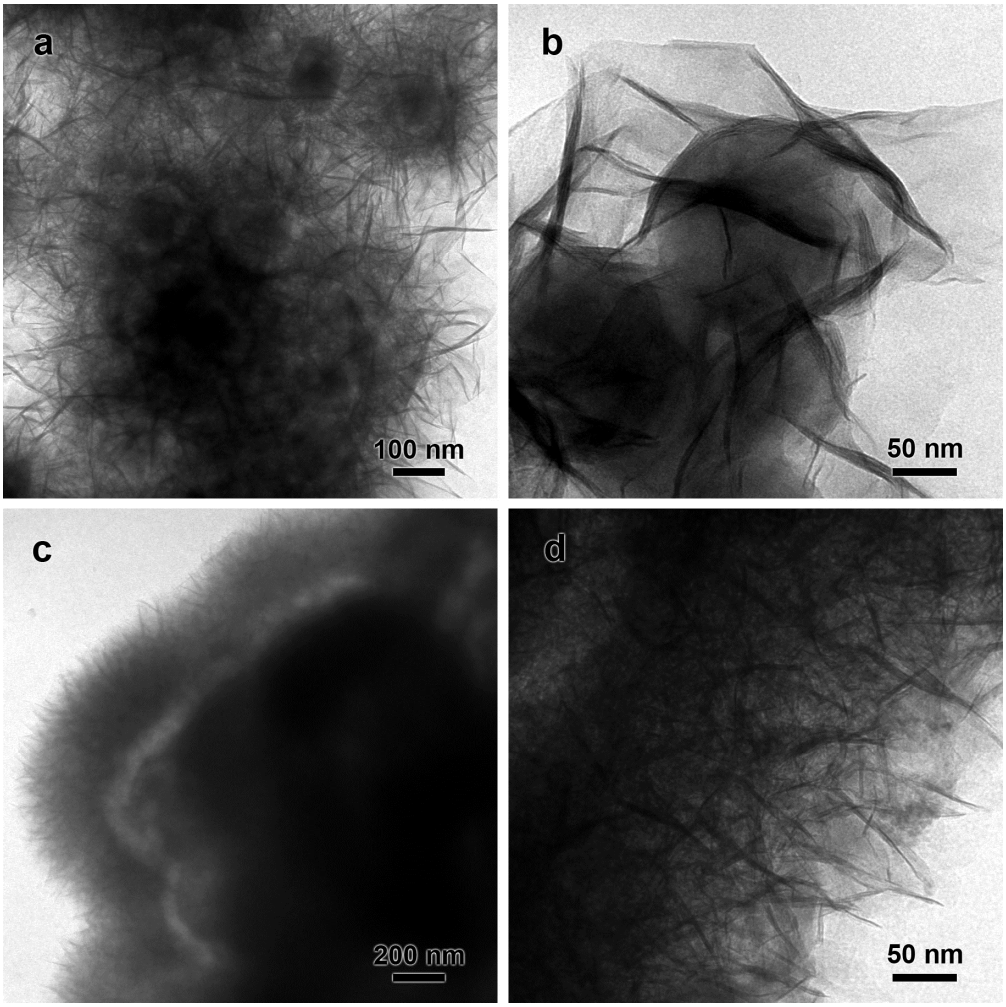

Figure 7.6. TEM images of (a,b) 4nZ@RF@CZS, (c,d) 4cZ@RF@CZS.

After calcination, the RF layer is removed by oxidation with air. The space left between the zeolite cores and the silicate shells in 2nZ@CZS is clearly identified in Figure 7.7a,b. Morphological effects of calcination on the silicate shells are minimal; no noticeable collapse of the tubular or sheet-like structures is observed. Interestingly, particles with sizes of *ca*. 10 nm formed on the surface of the zeolite cores, which are more obvious on the less covered (Figure 7.7c) and bare (Figure 7.7e) ZSM-5 particles. Continuous lattice fringes are observed in these particles at high magnification, indicating their crystalline nature. The fringes in Figure 7.7d, for example, can be assigned to the (110), (200), and (020) planes of monoclinic CuO with interplanar spacings of 2.8, 2.3, and 1.7 Å, respectively. Therefore the direction of electron beam during acquisition of Figure 7.7d can be regarded as parallel to the

[001] zone axis of the CuO nanocrystal observed. The elemental mapping in Figure 7.7e confirms the particles on the zeolite cores to be Cu-rich and thus supports the above conclusion drawn from TEM analysis. Given the incorporation of Cu and Zn in the RF layer (Figure 7.5c), the formation of the metal oxide particles can be attributed to oxidation of the Cu/Zn-containing RF resin. Indeed, Zn is also detected in the calcined sample with low abundance (Figure 7.7e), but it is in a highly dispersed state unlike Cu; no evidence of crystalline ZnO is found by TEM.

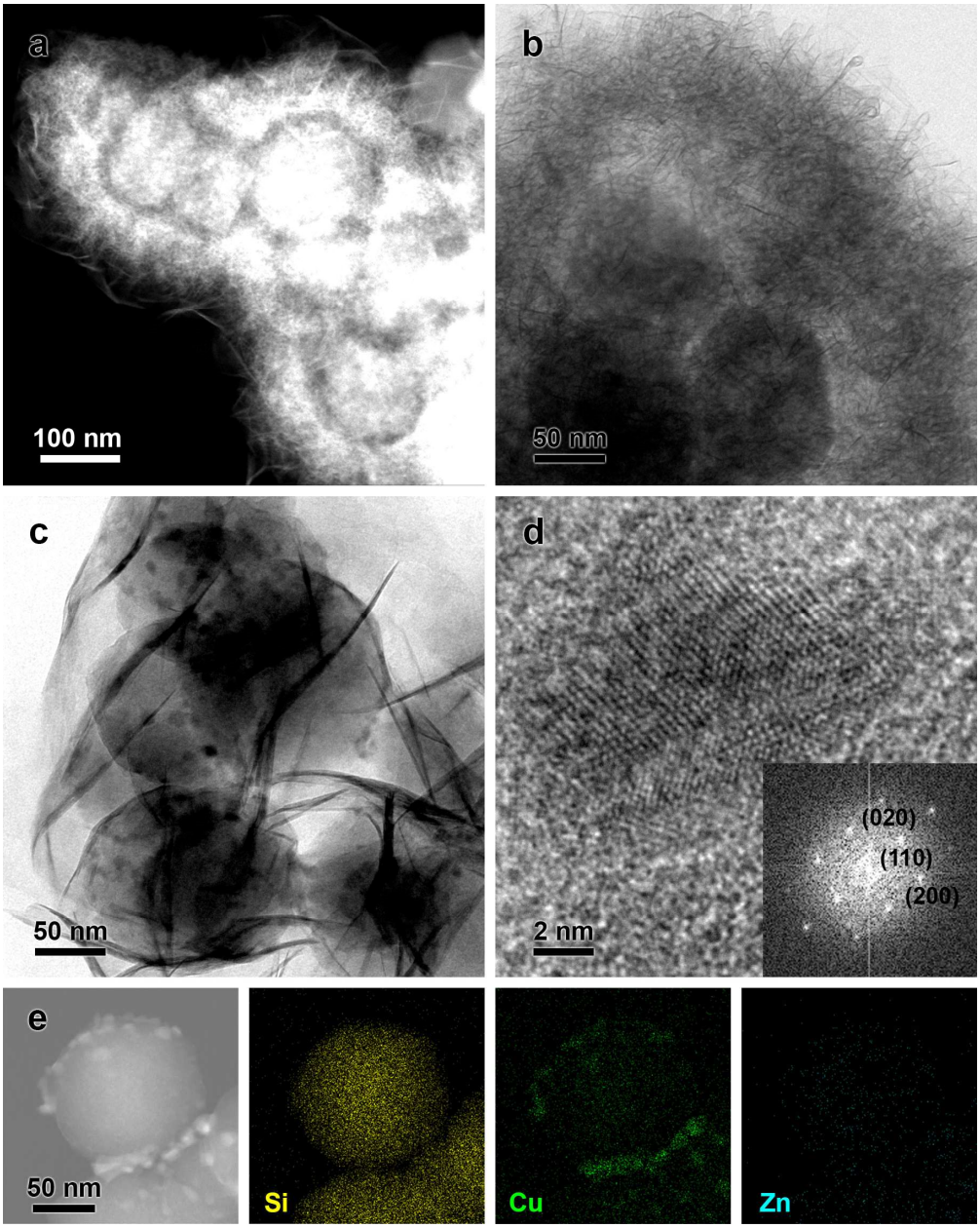

Figure 7.7. (a) HAADF image, (b–d) TEM images, and (e) STEM-EDX elemental mapping of 2nZ@CZS. The inset in (d) is the FFT result of the image.

Figure 7.8 shows similar morphology of 4nZ@CZS and 4cZ@CZS compared with that of 2nZ@CZS. The metal oxide particles in 4cZ@CZS are larger (up to 40 nm) than those in the other two samples, presumably due to the thicker Cu/Zn-containing RF layer in 4cZ@RF@CZS.

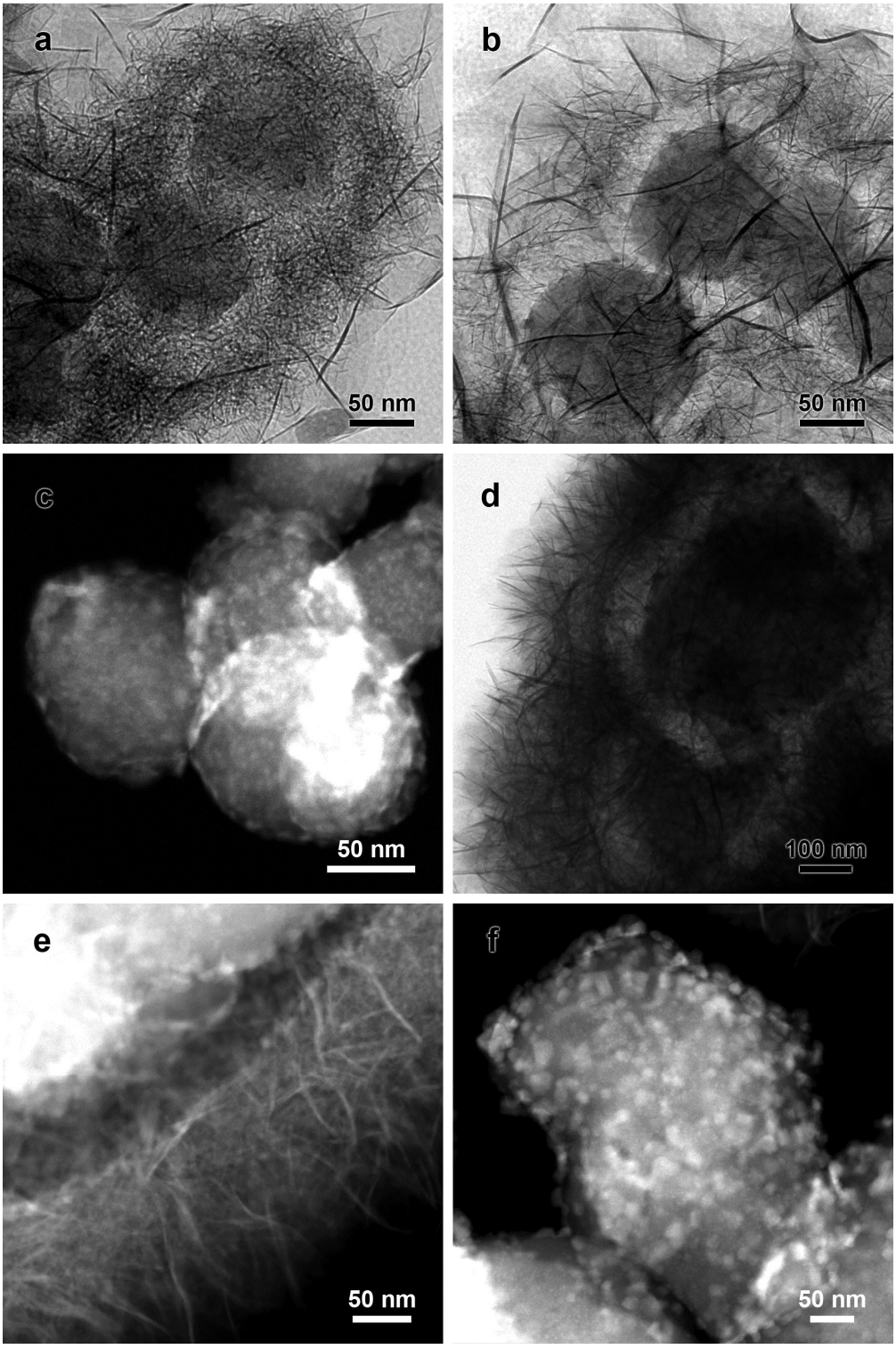

Figure 7.8. TEM and HAADF images of (a–c) 4nZ@CZS and (d–f) 4cZ@CZS.

The size difference of the CuO particles are also reflected by the XRD patterns in Figure 7.9a. The broadening of the diffraction peaks of CuO increases in the order of 4cZ@CZS < 4nZ@CZS < 2nZ@CZS, indicating a change in particle size in the reverse order. However, these signals are generally weak due to low abundance of CuO compared with ZSM-5 which generates strong peaks. The relatively weaker signals of ZSM-5 in 2nZ@CZS are apparently a result of lower zeolite loading. As mentioned earlier, the Cu/Zn silicates are undetected by XRD because of their thin, curled shape. While it is possible that the silicates generate broad peaks similar to those in Figure 4.3, they may be covered by the signals from ZSM-5.

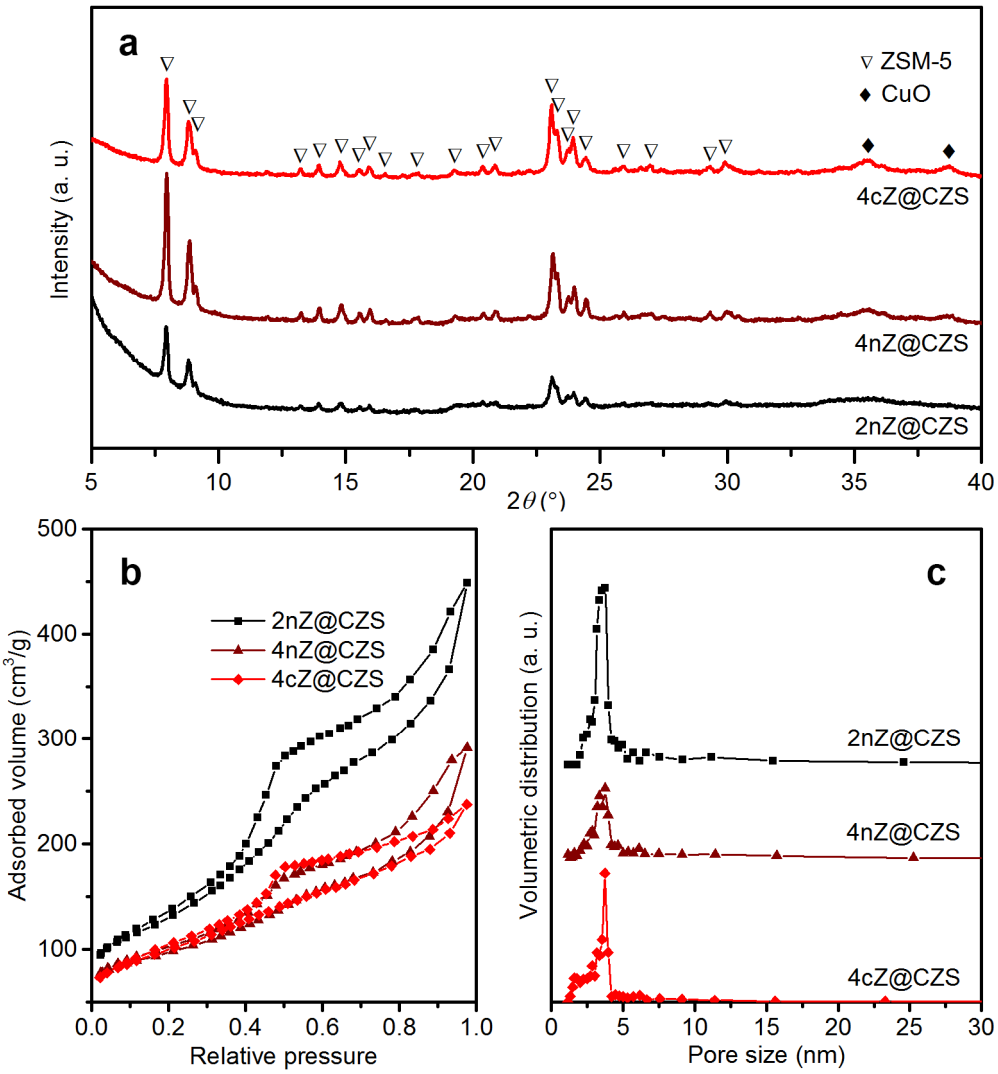

Figure 7.9. (a) Powder XRD patterns, (b) N_2 sorption isotherms, and (c) BJH pore size distributions of the ZSM-5@CZS catalysts.

The textural properties of the ZSM-5@CZS catalysts were studied by N_2 sorption experiments. The isotherms shown in Figure 7.9b have the type IV shape with H4 hysteresis loops according to definition by IUPAC, indicating the samples to be mesoporous.[245] The step increase in adsorbed gas volume between the relative pressure of 0.4 and 0.5 suggests a narrow size distribution of mesopores, which is confirmed by the BJH calculation results in Figure 7.9c. Peaking at 3.4–3.6 nm, the pore size distributions compare closely with that of single-walled Cu silicate nanotubes reported in Chapter 4. The volume of mesopores, however, differs in the order of 4cZ@CZS < 4nZ@CZS < 2nZ@CZS as listed in Table 7.1. Since the zeolite cores are microporous only, the mesopore volume should correlate with amount of Cu/Zn silicate shells which is in turn associated with Cu/Zn content of the catalysts. Indeed, similar trends are observed in total metal loading and mesopore volume. The metal loading and amount of Cu/Zn silicate are apparently affected by zeolite loading, as the zeolite remained inert during the growth of silicate shells.

Table 7.1. Properties of ZSM-5@CZS catalysts

Sample name	Zeolite content (%)	Cu content (%)*	Zn content (%)*	S_{BET} (m^2/g)	V_{micro} (cm^3/g)	V_{meso} (cm^3/g)
2nZ@CZS	20	21.8	11.8	454	0.02	0.68
4nZ@CZS	36	15.9	9.8	350	0.05	0.40
4cZ@CZS	40	12.5	10.2	351	0.03	0.31

*determined by ICP-OES

Dividing the specific micropore volumes of the ZSM-5@CZS catalysts by their zeolite contents gives corresponding specific micropore volumes of the ZSM-5 phase. The values for the ZSM-5 nanocrystals in 2nZ@CZS (0.12 cm^3/g) and 4nZ@CZS (0.15 cm^3/g) are comparable with reported values of 0.1–0.2 cm^3/g.[105, 306, 323] However, the value for the commercial ZSM-5 in 4cZ@CZS at 0.07 cm^3/g is significantly lower, probably due to blocking of its micropores by CuO particles; the external surface area

of the commercial ZSM-5 is smaller than that of the ZSM-5 nanocrystals, making the former more susceptible to pore clogging.

7.3.4. Catalytic performance

At 260 °C, 30 bar, the ZSM-5@CZS catalysts exhibit significant activity in CO_2 hydrogenation with long-term CO_2 conversions of 9% for 4cZ@CZS, 12% for 4nZ@CZS, and 14% for 2nZ@CZS. CO, methanol, dimethyl ether (DME) are the main products. As the Cu and Zn species are responsible for the CO_2 hydrogenation, the activity was normalized by the total metal content for a meaningful comparison. While the CO_2 conversion on 2nZ@CZS is higher than on 4nZ@CZS, Figure 7.10a shows that the specific activity of 2nZ@CZS is in fact lower. Similarly, the organics selectivity (defined as moles of C forming organic products divided by moles of CO_2 converted) presented in Figure 7.10b is also lower for 2nZ@CZS. The promoting role of Zn in Cu-based methanol synthesis catalysts is well-established,[155, 324] and such difference may be attributed to the higher Zn/Cu ratio in 4nZ@CZS (Table 7.1). Note that the Zn/Cu ratios of the ZSM-5@CZS catalysts are close to those of Zn34-CuSiNT and Zn43-CuSiNT studied in Chapter 4 where the more Zn-rich Zn43-CuSiNT showed a lower specific activity and no significant difference in selectivity was found. It can be explained by poorer mixing of Cu and Zn in the ZSM-5@CZS catalysts which is evident from the presence of separate Cu-rich, Zn-rich silicate phases and Cu-rich oxide phases, because in such conditions a higher Zn content is required to achieve the same degree of contact between Cu and Zn species. In the CuSiNTs, a small amount of post-synthesis Zn doping highly dispersed in the Cu silicate structure was enough to influence the entire surface of the catalyst. The promoting role of excess Zn doping in CuSiNT was insignificant and specific activity decreased as the excess Zn was taken into account when calculating total metal content. Apparently, in the nZ@CZS catalysts the promoting effect of Zn is more important, increasing both activity and organics selectivity. However, the even higher

Zn/Cu ratio in 4cZ@CZS does not lead to further increase in organics selectivity, which is consistent with the observation in Chapter 4. It is worth mentioning that the relatively low specific activity of 4cZ@CZS is not solely attributed to the dilution effect of Zn; the larger CuO particle size and hence lower metal dispersity should instead be the main factor (see Figure 7.8 & 7.9a).

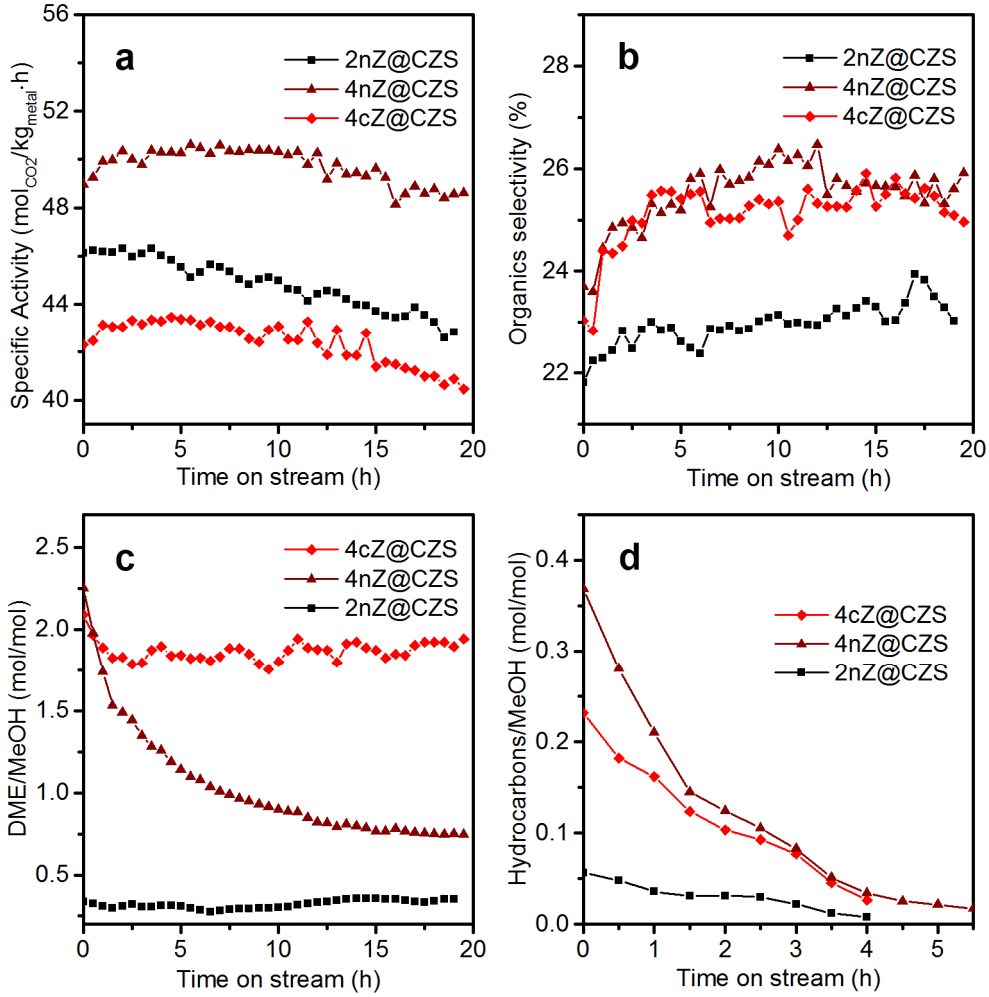

Figure 7.10. Performance of the ZSM-5@CZS catalysts: (a) normalized activity, (b) organics selectivity, (c) DME/methanol mole ratio, and (d) hydrocarbons/methanol mole ratio.

The catalytic dehydration activity of ZSM-5 has been widely recognized in DME synthesis from methanol.[16] Figure 7.10c shows that the degree of such conversion has strong dependence on both the amount and nature of the ZSM-5 component. The advantage of higher zeolite loading is obvious in the comparison between 2nZ@CZS and 4nZ@CZS, and at similar zeolite loadings, 4cZ@CZS has a stronger dehydration

activity than 4nZ@CZS due to the higher Al content and hence concentration of acid sites in the commercial ZSM-5. However, due to the significantly higher methanol synthesis activity of 4nZ@CZS, its DME yield compares rather closely with that of 4cZ@CZS as shown in Table 7.2. In terms of stability, a notable decrease in dehydration activity over time sets 4nZ@CZS apart from the other two catalysts. The decrease can be attributed to ion exchange and neutralization of the zeolitic acid sites with Cu^{2+}, which has been reported for hybrid catalysts consisting of ZSM-5 and $Cu/ZnO/Al_2O_3$.[325] Similarly, migration of Cu species may also play a role in the evolution of CO_2 hydrogenation activity by causing sintering of Cu particles, though it occurs in all of the three catalysts unlike in the case of dehydration activity. The relatively fast decrease in dehydration activity of 4nZ@CZS may be associated with higher exposure of its zeolite cores (4nZ@CZS contains the largest amount of bare ZSM-5 cores among the three catalysts according to TEM observation), but additional evidence is needed for a definite conclusion.

Table 7.2. Yield of organics at the end of stability test

Catalyst	Steady-state methanol yield ($mol/kg_{metal}·h$)	Steady-state DME yield ($mol/kg_{metal}·h$)
2nZ@CZS	5.8	2.0
4nZ@CZS	5.1	3.8
4cZ@CZS	2.1	4.0

In addition to DME, long-chain hydrocarbons (C_{6+}) were also detected in the product stream during the early stage of the catalyst evaluation, indicating the presence of strong acid sites in the ZSM-5 cores that catalyze the MTO reactions.[326] The evolution of such activity follows the trend in the initial DME synthesis activity, but the strong acid sites are deactivated quickly. The deactivation can be related to the neutralization of acidity by Cu^{2+} and/or coking.[326]

The spent catalysts were studied by powder XRD. The diffraction patterns in Figure 7.11 show that the crystal structure of ZSM-5 is preserved. Formation of Cu nanoparticles and a more dispersed Cu_2O phase is evident. However, it is believed that Cu_2O formed by oxidation of Cu after the catalysts were unloaded from the reactor and exposed to air instead of during the hydrogenation experiment. From the broadening of Cu (111) peaks, the crystallite size of Cu is estimated to be 10 nm for 2nZ@CZS and 4nZ@CZS, and 12 nm for 4cZ@CZS. While the effect of oxidation on the size of Cu particles has to be taken into account in determining their actual size during catalyst evaluation, the as-calculated Cu particle sizes of the three spent catalysts are nevertheless consistent with the relative CO_2 hydrogenation activity; 4cZ@CZS with the largest Cu particle size (and hence lowest metal dispersity) is least active despite its highest Zn/Cu ratio.

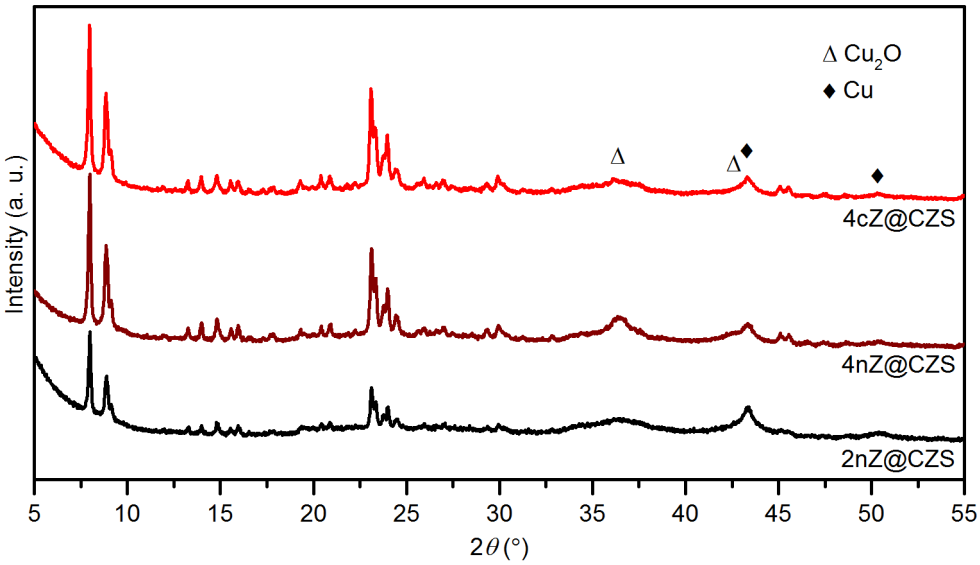

Figure 7.11. Powder XRD patterns of spent catalysts.

7.4. Conclusions

In summary, ZSM-5 nanocrystals have been successfully integrated into hydrothermally synthesized porous Cu/Zn phyllosilicate nanostructures using RF

resin as a removable protective layer. The resistant RF layer separated the zeolite cores from the corrosive chemical environment during the synthesis of the phyllosilicates and preserved the acidity of ZSM-5. The resulting bi-functional catalyst exhibited high activity in CO_2-to-methanol and subsequent methanol dehydration and MTO reactions which confirms the acidity of the incorporated ZSM-5. It should be noted that the use of protective RF coating is not limited to the construction of multi-phase silicate structures. Other nanocomposites comprising materials that need to be synthesized in harsh environments and materials that are unstable in such environments can be prepared using this approach, as long as the less stable material is compatible with the synthesis conditions of RF resin. In addition, the transformation of metal species absorbed in RF resin into crystalline phases may serve as a novel synthesis strategy for nanomaterials. Despite being beyond the scope of the thesis, it is worth further investigation and development.

Chapter 8. Concluding Remarks

The diversity in chemical property and structure of silicate materials is enormous. Using hard template-based, soft template-based, template-free methods or their combination, novel hierarchically porous silicate materials including transition metal phyllosilicate nanotube assemblages, macro-meso-microporous aluminosilicate spheres, hierarchical zeolite EMT, and integrated zeolite-phyllosilicate nanocomposites were developed in this thesis, which demonstrates the large potential of silicate materials in the emerging field of complex nanomaterials design. In-depth knowledge about the physicochemical properties and formation mechanism of these materials was gained through extensive characterization of the as-synthesized materials by electron microscopy, X-ray diffraction, N_2 sorption and various spectroscopic techniques. Furthermore, encouraging results were obtained on the catalytic performance of the hierarchically porous materials in CO_2 hydrogenation, indicating possible applications in CO_2 utilization in general. Sorted according to the relevant type of materials, the major findings are summarized as follows.

i. Chrysocolla-type Cu phyllosilicate synthesized hydrothermally in the presence of NH_3 in high concentrations has the tendency to form uniform single-walled nanotubes which can organize into a hexagonal packing. The growth of the Cu silicate nanotubes and hence the secondary structure of these nanotubes are controlled by alkalinity and availability of Cu^{2+} in the precursor solution. In contrast to conventional ion exchange processes of clay materials that are limited to changing the interlamellar species, the NH_3 complexation-assisted ion exchange provides a strong driving force to alter the composition of the silicate lamellae, and doping of the Cu silicate nanotubes with Mn^{2+}, Fe^{2+}, Co^{2+}, Ni^{2+} and/or Zn^{2+} in significant amounts is

thereby possible without damaging the tubular structure. Supported Cu nanoparticle catalysts derived from the doped nanotubes have better metal utilization than commercial $Cu/ZnO/Al_2O_3$ catalysts in CO_2 hydrogenation reactions and the catalytic properties of the nanocatalysts are easily tuned by the doping.

ii. A water-ethanol-toluene-CTAB microemulsion system can facilitate simultaneous incorporation of Al and generation of macro-meso-microporous structures in silica particles with minimal impact on the uniformity of their size. The high viscosity of the microemulsion probably plays an important role in controlling the particle size distribution by decreasing collision and coalescence. The size and shape of the soft templates involved in the synthesis, *i.e.* surfactant micelles and giant vesicles, are remarkably affected by Hofmeister anion effects of the Al source, $[Al(OH)_4]^-$, which lead to tunable pore size and topology of the resultant material. Although the presence of Al decreases metal dispersity and CO_2 hydrogenation activity of Cu/ZnO catalysts supported on the hierarchically porous silicate particles, it adds functionality to the methanol synthesis catalysts by generating acid sites for dehydration of methanol into dimethyl ether.

iii. Simple alcohols including methanol, ethanol, isopropanol and n-propanol have beneficial effects on control of polymorphism during the synthesis of EMT-type zeolite without conventional organic structure-directing agents. In addition, heterogeneous nucleation of the zeolite is accelerated in the presence of the alcohols, which facilitates formation of nanometer-sized zeolite crystallites and their assembly into larger, uniform particles. Compared with commercial products with large crystallite sizes, the hierarchically structured zeolite nanoparticles disperse Pt better. Na-promoted Pt nanocatalysts supported on the hierarchical EMT-type zeolite thus show superior reverse water gas shift reactivity.

iv. Resorcinol-formaldehyde resin exhibits good chemical resistance in the harsh conditions involved in the hydrothermal synthesis of transition metal silicate nanostructures. It can therefore serve as a removable protective layer in the integration of hydrothermally unstable materials, for example zeolite ZSM-5 nanocrystals, within transition metal silicate shells. The acidity of the zeolite ZSM-5 is thus preserved during the synthesis procedure, which in combination with the methanol synthesis activity of the Cu/Zn silicate shells realizes the direct synthesis of dimethyl ether and hydrocarbons from CO_2/H_2 mixture.

Due to limited time and resources, however, the studies carried out in this thesis are by no means comprehensive. Catalytic properties of the silicate catalysts, for example, are worth significant further investigation in general. On the basis of the results obtained, specific limitations of the current studies and recommendations on possible future work are summarized as follows.

i. The detailed crystallographic structure of the CuSiNT (as well as chrysocolla) remains to be solved. Diffraction experiments using synchrotron sources may yield data of enough quality for this purpose. While only 3*d* transition metal elements were involved in the current work, it would be interesting to test ion exchange of Cu^{2+} in the CuSiNT with heavier elements for further diversity in chemical composition. In addition, decoration of the nanotubes with noble metal nanoparticles is also a viable strategy of designing more complex materials. In terms of catalytic performance, the incorporation of Zn in the silicate framework may have an impact on its interaction with Cu and hence activity/selectivity of the catalyst. Introducing an additional ZnO phase to the surface should thus be beneficial. Moreover, the incorporation of Mn, Fe, Co, and Ni in the CuSiNT leads to possible activity in reactions other than RWGS and methanol synthesis, for example alcohol oxidation, Fischer-Tropsch

synthesis, methane reforming and fine chemical hydrogenation that can be experimented on.

ii. The macropores in the macro-meso-microporous silica/aluminosilicate spheres are large enough to accommodate pre-synthesized nanomaterials such as noble metals and $CuO/ZnO/Al_2O_3$ particles. Integration of the already optimized metal catalysts in the macropores affords higher loading and better contact between active component and promoter than those achieved by the impregnation method, which can potentially lead to better catalytic performance. For the support material itself, the incorporation of Al and Na makes further transformation to zeolite possible, for example through steam-assisted solid-state synthesis. Uniform and hierarchically ordered zeolite spheres may thus be obtained with similar overall morphology as the amorphous precursor particles.

iii. Mechanisms through which alcohols affect the crystallization of zeolite EMT/FAU are largely unclear, and only speculations can be made currently. More advanced characterization techniques such as extended X-ray absorption fine structure calculations and *in-situ* NMR may be helpful in this regard. Better understanding of the interactions involving the structure-directing species would an important guide to experiments on synthesis of other zeolites using the alcohol-assisted method. In addition, efforts should be made on increasing the Si/Al ratio of the zeolite product for a wider spectrum of applications in catalysis. Addition of Al chelating agents to control its available concentration, for example, is a possible solution.

iv. Morphological control of multi-metal silicate nanostructures remains difficult in one-pot synthesis. While the post-synthesis modification method in Chapter 4 will probably yield better results, the simpler one-pot synthesis is still worth further development. Since the pore size of the phyllosilicate shells is large compared with common chemical species encountered in gas-

phase reactions, size exclusion effects which are desired properties of a core-shell structure are absent in the current study. It could be possible, however, to encapsulate various other catalytically active materials inside zeolite shells using the resorcinol-formaldehyde resin-assisted method for size-selective applications.

References

1. Yang, J.; Sargent, E. H.; Kelley, S. O.; Ying, J. Y., A general phase-transfer protocol for metal ions and its application in nanocrystal synthesis. *Nat. Mater.* **2009,** *8*, 683-689.
2. Yu, Y.; Zhang, Q.; Xie, J.; Lee, J. Y., Engineering the architectural diversity of heterogeneous metallic nanocrystals. *Nat. Commun.* **2013,** *4*, 1454.
3. Ma, T. Y.; Liu, L.; Yuan, Z. Y., Direct synthesis of ordered mesoporous carbons. *Chem. Soc. Rev.* **2013,** *42*, 3977-4003.
4. Wan, Y.; Zhao, D., On the controllable soft-templating approach to mesoporous silicates. *Chem. Rev.* **2007,** *107*, 2821-2860.
5. Li, W.; Yue, Q.; Deng, Y.; Zhao, D., Ordered mesoporous materials based on interfacial assembly and engineering. *Adv. Mater.* **2013,** *25*, 5129-5152.
6. Gu, D.; Schüth, F., Synthesis of non-siliceous mesoporous oxides. *Chem. Soc. Rev.* **2014,** *43*, 313-344.
7. Astruc, D.; Lu, F.; Aranzaes, J. R., Nanoparticles as recyclable catalysts: the frontier between homogeneous and heterogeneous catalysis. *Angew. Chem., Int. Ed. Engl.* **2005,** *44*, 7852-7872.
8. Ge, J.; Zhang, Q.; Zhang, T.; Yin, Y., Core-satellite nanocomposite catalysts protected by a porous silica shell: controllable reactivity, high stability, and magnetic recyclability. *Angew. Chem., Int. Ed. Engl.* **2008,** *47*, 8924-8928.
9. Li, J.; Zeng, H. C., Size tuning, functionalization, and reactivation of Au in TiO2 nanoreactors. *Angew. Chem., Int. Ed. Engl.* **2005,** *44*, 4342-4345.
10. Yao, K. X.; Zeng, H. C., Simultaneous chemical modification and structural transformation of Stöber silica spheres for integration of nanocatalysts. *Chem. Mater.* **2012,** *24*, 140-148.
11. Zeng, H. C., Synthesis and self-assembly of complex hollow materials. *J. Mater. Chem.* **2011,** *21*, 7511.
12. Zeng, H. C., Integrated nanocatalysts. *Acc. Chem. Res.* **2013,** *46*, 226-235.
13. Petkovich, N. D.; Stein, A., Controlling macro- and mesostructures with hierarchical porosity through combined hard and soft templating. *Chem. Soc. Rev.* **2013,** *42*, 3721-3739.
14. Eitel, W., Section A - Silicate Crystal Structure. In *Silicate Structures and Dispersion System*, Academic Press: **1975**, pp 1-273.
15. Corma, A., From microporous to mesoporous molecular sieve materials and their use in catalysis. *Chem. Rev.* **1997,** *97*, 2373-2419.
16. Wang, W.; Wang, S.; Ma, X.; Gong, J., Recent advances in catalytic hydrogenation of carbon dioxide. *Chem. Soc. Rev.* **2011,** *40*, 3703-3727.
17. Porosoff, M. D.; Yan, B.; Chen, J. G., Catalytic reduction of CO_2 by H_2 for synthesis of CO, methanol and hydrocarbons: challenges and opportunities. *Energy Environ. Sci.* **2016,** *9*, 62-73.

18. Olah, G. A., Beyond oil and gas: the methanol economy. *Angew. Chem., Int. Ed. Engl.* **2005,** *44*, 2636-2639.

19. Brigatti, M. F.; Galán, E.; Theng, B. K. G., Chapter 2 - Structure and Mineralogy of Clay Minerals. In *Developments in Clay Science*, Faïza, B.; Gerhard, L., Eds. Elsevier: **2013**, vol 5A, pp 21-81.

20. Bergaya, F.; Lagaly, G.; Vayer, M., Chapter 2.11 - Cation and Anion Exchange. In *Developments in Clay Science*, Faïza, B.; Gerhard, L., Eds. Elsevier: **2013**, vol 5B, pp 333-359.

21. Murray, H. H., Applied clay mineralogy today and tomorrow. *Clay Miner.* **1999,** *34*, 39-49.

22. Cool, P.; Vansant, E. F., Pillared Clays: Preparation, Characterization and Applications. In *Molecular Sieves - Science and Technology*, Karge, H. G.; Weitkamp, J., Eds. Springer: Berlin, **1998**, vol 1, pp 265-288.

23. Vicente, M. A.; Gil, A.; Bergaya, F., Chapter 10.5 - Pillared Clays and Clay Minerals. In *Developments in Clay Science*, Faïza, B.; Gerhard, L., Eds. Elsevier: **2013**, vol 5A, pp 523-557.

24. Cardwick, P. D. G.; Farmer, V. C.; Russel, J. D.; Masson, C. R.; Wada, K.; Yoshinaga, N., Imogolite, a hydrated aluminium silicate of tubular structure. *Nature* **1972,** *240*, 187-189.

25. Johnson, I. D.; Werpy, T. A.; Pinnavaia, T. J., Tubular silicate-layered silicate intercalation compounds: a new family of pillared clays. *J. Am. Chem. Soc.* **1988,** *110*, 8545-8547.

26. Pinnavaia, T. J., Approaches to the Synthesis of Supergallery Pillared Clays. In *Expanded Clays and Other Microporous Solids*, Occelli, M. L.; Robson, H. E., Eds. Springer: **1992**.

27. Joussein, E.; Petit, S.; Churchman, J.; Theng, B.; Righi, D.; Delvaux, B., Halloysite clay minerals - a review. *Clay Miner.* **2005,** *40*, 383-426.

28. Yuan, P.; Tan, D.; Annabi-Bergaya, F., Properties and applications of halloysite nanotubes: recent research advances and future prospects. *Appl. Clay Sci.* **2015,** *112-113*, 75-93.

29. Churchman, G. J.; Davy, T. J.; Aylmore, L. A. G.; Gilkes, R. J.; Self, P. G., Characteristics of fine pores in some halloysites. *Clay Miner.* **1995,** *30*, 89-98.

30. Carrillo, A. M.; Carriazo, J. G., Cu and Co oxides supported on halloysite for the total oxidation of toluene. *Appl. Catal. B* **2015,** *164*, 443-452.

31. Li, X.; Ouyang, J.; Zhou, Y.; Yang, H., Assembling strategy to synthesize palladium modified kaolin nanocomposites with different morphologies. *Sci. Rep.* **2015,** *5*, 13763.

32. Lvov, Y.; Wang, W.; Zhang, L.; Fakhrullin, R., Halloysite clay nanotubes for loading and sustained release of functional compounds. *Adv. Mater.* **2016,** *28*, 1227-1250.

33. Kuroda, Y.; Ito, K.; Itabashi, K.; Kuroda, K., One-step exfoliation of kaolinites and their transformation into nanoscrolls. *Langmuir* **2011,** *27*, 2028-2035.

34. Yuan, P.; Tan, D.; Annabi-Bergaya, F.; Yan, W.; Liu, D.; Liu, Z., From platy kaolinite to aluminosilicate nanoroll via one-step delamination of kaolinite: Effect of the temperature of intercalation. *Appl. Clay Sci.* **2013,** *83-84*, 68-76.

35. Weiss, A., A secret of chinese porcelain manufacture. *Angew. Chem., Int. Ed. Engl.* **1963,** *2*, 697-703.

36. Valášková, M.; Rieder, M.; Matějka, V.; Čapková, P.; Slíva, A., Exfoliation/delamination of kaolinite by low-temperature washing of kaolinite–urea intercalates. *Appl. Clay Sci.* **2007,** *35*, 108-118.

37. Singh, B.; Mackinnon, I. D. R., Experimental transformation of kaolinite to halloysite. *Clays Clay Miner.* **1996,** *44*, 825-834.

38. Gardolinski, J. E. F. C.; Lagaly, G., Grafted organic derivatives of kaolinite: II. Intercalation of primary n-alkylamines and delamination. *Clay Miner.* **2005,** *40*, 547-556.

39. Letaief, S.; Detellier, C., Clay-polymer nanocomposite material from the delamination of kaolinite in the presence of sodium polyacrylate. *Langmuir* **2009,** *25*, 10975-10979.

40. Jaber, M.; Komarneni, S.; Zhou, C. H., Chapter 7.2 - Synthesis of Clay Minerals. In *Developments in Clay Science*, Faïza, B.; Gerhard, L., Eds. Elsevier: **2013**, vol 5A, pp 223-241.

41. Wang, X.; Zhuang, J.; Chen, J.; Zhou, K.; Li, Y., Thermally stable silicate nanotubes. *Angew. Chem., Int. Ed. Engl.* **2004,** *43*, 2017-2020.

42. White, R. D.; Bavykin, D. V.; Walsh, F. C., Morphological control of synthetic $Ni_3Si_2O_5(OH)_4$ nanotubes in an alkaline hydrothermal environment. *J. Mater. Chem. A* **2013,** *1*, 548-556.

43. Yue, H.; Zhao, Y.; Zhao, S.; Wang, B.; Ma, X.; Gong, J., A copper-phyllosilicate core-sheath nanoreactor for carbon-oxygen hydrogenolysis reactions. *Nat. Commun.* **2013,** *4*, 2339.

44. Zhu, W.; Yang, Y.; Hu, S.; Xiang, G.; Xu, B.; Zhuang, J.; Wang, X., $(Ni,Mg)_3Si_2O_5(OH)_4$ solid-solution nanotubes supported by sub-0.06 wt % palladium as a robust high-efficiency catalyst for Suzuki-Miyaura cross-coupling reactions. *Inorg. Chem.* **2012,** *51*, 6020-6031.

45. Qu, S.; Pei, S.; Zhang, S.; Song, P., Preparation of silicate nanotubes and its application for electrochemical sensing of clozapine. *Mater. Lett.* **2013,** *102-103*, 56-58.

46. Shannon, R. D., Revised effective ionic radii and systematic studies of interatomic distances in halides and chalcogenides. *Acta Crystallogr.* **1976,** *A32*, 751-767.

47. Jin, R.; Yang, Y.; Xing, Y.; Chen, L.; Song, S.; Jin, R., Facile synthesis and properties of hierarchical double-walled copper silicate hollow nanofibers assembled by nanotubes. *ACS Nano* **2014,** *8*, 3664-3670.

48. Yec, C. C.; Zeng, H. C., Nanobubbles within a microbubble: synthesis and self-assembly of hollow manganese silicate and its metal-doped derivatives. *ACS Nano* **2014,** *8*, 6407-6416.

49. Zheng, J.; Wu, B.-H.; Jiang, Z.-Y.; Kuang, Q.; Fang, X.-L.; Xie, Z.-X.; Huang, R.-B.; Zheng, L.-S., General and facile syntheses of metal silicate porous hollow nanostructures. *Chem. - Asian J.* **2010,** *5*, 1439-1444.

50. Wang, Y.; Wang, G.; Wang, H.; Cai, W.; Zhang, L., One-pot synthesis of nanotube-based hierarchical copper silicate hollow spheres. *Chem. Commun. (Cambridge, U. K.)* **2008**, 6555-6557.

51. Qu, J.; Li, W.; Cao, C.-Y.; Yin, X.-J.; Zhao, L.; Bai, J.; Qin, Z.; Song, W.-G., Metal silicate nanotubes with nanostructured walls as superb adsorbents for uranyl ions and lead ions in water. *J. Mater. Chem.* **2012,** *22*, 17222-17226.

52. Wang, Y.; Tang, C.; Deng, Q.; Liang, C.; Ng, D. H. L.; Kwong, F. L.; Wang, H.; Cai, W.; Zhang, L.; Wang, G., A versatile method for controlled synthesis of porous hollow spheres. *Langmuir* **2010,** *26*, 14830-14834.

53. Zhan, G.; Yec, C. C.; Zeng, H. C., Mesoporous bubble-like manganese silicate as a versatile platform for design and synthesis of nanostructured catalysts. *Chem. - Eur. J.* **2015,** *21*, 1882-1887.

54. Cao, C. Y.; Wei, F.; Qu, J.; Song, W. G., Programmed synthesis of magnetic magnesium silicate nanotubes with high adsorption capacities for lead and cadmium ions. *Chem. - Eur. J.* **2013,** *19*, 1558-1562.

55. Chen, H.; Lu, X.; Deng, C.; Yan, X., Facile synthesis of uniform microspheres composed of a magnetite core and copper silicate nanotube shell for removal of microcystins in water. *J. Phys. Chem. C* **2009,** *113*, 21068-21073.

56. Zhang, S.; Xu, W.; Zeng, M.; Li, J.; Li, J.; Xu, J.; Wang, X., Superior adsorption capacity of hierarchical iron oxide@magnesium silicate magnetic nanorods for fast removal of organic pollutants from aqueous solution. *J. Mater. Chem. A* **2013,** *1*, 11691-11697.

57. Kresge, C. T.; Leonowicz, M. E.; Roth, W. J.; Vartuli, J. C.; Beck, J. S., Ordered mesoporous molecular sieves synthesized by a liquid-crystal template mechanism. *Nature* **1992,** *359*, 710-712.

58. Qiao, Z.-A.; Zhang, L.; Guo, M.; Liu, Y.; Huo, Q., Synthesis of mesoporous silica nanoparticles via controlled hydrolysis and condensation of silicon alkoxide. *Chem. Mater.* **2009,** *21*, 3823-3829.

59. Zhao, D.; Huo, Q.; Feng, J.; Chmelka, B. F.; Stucky, G. D., Nonionic triblock and star diblock copolymer and oligomeric surfactant syntheses of highly ordered, hydrothermally stable, mesoporous silica structures. *J. Am. Chem. Soc.* **1998,** *120*, 6024-6036.

60. Anderson, M. T.; Martin, J. E.; Odinek, J. G.; Newcomer, P. P., Surfactant-templated silica mesophases formed in water:cosolvent mixtures. *Chem. Mater.* **1998,** *10*, 311-321.

61. Che, S.; Li, H.; Lim, S.; Sakamoto, Y.; Terasaki, O.; Tatsumi, T., Synthesis mechanism of cationic surfactant templating mesoporous silica under an acidic synthesis process. *Chem. Mater.* **2005,** *17*, 4103-4113.

62. Omer, L.; Ruthstein, S.; Goldfarb, D.; Talmon, Y., High-resolution cryogenic-electron microscopy reveals details of a hexagonal-to-bicontinuous cubic phase transition in mesoporous silica synthesis. *J. Am. Chem. Soc.* **2009,** *131*, 12466-12473.

63. Wu, S.-H.; Mou, C.-Y.; Lin, H.-P., Synthesis of mesoporous silica nanoparticles. *Chem. Soc. Rev.* **2013,** *42*, 3862-3875.

64. Meynen, V.; Cool, P.; Vansant, E. F., Verified syntheses of mesoporous materials. *Microporous Mesoporous Mater.* **2009,** *125*, 170-223.

65. Shin, Y.; Wang, L.-Q.; Chang, J. H.; Samuels, W. D.; Exarhos, G. J., Morphology control of hierarchically ordered ceramic materials prepared by surfactant-directed sol-gel mineralization of wood cellular structures. In

Studies in Surface Science and Catalysis, Park, S.-E.; Ryoo, R.; Ahn, W.-S.; Lee, C. W.; Chang, J.-S., Eds. Elsevier: **2003**, vol 146, pp 447-451.

66. Liu, Y.; Goebl, J.; Yin, Y., Templated synthesis of nanostructured materials. *Chem. Soc. Rev.* **2013,** *42*, 2610-2653.

67. Yang, P.; Deng, T.; Zhao, D.; Feng, P.; Pine, D.; Chmelka, B. F.; Whitesides, G. M.; Stucky, G. D., Hierarchically ordered oxides. *Science* **1998,** *282*, 2244-2246.

68. Sun, Z.; Deng, Y.; Wei, J.; Gu, D.; Tu, B.; Zhao, D., Hierarchically ordered macro-/mesoporous dilica monolith: tuning macropore entrance size for size-selective adsorption of proteins. *Chem. Mater.* **2011,** *23*, 2176-2184.

69. Tan, B.; Rankin, S. E., Dual latex/surfactant templating of hollow spherical silica particles with ordered mesoporous shells. *Langmuir* **2005,** *21*, 8180-8187.

70. Blas, H.; Save, M.; Pasetto, P.; Boissiere, C.; Sanchez, C.; Charleux, B., Elaboration of monodisperse spherical hollow particles with ordered mesoporous silica shells via dual latex/surfactant templating: radial orientation of mesopore channels. *Langmuir* **2008,** *24*, 13132-13137.

71. Capek, I., Sterically and electrosterically stabilized emulsion polymerization. Kinetics and preparation. *Adv. Colloid Interface Sci.* **2002,** *99*, 77-162.

72. Xue, C.; Wang, J.; Tu, B.; Zhao, D., Hierarchically porous silica with ordered mesostructure from confinement self-assembly in skeleton scaffolds. *Chem. Mater.* **2010,** *22*, 494-503.

73. Maekawa, H.; Esquena, J.; Bishop, S.; Solans, C.; Chmelka, B. F., Meso/macroporous inorganic oxide monoliths from polymer foams. *Adv. Mater.* **2003,** *15*, 591-596.

74. Yang, Z.; Niu, Z.; Cao, X.; Yang, Z.; Lu, Y.; Hu, Z.; Han, C. C., Template synthesis of uniform 1D mesostructured silica materials and their arrays in anodic alumina membranes. *Angew. Chem., Int. Ed. Engl.* **2003,** *42*, 4201-4203.

75. Platschek, B.; Keilbach, A.; Bein, T., Mesoporous structures confined in anodic alumina membranes. *Adv. Mater.* **2011,** *23*, 2395-2412.

76. Lee, W.; Ji, R.; Gosele, U.; Nielsch, K., Fast fabrication of long-range ordered porous alumina membranes by hard anodization. *Nat. Mater.* **2006,** *5*, 741-747.

77. Fang, X.; Liu, Z.; Hsieh, M.-F.; Chen, M.; Liu, P.; Chen, C.; Zheng, N., Hollow mesoporous aluminosilica spheres with perpendicular pore channels as catalytic nanoreactors. *ACS Nano* **2012,** *6*, 4434-4444.

78. Zhang, Q.; Zhang, T.; Ge, J.; Yin, Y., Permeable silica shell through surface-protected etching. *Nano Lett.* **2008,** *8*, 2867-2871.

79. Wong, Y. J.; Zhu, L.; Teo, W. S.; Tan, Y. W.; Yang, Y.; Wang, C.; Chen, H., Revisiting the Stöber method: inhomogeneity in silica shells. *J. Am. Chem. Soc.* **2011,** *133*, 11422-11425.

80. Wang, D. P.; Zeng, H. C., Creation of interior space, architecture of shell structure, and encapsulation of functional materials for mesoporous SiO_2 spheres. *Chem. Mater.* **2011,** *23*, 4886-4899.

81. Hwang, J.; Jo, C.; Hur, K.; Lim, J.; Kim, S.; Lee, J., Direct access to hierarchically porous inorganic oxide materials with three-dimensionally interconnected networks. *J. Am. Chem. Soc.* **2014,** *136*, 16066-16072.

82. Nishihara, H.; Mukai, S. R.; Yamashita, D.; Tamon, H., Ordered macroporous silica by ice templating. *Chem. Mater.* **2005,** *17*, 683-689.

83. Song, M.-G.; Kim, J.-Y.; Cho, S.-H.; Kim, J.-D., Mixed cationic–nonionic surfactant templating approach for the synthesis of mesoporous silica. *Langmuir* **2002,** *18*, 6110-6115.

84. Tian, B.; Liu, X.; Zhang, Z.; Tu, B.; Zhao, D., Syntheses of high-quality mesoporous materials directed by blends of nonionic amphiphiles under nonaqueous conditions. *J. Solid State Chem.* **2002,** *167*, 324-329.

85. Kuang, D.; Brezesinski, T.; Smarsly, B., Hierarchical porous silica materials with a trimodal pore system using surfactant templates. *J. Am. Chem. Soc.* **2004,** *126*, 10534-10535.

86. Schacht, S.; Huo, Q.; Voigt-Martin, I. G.; Stucky, G. D.; Schüth, F., Oil-water interface templating of mesoporous macroscale structures. *Science* **1996,** *273*, 768-771.

87. Imhof, A.; Pine, D. J., Ordered macroporous materials by emulsion templating. *Nature* **1997,** *389*, 948-951.

88. Moulik, S. P.; Paul, B. K., Structure, dynamics and transport properties of microemulsions. *Adv. Colloid Interface Sci.* **1998,** *78*, 99-195.

89. Du, X.; Shi, B.; Liang, J.; Bi, J.; Dai, S.; Qiao, S. Z., Developing functionalized dendrimer-like silica nanoparticles with hierarchical pores as advanced delivery nanocarriers. *Adv. Mater.* **2013,** *25*, 5981-5985.

90. Moon, D.-S.; Lee, J.-K., Tunable synthesis of hierarchical mesoporous silica nanoparticles with radial wrinkle structure. *Langmuir* **2012,** *28*, 12341-12347.

91. Polshettiwar, V.; Cha, D.; Zhang, X.; Basset, J. M., High-surface-area silica nanospheres (KCC-1) with a fibrous morphology. *Angew. Chem., Int. Ed. Engl.* **2010,** *49*, 9652-9656.

92. Choi, Y.; Yun, Y. S.; Park, H.; Park, D. S.; Yun, D.; Yi, J., A facile approach for the preparation of tunable acid nano-catalysts with a hierarchically mesoporous structure. *Chem. Commun. (Cambridge, U. K.)* **2014,** *50*, 7652-7655.

93. Zhao, D.; Yang, P.; Chmelka, B. F.; Stucky, G. D., Multiphase assembly of mesoporous–macroporous membranes. *Chem. Mater.* **1999,** *11*, 1174-1178.

94. Baerlocher, C.; McCusker, L. B.; Olson, D. H., *Atlas of Zeolite Framework Types*. 6 ed.; Elsevier: Amsterdam, **2007**.

95. Primo, A.; Garcia, H., Zeolites as catalysts in oil refining. *Chem. Soc. Rev.* **2014,** *43*, 7548-7561.

96. Robson, H.; Lillerud, K. P., *Veryfied Syntheses of Zeolitic Materials*. 2 ed.; Elsevier: Amsterdam, **2001**.

97. Serrano, D. P.; Escola, J. M.; Pizarro, P., Synthesis strategies in the search for hierarchical zeolites. *Chem. Soc. Rev.* **2013,** *42*, 4004-4035.

98. Moller, K.; Bein, T., Mesoporosity -- a new dimension for zeolites. *Chem. Soc. Rev.* **2013,** *42*, 3689-3707.

99. Perez-Ramirez, J., Zeolite nanosystems: imagination has no limits. *Nat. Chem.* **2012,** *4*, 250-251.

100. Tao, Y.; Kanoh, H.; Abrams, L.; Kaneko, K., Mesopore-modified zeolites: preparation, characterization, and applications. *Chem. Rev.* **2006,** *106*, 896-910.

101. Perez-Ramirez, J.; Christensen, C. H.; Egeblad, K.; Christensen, C. H.; Groen, J. C., Hierarchical zeolites: enhanced utilisation of microporous crystals in catalysis by advances in materials design. *Chem. Soc. Rev.* **2008,** *37*, 2530-2542.

102. Cundy, C. S.; Cox, P. A., The hydrothermal synthesis of zeolites: precursors, intermediates and reaction mechanism. *Microporous Mesoporous Mater.* **2005,** *82*, 1-78.

103. Jacobsen, C. J. H.; Madsen, C.; Houzvicka, J.; Schmidt, I.; Carlsson, A., Mesoporous zeolite single crystals. *J. Am. Chem. Soc.* **2000,** *122*, 7116-7117.

104. Fan, W.; Snyder, M. A.; Kumar, S.; Lee, P.-S.; Yoo, W. C.; McCormick, A. V.; Lee Penn, R.; Stein, A.; Tsapatsis, M., Hierarchical nanofabrication of microporous crystals with ordered mesoporosity. *Nat. Mater.* **2008,** *7*, 984-991.

105. White, R. J.; Fischer, A.; Goebel, C.; Thomas, A., A sustainable template for mesoporous zeolite synthesis. *J. Am. Chem. Soc.* **2014,** *136*, 2715-2718.

106. Madsen, C.; Madsen, C.; J. H. Jacobsen, C., Nanosized zeolite crystals-convenient control of crystal size distribution by confined space synthesis. *Chem. Commun. (Cambridge, U. K.)* **1999**, 673-674.

107. Cho, S. I.; Choi, S. D.; Kim, J. H.; Kim, G. J., Synthesis of ZSM-5 films and monoliths with bimodal micro/mesoscopic structures. *Adv. Funct. Mater.* **2004,** *14*, 49-54.

108. Tao, Y.; Kanoh, H.; Kaneko, K., ZSM-5 monolith of uniform mesoporous channels. *J. Am. Chem. Soc.* **2003,** *125*, 6044-6045.

109. Kustova, M.; Egeblad, K.; Zhu, K.; Christensen, C. H., Versatile route to zeolite single crystals with controlled mesoporosity: in situ sugar decomposition for templating of hierarchical zeolites. *Chem. Mater.* **2007,** *19*, 2915-2917.

110. Zhu, H.; Liu, Z.; Wang, Y.; Kong, D.; Yuan, X.; Xie, Z., Nanosized $CaCO_3$ as hard template for creation of intracrystal pores within silicalite-1 crystal. *Chem. Mater.* **2008,** *20*, 1134-1139.

111. Schmidt, I.; Boisen, A.; Gustavsson, E.; Ståhl, K.; Pehrson, S.; Dahl, S.; Carlsson, A.; Jacobsen, C. J. H., Carbon nanotube templated growth of mesoporous zeolite single crystals. *Chem. Mater.* **2001,** *13*, 4416-4418.

112. Chen, H.; Wydra, J.; Zhang, X.; Lee, P. S.; Wang, Z.; Fan, W.; Tsapatsis, M., Hydrothermal synthesis of zeolites with three-dimensionally ordered mesoporous-imprinted structure. *J. Am. Chem. Soc.* **2011,** *133*, 12390-12393.

113. Holland, B. T.; Abrams, L.; Stein, A., Dual templating of macroporous silicates with zeolitic microporous frameworks. *J. Am. Chem. Soc.* **1999,** *121*, 4308-4309.

114. Li, W. C.; Lu, A. H.; Palkovits, R.; Schmidt, W.; Spliethoff, B.; Schuth, F., Hierarchically structured monolithic silicalite-1 consisting of crystallized nanoparticles and its performance in the Beckmann rearrangement of cyclohexanone oxime. *J. Am. Chem. Soc.* **2005,** *127*, 12595-12600.

115. Wang, L.; Yin, C.; Shan, Z.; Liu, S.; Du, Y.; Xiao, F.-S., Bread-template synthesis of hierarchical mesoporous ZSM-5 zeolite with hydrothermally stable mesoporosity. *Colloids Surf. A* **2009,** *340*, 126-130.

116. Tao, H.; Li, C.; Ren, J.; Wang, Y.; Lu, G., Synthesis of mesoporous zeolite single crystals with cheap porogens. *J. Solid State Chem.* **2011,** *184*, 1820-1827.

117. Dong, A.; Wang, Y.; Tang, Y.; Zhang, Y.; Ren, N.; Gao, Z., Mechanically stable zeolite monoliths with three-dimensional ordered macropores by the transformation of mesoporous silica spheres. *Adv. Mater.* **2002,** *14*, 1506-1510.

118. Karlsson, A.; Stöcker, M.; Schmidt, R., Composites of micro- and mesoporous materials: simultaneous syntheses of MFI/MCM-41 like phases by a mixed template approach. *Microporous Mesoporous Mater.* **1999,** *27*, 181-192.

119. Zhu, J.; Zhu, Y.; Zhu, L.; Rigutto, M.; van der Made, A.; Yang, C.; Pan, S.; Wang, L.; Zhu, L.; Jin, Y.; Sun, Q.; Wu, Q.; Meng, X.; Zhang, D.; Han, Y.; Li, J.; Chu, Y.; Zheng, A.; Qiu, S.; Zheng, X.; Xiao, F. S., Highly mesoporous single-crystalline zeolite beta synthesized using a nonsurfactant cationic polymer as a dual-function template. *J. Am. Chem. Soc.* **2014,** *136*, 2503-2510.

120. Choi, M.; Na, K.; Kim, J.; Sakamoto, Y.; Terasaki, O.; Ryoo, R., Stable single-unit-cell nanosheets of zeolite MFI as active and long-lived catalysts. *Nature* **2009,** *461*, 246-249.

121. Na, K.; Jo, C.; Kim, J.; Cho, K.; Jung, J.; Seo, Y.; Messinger, R. J.; Chmelka, B. F.; Ryoo, R., Directing zeolite structures into hierarchically nanoporous architectures. *Science* **2011,** *333*, 328-332.

122. Choi, M.; Cho, H. S.; Srivastava, R.; Venkatesan, C.; Choi, D. H.; Ryoo, R., Amphiphilic organosilane-directed synthesis of crystalline zeolite with tunable mesoporosity. *Nat. Mater.* **2006,** *5*, 718-723.

123. Wang, H.; Pinnavaia, T. J., MFI zeolite with small and uniform intracrystal mesopores. *Angew. Chem., Int. Ed. Engl.* **2006,** *45*, 7603-7606.

124. Inayat, A.; Knoke, I.; Spiecker, E.; Schwieger, W., Assemblies of mesoporous FAU-type zeolite nanosheets. *Angew. Chem., Int. Ed. Engl.* **2012,** *51*, 1962-1965.

125. Serrano, D. P.; Aguado, J.; Escola, J. M.; Rodríguez, J. M.; Peral, Á., Hierarchical zeolites with enhanced textural and catalytic properties dynthesized from organofunctionalized seeds. *Chem. Mater.* **2006,** *18*, 2462-2464.

126. Serrano, D. P.; Aguado, J.; Morales, G.; Rodríguez, J. M.; Peral, A.; Thommes, M.; Epping, J. D.; Chmelka, B. F., Molecular and meso- and macroscopic properties of hierarchical nanocrystalline ZSM-5 zeolite prepared by seed silanization. *Chem. Mater.* **2009,** *21*, 641-654.

127. Srivastava, R.; Iwasa, N.; Fujita, S.; Arai, M., Synthesis of nanocrystalline MFI-zeolites with intracrystal mesopores and their application in fine chemical synthesis involving large molecules. *Chem. - Eur. J.* **2008,** *14*, 9507-9511.

128. Ohsuna, T.; Terasaki, O.; Nakagawa, Y.; Zones, S. I.; Hiraga, K., Electron microscopic study of intergrowth of MFI and MEL: crystal faults in B-MEL. *J. Phys. Chem. B* **1997,** *101*, 9881-9885.

129. Treacy, M. M. J.; Vaughan, D. E. W.; Strohmaier, K. G.; Newsam, J. M., Intergrowth segregation in FAU-EMT zeolite materials. *Proc. R. Soc. London Ser. A* **1996,** *452*, 813-840.

130. Okubo, T.; Wakihara, T.; Plévert, J.; Nair, S.; Tsapatsis, M.; Ogawa, Y.; Komiyama, H.; Yoshimura, M.; Davis, M. E., Heteroepitaxial growth of a zeolite. *Angew. Chem., Int. Ed. Engl.* **2001,** *40*, 1069-1071.

131. Zhang, X.; Liu, D.; Xu, D.; Asahina, S.; Cychosz, K. A.; Agrawal, K. V.; Al Wahedi, Y.; Bhan, A.; Al Hashimi, S.; Terasaki, O.; Thommes, M.; Tsapatsis, M., Synthesis of self-pillared zeolite nanosheets by repetitive branching. *Science* **2012,** *336*, 1684-1687.

132. Inayat, A.; Schneider, C.; Schwieger, W., Organic-free synthesis of layer-like FAU-type zeolites. *Chem. Commun. (Cambridge U. K.)* **2015,** *51*, 279-281.

133. Khaleel, M.; Wagner, A. J.; Mkhoyan, K. A.; Tsapatsis, M., On the rotational intergrowth of hierarchical FAU/EMT zeolites. *Angew. Chem., Int. Ed. Engl.* **2014,** *53*, 9456-9461.

134. Chal, R.; Gérardin, C.; Bulut, M.; van Donk, S., Overview and industrial assessment of synthesis strategies towards zeolites with mesopores. *ChemCatChem* **2011,** *3*, 67-81.

135. Kubelková, L.; Beran, S.; Malecka, A.; Mastikhin, V. M., Acidity of modified Y zeolites: Effect of nonskeletal Al, formed by hydrothermal treatment, dealumination with SiCl4, and cationic exchange with Al. *Zeolites* **1989,** *9*, 12-17.

136. Hong, Y.; Fripiat, J. J., Microporous characteristics of H・Y, H-ZSM-5 and H-mordenite dealuminated by calcination. *Microporous Mater.* **1995,** *4*, 323-334.

137. O'Donovan, A. W.; O'Connor, C. T.; Koch, K. R., Effect of acid and steam treatment of Na- and H-mordenite on their structural, acidic and catalytic properties. *Microporous Mater.* **1995,** *5*, 185-202.

138. McDaniel, C. V.; Maher, P. K. Stabilized zeolites. U. S. Patent 3449070, June 10, **1969**.

139. Scherzer, J., Dealuminated faujasite-type structures with SiO_2/Al_2O_3 ratios over 100. *J. Catal.* **1978,** *54*, 285-288.

140. Lynch, J.; Raatz, F.; Dufresne, P., Characterization of the textural properties of dealuminated HY forms. *Zeolites* **1987,** *7*, 333-340.

141. van Donk, S.; Janssen, A. H.; Bitter, J. H.; de Jong, K. P., Generation, characterization, and impact of mesopores in zeolite catalysts. *Catal. Rev.* **2003,** *45*, 297-319.

142. Kortunov, P.; Vasenkov, S.; Karger, J.; Valiullin, R.; Gottschalk, P.; Elia, M. F.; Perez, M.; Stocker, M.; Drescher, B.; McElhiney, G.; Berger, C.; Glaser, R.; Weitkamp, J., The role of mesopores in intracrystalline transport in USY zeolite: PFG NMR diffusion study on various length scales. *J. Am. Chem. Soc.* **2005,** *127*, 13055-13059.

143. Groen, J. C.; Moulijn, J. A.; Pérez-Ramírez, J., Desilication: on the controlled generation of mesoporosity in MFI zeolites. *J. Mater. Chem.* **2006,** *16*, 2121-2131.

144. Groen, J. C.; Bach, T.; Ziese, U.; Paulaime-van Donk, A. M.; de Jong, K. P.; Moulijn, J. A.; Perez-Ramirez, J., Creation of hollow zeolite architectures by

controlled desilication of Al-zoned ZSM-5 crystals. *J. Am. Chem. Soc.* **2005,** *127*, 10792-10793.

145. Groen, J. C.; Jansen, J. C.; Moulijn, J. A.; Pérez-Ramírez, J., Optimal aluminum-assisted mesoporosity development in MFI zeolites by desilication. *J. Phys. Chem. B* **2004,** *108*, 13062-13065.

146. Verboekend, D.; Mitchell, S.; Milina, M.; Groen, J. C.; Pérez-Ramírez, J., Full compositional flexibility in the preparation of mesoporous MFI zeolites by desilication. *J. Phys. Chem. C* **2011,** *115*, 14193-14203.

147. Verboekend, D.; Perez-Ramirez, J., Desilication mechanism revisited: highly mesoporous all-silica zeolites enabled through pore-directing agents. *Chem. - Eur. J.* **2011,** *17*, 1137-1147.

148. Verboekend, D.; Pérez-Ramírez, J., Design of hierarchical zeolite catalysts by desilication. *Catal. Sci. Technol.* **2011,** *1*, 879-890.

149. Verboekend, D.; Vilé, G.; Pérez-Ramírez, J., Mesopore formation in USY and beta zeolites by base leaching: selection criteria and optimization of pore-directing agents. *Cryst. Growth Des.* **2012,** *12*, 3123-3132.

150. Wender, I., Reactions of synthesis gas. *Fuel Process. Technol.* **1996,** *48*, 189-297.

151. Chinchen, G. C.; Denny, P. J.; Jennings, J. R.; Spencer, M. S.; Waugh, K. C., Synthesis of methanol: Part 1. catalysts and kinetics. *Appl. Catal.* **1988,** *36*, 1-65.

152. Behrens, M., Coprecipitation: An excellent tool for the synthesis of supported metal catalysts – From the understanding of the well known recipes to new materials. *Catal. Today* **2015,** *246*, 46-54.

153. Grabow, L. C.; Mavrikakis, M., Mechanism of methanol synthesis on Cu through CO_2 and CO hydrogenation. *ACS Catal.* **2011,** *1*, 365-384.

154. Natesakhawat, S.; Lekse, J. W.; Baltrus, J. P.; Ohodnicki, P. R.; Howard, B. H.; Deng, X.; Matranga, C., Active sites and structure–activity relationships of copper-based catalysts for carbon dioxide hydrogenation to methanol. *ACS Catal.* **2012,** *2*, 1667-1676.

155. Behrens, M.; Studt, F.; Kasatkin, I.; Kühl, S.; Hävecker, M.; Abild-Pedersen, F.; Zander, S.; Girgsdies, F.; Kurr, P.; Kniep, B.-L.; Tovar, M.; Fischer, R. W.; Norskov, J. K.; Schlögl, R., The active site of methanol synthesis over $Cu/ZnO/Al_2O_3$ industrial catalysts. *Science* **2012,** *336*, 893-897.

156. Zander, S.; Kunkes, E. L.; Schuster, M. E.; Schumann, J.; Weinberg, G.; Teschner, D.; Jacobsen, N.; Schlogl, R.; Behrens, M., The role of the oxide component in the development of copper composite catalysts for methanol synthesis. *Angew. Chem., Int. Ed. Engl.* **2013,** *52*, 6536-6540.

157. Klier, K.; Chatikavanij, V.; Herman, R. G.; Simmons, G. W., Catalytic synthesis of methanol from CO/H_2. *J. Catal.* **1982,** *74*, 343-360.

158. Wu, J.; Saito, M.; Takeuchi, M.; Watanabe, T., The stability of Cu/ZnO-based catalysts in methanol synthesis from a CO_2-rich feed and from a CO-rich feed. *Appl. Catal. A* **2001,** *218*, 235-240.

159. Gao, P.; Li, F.; Zhan, H.; Zhao, N.; Xiao, F.; Wei, W.; Zhong, L.; Wang, H.; Sun, Y., Influence of Zr on the performance of Cu/Zn/Al/Zr catalysts via hydrotalcite-like precursors for CO_2 hydrogenation to methanol. *J. Catal.* **2013,** *298*, 51-60.

160. Arena, F.; Barbera, K.; Italiano, G.; Bonura, G.; Spadaro, L.; Frusteri, F., Synthesis, characterization and activity pattern of Cu–ZnO/ZrO_2 catalysts in the hydrogenation of carbon dioxide to methanol. *J. Catal.* **2007,** *249*, 185-194.

161. Meshkini, F.; Taghizadeh, M.; Bahmani, M., Investigating the effect of metal oxide additives on the properties of Cu/ZnO/Al_2O_3 catalysts in methanol synthesis from syngas using factorial experimental design. *Fuel* **2010,** *89*, 170-175.

162. Arena, F.; Mezzatesta, G.; Zafarana, G.; Trunfio, G.; Frusteri, F.; Spadaro, L., Effects of oxide carriers on surface functionality and process performance of the Cu–ZnO system in the synthesis of methanol via CO_2 hydrogenation. *J. Catal.* **2013,** *300*, 141-151.

163. Guo, X.; Mao, D.; Wang, S.; Wu, G.; Lu, G., Combustion synthesis of CuO–ZnO–ZrO_2 catalysts for the hydrogenation of carbon dioxide to methanol. *Catal. Commun.* **2009,** *10*, 1661-1664.

164. Guo, X.; Mao, D.; Lu, G.; Wang, S.; Wu, G., Glycine–nitrate combustion synthesis of CuO–ZnO–ZrO_2 catalysts for methanol synthesis from CO_2 hydrogenation. *J. Catal.* **2010,** *271*, 178-185.

165. Zhang, L.; Zhang, Y.; Chen, S., Effect of promoter SiO_2, TiO_2 or SiO_2-TiO_2 on the performance of CuO-ZnO-Al_2O_3 catalyst for methanol synthesis from CO_2 hydrogenation. *Appl. Catal. A* **2012,** *415-416*, 118-123.

166. Wu, J.; Luo, S.; Toyir, J.; Saito, M.; Takeuchi, M.; Watanabe, T., Optimization of preparation conditions and improvement of stability of Cu/ZnO-based multicomponent catalysts for methanol synthesis from CO_2 and H_2. *Catal. Today* **1998,** *45*, 215-220.

167. Graciani, J.; Mudiyanselage, K.; Xu, F.; Baber, A. E.; Evans, J.; Senanayake, S. D.; Stacchiola, D. J.; Liu, P.; Hrbek, J.; Fernandez Sanz, J.; Rodriguez, J. A., Catalysis. Highly active copper-ceria and copper-ceria-titania catalysts for methanol synthesis from CO_2. *Science* **2014,** *345*, 546-550.

168. Toyir, J.; de la Piscina, P. R. r.; Fierro, J. L. G.; Homs, N. s., Highly effective conversion of CO_2 to methanol over supported and promoted copper-based catalysts: influence of support and promoter. *Appl. Catal. B* **2001,** *29*, 207-215.

169. Ladera, R.; Pérez-Alonso, F. J.; González-Carballo, J. M.; Ojeda, M.; Rojas, S.; Fierro, J. L. G., Catalytic valorization of CO_2 via methanol synthesis with Ga-promoted Cu–ZnO–ZrO_2 catalysts. *Appl. Catal. B* **2013,** *142-143*, 241-248.

170. Toyir, J.; Ramírez de la Piscina, P.; Fierro, J. L. G.; Homs, N., Catalytic performance for CO_2 conversion to methanol of gallium-promoted copper-based catalysts: influence of metallic precursors. *Appl. Catal. B* **2001,** *34*, 255-266.

171. Słoczyński, J.; Grabowski, R.; Olszewski, P.; Kozłowska, A.; Stoch, J.; Lachowska, M.; Skrzypek, J., Effect of metal oxide additives on the activity and stability of Cu/ZnO/ZrO_2 catalysts in the synthesis of methanol from CO2 and H2. *Appl. Catal. A* **2006,** *310*, 127-137.

172. Dong, X.; Zhang, H.-B.; Lin, G.-D.; Yuan, Y.-Z.; Tsai, K. R., Highly active CNT-promoted Cu-ZnO-Al_2O_3 catalyst for methanol synthesis from H_2/CO/CO_2. *Catal. Lett.* **2003,** *85*, 237-246.

173. Zhang, M.-H.; Liu, Z.-M.; Lin, G.-D.; Zhang, H.-B., Pd/CNT-promoted Cu·ZrO_2/HZSM-5 hybrid catalysts for direct synthesis of DME from CO_2/H_2. *Appl. Catal. A* **2013,** *451*, 28-35.

174. Słoczyński, J.; Grabowski, R.; Kozłowska, A.; Olszewski, P.; Stoch, J.; Skrzypek, J.; Lachowska, M., Catalytic activity of the M/(3ZnO·ZrO_2) system (M=Cu, Ag, Au) in the hydrogenation of CO_2 to methanol. *Appl. Catal. A* **2004,** *278*, 11-23.

175. Liang, X.-L.; Dong, X.; Lin, G.-D.; Zhang, H.-B., Carbon nanotube-supported Pd–ZnO catalyst for hydrogenation of CO_2 to methanol. *Appl. Catal. B* **2009,** *88*, 315-322.

176. Collins, S. E.; Chiavassa, D. L.; Bonivardi, A. L.; Baltanás, M. A., Hydrogen spillover in Ga_2O_3–Pd/SiO_2 catalysts for methanol synthesis from CO_2/H_2. *Catal. Lett.* **2005,** *103*, 83-88.

177. Studt, F.; Sharafutdinov, I.; Abild-Pedersen, F.; Elkjaer, C. F.; Hummelshoj, J. S.; Dahl, S.; Chorkendorff, I.; Norskov, J. K., Discovery of a Ni-Ga catalyst for carbon dioxide reduction to methanol. *Nat. Chem.* **2014,** *6*, 320-324.

178. Bansode, A.; Urakawa, A., Towards full one-pass conversion of carbon dioxide to methanol and methanol-derived products. *J. Catal.* **2014,** *309*, 66-70.

179. Joo, O.-S.; Jung, K.-D.; Moon, I.; Rozovskii, A. Y.; Lin, G. I.; Han, S.-H.; Uhm, S.-J., Carbon dioxide hydrogenation to form methanol via a reverse-water-gas-shift reaction (the CAMERE process). *Ind. Eng. Chem. Res.* **1999,** *38*, 1808-1812.

180. Xu, X.; Moulijn, J. A., Mitigation of CO_2 by chemical conversion: plausible chemical reactions and promising products. *Energy Fuels* **1996,** *10*, 305-325.

181. Ratnasamy, C.; Wagner, J. P., Water gas shift catalysis. *Catal. Rev.* **2009,** *51*, 325-440.

182. Chen, C.-S.; Cheng, W.-H.; Lin, S.-S., Enhanced activity and stability of a Cu/SiO_2 catalyst for the reverse water gas shift reaction by an iron promoter. *Chem. Commun. (Cambridge U. K.)* **2001**, 1770-1771.

183. Chen, C. S.; Cheng, W. H.; Lin, S. S., Study of iron-promoted Cu/SiO_2 catalyst on high temperature reverse water gas shift reaction. *Appl. Catal. A* **2004,** *257*, 97-106.

184. Iijima, S., Helical microtubules of graphitic carbon. *Nature* **1991,** *354*, 56-58.

185. Planeix, J. M.; Coustel, N.; Coq, B.; Brotons, V.; Kumbhar, P. S.; Dutartre, R.; Geneste, P.; Bernier, P.; Ajayan, P. M., Application of carbon nanotubes as supports in heterogeneous catalysis. *J. Am. Chem. Soc.* **1994,** *116*, 7935-7936.

186. Wang, D.; Liu, Y.; Yu, B.; Zhou, F.; Liu, W., TiO_2 Nanotubes with tunable morphology, diameter, and length: synthesis and photo-electrical/catalytic performance. *Chem. Mater.* **2009,** *21*, 1198-1206.

187. Kong, J.; Franklin, N. R.; Zhou, C.; Chapline, M. G.; Peng, S.; Cho, K.; Dai, H., Nanotube molecular wires as chemical sensors. *Science* **2000,** *287*, 622-625.

188. Son, S. J.; Reichel, J.; He, B.; Schuchman, M.; Lee, S. B., Magnetic nanotubes for magnetic-field-assisted bioseparation, biointeraction, and drug delivery. *J. Am. Chem. Soc.* **2005,** *127*, 7316-7317.

189. Dai, H., Carbon nanotubes: synthesis, integration, and properties. *Acc. Chem. Res.* **2002,** *35*, 1035-1044.

190. Kijima, T.; Yoshimura, T.; Uota, M.; Ikeda, T.; Fujikawa, D.; Mouri, S.; Uoyama, S., Noble-metal nanotubes (Pt, Pd, Ag) from lyotropic mixed-surfactant liquid-crystal templates. *Angew. Chem., Int. Ed. Engl.* **2004,** *43*, 228-232.

191. Fan, H. J.; Knez, M.; Scholz, R.; Nielsch, K.; Pippel, E.; Hesse, D.; Zacharias, M.; Gösele, U., Monocrystalline spinel nanotube fabrication based on the Kirkendall effect. *Nat. Mater.* **2006,** *5*, 627-631.

192. Brigatti, M. F.; Galan, E.; Theng, B. K. G., Chapter 2 Structures and Mineralogy of Clay Minerals. In *Developments in Clay Science*, Bergaya, F.; Theng, B. K. G.; Lagaly, G., Eds. Elsevier: Amsterdam, **2006**, vol 1, pp 19-86.

193. Bradl, H. B., Adsorption of heavy metal ions on soils and soils constituents. *J. Colloid Interface Sci.* **2004,** *277*, 1-18.

194. Bhattacharyya, K. G.; Gupta, S. S., Adsorption of a few heavy metals on natural and modified kaolinite and montmorillonite: a review. *Adv. Colloid Interface Sci.* **2008,** *140*, 114-131.

195. Mukherjee, S.; Bartlow, V. M.; Nair, S., Phenomenology of the growth of single-walled aluminosilicate and aluminogermanate nanotubes of precise dimensions. *Chem. Mater.* **2005,** *17*, 4900-4909.

196. Amara, M. S.; Rouzière, S.; Paineau, E.; Bacia-Verloop, M.; Thill, A.; Launois, P., Hexagonalization of aluminogermanate imogolite nanotubes organized into closed-packed bundles. *J. Phys. Chem. C* **2014,** *118*, 9299-9306.

197. Srinivas, M.; Srinivasu, P.; Bhargava, S. K.; Kantam, M. L., Direct synthesis of two-dimensional mesoporous copper silicate as an efficient catalyst for synthesis of propargylamines. *Catal. Today* **2013,** *208*, 66-71.

198. Van Oosterwyck-Gastuche, M.-C., La structure de la chrysocolle. *C. R. Acad. Sci. Paris, Sér. D* **1970,** *271*, 1837-1840.

199. Decarreau, A.; Grauby, O.; Petit, S., The actual distribution of octahedral cations in 2:1 clay minerals: results from clay synthesis. *Appl. Clay Sci.* **1992,** *7*, 147-167.

200. Kelm, U.; Sanhueza, V.; Madejová, J.; Šucha, V.; Elsass, F., Evaluation of identification methods for chrysocolla - a Cu-smectite-like hydrous silicate: implications for heap-leaching extraction of copper. *Geol. Carpathica* **2001,** *52*, 111-121.

201. Frost, R. L.; Xi, Y., Is chrysocolla $(Cu,Al)_2H_2Si_2O_5(OH)_4 \cdot nH_2O$ related to spertiniite $Cu(OH)_2$?—A vibrational spectroscopic study. *Vib. Spectrosc.* **2013,** *64*, 33-38.

202. Mosser, C.; Mosser, A.; Romeo, M.; Petit, S.; Decarreau, A., Natural and synthetic copper phyllosilicates studied by XPS. *Clays Clay Miner.* **1992,** *40*, 593-599.

203. Frost, R. L.; Xi, Y.; Wood, B. J., Thermogravimetric analysis, PXRD, EDX and XPS study of chrysocolla $(Cu,Al)_2H_2Si_2O_5(OH)_4 \cdot nH_2O$-structural implications. *Thermochim. Acta* **2012,** *545*, 157-162.

204. Biesinger, M. C.; Lau, L. W. M.; Gerson, A. R.; Smart, R. S. C., Resolving surface chemical states in XPS analysis of first row transition metals, oxides and hydroxides: Sc, Ti, V, Cu and Zn. *Appl. Surf. Sci.* **2010,** *257*, 887-898.

205. Downs, R. T. In *The RRUFF Project: an integrated study of the chemistry, crystallography, Raman and infrared spectroscopy of minerals.*, the 19th General Meeting of the International Mineralogical Association, Kobe, Japan, Kobe, Japan, **2006**.

206. Bingöl, D.; Canbazoğlu, M.; Aydoğan, S., Dissolution kinetics of malachite in ammonia/ammonium carbonate leaching. *Hydrometallurgy* **2005,** *76*, 55-62.

207. Pauling, L., The structure of the chlorites. *Proc. Natl. Acad. Sci. U. S. A.* **1930,** *16*, 578-582.

208. Tenne, R., Inorganic nanotubes and fullerene-like nanoparticles. *Nat. Nanotechnol.* **2006,** *1*, 103-111.

209. Ravikovitch, P. I.; Wei, D.; Chueh, W. T.; Haller, G. L.; Neimark, A. V., Evaluation of pore structure parameters of MCM-41 catalyst supports and catalysts by means of nitrogen and argon adsorption. *J. Phys. Chem. B* **1997,** *101*, 3671-3679.

210. Solomon, E. I.; Jones, P. M.; May, J. A., Electronic structures of active sites on metal oxide surfaces: definition of the Cu/ZnO methanol synthesis catalyst by photoelectron spectroscopy. *Chem. Rev.* **1993,** *93*, 2623-2644.

211. Vesselli, E.; Rogatis, L. D.; Ding, X.; Baraldi, A.; Savio, L.; Vattuone, L.; Rocca, M.; Fornasiero, P.; Peressi, M.; Baldereschi, A.; Rosei, R.; Comelli, G., Carbon dioxide hydrogenation on Ni(110). *J. Am. Chem. Soc.* **2008,** *130*, 11417-11422.

212. Yang, Y.; White, M. G.; Liu, P., A Theoretical study of methanol synthesis from CO_2 hydrogenation on metal-doped Cu(111) surfaces. *J. Phys. Chem. C* **2012,** *116*, 248-256.

213. Davis, M. E., Ordered porous materials for emerging applications. *Nature* **2002,** *417*, 813-821.

214. Thoelen, C.; Walle, K. V. d.; Vankelecom, I. F. J.; Jacobs, P. A., The Use of M41S materials in chiral HPLC. *Chem. Commun. (Cambridge U. K.)* **1999**, 1841-1842.

215. Dou, J.; Zeng, H. C., Targeted synthesis of silicomolybdic acid (Keggin acid) inside mesoporous silica hollow spheres for Friedel-Crafts alkylation. *J. Am. Chem. Soc.* **2012,** *134*, 16235-16246.

216. Liu, Y.; Pinnavaia, T. J., Aluminosilicate nanoparticles for catalytic hydrocarbon cracking. *J. Am. Chem. Soc.* **2003,** *125*, 2376-2377.

217. Li, Z.; Zeng, H. C., Armored MOFs: enforcing soft microporous MOF nanocrystals with hard mesoporous silica. *J. Am. Chem. Soc.* **2014,** *136*, 5631-5639.

218. Schumacher, K.; du Fresne von Hohenesche, C.; Unger, K. K.; Ulrich, R.; Chesne, A. D.; Wiesner, U.; Spiess, H. W., The synthesis of spherical mesoporous molecular sieves MCM-48 with heteroatoms incorporated into the silica framework. *Adv. Mater.* **1999,** *11*, 1194-1198.

219. Vinu, A.; Murugesan, V.; Böhlmann, W.; Hartmann, M., An optimized procedure for the synthesis of AlSBA-15 with large pore diameter and high aluminum content. *J. Phys. Chem. B* **2004,** *108*, 11496-11505.

220. Ribeiro Carrott, M. M. L.; Conceição, F. L.; Lopes, J. M.; Carrott, P. J. M.; Bernardes, C.; Rocha, J.; Ramôa Ribeiro, F., Comparative study of Al-MCM materials prepared at room temperature with different aluminium sources and by some hydrothermal methods. *Microporous Mesoporous Mater.* **2006,** *92*, 270-285.

221. Muthu Kumaran, G.; Garg, S.; Soni, K.; Kumar, M.; Gupta, J. K.; Sharma, L. D.; Rama Rao, K. S.; Murali Dhar, G., Synthesis and characterization of acidic properties of Al-SBA-15 materials with varying Si/Al ratios. *Microporous Mesoporous Mater.* **2008,** *114*, 103-109.

222. Russo, P. A.; Ribeiro Carrott, M. M. L.; Carrott, P. J. M.; Lopes, J. M.; Ramôa Ribeiro, F.; Rocha, J., Structure and catalytic activity of Al-MCM-48 materials synthesised at room temperature: influence of the aluminium source and calcination conditions. *Microporous Mesoporous Mater.* **2008,** *114*, 293-302.

223. Lemaire, A.; Su, B.-L., Tailoring the porous hierarchy and the tetrahedral aluminum content by using carboxylate ligands: hierarchically structured macro-mesoporous aluminosilicates from a single molecular source. *Langmuir* **2010,** *26*, 17603-17616.

224. Wang, L.; Wang, A.; Li, X.; Zhou, F.; Hu, Y., Highly acidic mesoporous aluminosilicates prepared from preformed HY zeolite in Na_2SiO_3 alkaline buffer system. *J. Mater. Chem.* **2010,** *20*, 2232-2239.

225. El-Safty, S.; Shahat, A.; Ogawa, K.; Hanaoka, T., Highly ordered, thermally/hydrothermally stable cubic Ia3d aluminosilica monoliths with low silica in frameworks. *Microporous Mesoporous Mater.* **2011,** *138*, 51-62.

226. Lemaire, A.; Wang, Q.-Y.; Wei, Y.; Liu, Z.; Su, B.-L., Hierarchically structured meso-macroporous aluminosilicates with high tetrahedral aluminium content in acid catalysed esterification of fatty acids. *J. Colloid Interface Sci.* **2011,** *363*, 511-520.

227. El-Safty, S. A.; Shenashen, M. A.; Ismael, M.; Khairy, M., Mesocylindrical aluminosilica monolith biocaptors for size-selective macromolecule cargos. *Adv. Funct. Mater.* **2012,** *22*, 3013-3021.

228. Zou, J.-J.; Chang, N.; Zhang, X.; Wang, L., Isomerization and dimerization of pinene using Al-incorporated MCM-41 mesoporous materials. *ChemCatChem* **2012,** *4*, 1289-1297.

229. Fu, W. H.; Wu, S. J.; Wang, Y. M.; He, M. Y., Cubic Pm3n supermicroporous silicas and aluminosilicates templated by short-chain alkyltrimethylammonium surfactants. *J. Mater. Chem. A* **2014,** *2*, 14908-14917.

230. Parker, W. O. N.; Wegner, S., Aluminum in mesoporous silica–alumina. *Microporous Mesoporous Mater.* **2012,** *158*, 235-240.

231. Radnai, T., Structure of aqueous sodium aluminate solutions: a solution X-ray diffraction study. *J. Phys. Chem. A* **1998,** *102*, 7841-7850.

232. Sipos, P., The structure of Al(III) in strongly alkaline aluminate solutions — a review. *J. Mol. Liq.* **2009,** *146*, 1-14.

233. Hofmeister, F., Zur Lehre von der Wirkung der Salze. *Arch. Exp. Pathol. Pharmacol.* **1888,** *24*, 247-260.

234. Leontidis, E., Hofmeister anion effects on surfactant self-assembly and the formation of mesoporous solids. *Curr. Opin. Colloid Interface Sci.* **2002,** *7*, 81-91.

235. Jakubowska, A., Interactions of different counterions with cationic and anionic surfactants. *J. Colloid Interface Sci.* **2010,** *346*, 398-404.

236. Subramanian, V.; Ducker, W. A., Counterion effects on adsorbed micellar shape: experimental study of the role of polarizability and charge. *Langmuir* **2000,** *16*, 4447-4454.

237. Murgia, S.; Monduzzi, M.; Ninham, B. W., Hofmeister effects in cationic microemulsions. *Curr. Opin. Colloid Interface Sci.* **2004,** *9*, 102-106.

238. Wojciechowski, K.; Bitner, A.; Warszyński, P.; Żubrowska, M., The Hofmeister effect in zeta potentials of CTAB-stabilised toluene-in-water emulsions. *Colloids Surf. A* **2011,** *376*, 122-126.

239. Liu, M.-C.; Sheu, H.-S.; Cheng, S., Anion-exchange induced phase transformation of mesostructured silica. *J. Am. Chem. Soc.* **2009,** *131*, 3998-4005.

240. Zhou, Y.; Zeng, H. C., Simultaneous synthesis and assembly of noble metal nanoclusters with variable micellar templates. *J. Am. Chem. Soc.* **2014,** *136*, 13805-13817.

241. Lu, F.; Wu, S.-H.; Hung, Y.; Mou, C.-Y., Size effect on cell uptake in well-suspended, uniform mesoporous silica nanoparticles. *Small* **2009,** *5*, 1408-1413.

242. Chiang, Y.-D.; Lian, H.-Y.; Leo, S.-Y.; Wang, S.-G.; Yamauchi, Y.; Wu, K. C.-W., Controlling particle size and structural properties of mesoporous silica nanoparticles using the Taguchi method. *J. Phys. Chem. C* **2011,** *115*, 13158-13165.

243. Matsumoto, S.; Sherman, P., The viscosity of microemulsions. *J. Colloid Interface Sci.* **1969,** *30*, 525-536.

244. Qureshi, M.; Varshney, K. G., *Inorganic Ion Exchangers in Chemical Analysis*. CRC Press: Boca Raton, FL, **1991**.

245. Sing, K. S. W., Reporting physisorption data for gas/solid systems. *Pure Appl. Chem.* **1982,** *54*, 2201-2218.

246. Sakamoto, Y.; Kaneda, M.; Terasaki, O.; Zhao, D. Y.; Kim, J. M.; Stucky, G.; Shin, H. J.; Ryoo, R., Direct imaging of the pores and cages of three-dimensional mesoporous materials. *Nature* **2000,** *408*, 449-453.

247. Haag, W. O.; Lago, R. M.; Weisz, P. B., The active site of acidic aluminosilicate catalysts. *Nature* **1984,** *309*, 589-591.

248. Romero, A. A.; Alba, M. D.; Zhou, W.; Klinowski, J., Synthesis and characterization of the mesoporous silicate molecular sieve MCM-48. *J. Phys. Chem. B* **1997,** *101*, 5294-5300.

249. Handke, M.; Mozgawa, W., Vibrational spectroscopy of the amorphous silicates. *Vib. Spectrosc.* **1993,** *5*, 75-84.

250. Decottignies, M.; Phalippou, J.; Zarzycki, J., Synthesis of glasses by hot-pressing of gels. *J. Mater. Sci.* **1978,** *13*, 2605-2618.

251. Takahashi, R.; Sato, S.; Sodesawa, T.; Kawakita, M.; Ogura, K., High surface-area silica with controlled pore size prepared from nanocomposite of silica and citric acid. *J. Phys. Chem. B* **2000,** *104*, 12184-12191.

252. Yu, K. M. K.; Thompsett, D.; Tsang, S. C., Ultra-thin porous silica coated silver-platinum alloy nano-particle as a new catalyst precursor. *Chem. Commun. (Cambridge U. K.)* **2003**, 1522-1523.

253. Saniger, J. M., Al-O Infrared vibrational frequencies of γ-alumina. *Mater. Lett.* **1995,** *22*, 109-113.

254. Shen, J.; Cortright, R. D.; Chen, Y.; Dumesic, J. A., Microcalorimetric and infrared spectroscopic studies of γ-$A1_2O_3$ modified by basic metal oxides. *J. Phys. Chem.* **1994,** *98*, 8067-8073.

255. Gu, F. N.; Zhou, Y.; Wei, F.; Wang, Y.; Zhu, J. H., Creating the adsorptive sites with high performance toward nitrosamines in mesoporous silica MCM-41 by alumina modifier. *Microporous Mesoporous Mater.* **2009,** *126*, 143-151.

256. Miller, F. A.; Wilkins, C. H., Infrared spectra and characteristic frequencies of inorganic ions. *Anal. Chem.* **1952,** *24*, 1253-1294.

257. Cheralathan, K. K.; Hayashi, T.; Ogura, M., Post-synthesis coating of alumina on the mesopore walls of SBA-15 by ammonia/water vapour induced internal hydrolysis and its consequences on pore structure and acidity. *Microporous Mesoporous Mater.* **2008,** *116*, 406-415.

258. Tarte, P., Infra-red spectra of inorganic aluminates and characteristic vibrational frequencies of AlO_4 tetrahedra and AlO_6 octahedra. *Spectrochim. Acta* **1967,** *23A*, 2127-2143.

259. Kwon, S. G.; Hyeon, T., Formation mechanisms of uniform nanocrystals via hot-injection and heat-up methods. *Small* **2011,** *7*, 2685-2702.

260. Nakamura, T.; Mizutani, M.; Nozaki, H.; Suzuki, N.; Yano, K., Formation mechanism for monodispersed mesoporous silica spheres and its application to the synthesis of core/shell particles. *J. Phys. Chem. C* **2007,** *111*, 1093-1100.

261. Prieto, G.; Zečević, J.; Friedrich, H.; de Jong, K. P.; de Jongh, P. E., Towards stable catalysts by controlling collective properties of supported metal nanoparticles. *Nat. Mater.* **2013,** *12*, 34-39.

262. Meng, X.; Xiao, F. S., Green routes for synthesis of zeolites. *Chem. Rev.* **2014,** *114*, 1521-1543.

263. Dixit, S.; Crain, J.; Poon, W. C.; Finney, J. L.; Soper, A. K., Molecular segregation observed in a concentrated alcohol-water solution. *Nature* **2002,** *416*, 829-832.

264. Dutta, P. K.; Puri, M.; Bowers, C., Influence of D_2O and alcohols on the crystallization of zeolites. *ACS Symp. Ser.* **1989,** *398*, 98-109.

265. Huang, Y.; Yao, J.; Zhang, X.; Kong, C.; Chen, H.; Liu, D.; Tsapatsis, M.; Hill, M. R.; Hill, A. J.; Wang, H., Role of ethanol in sodalite crystallization in an ethanol–Na_2O–Al_2O_3–SiO_2–H_2O system. *CrystEngComm* **2011,** *13*, 4714.

266. Haas, A.; Harding, D. A.; Nee, J. R. D., FCC Catalysts containing the high-silica faujasites EMO and EMT for gas-oil cracking. *Microporous Mesoporous Mater.* **1999,** *28*, 325-333.

267. Delprato, F.; Delmotte, L.; Guth, J. L.; Huve, L., Synthesis of new silica-rich cubic and hexagonal faujasites using crown-ether-based supramolecules as templates. *Zeolites* **1990,** *10*, 546-552.

268. Ng, E.-P.; Chateigner, D.; Bein, T.; Valtchev, V.; Mintova, S., Capturing ultrasmall EMT zeolite from template-free systems. *Science* **2012,** *335*, 70-73.

269. Bullot, L.; Mulot, B.; Simon-Masseron, A.; Daou, T. J.; Chaplais, G.; Patarin, J., One shot synthesis of EMT-type zeolite nanocrystals aggregates for potential industrial applications. *Microporous Mesoporous Mater.* **2015,** *210*, 194-198.

270. Valtchev, V.; Tosheva, L., Porous nanosized particles: preparation, properties, and applications. *Chem. Rev.* **2013,** *113*, 6734-6760.

271. Roth, W. J.; Nachtigall, P.; Morris, R. E.; Cejka, J., Two-dimensional zeolites: current status and perspectives. *Chem. Rev.* **2014,** *114*, 4807-4837.

272. Zhai, Y.; Pierre, D.; Si, R.; Deng, W.; Ferrin, P.; Nilekar, A. U.; Peng, G.; Herron, J. A.; Bell, D. C.; Saltsburg, H.; Mavrikakis, M.; Flytzani-Stephanopoulos, M., Alkali-stabilized Pt-OHx species catalyze low-temperature water-gas shift reactions. *Science* **2010,** *329*, 1633-1636.

273. Yang, M.; Li, S.; Wang, Y.; Herron, J. A.; Xu, Y.; Allard, L. F.; Lee, S.; Huang, J.; Mavrikakis, M.; Flytzani-Stephanopoulos, M., Catalytically active Au-O(OH)x-species stabilized by alkali ions on zeolites and mesoporous oxides. *Science* **2014,** *346*, 1498-1501.

274. Kim, S. S.; Lee, H. H.; Hong, S. C., The effect of the morphological characteristics of TiO_2 supports on the reverse water–gas shift reaction over Pt/TiO_2 catalysts. *Appl. Catal. B* **2012,** *119-120*, 100-108.

275. Iwamoto, M.; Hasuwa, T.; Furukawa, H.; Kagawa, S., Water gas shift reaction catalyzed by metal ion-exchanged zeolites. *J. Catal.* **1983,** *79*, 291-297.

276. Jaeger, N. I.; Rathousky, J.; Schulz-Ekloff, G.; Svensson, A.; Zukal, A., Faujasite embedded platinum: zeolite framework texture and effect of metal dispersion on syngas conversion. *Stud. Surf. Sci. Catal.* **1989,** *49*, 1005-1013.

277. Borgschulte, A.; Callini, E.; Stadie, N.; Arroyo, Y.; Rossell, M. D.; Erni, R.; Geerlings, H.; Züttel, A.; Ferri, D., Manipulating the reaction path of the CO_2 hydrogenation reaction in molecular sieves. *Catal. Sci. Technol.* **2015,** *5*, 4613-4621.

278. Treacy, M. M. J.; Higgins, J. B., *Collection of Simulated XRD Powder Patterns for Zeolites*. 4 ed.; Elsevier: Amsterdam, **2001**.

279. Baerlocher, C.; McCusker, L. B.; Chiappetta, R., Location of the 18-Crown-6 template in EMC-2 (EMT) Rietveld refinement of the calcined and as-synthesized forms. *Microporous Mater.* **1994,** *2*, 269-280.

280. Lutterotti, L.; Matthies, S.; Wenk, H.-R., MAUD (Material Analysis Using Diffraction): a user friendly Java program for Rietveld texture analysis and more. *Proc. Int. Conf. Textures Mater., 12th* **1999,** *1*, 1599.

281. Popa, N. C., The (hkl) dependence of diffraction-line broadening caused by strain and size for all Laue groups in Rietveld refinement. *J. Appl. Crystallogr.* **1998,** *31*, 176-180.

282. Matthies, S.; Lutterotti, L.; Wenk, H. R., Advances in texture analysis from diffraction spectra. *J. Appl. Crystallogr.* **1997,** *30*, 31-42.

283. Treacy, M. M. J.; Newsam, J. M.; Deem, M. W., A general recursion method for calculating diffracted intensities from crystals containing planar faults. *Proc. R. Soc. London Ser. A* **1991,** *433*, 499-520.

284. Dougnier, F.; Patarin, J.; Guth, J. L.; Anglerot, D., Synthesis, characterization, and catalytic properties of silica-rich faujasite-type zeolite (FAU) and its hexagonal analog (EMT) prepared by using crown-ethers as templates. *Zeolites* **1992,** *12*, 160-166.

285. Martens, J. A.; Xiong, Y. L.; Feijen, E. J. P.; Grobet, P. J.; Jacobs, P. A., Phase discrimination with ^{29}Si MAS NMR in EMT/FAU zeolite intergrowths. *J. Phys. Chem.* **1993,** *97*, 5132-5135.

286. Sacco, A., Structure and dynamics of electrolyte solutions. a NMR relaxation approach. *Chem. Soc. Rev.* **1994,** *23*, 129-136.

287. Haramaki, H.; Shimomura, T.; Umecky, T.; Takamuku, T., SANS, Infrared, and ^{7}Li and ^{23}Na NMR studies on phase separation of alkali halide-acetonitrile-water mixtures by cooling. *J. Phys. Chem. B* **2013,** *117*, 2438-2448.

288. Holz, M.; Weingärtner, H.; Hertz, H.-G., Nuclear magnetic relaxation of alkali halide nuclei and preferential solvation in methanol+water mixtures. *J. Chem. Soc., Faraday Trans. 1* **1976,** *73*, 71-83.

289. Lange, K. M.; Bergmann, U.; Hodeck, K. F.; Konnecke, R.; Schade, U.; Aziz, E. F., Shared solvation of sodium ions in alcohol-water solutions explains the non-ideality of free energy of solvation. *Phys. Chem. Chem. Phys.* **2011,** *13*, 15423-15427.

290. Awala, H.; Gilson, J. P.; Retoux, R.; Boullay, P.; Goupil, J. M.; Valtchev, V.; Mintova, S., Template-free nanosized faujasite-type zeolites. *Nat. Mater.* **2015,** *14*, 447-451.

291. Itzel Meza, L.; Anderson, M. W.; Slater, B.; Agger, J. R., In situ atomic force microscopy of zeolite A dissolution. *Phys. Chem. Chem. Phys.* **2008,** *10*, 5066-5076.

292. Román-Martínez, M. C.; Cazorla-Amorós, D.; Linares-Solano, A.; Lecea, C. S.-M., CO_2 hydrogenation under pressure on catalysts Pt-Ca/C. *Appl. Catal. A* **1996,** *134*, 159-167.

293. Zugic, B.; Zhang, S.; Bell, D. C.; Tao, F. F.; Flytzani-Stephanopoulos, M., Probing the low-temperature water-gas shift activity of alkali-promoted platinum catalysts stabilized on carbon supports. *J. Am. Chem. Soc.* **2014,** *136*, 3238-3245.

294. Yang, M.; Liu, J.; Lee, S.; Zugic, B.; Huang, J.; Allard, L. F.; Flytzani-Stephanopoulos, M., A common single-site Pt(II)-O(OH)x- species stabilized by sodium on "active" and "inert" supports catalyzes the water-gas shift reaction. *J. Am. Chem. Soc.* **2015,** *137*, 3470-3473.

295. Moulder, J. F.; Stickle, W. F.; Sobol, P. E.; Bomben, K. D., *Handbook of X-ray Photoelectron Spectroscopy*. Perkin Elmer Corporation: Eden Prairie, **1992**.

296. Barr, T. L., An XPS study of Si as it occurs in adsorbents, catalysts, and thin films. *Appl. Surf. Sci.* **1983,** *15*, 1-35.

297. Estrade-szwarckopf, H.; Rousseau, B.; Herold, C.; Lagrange, P., Sodium - oxygen graphite intercalation compound: XPS, UPS and STM study. *Mol. Cryst. Liq. Cryst. Sci. Technol., Sect. A* **1998,** *310*, 231-236.

298. Liu, J.; Cheng, J.; Che, R.; Xu, J.; Liu, M.; Liu, Z., Synthesis and microwave absorption properties of yolk-shell microspheres with magnetic iron oxide cores and hierarchical copper silicate shells. *ACS Appl. Mater. Interfaces* **2013,** *5*, 2503-2509.

299. Liu, J.; Qiao, S. Z.; Liu, H.; Chen, J.; Orpe, A.; Zhao, D.; Lu, G. Q., Extension of the Stober method to the preparation of monodisperse resorcinol-formaldehyde resin polymer and carbon spheres. *Angew. Chem., Int. Ed. Engl.* **2011,** *50*, 5947-5951.

300. Fuertes, A. B.; Valle-Vigon, P.; Sevilla, M., One-step synthesis of silica@resorcinol-formaldehyde spheres and their application for the fabrication of polymer and carbon capsules. *Chem. Commun. (Cambridge, U. K.)* **2012,** *48*, 6124-6126.

301. Zhang, X.-B.; Tong, H.-W.; Liu, S.-M.; Yong, G.-P.; Guan, Y.-F., An improved Stöber method towards uniform and monodisperse Fe_3O_4@C nanospheres. *J. Mater. Chem. A* **2013,** *1*, 7488.

302. Fang, X.; Liu, S.; Zang, J.; Xu, C.; Zheng, M. S.; Dong, Q. F.; Sun, D.; Zheng, N., Precisely controlled resorcinol-formaldehyde resin coating for fabricating core-shell, hollow, and yolk-shell carbon nanostructures. *Nanoscale* **2013,** *5*, 6908-6916.

303. Zhang, F.; Meng, Y.; Gu, D.; Yan; Chen, Z.; Tu, B.; Zhao, D., An aqueous cooperative assembly route to synthesize ordered mesoporous carbons with controlled structures and morphology. *Chem. Mater.* **2006,** *18*, 5279-5288.

304. Liu, J.; Wickramaratne, N. P.; Qiao, S. Z.; Jaroniec, M., Molecular-based design and emerging applications of nanoporous carbon spheres. *Nat. Mater.* **2015,** *14*, 763-774.

305. Aguado, J.; Serrano, D. P.; Escola, J. M.; Rodríguez, J. M., Low temperature synthesis and properties of ZSM-5 aggregates formed by ultra-small nanocrystals. *Microporous Mesoporous Mater.* **2004,** *75*, 41-49.

306. Qin, Z.; Lakiss, L.; Tosheva, L.; Gilson, J.-P.; Vicente, A.; Fernandez, C.; Valtchev, V., Comparative study of nano-ZSM-5 catalysts synthesized in OH^- and F^- media. *Adv. Funct. Mater.* **2014,** *24*, 257-264.

307. Yaripour, F.; Shariatinia, Z.; Sahebdelfar, S.; Irandoukht, A., Effect of boron incorporation on the structure, products selectivities and lifetime of H-ZSM-5 nanocatalyst designed for application in methanol-to-olefins (MTO) reaction. *Microporous Mesoporous Mater.* **2015,** *203*, 41-53.

308. Qi, L.; Wei, Y.; Xu, L.; Liu, Z., Reaction behaviors and kinetics during induction period of methanol conversion on HZSM-5 zeolite. *ACS Catalysis* **2015,** *5*, 3973-3982.

309. Wang, C.; Zhang, D.; Fang, C.; Ge, Q.; Xu, H., Synthesis of gasoline from syngas in a dual layer catalyst system. *Fuel* **2014,** *134*, 11-16.

310. Montesano, R.; Narvaez, A.; Chadwick, D., Shape-selectivity effects in syngas-to-dimethyl ether conversion over $Cu/ZnO/Al_2O_3$ and zeolite mixtures: Carbon deposition and by-product formation. *App. Catal. A* **2014,** *482*, 69-77.

311. Li, C.; Yuan, X.; Fujimoto, K., Direct synthesis of LPG from carbon dioxide over hybrid catalysts comprising modified methanol synthesis catalyst and β-type zeolite. *App. Catal. A* **2014,** *475*, 155-160.

312. Kim, J.-H.; Park, M. J.; Kim, S. J.; Joo, O.-S.; Jung, K.-D., DME synthesis from synthesis gas on the admixed catalysts of $Cu/ZnO/Al_2O_3$ and ZSM-5. *App. Catal. A* **2004,** *264*, 37-41.

313. Nikolakis, V.; Tsapatsis, M.; Vlachos, D. G., Physicochemical characterization of silicalite-1 surface and its implications on crystal growth. *Langmuir* **2003,** *19*, 4619-4626.

314. Tung, V. C.; Allen, M. J.; Yang, Y.; Kaner, R. B., High-throughput solution processing of large-scale graphene. *Nat. Nanotechnol.* **2009,** *4*, 25-29.

315. Mackie, N. M.; Castner, D. G.; Fisher, E. R., Characterization of pulsed-plasma-polymerized aromatic films. *Langmuir* **1998,** *14*, 1227-1235.

316. Yang, D. Q.; Rochette, J. F.; Sacher, E., Spectroscopic evidence for pi-pi interaction between poly(diallyl dimethylammonium) chloride and multiwalled carbon nanotubes. *J. Phys. Chem. B* **2005,** *109*, 4481-4484.

317. Li, N.; Zhang, Q.; Liu, J.; Joo, J.; Lee, A.; Gan, Y.; Yin, Y., Sol-gel coating of inorganic nanostructures with resorcinol-formaldehyde resin. *Chem. Commun. (Cambridge, U. K.)* **2013,** *49*, 5135-5137.

318. Nellist, P. D.; Pennycook, S. J., The principles and interpretation of annular dark-field Z-contrast imaging. In *Adv. Imaging Electron Phys.*, Peter, W. H., Ed. Elsevier: **2000**, pp 147-203.

319. Rule, A. C.; Radke, F., Baileychlore, the Zn end member of the trioctahedral chlorite series. *Am. Mineral.* **1988,** *73*, 135-139.

320. Ernest, M. V.; Bibler, J. P.; Whitley, R. D.; Wang, N. H. L., Development of a carousel ion-exchange process for removal of cesium-137 from alkaline nuclear waste. *Ind. Eng. Chem. Res.* **1997,** *36*, 2775-2788.

321. Trevani, L. N.; Roberts, J. C.; Tremaine, P. R., Copper(II)–ammonia complexation equilibria in aqueous solutions at temperatures from 30 to 250°C by visible spectroscopy. *J. Solution Chem.* **2001,** *30*, 585-622.

322. Reinisch, M.; Perkins, C. L.; Steirer, K. X., Quantitative study on the chemical solution deposition of zinc oxysulfide. *ECS J. Solid State Sci. Technol.* **2015,** *5*, 58-66.

323. Singh, B. K.; Xu, D.; Han, L.; Ding, J.; Wang, Y.; Che, S., Synthesis of single-crystalline mesoporous ZSM-5 with three-dimensional pores via the self-assembly of a designed triply branched cationic surfactant. *Chem. Mater.* **2014,** *26*, 7183-7188.

324. Lunkenbein, T.; Schumann, J.; Behrens, M.; Schlogl, R.; Willinger, M. G., Formation of a ZnO overlayer in industrial $Cu/ZnO/Al_2O_3$ catalysts induced by strong metal-support interactions. *Angew. Chem., Int. Ed. Engl.* **2015,** *54*, 4544-4548.

325. Ordomsky, V. V.; Cai, M.; Sushkevich, V.; Moldovan, S.; Erson, O.; Lancelot, C.; Valtchev, V.; Khodakov, A. Y., The role of external acid sites of ZSM-5 in deactivation of hybrid CuZnAl/ZSM-5 catalyst for direct dimethyl ether synthesis from syngas. *Appl. Catal. A* **2014,** *486*, 266-275.

326. Stöcker, M., Methanol-to-hydrocarbons: catalytic materials and their behavior. *Microporous Mesoporous Mater.* **1999,** *29*, 3-48.

Appendix 1. Supplementary Materials for Chapter 5

A1.1. Morphology of MASS with varied Al contents

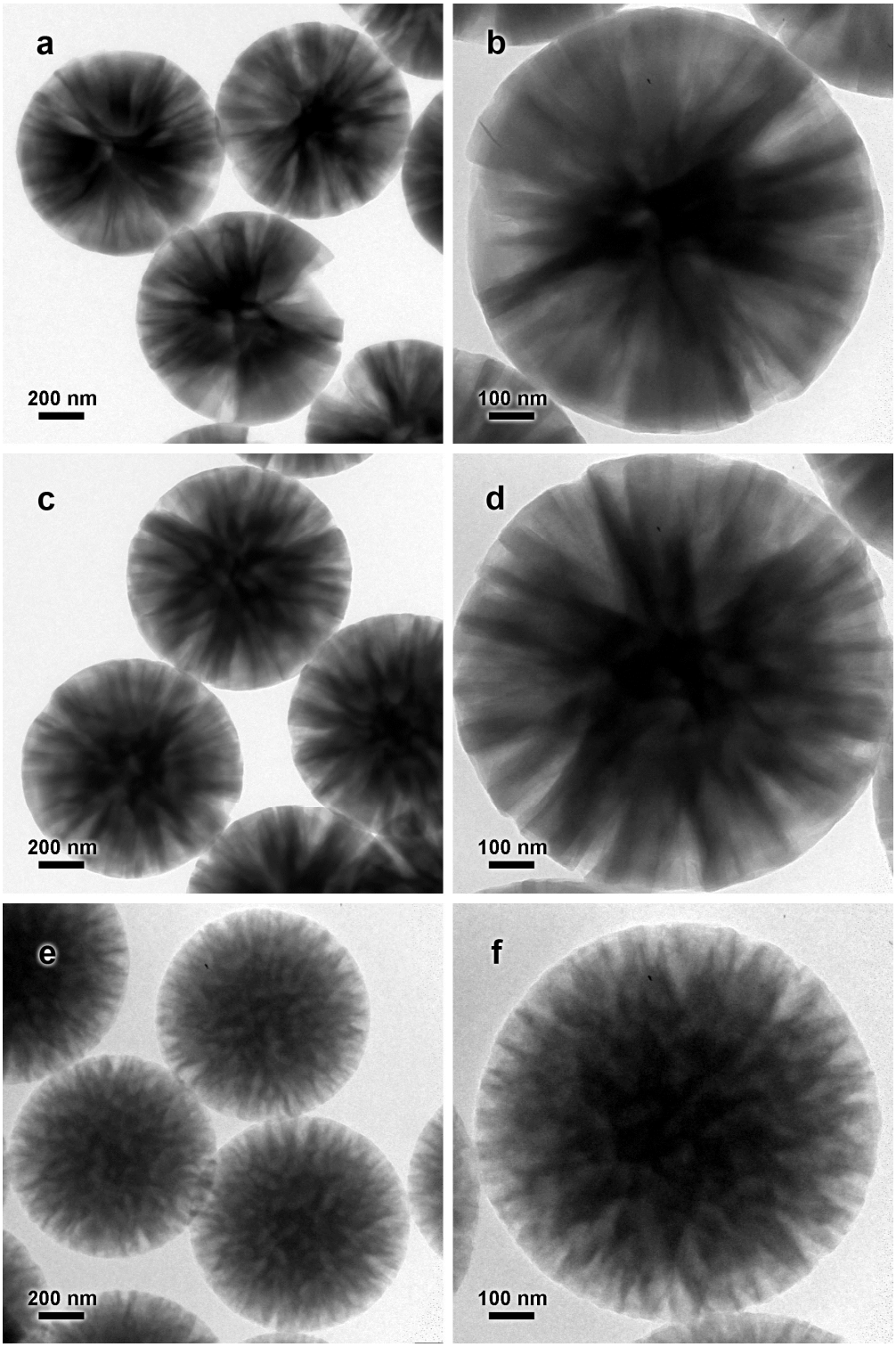

Figure A1.1. TEM images of (a,b) MASS-5, (c,d) MASS-10, (e,f) MASS-20, (g,h) MASS-25, (i,j) MASS-35 and (k,l) MASS-40

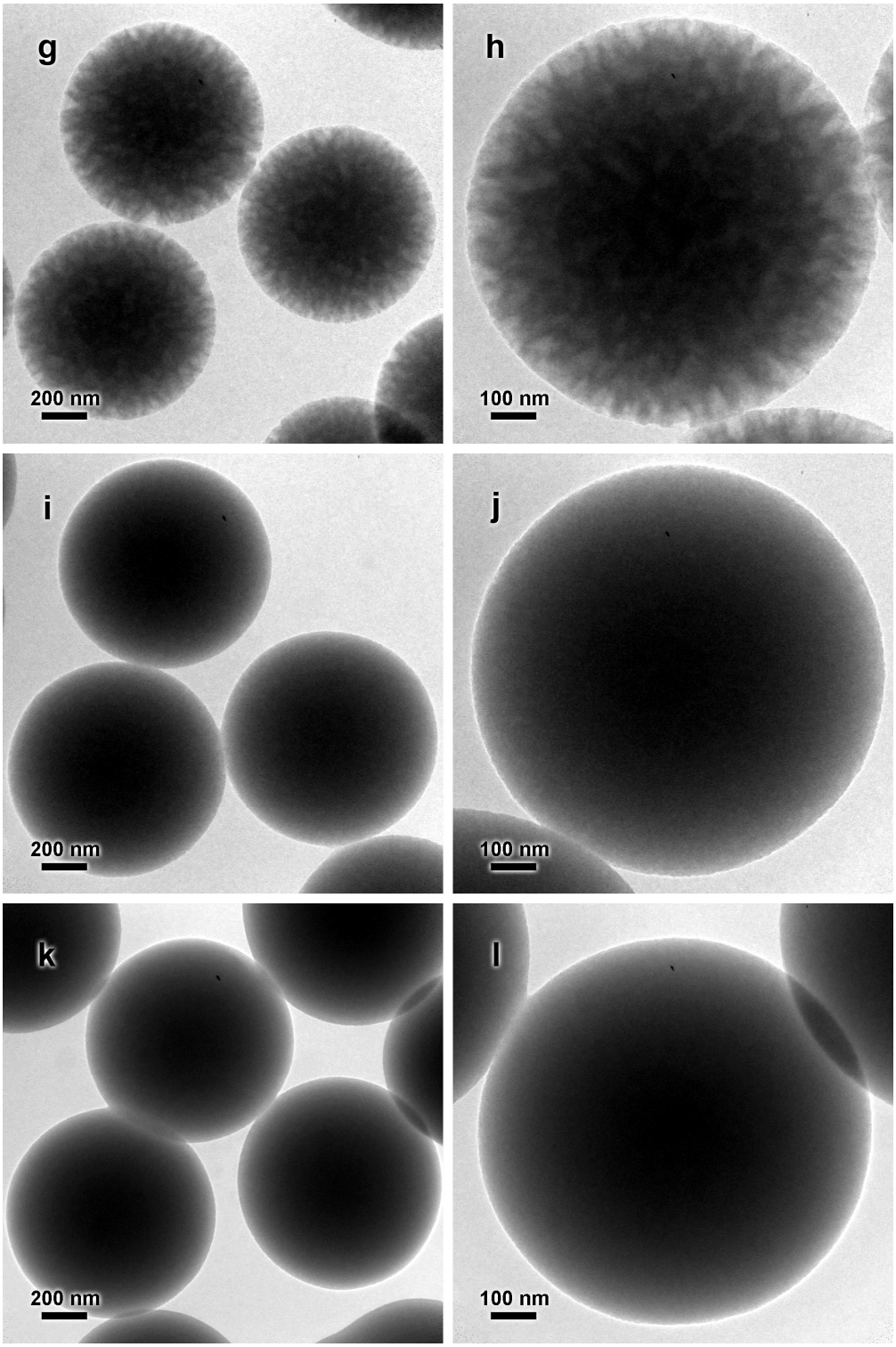

Figure A1.1 continued

A1.2. Morphology of MASS synthesized with varied water concentration

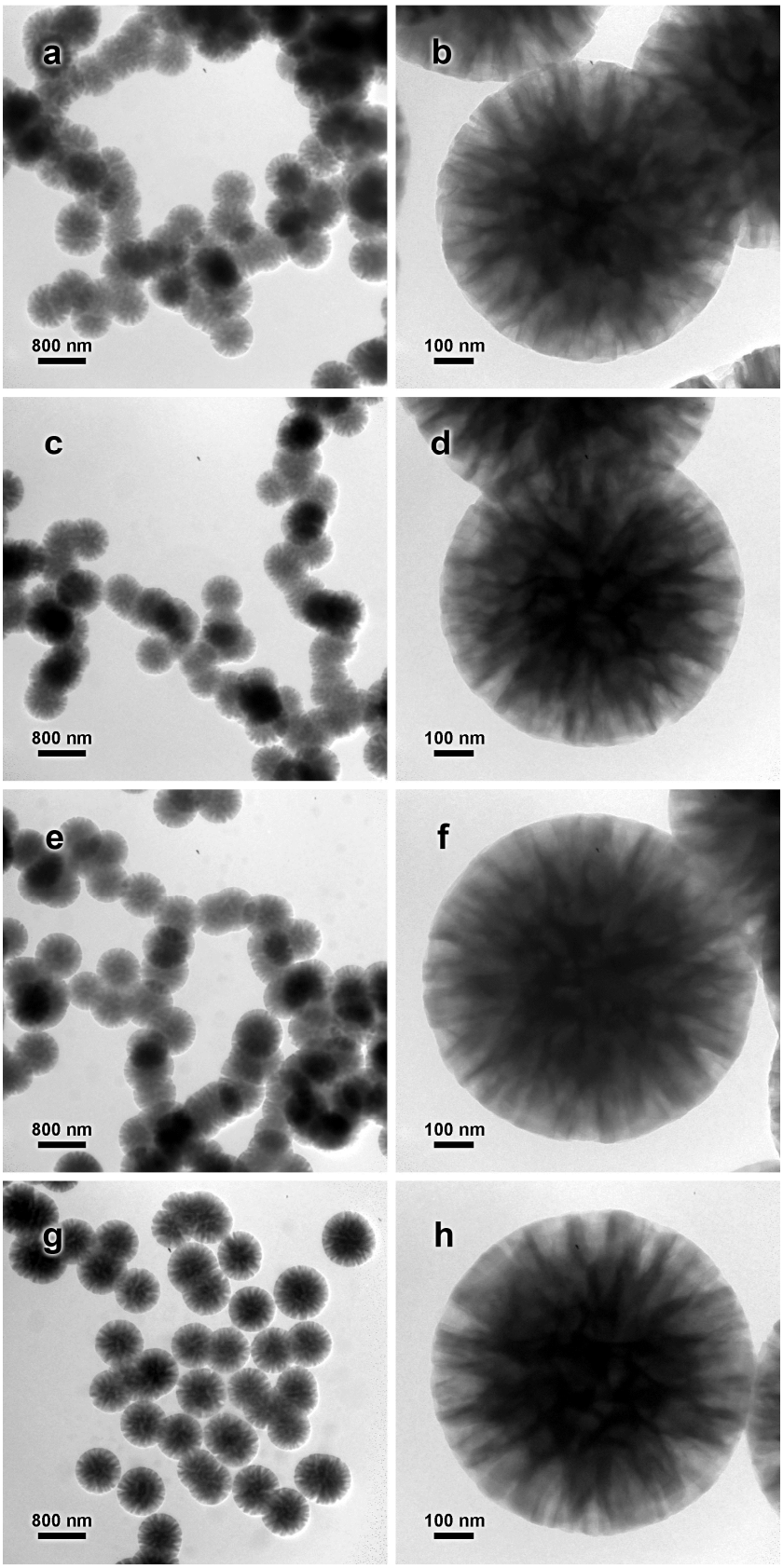

Figure A1.2. TEM images of MASS synthesized by a scaled-down procedure* with varied amounts of water: (a,b) 7.0 mL, (c,d) 7.25 mL, (e,f) 7.5 mL, (g,h) 7.75 mL, (i,j) 8.0 mL, (k,l) 8.25 mL, (m,n) 8.5 mL, and (o,p) 8.75 mL.

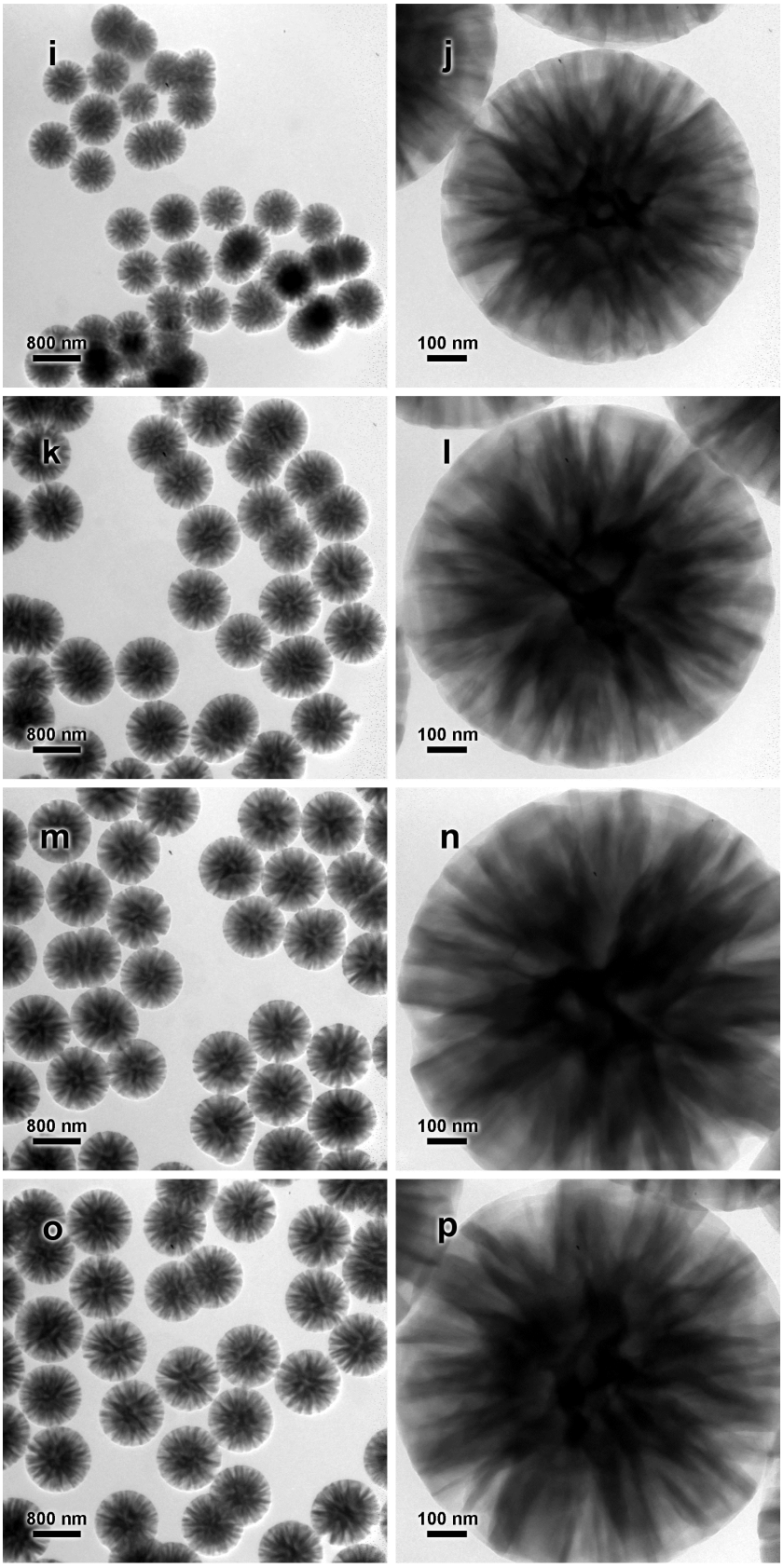

Figure A1.2 continued.
*Synthesis: 50 mg of CTAB, 60 μL of TEOS and 250 μL of toluene were dissolved in 8 mL of ethanol, and 4 mg of $NaAlO_2$ and 0.25 mL of 32% NH_3 were dissolved in certain amount of water. The aqueous phase was poured into the organic phase under stirring and the mixture was aged for 4 h at ambient temperature.

A1.3. Morphological effects of NH_3, CTAB and TEOS in MASS synthesis

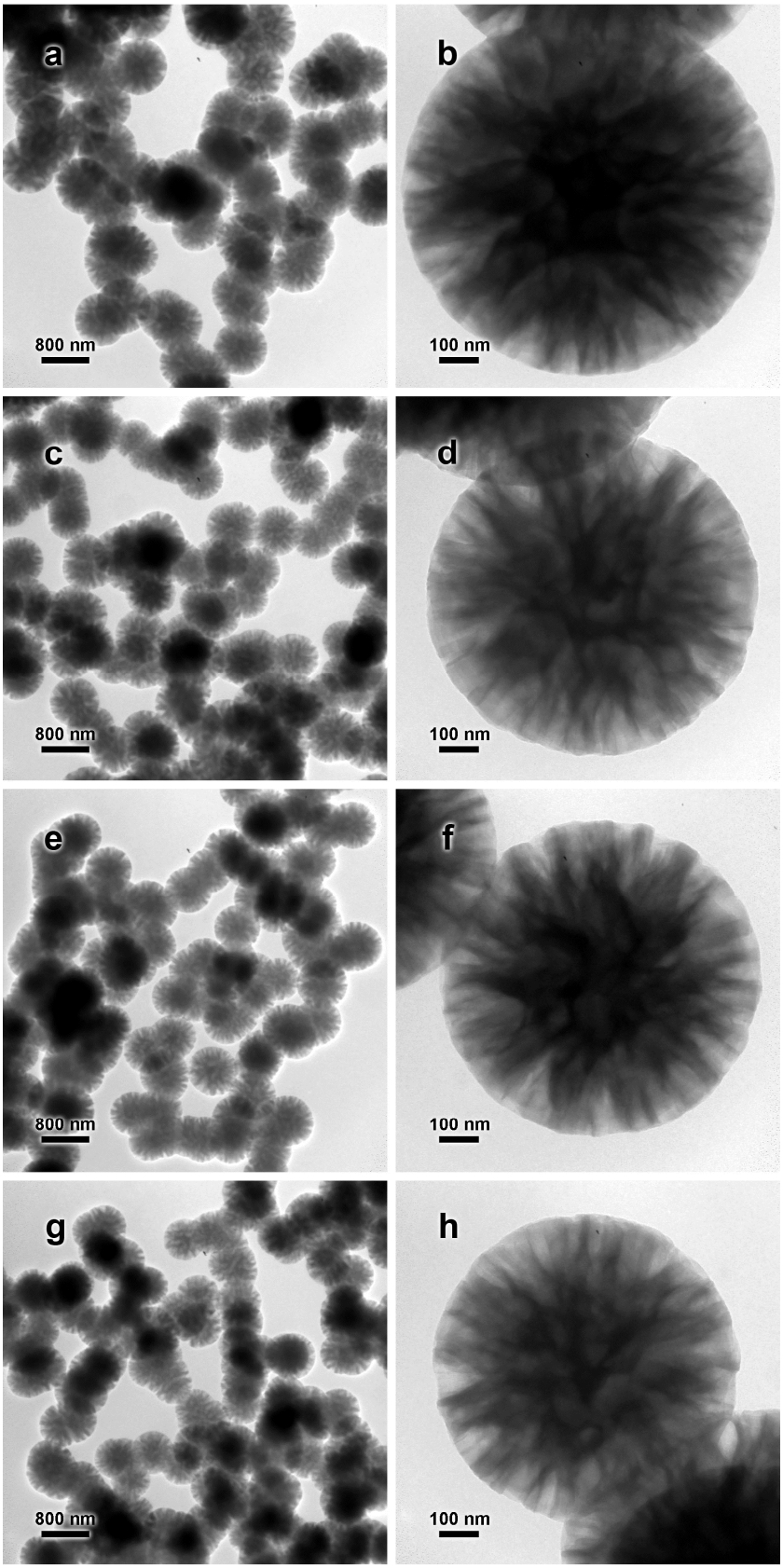

Figure A1.3. TEM images of MASS synthesized by the scaled-down procedure (see the note in Figure A1.2) using 7 mL of water and different amounts of 32% NH_3: (a,b) 0.1 mL, (c,d) 0.15 mL, (e,f) 0.2 mL, and (g,h) 0.3 mL.

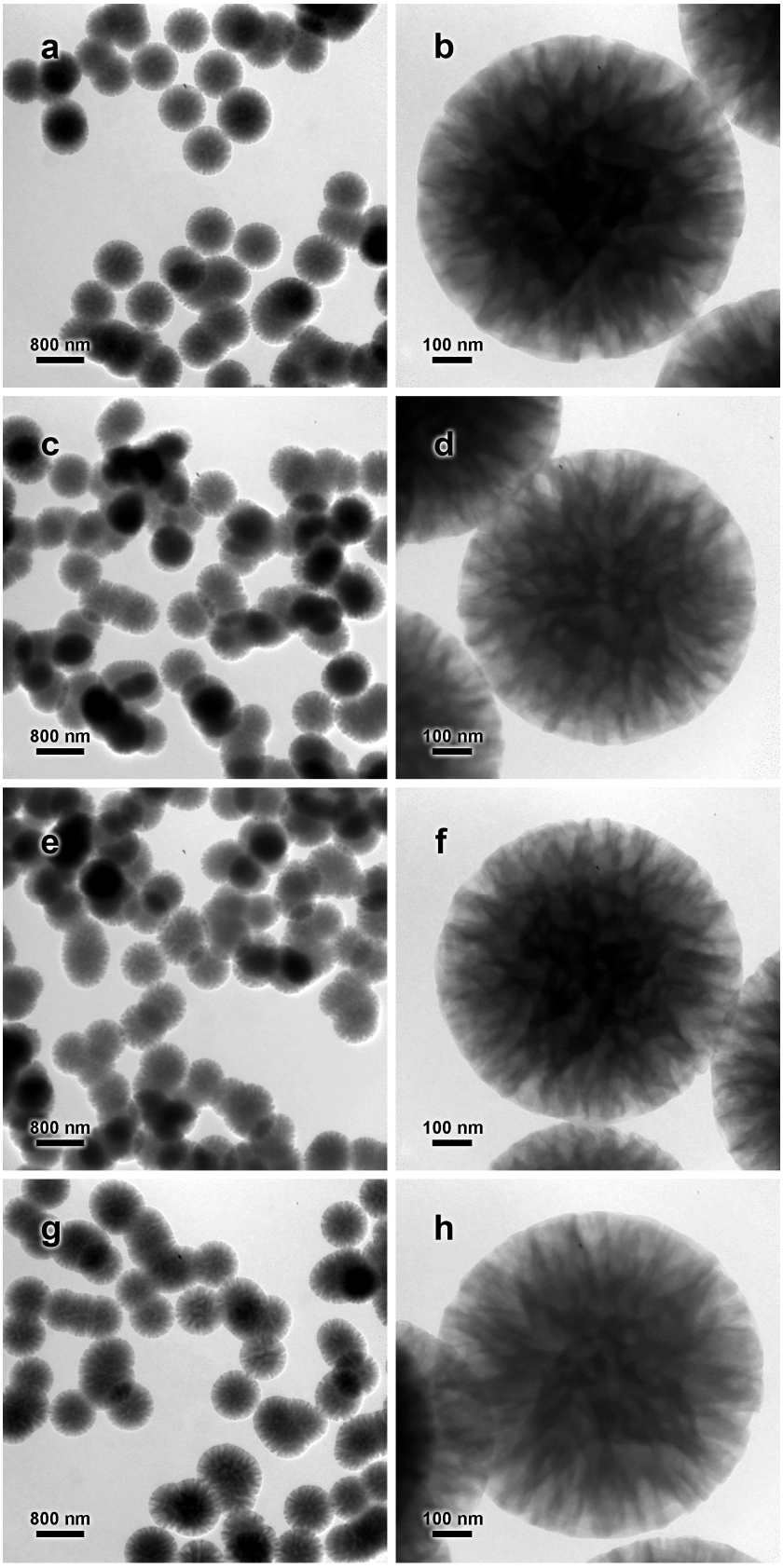

Figure A1.4. TEM images of MASS synthesized by the scaled-down procedure (see the note in Figure A1.2) using 5 mg of $NaAlO_2$, 7 mL of water, 0.25 mL of 32% NH_3 and different amounts of CTAB: (a,b) 50 mg, (c,d) 75 mg, (e,f) 100 mg, and (g,h) 150 mg.

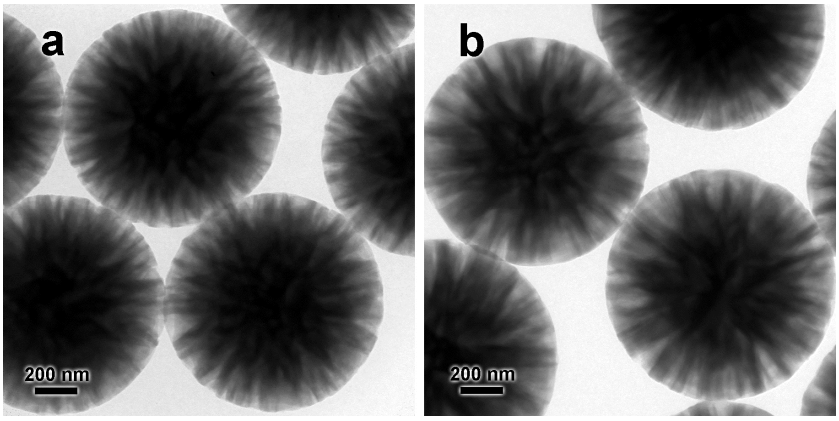

Figure A1.5. TEM images of MASS-15 synthesized with different amount of TEOS: (a) 180 μL and (b) 240 μL.

A1.4. Additional experiments on Cu/ZnO-loaded MSS and MASS

Table A1.1 summarizes the composition of the catalysts. Note that the syntheses of CZMASS-15-550 and CZMASS-15-550Mg were not mentioned in Chapter 5. For the former, the MASS-15 support was calcined at 550 °C for 6 h before impregnation. For the latter, before impregnation the MASS-15 support was calcined at 550 °C for 6 h, treated with 0.2 mol/L $Mg(NO_3)_2$ solution (25 mL solution for every gram of support) at ambient temperature for 2 h, washed thoroughly with water and calcined again at 350 °C for 4 h before impregnation. The treatment with $Mg(NO_3)_2$ replaced the Na^+ in MASS-15 with Mg^{2+} by ion exchange.

Table A1.1. Elemental analysis of fresh catalysts by EDX

Catalyst	Cu (wt %)	Zn (wt %)	Al/Si (mol/mol)	Na/Al (mol/mol)	Mg/Al (mol/mol)
CZMSS	6.67	3.87	0	0	0
CZMASS-15	6.91	3.99	0.170	0.319	0
CZMASS-15-550	6.01	4.21	0.175	0.288	0
CZMASS-15-550Mg	6.21	4.49	0.170	0	0.101

Figure A1.6 shows clearly that the introduction of Al into MSS decreased the total CO_2 hydrogenation activity but allowed for significant production of dimethyl ether.

The main factor in the decrease of activity is believed to be limited pore accessibility as discussed in Chapter 5.

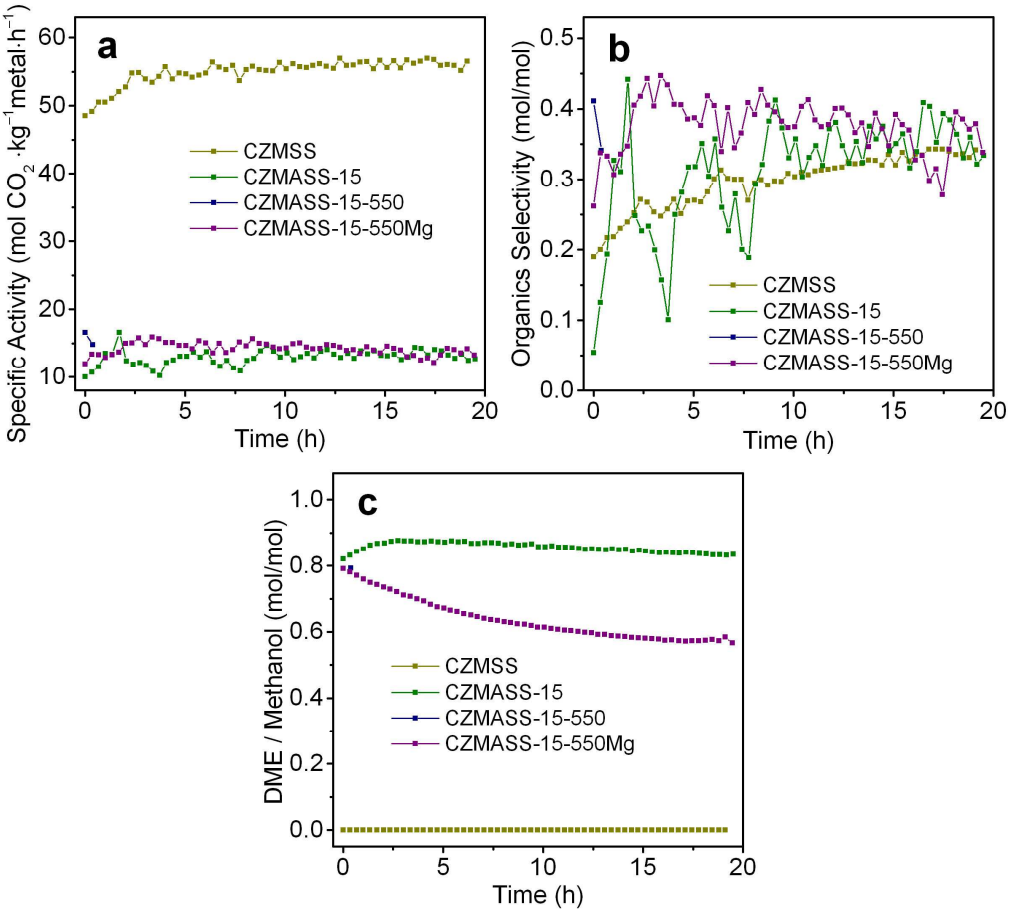

Figure A1.6. (a) Specific activity, (b) organics selectivity and (c) mole ratio between dimethyl ether and methanol in the effluent. The fluctuation in the organics selectivity of CZMASS-15 is due to low CO_2 conversion which amplified random error. Besides methanol and dimethyl ether, CO was the only carbon-containing product detected.

The explanation of the difference in activity is complicated when surface chemistry of the support is considered. During catalyst syntheses it was observed that the MASS-15 calcined at 500 °C appeared brown to naked eyes. Since FTIR analysis showed no trace of organic compounds (see Figure 5.8 of the main text), it was suspected that carbon deposition occurred due to either poor air accessibility in the pore network or the ability of aluminosilicate to catalyze coking or both. By raising the calcination temperature to 550 °C, the resulting product appeared white and carbon deposit was considered completely removed. From the initial activities of

CZMASS-15 and CZMASS-15-550 in Figure A1.6a, approximately 50% increase can be observed as a result of higher calcination temperature, though the activity of both catalysts appears to have the tendency to approach towards the same value. It thus remains an open question whether carbon deposition could affect the surface chemistry of the catalyst and be an issue in catalyst preparation. On the other hand, based on previous discussion the removal of carbon deposit could also contribute to increased activity by allowing access to the pores that were otherwise blocked by carbon. To evaluate this possibility the textural properties were examined for MASS-15 calcined at 550 °C (MASS-15cal550). Comparison in Figure A1.7 shows that the increase in calcination temperature did not increase pore accessibility, nor did it affect the pore structure. Therefore the pore blocking effect of carbon deposition is ruled out.

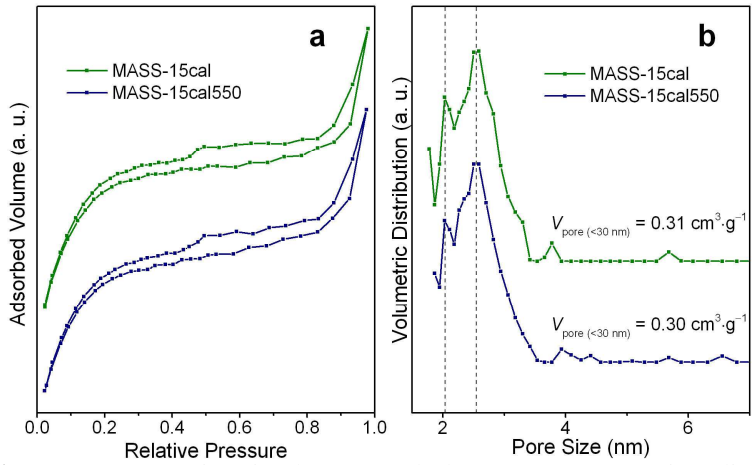

Figure A1.7. (a) N_2 sorption isotherms and (b) NLDFT pore size distribution of MASS-15 calcined at different temperatures.

Another important consideration was inspired by the study of traditional $Cu/ZnO/Al_2O_3$ methanol synthesis catalyst. The deactivation effect of Na has been proven[1] and in the present system it could also be a contributing factor. Following this logic, ion exchange was carried out in attempt to enhance the activity of CZMASS-15. Results in Figure A1.6a show that the replacement of Na with Mg increased the initial activity (by *ca.* 20%) but as the reaction continued the difference disappeared. To explain such changes the evolution of the metal surface must be

examined. Here CZMSS is a good model catalyst because it has the highest activity and most noticeable trend in time-dependent activity and selectivity. During the entire 20 h period, CZMSS showed slowly increasing activity as well as organics selectivity (Figure A1.6b), which could be attributed to diffusion of Zn towards Cu surfaces as discussed in Chapter 5. Although not obvious, CZMASS-15 exhibited similar trends in activity and organics selectivity which are also believed to be the result of Zn migration. In contrast, in CZMASS-15-550Mg the Mg atoms could compete with Zn for Cu surfaces (Mg^{2+} has similar ionic radius with Zn^{2+}) and inhibit the formation of highly active methanol synthesis sites. Indeed, the activity and organics selectivity of CZMASS-15-550Mg decreased in the long term.

In terms of dimethyl ether production, the effect of Al incorporation is remarkable. The selectivity of dimethyl ether relative to that of methanol reflects the acidity of the support to a large degree. Interestingly, the replacement of Na with Mg did not affect the initial relative selectivity but caused a significant difference as the experiments continued. The decreasing activity of acid sites in dimethyl ether synthesis has been attributed to neutralization by diffusing metal cations,[2] which is believed to be the mechanism in the present system. As Mg^{2+} has stronger neutralizing power than Na^{+} (one Mg^{2+} ion can neutralize two acid sites), more significant deactivation of acid sites is also expected for the Mg-exchanged catalyst assuming comparable diffusion rates of Na^{+} and Mg^{2+}.

The XRD patterns of spent catalysts in Figure A1.8 show that Cu and Cu_2O (due to oxidation of Cu during sample handling) were present in the samples. All of the Al-containing catalysts show remarkably stronger diffraction signals from Cu than CZMSS does, which is an indication of more severe sintering than CZMSS. For CZMASS-15 in particular, Cu_2O formation is insignificant due to limited Cu surface area. Here it should be pointed out that the CO_2 hydrogenation experiment with CZMASS-15-550 only lasted 3 h instead of over 20 h for CZMASS-15-550Mg. In

the initial stage of the catalytic experiments CZMASS-15-550Mg might have better dispersed Cu particles, but the extended reaction time caused probably a larger degree of sintering, which made the Cu particle size appear the same for the two spent catalysts. Taking the difference in reaction time into consideration, positive effects of higher calcination temperature and/or ion exchange with Mg^{2+} on the dispersity of Cu are likely.

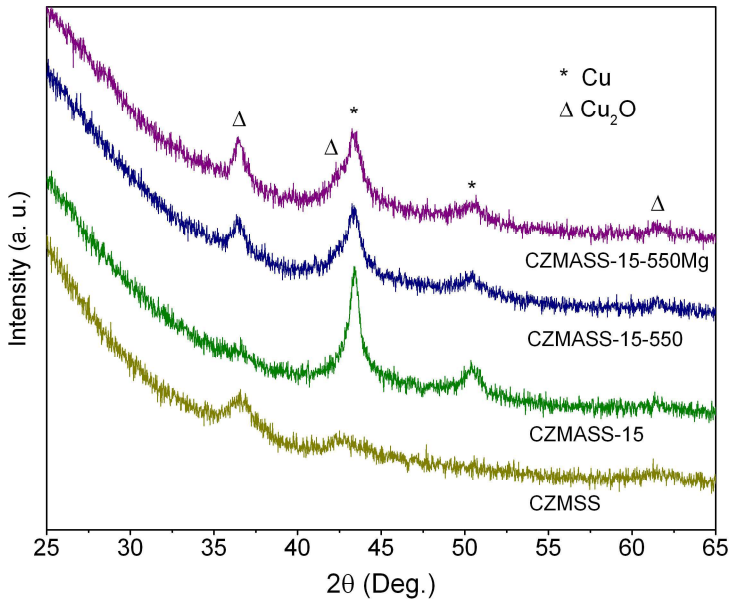

Figure A1.8. Powder XRD patterns of spent catalysts.

Using the crystallite sizes estimated from the peak broadening of the XRD patterns and assuming that all the Cu particles in the active catalyst were single crystalline and were fully accessible, the approximate dispersity of Cu (*i.e.*, percentage of exposed Cu atoms in the total number of Cu atoms) can be calculated. Further assuming that all the exposed Cu atoms were active in CO_2 hydrogenation, the TOF and TON of the catalysts are derived. The results are summarized in Table A1.2. Note that the above assumptions cause significant underestimation of TOF/TON, as it has already been shown that only certain surface features of Cu particles are active in CO_2 conversion.[3] Moreover, the Cu particles are not fully exposed in a realistic situation.

Table A1.2. Catalytic properties of Cu/ZnO-loaded catalysts

Catalyst	Cu/Cu_2O crystallite size* (nm)	Cu dispersity (%)	Steady-state TOF† (h^{-1})	TON‡
CZMSS	3.7	29.2	19.3	378
CZMASS-15	11.3	9.6	14.0	269
CZMASS-15-550Mg	10.4	12.2	11.9	255

*When both phases coexist, the larger crystallite size is used.

†defined as number of CO_2 molecules converted at a single surface Cu atom per hour, calculated based on the average activity during the last 3 h of reaction

‡defined as the total number of CO_2 molecules converted at a single surface Cu atom during the 20 h reaction

To complement the XRD analysis, the spent catalysts were also examined by high-angle annular dark-field (HAADF) imaging. The significantly different atomic numbers of transition metals and O, Al, Si make the z-contrast images useful in locating the Cu particles within the complex structure of MSS / MASS; they appear as especially bright spots in such images. It can be seen from Figure A1.9a,b that Cu is indeed highly dispersed in CZMSS. Particularly, in Figure A1.9b the Cu particles (appearing as tiny bright spots 3–4 nm in size) are evenly distributed within the aluminosilicate framework, suggesting significant degree of Cu incorporation in the mesopores. In comparison, much larger Cu particles can be observed in the Al-containing catalysts (Figure A1.9c–h), which is direct evidence of the more severe sintering. The Cu particles in CZMASS-15-550 are poorly resolved (Figure A1.9e,f), probably because the sample was characterized long (weeks) after removal from the reactor compared with other samples (1 day).

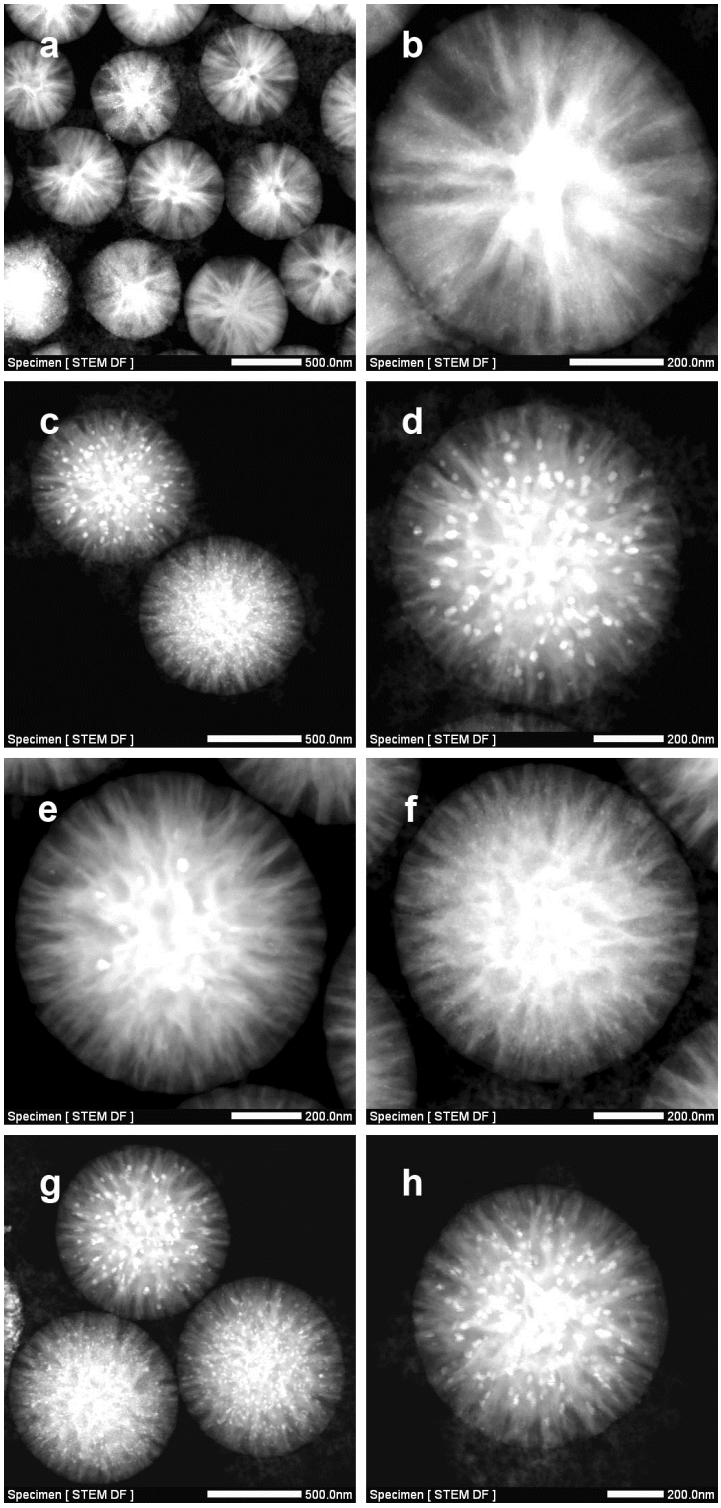

Figure A1.9. HAADF images of spent catalysts: (a,b) CZMSS, (c,d) CZMASS-15, (e,f) CZMASS-15-550 and (g,h) CZMASS-15-550Mg. Scattered low-contrast bright spots outside the boundaries of MSS and MASS are due to the SiO_2 aerogel used as diluent.

In addition, EDX elemental analysis coupled with HAADF imaging was used to further confirm the chemical nature of the particles corresponding to the bright spots observed in Figure A1.9. Figure A1.10–A1.12 show that they are indeed Cu particles.

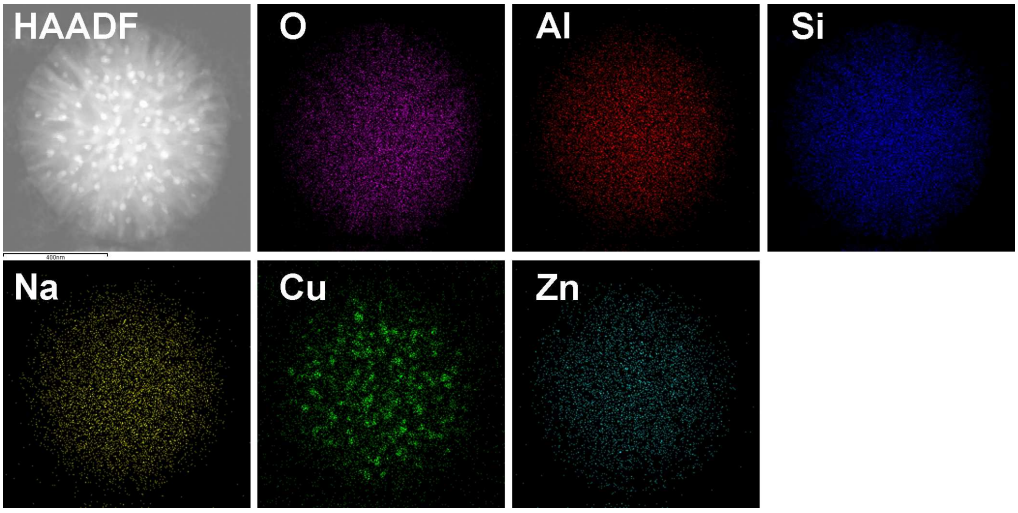

Figure A1.10. EDX elemental mapping of spent CZMASS-15. Length of the scale bar: 400 nm.

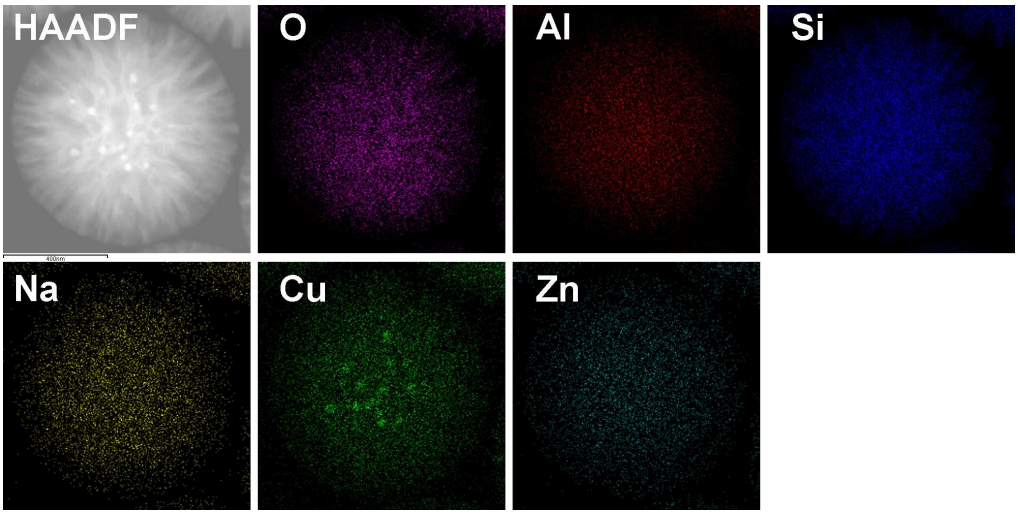

Figure A1.11. EDX elemental mapping of spent CZMASS-15-550. Length of the scale bar: 400 nm.

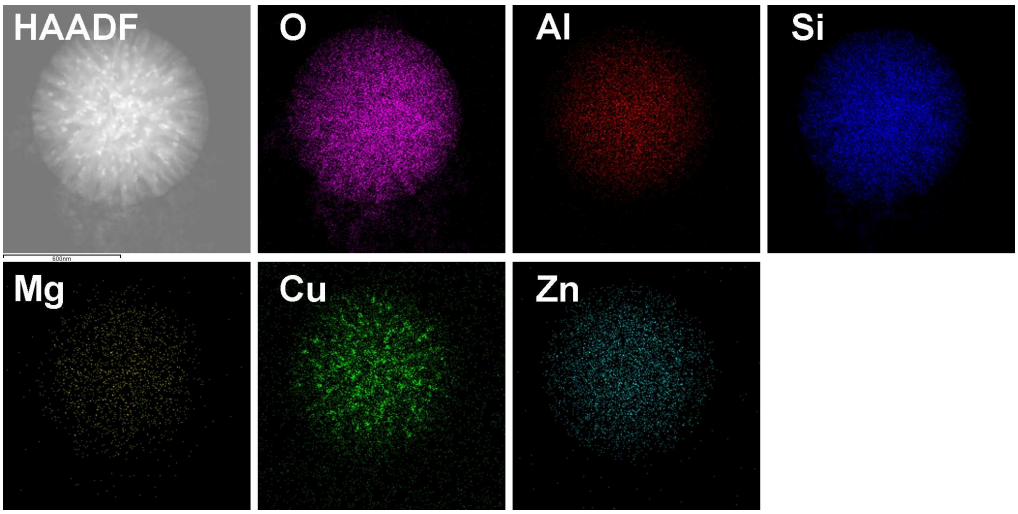

Figure A1.12. EDX elemental mapping of spent CZMASS-15-550Mg. Length of the scale bar: 600 nm.

Besides the Cu/ZnO-loaded catalysts, Cu/ZnO/Ga_2O_3-loaded catalysts were also synthesized in this work in hope that the introduction of Ga could enhance the catalytic performance. When loaded onto the Al-free MSS (nominal loading by weight percent: Cu 4.5%, ZnO 2.5%, Ga_2O_3 1.5%), the Cu/ZnO/Ga_2O_3 system exhibited a good initial CO_2 hydrogenation activity of 35.0 mol CO_2/kg metal·h, albeit still lower than that of CZMSS. After 20 h of reaction, the activity increased by *ca.* 10% similar to the case of CZMSS. On the other hand, the total organics selectivity was improved noticeably by the introduction of Ga; it reached and maintained at 0.43. Such effects can be explained as the result of surface modification of active Cu particles by Ga.[4] The migration of Ga onto Cu particles reduces the exposed Cu surface and hence lowers the activity. Along with the introduction of Ga, finite amount of dimethyl ether was also produced, giving a relative selectivity of 0.059 with respect to methanol. It is probably due to the similar chemical properties of Ga_2O_3 and Al_2O_3 that allowed acid sites to form on Ga_2O_3. From Figure A1.13a,b it can be seen that the metals are highly dispersed, and Figure A1.13c shows that the Cu particles possess sizes small enough to be undetectable by XRD technique. Compared with CZMSS, the higher metal dispersity brought by Ga may be a result of surface-stabilizing effect of Ga on Cu particles.

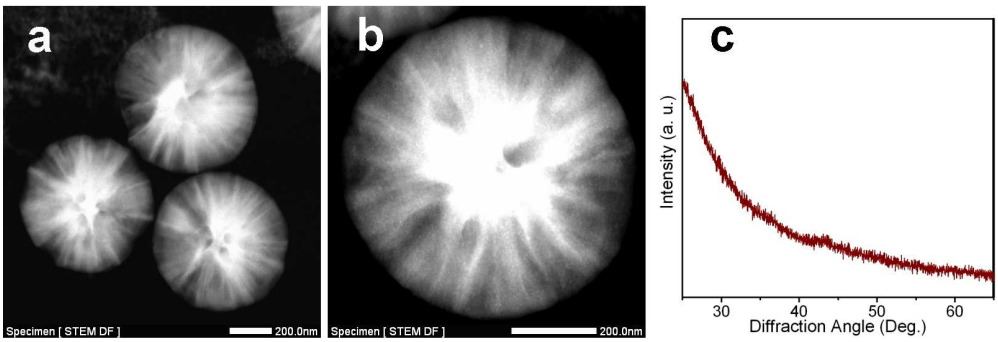

Figure A1.13. (a,b) HAADF images and (c) XRD pattern of spent Cu/ZnO/Ga_2O_3-loaded MSS catalyst

Furthermore, during the development of Cu/ZnO/Ga_2O_3-loaded catalysts it was found that calcination before impregnation was crucial to achieving high metal

dispersity. Briefly, ion exchange of MASS-15cal with aqueous solutions of different salts including NH_4NO_3, $Cu(NO_3)_2$ and $Al(NO_3)_3$ was carried out prior to catalyst impregnation in order to explore the effect of ion adsorption on the catalytic performance. As summarized in Table A1.3, without calcination immediately before impregnation, all of the catalysts thus synthesized exhibited poor CO_2 hydrogenation activity and no organics production. Analyses by electron microscopy and XRD revealed severe sintering of Cu particles, of which an example is given in Figure A1.14. It is believed that the ion exchange process produced partially soluble silicate species and/or metal hydroxides. Upon drying they precipitated and blocked most of the mesopores. Consequently during impregnation the catalytically active components could only accumulate in the macropores and form large particles.

Table A1.3. Preparation methods and catalytic activity of Cu/ZnO/Ga_2O_3-loaded MASS catalysts*

Catalyst	Activity (mol CO_2/kg metal·h)	Organics Selectivity (mol/mol)	Preparation Method
CZG-MASS-15	~12	~0.3	MASS-15cal directly impregnated with nitrates
CZG-MASS-15NH_4	~10	0	MASS-15cal ion-exchanged with 1M NH_4NO_3 twice at 60°C, dried at 60°C and impregnated with nitrates
CZG-MASS-15Al	~12	0	MASS-15cal ion-exchanged with 0.1M $Al(NO_3)_3$ at room temperature, dried at 60°C and impregnated with nitrates
CZGE-MASS-15NH_4	~12	0	MASS-15cal ion-exchanged with 1M NH_4NO_3 twice at 50°C, dried at 60°C and impregnated with nitrates and equimolar amount of $(NH_4)_4EDTA$
CZGE-MASS-15Cu	~12	0	MASS-15cal ion-exchanged with 0.2M $Cu(NO_3)_2$ twice at 50°C, dried at 60°C and impregnated with nitrates and equimolar amount of $(NH_4)_4EDTA$

*nominal loading Cu 4.5%, ZnO 2.5%, Ga_2O_3 1.5% for all of the catalysts

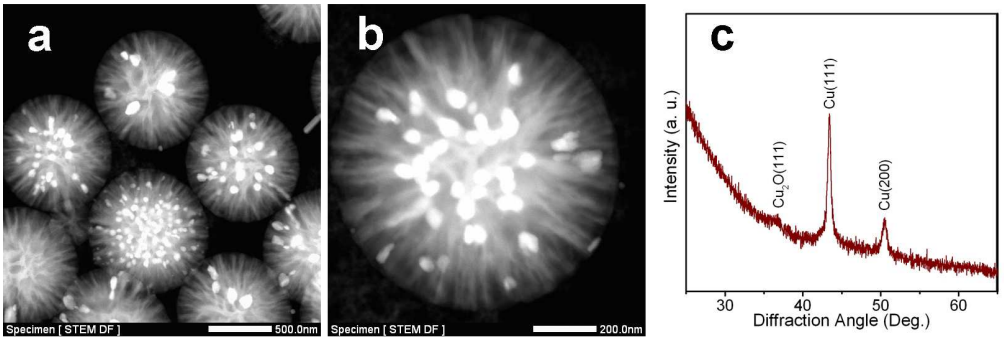

Figure A1.14. (a,b) HAADF images and (c) XRD pattern of spent CZG-MASS-15NH_4 catalyst.

A1.5. References

1. Jun, K.-W.; Shen, W.-J.; Rao, K. S. R.; Lee, K.-W., Residual sodium effect on the catalytic activity of Cu/ZnO/Al_2O_3 in methanol synthesis from CO_2 hydrogenation. *Appl. Catal. A* **1998,** *174*, 231-238.
2. Ordomsky, V. V.; Cai, M.; Sushkevich, V.; Moldovan, S.; Erson, O.; Lancelot, C.; Valtchev, V.; Khodakov, A. Y., The role of external acid sites of ZSM-5 in deactivation of hybrid CuZnAl/ZSM-5 catalyst for direct dimethyl ether synthesis from syngas. *Appl. Catal. A* **2014,** *486*, 266-275.
3. Behrens, M.; Studt, F.; Kasatkin, I.; Kühl, S.; Hävecker, M.; Abild-Pedersen, F.; Zander, S.; Girgsdies, F.; Kurr, P.; Kniep, B.-L.; Tovar, M.; Fischer, R. W.; Norskov, J. K.; Schlögl, R., The active site of methanol synthesis over Cu/ZnO/Al_2O_3 industrial catalysts. *Science* **2012,** *336*, 893-897.
4. Toyir, J.; de la Piscina, P. R.; Fierro, J. L. G.; Homs, N., Highly effective conversion of CO_2 to methanol over supported and promoted copper-based catalysts: influence of support and promoter. *Appl. Catal. B* **2001,** *29*, 207-215.

Appendix 2. Supplementary Materials for Chapter 6

A2.1. XRD survey of the crystallization process of different starting gels

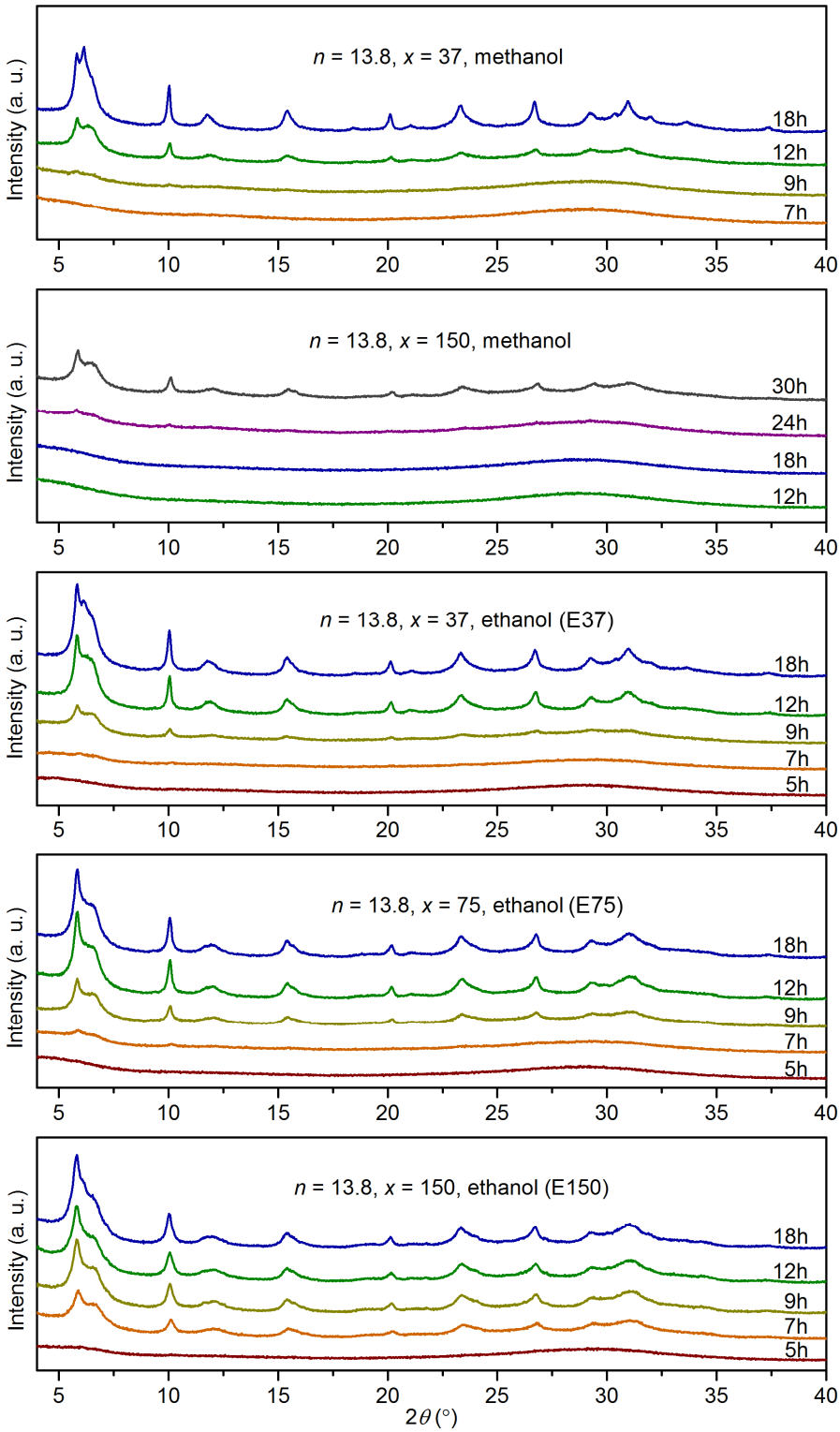

Figure A2.1. XRD patterns of products synthesized by crystallization of different starting gels for different periods of time. Gel composition as indicated in each panel.

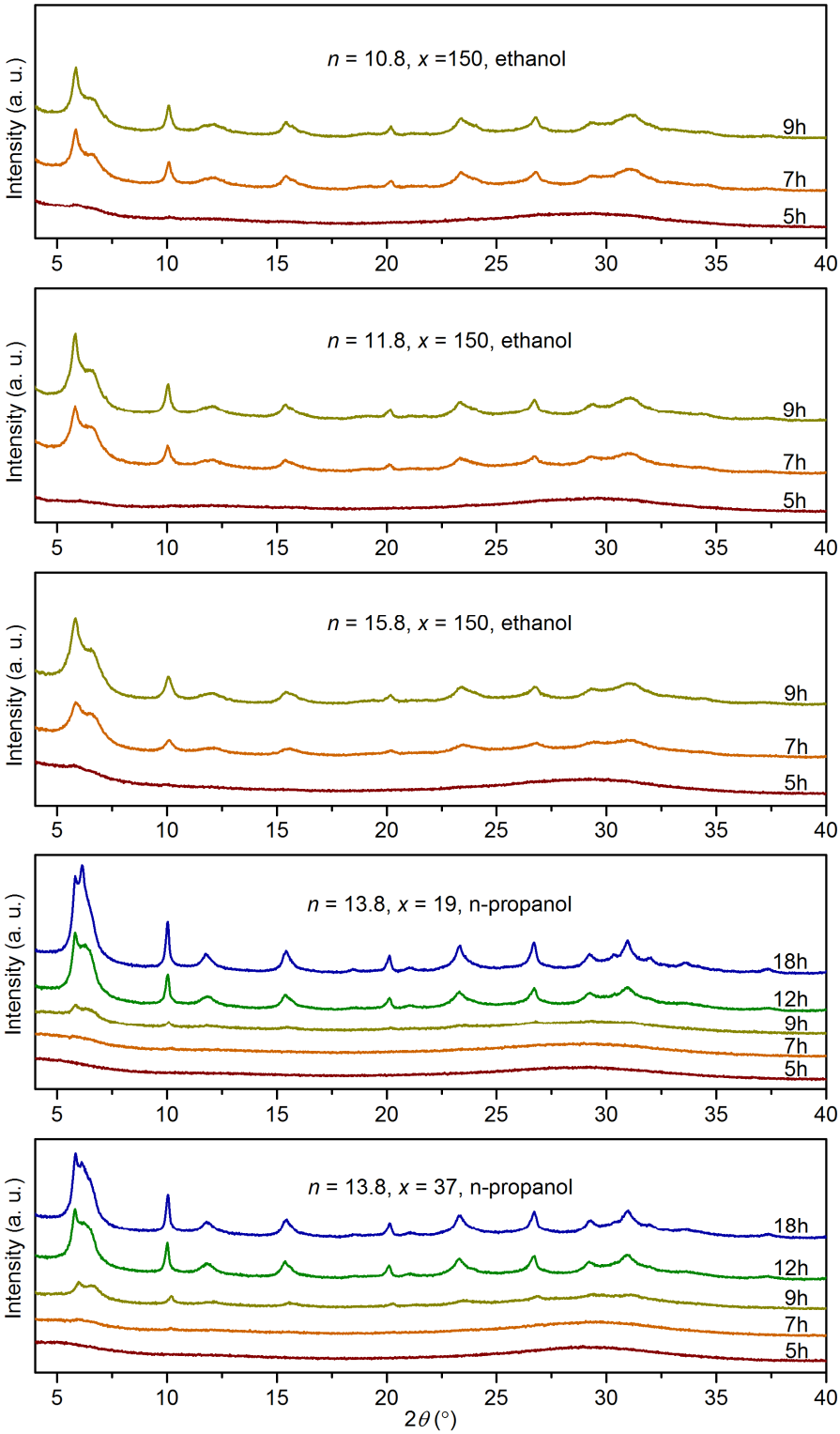

Figure A2.1 continued

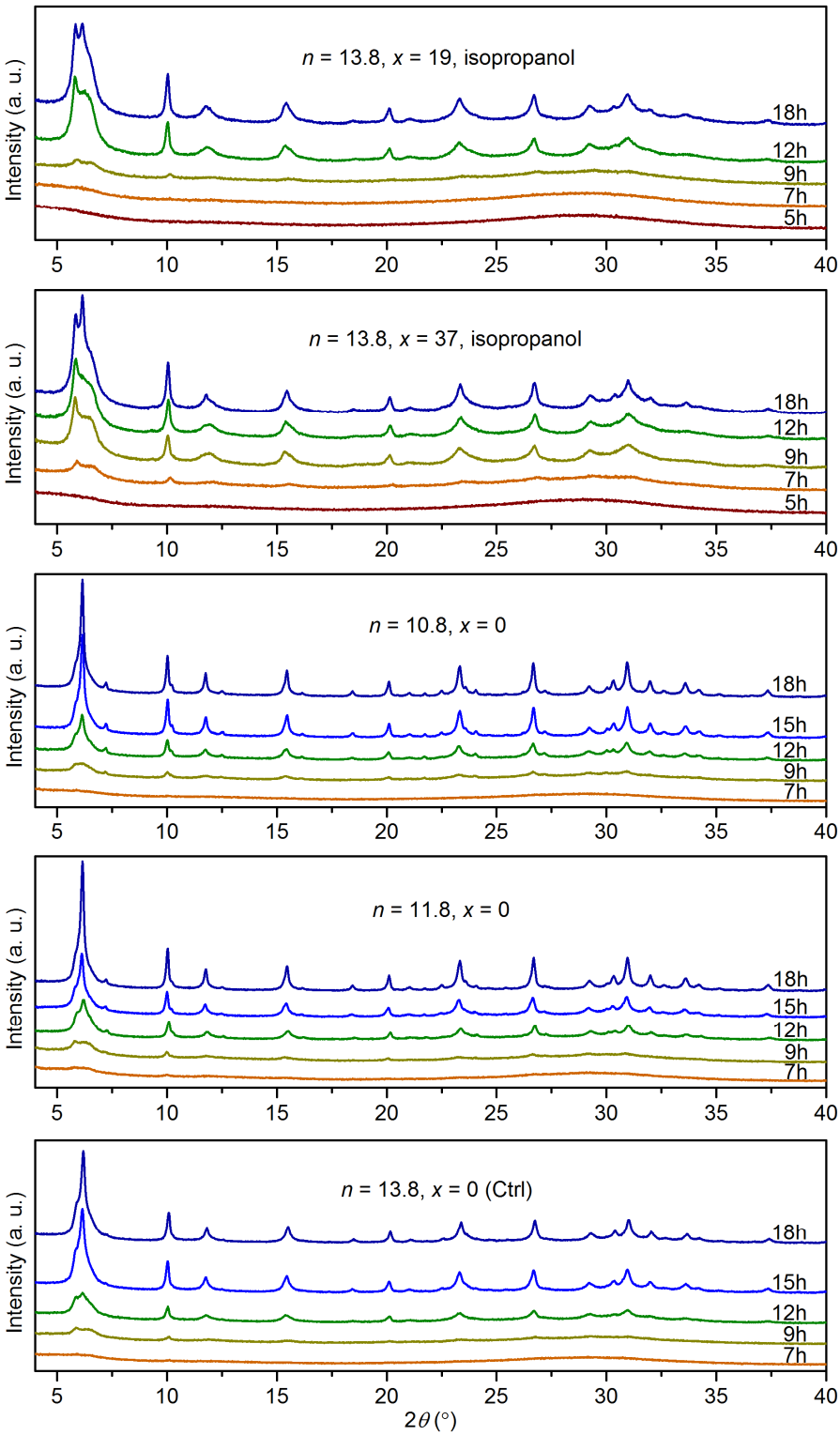

Figure A2.1 continued

A2.2. TEM survey of the crystallization process of different starting gels

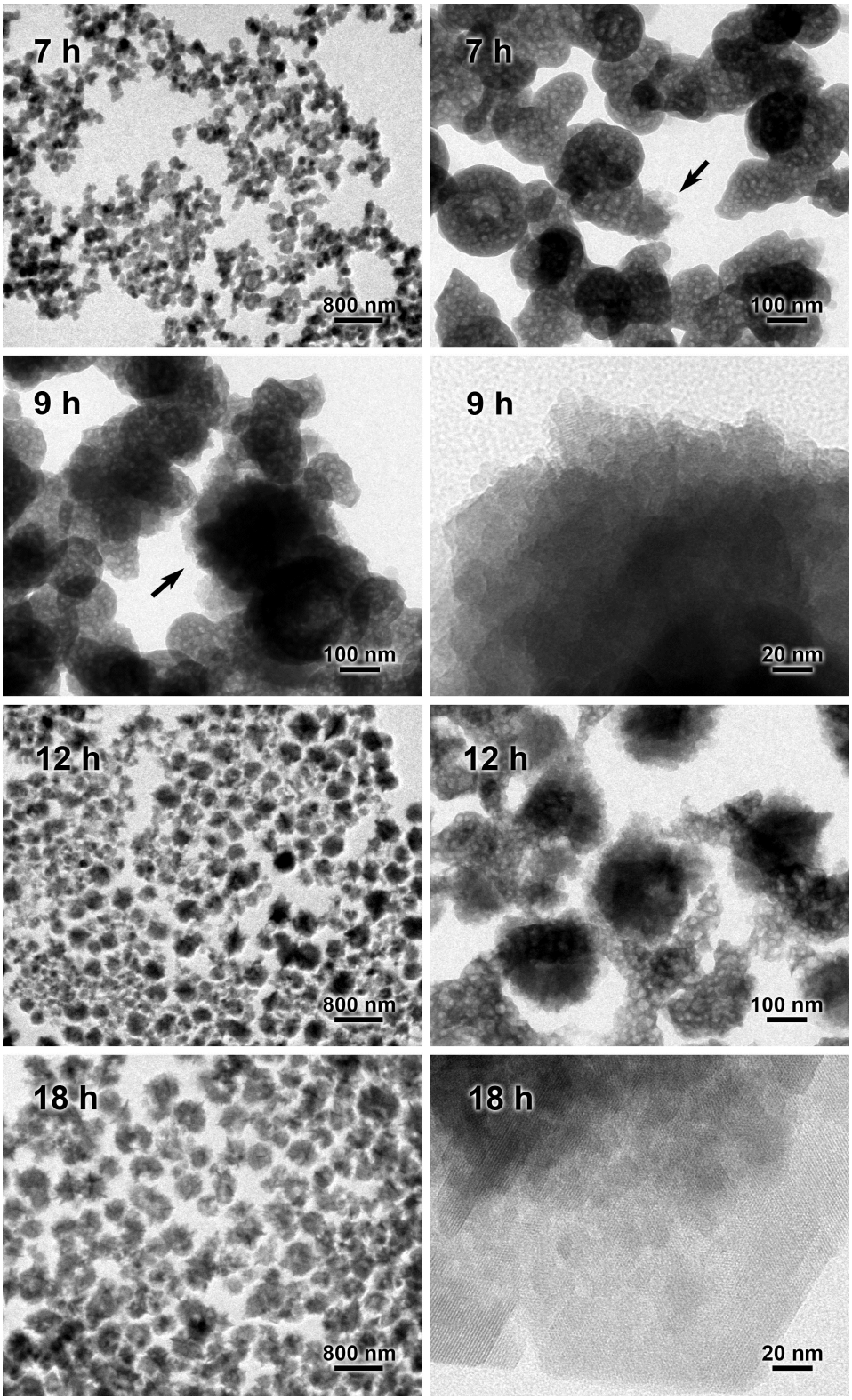

Figure A2.2a. TEM images (at different reaction time and magnifications) of products from the precursor gel where n = 13.8, x = 37, ROH = methanol. The arrows point to growing zeolite particles.

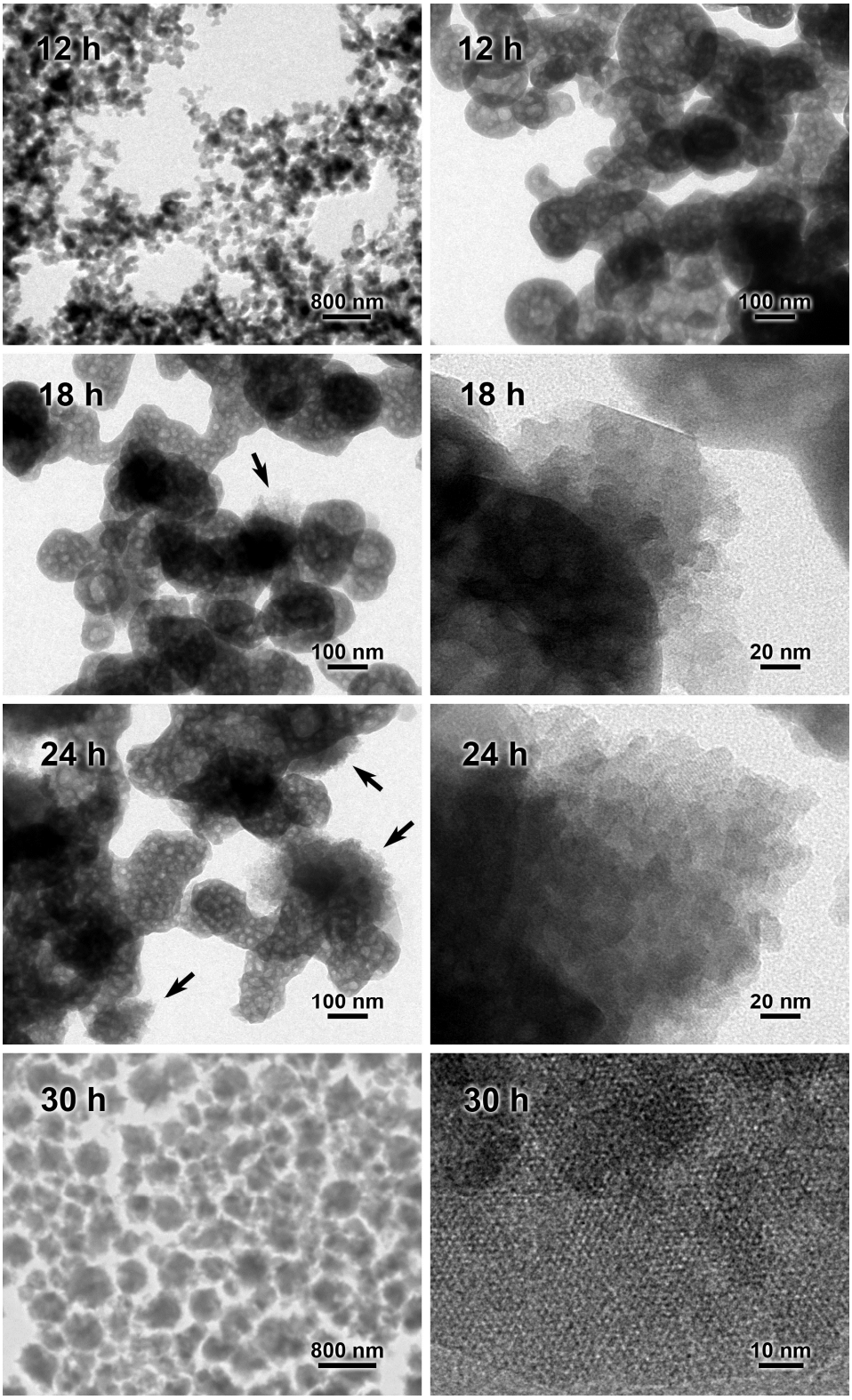

Figure A2.2b. TEM images (at different reaction time and magnifications) of products from the precursor gel where n = 13.8, x = 150, ROH = methanol. The arrows point to growing zeolite particles.

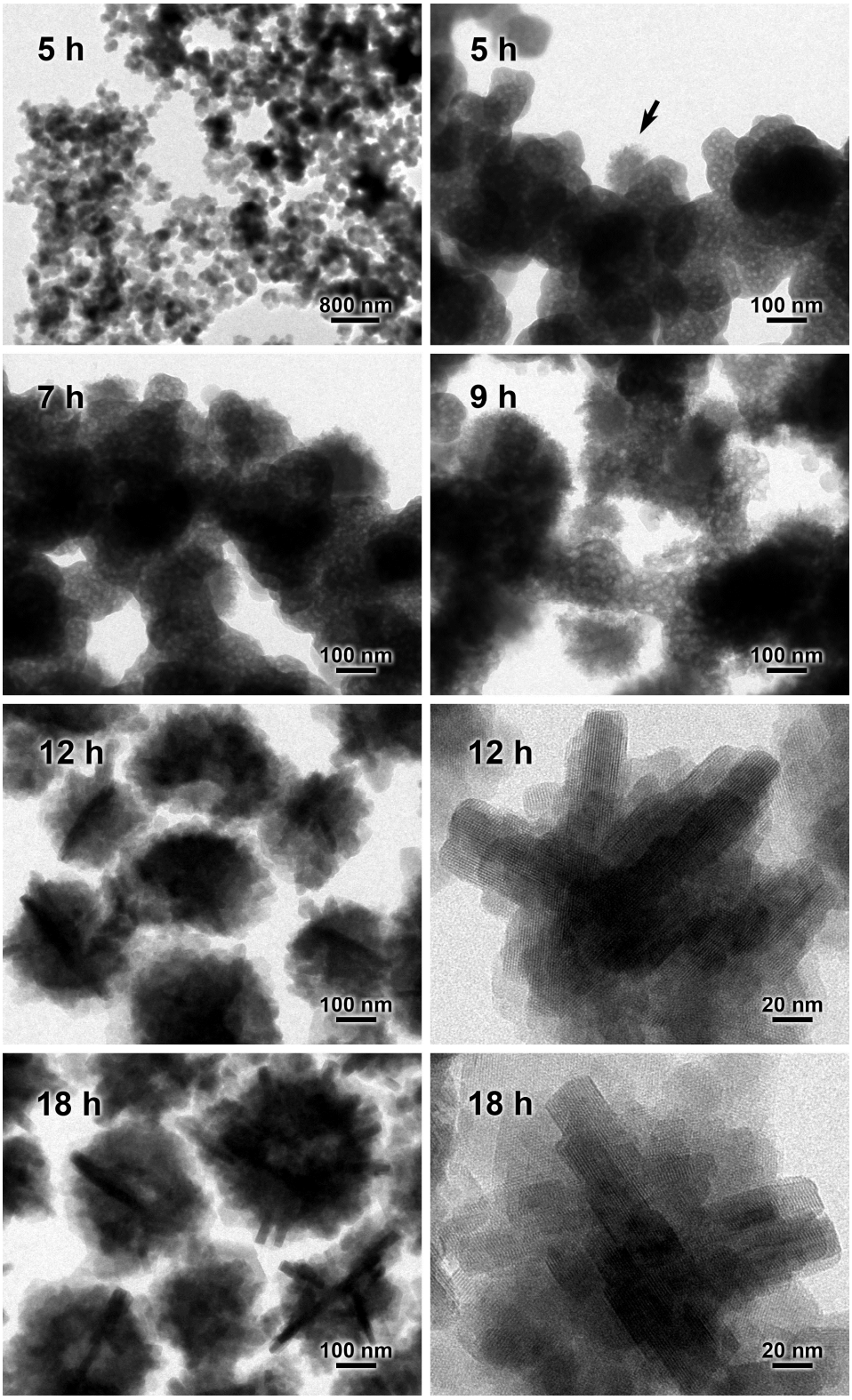

Figure A2.2c. TEM images (at different reaction time and magnifications) of products from the precursor gel where n = 13.8, x = 37, ROH = ethanol. The arrow points to growing zeolite particles.

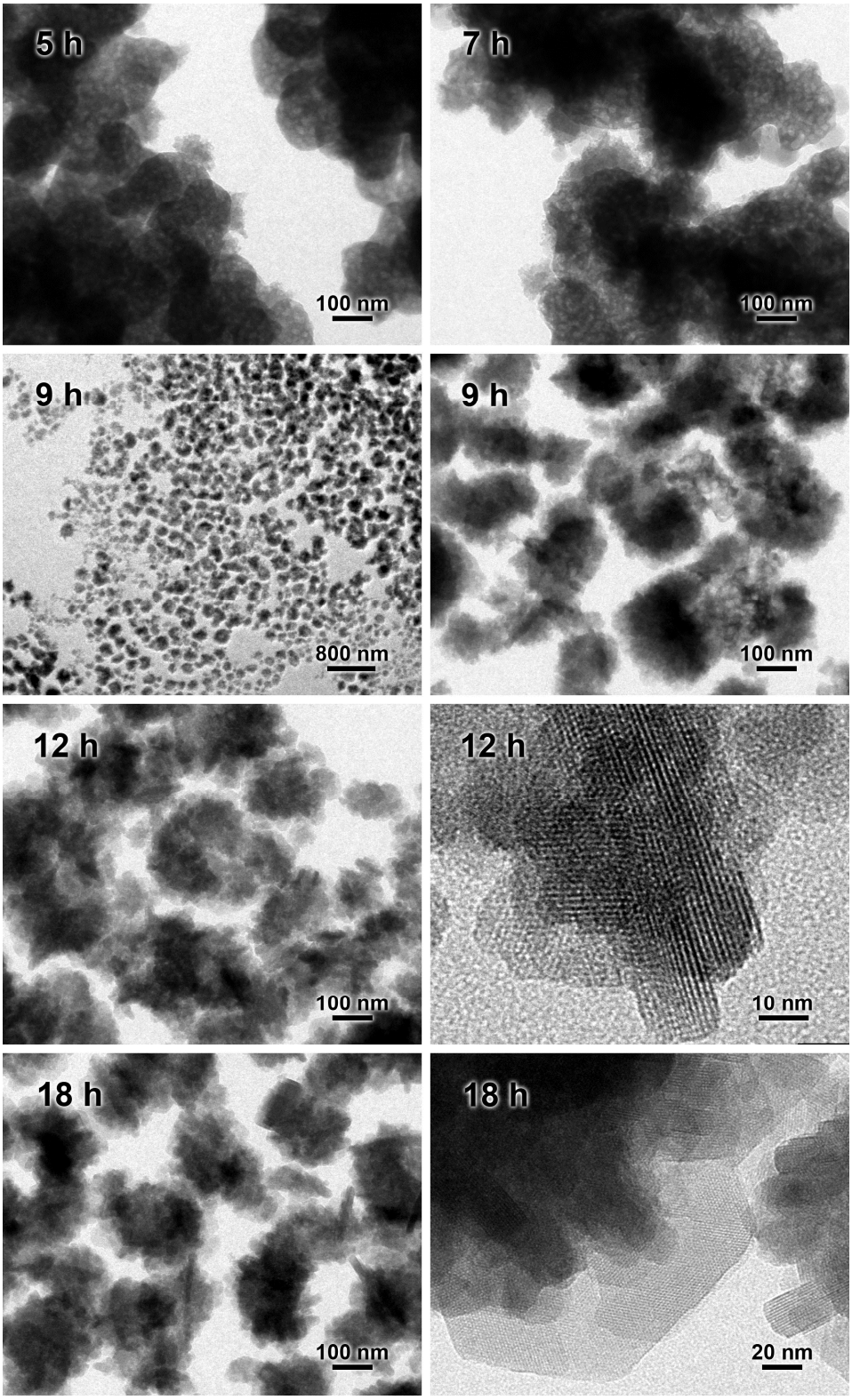

Figure A2.2d. TEM images (at different reaction time and magnifications) of products from the precursor gel where n = 13.8, x = 75, ROH = ethanol.

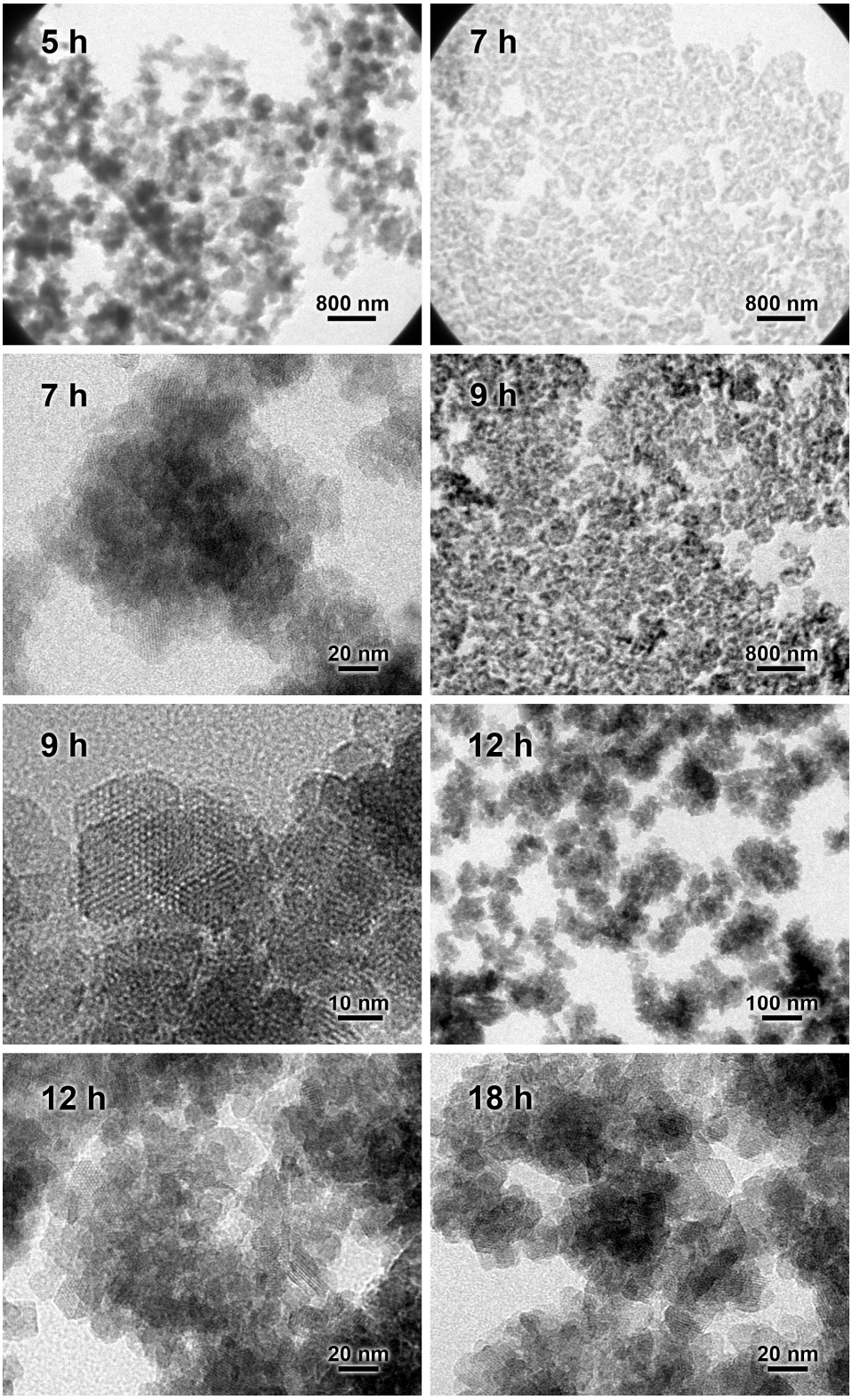

Figure A2.2e. TEM images (at different reaction time and magnifications) of products from the precursor gel where n = 13.8, x = 150, ROH = ethanol.

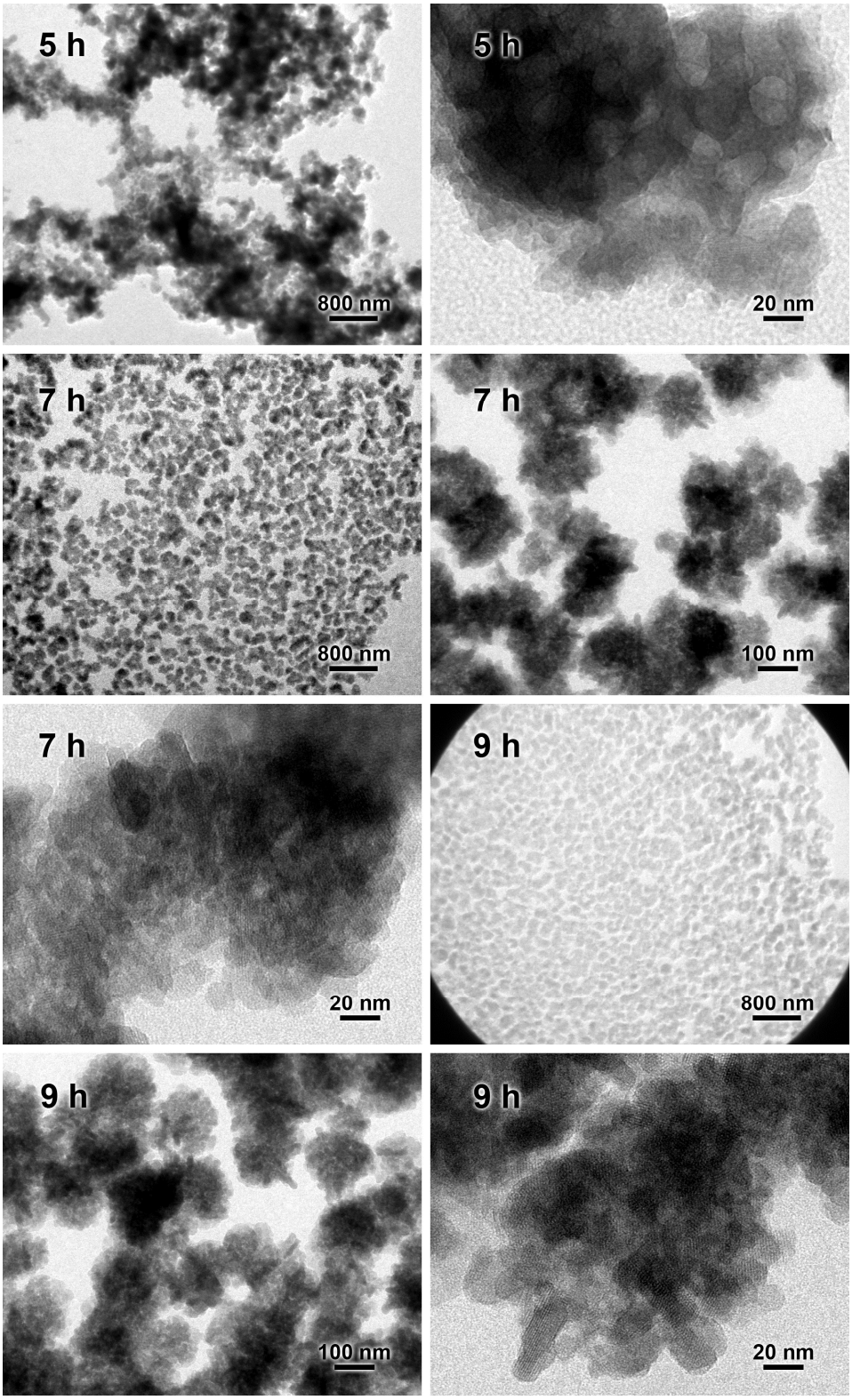

Figure A2.2f. TEM images (at different reaction time and magnifications) of products from the precursor gel where n = 10.8, x = 150, ROH = ethanol.

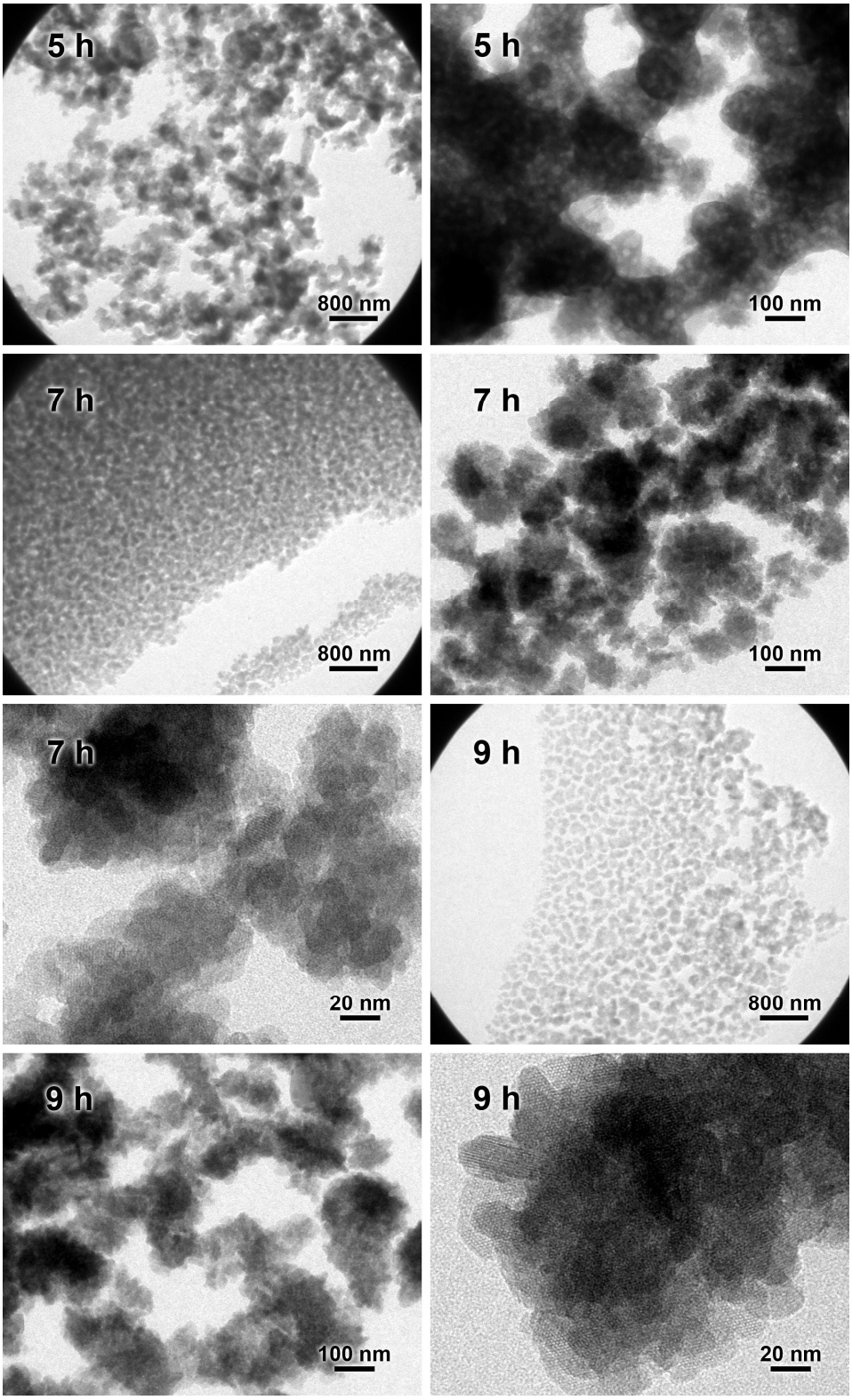

Figure A2.2g. TEM images (at different reaction time and magnifications) of products from the precursor gel where n = 11.8, x = 150, ROH = ethanol.

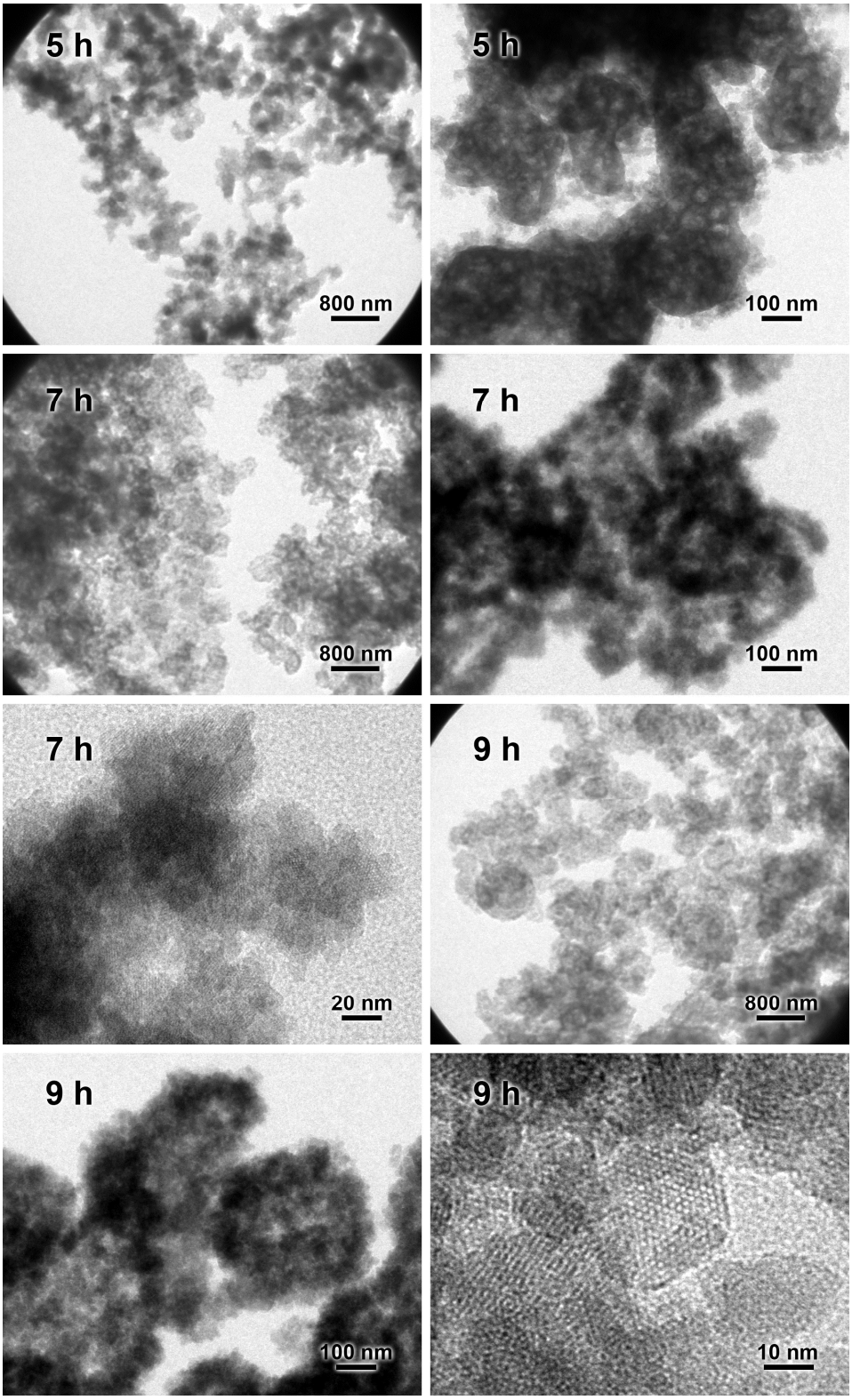

Figure A2.2h. TEM images (at different reaction time and magnifications) of products from the precursor gel where n = 15.8, x = 150, ROH = ethanol.

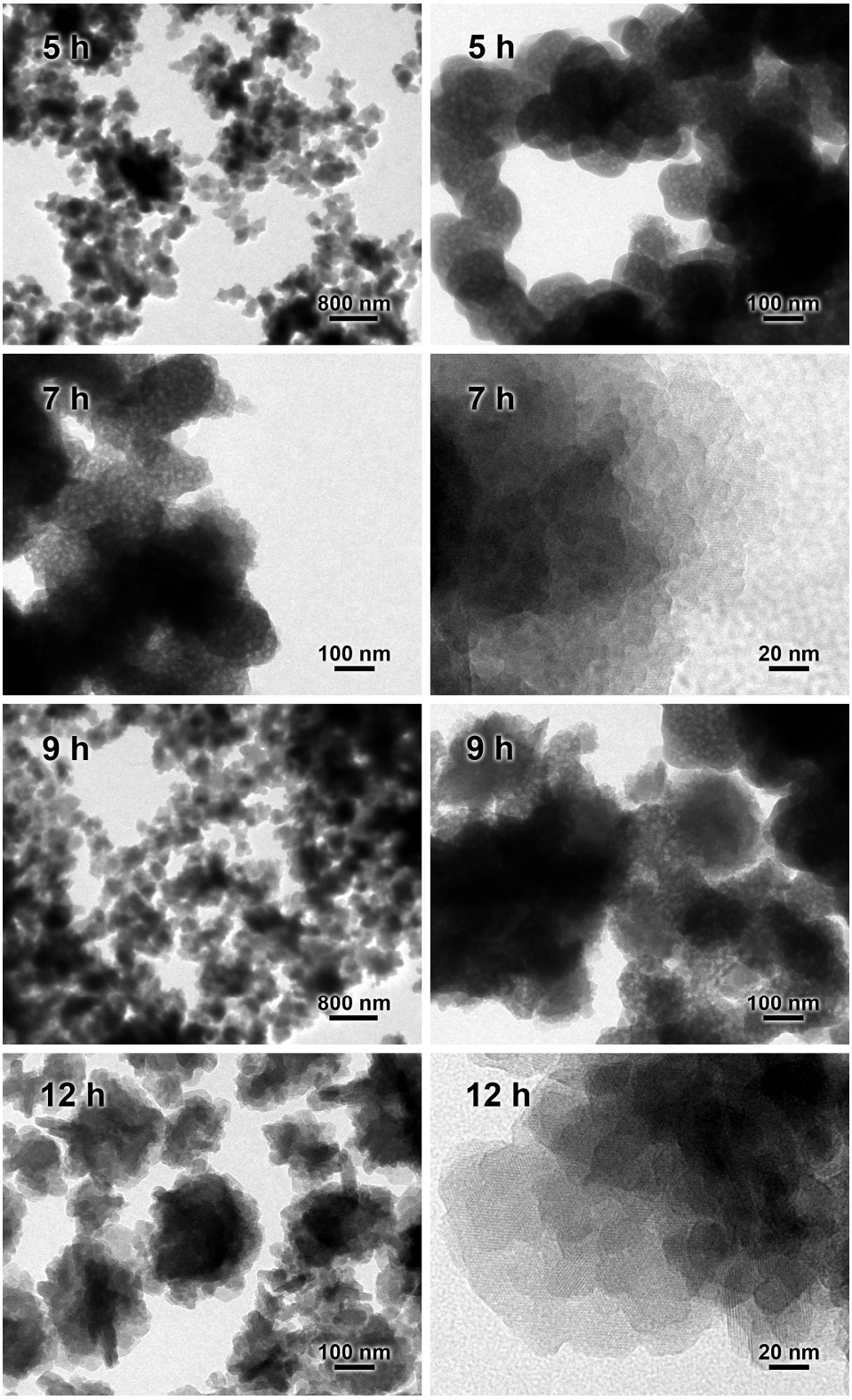

Figure A2.2i. TEM images (at different reaction time and magnifications) of products from the precursor gel where n = 13.8, x = 19, ROH = n-propanol.

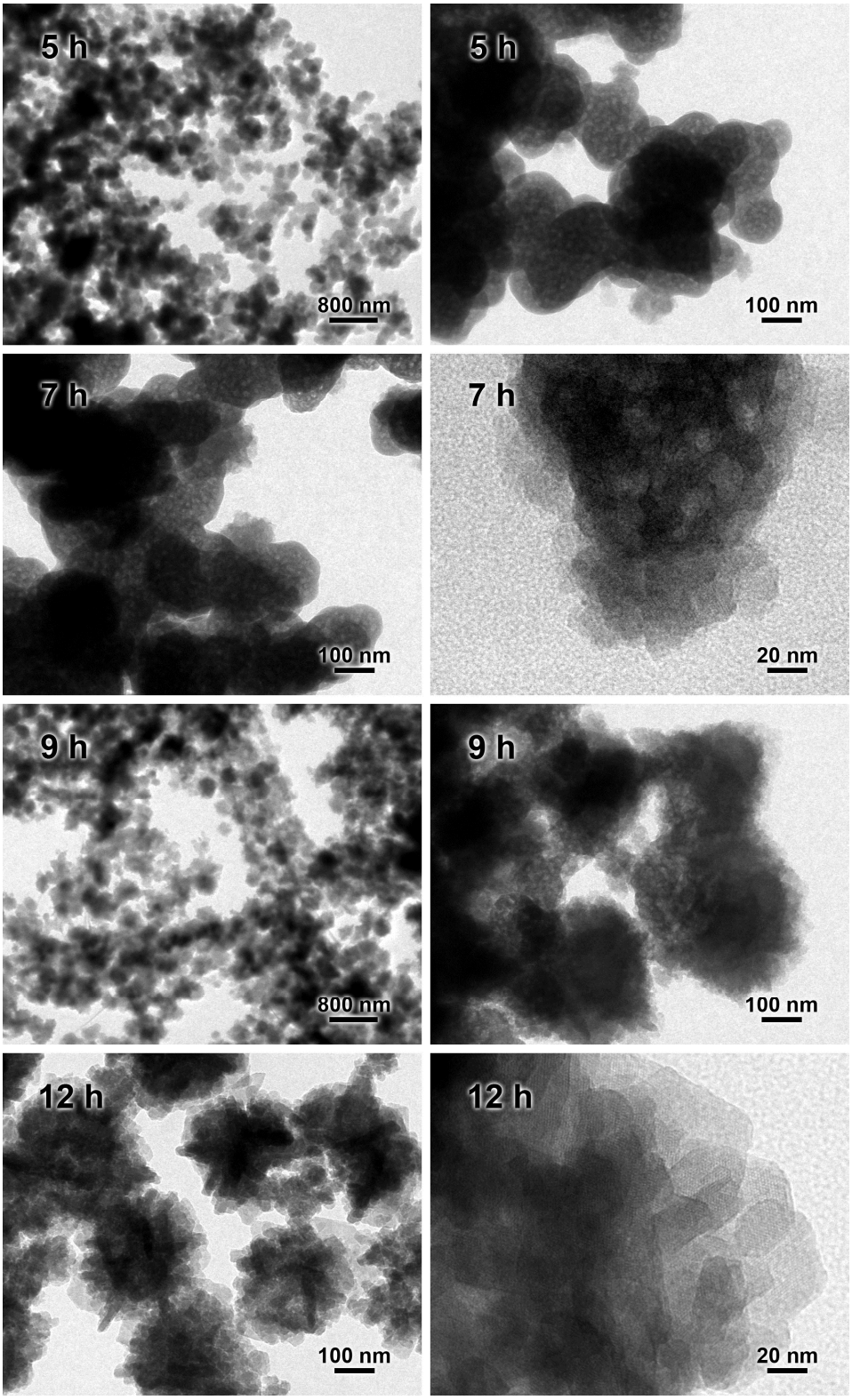

Figure A2.2j. TEM images (at different reaction time and magnifications) of products from the precursor gel where n = 13.8, x = 37, ROH = n-propanol.

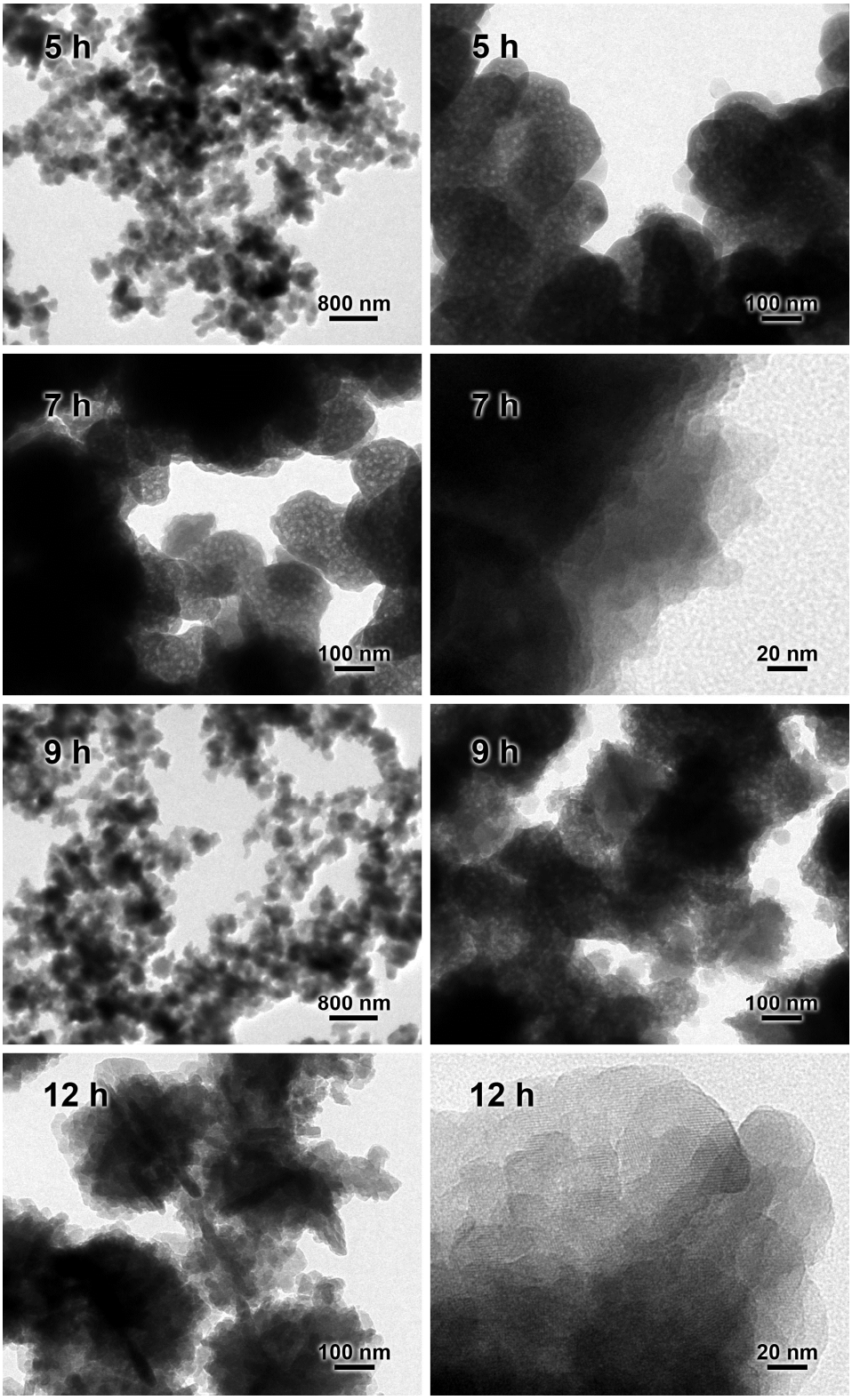

Figure A2.2k. TEM images (at different reaction time and magnifications) of products from the precursor gel where n = 13.8, x = 19, ROH = isopropanol.

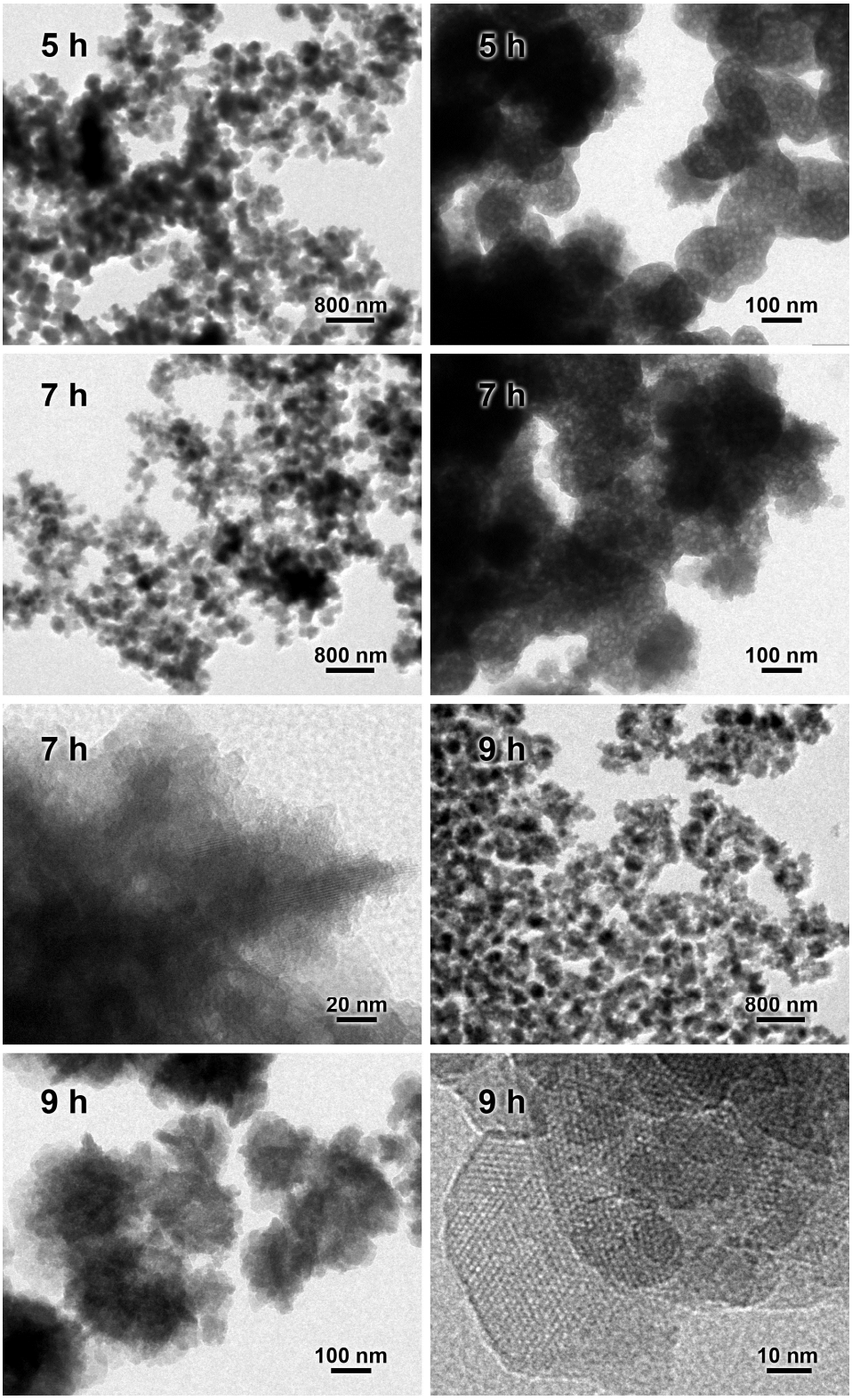

Figure A2.2l. TEM images (at different reaction time and magnifications) of products from the precursor gel where n = 13.8, x = 37, ROH = isopropanol.

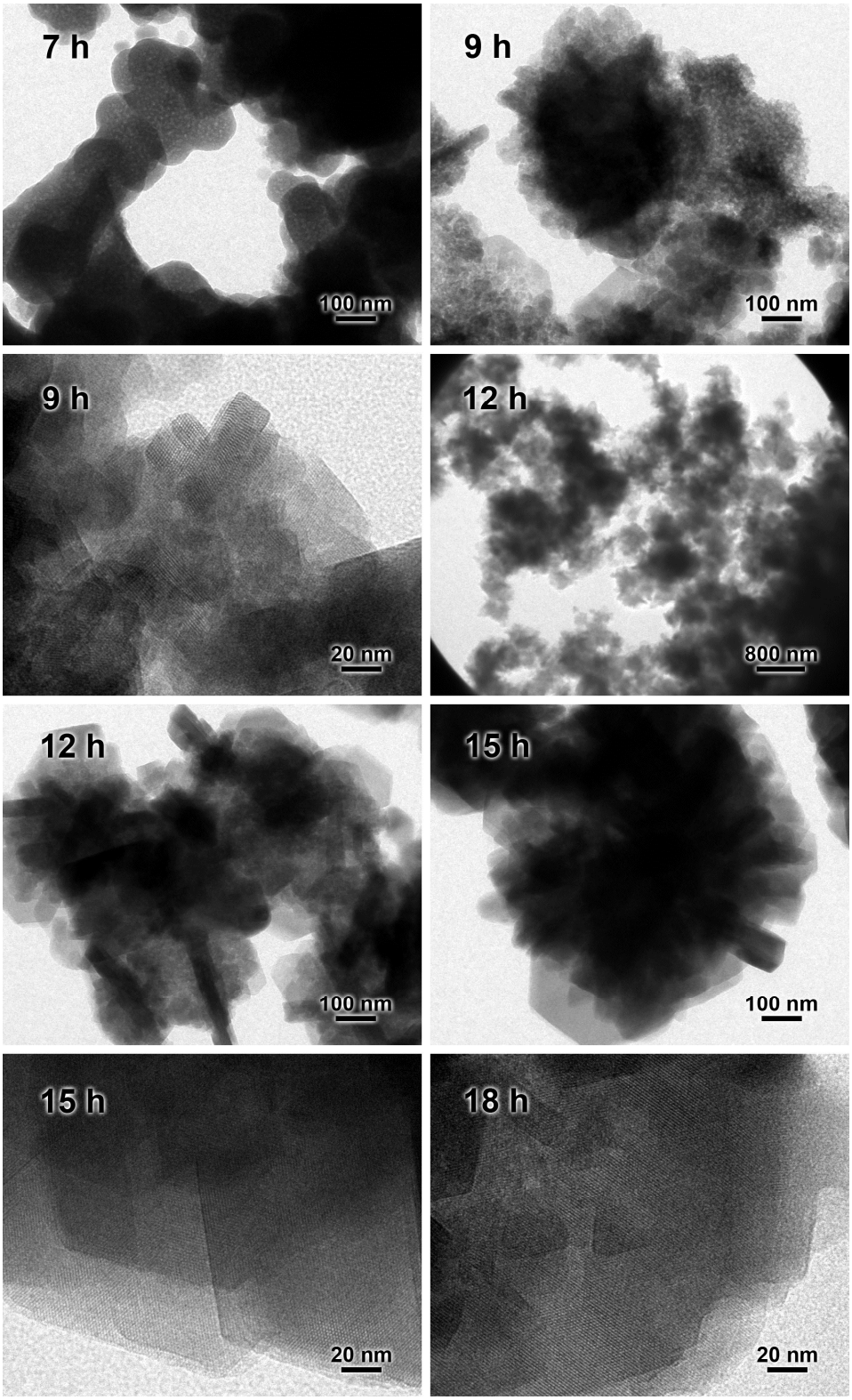

Figure A2.2m. TEM images (at different reaction time and magnifications) of products from the precursor gel where n = 10.8, x = 0.

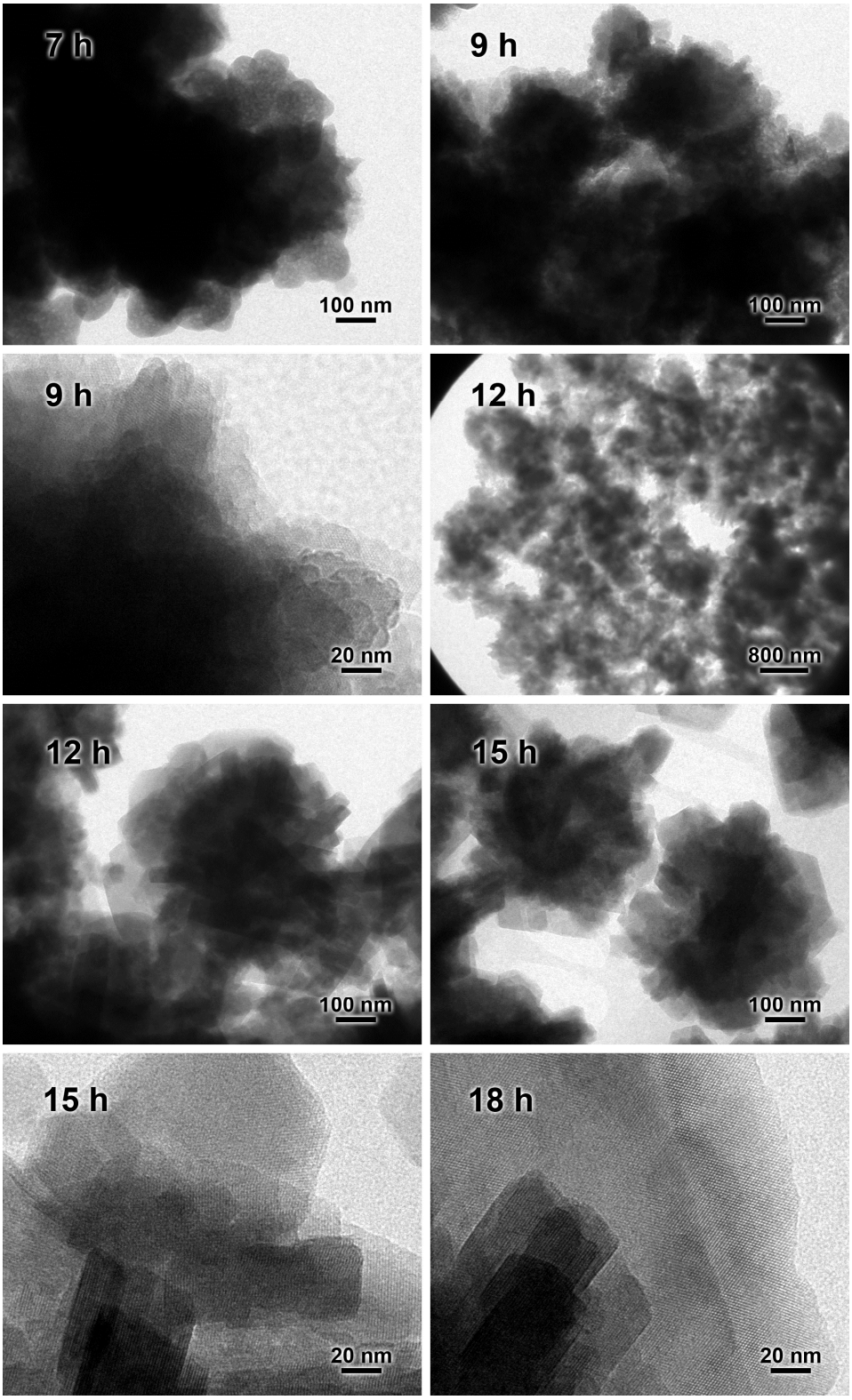

Figure A2.2n. TEM images (at different reaction time and magnifications) of products from the precursor gel where n = 11.8, x = 0.

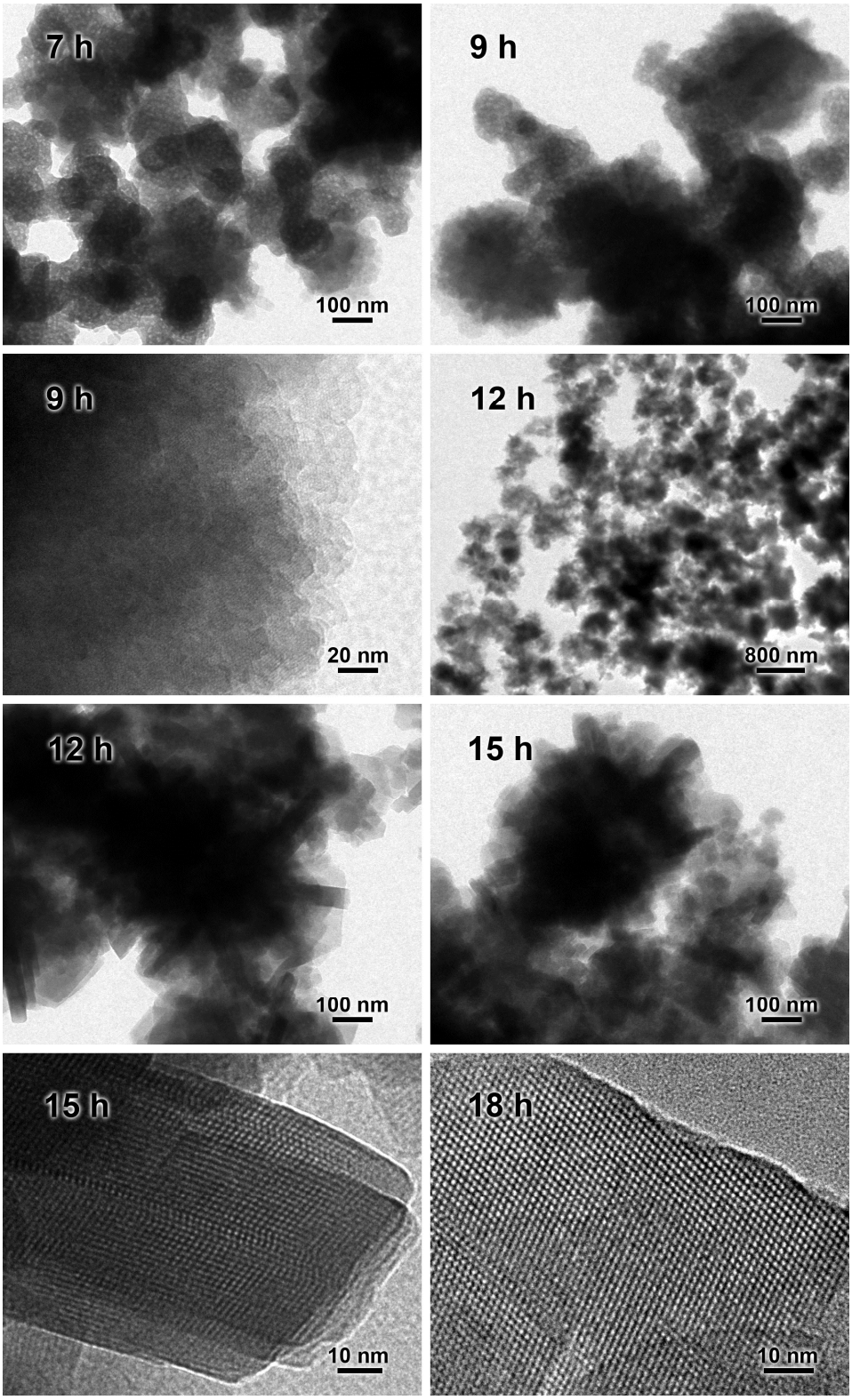

Figure A2.2o. TEM images (at different reaction time and magnifications) of products from the precursor gel where n = 13.8, x = 0.